frontiers | Research Topics

Forests under pressure: The need for interdisciplinary approaches to address forest vulnerability to tree mortality in response to drought

Edited by
Angelo Rita, Francesco Ripullone, Jesús Julio Camarero, Giovanna Battipaglia and Veronica De Micco

Published in
Frontiers in Plant Science
Frontiers in Forests and Global Change

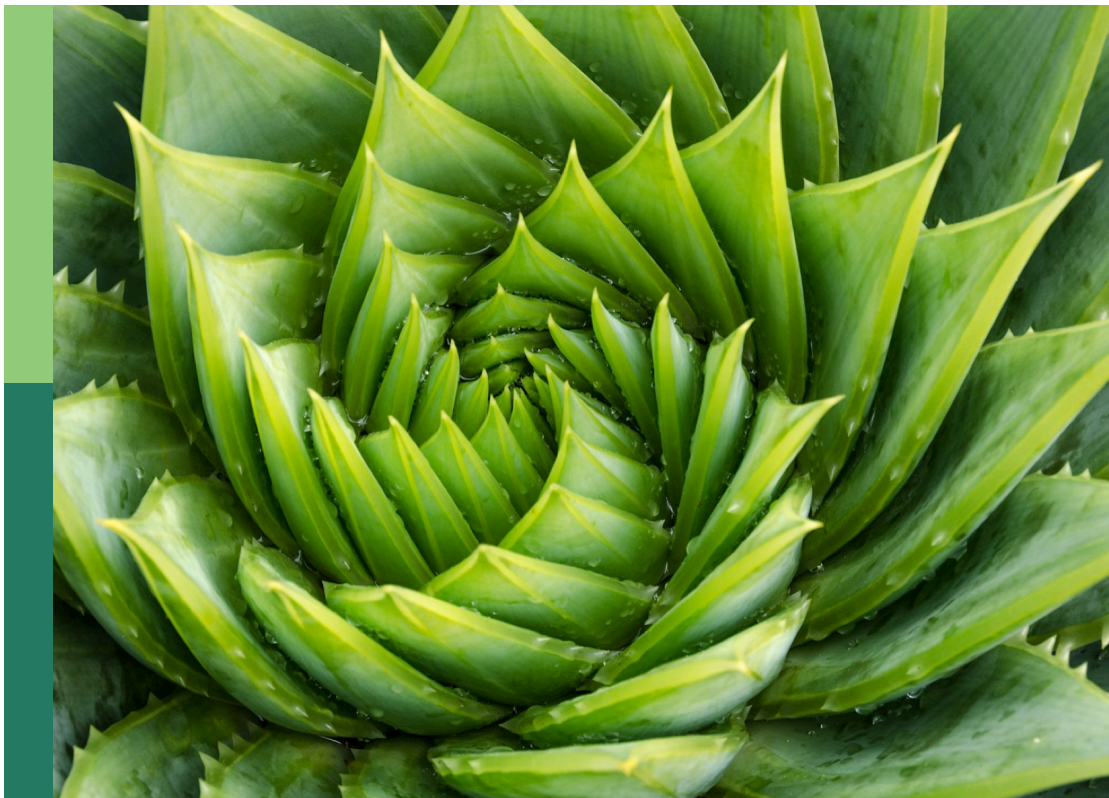

ISSN 1664-8714
ISBN 978-2-83251-091-9
DOI 10.3389/978-2-83251-091-9

About Frontiers

Frontiers is more than just an open access publisher of scholarly articles: it is a pioneering approach to the world of academia, radically improving the way scholarly research is managed. The grand vision of Frontiers is a world where all people have an equal opportunity to seek, share and generate knowledge. Frontiers provides immediate and permanent online open access to all its publications, but this alone is not enough to realize our grand goals.

Frontiers journal series

The Frontiers journal series is a multi-tier and interdisciplinary set of open-access, online journals, promising a paradigm shift from the current review, selection and dissemination processes in academic publishing. All Frontiers journals are driven by researchers for researchers; therefore, they constitute a service to the scholarly community. At the same time, the *Frontiers journal series* operates on a revolutionary invention, the tiered publishing system, initially addressing specific communities of scholars, and gradually climbing up to broader public understanding, thus serving the interests of the lay society, too.

Dedication to quality

Each Frontiers article is a landmark of the highest quality, thanks to genuinely collaborative interactions between authors and review editors, who include some of the world's best academicians. Research must be certified by peers before entering a stream of knowledge that may eventually reach the public - and shape society; therefore, Frontiers only applies the most rigorous and unbiased reviews. Frontiers revolutionizes research publishing by freely delivering the most outstanding research, evaluated with no bias from both the academic and social point of view. By applying the most advanced information technologies, Frontiers is catapulting scholarly publishing into a new generation.

What are Frontiers Research Topics?

Frontiers Research Topics are very popular trademarks of the *Frontiers journals series*: they are collections of at least ten articles, all centered on a particular subject. With their unique mix of varied contributions from Original Research to Review Articles, Frontiers Research Topics unify the most influential researchers, the latest key findings and historical advances in a hot research area.

Find out more on how to host your own Frontiers Research Topic or contribute to one as an author by contacting the Frontiers editorial office: frontiersin.org/about/contact

Forests under pressure: The need for interdisciplinary approaches to address forest vulnerability to tree mortality in response to drought

Topic editors

Angelo Rita — University of Naples Federico II, Italy
Francesco Ripullone — University of Basilicata, Italy
Jesús Julio Camarero — Spanish National Research Council (CSIC), Spain
Giovanna Battipaglia — University of Campania Luigi Vanvitelli, Italy
Veronica De Micco — University of Naples Federico II, Italy

Citation

Rita, A., Ripullone, F., Camarero, J. J., Battipaglia, G., De Micco, V., eds. (2023). *Forests under pressure: The need for interdisciplinary approaches to address forest vulnerability to tree mortality in response to drought*. Lausanne: Frontiers Media SA. doi: 10.3389/978-2-83251-091-9

Table of contents

frontiers | Frontiers in Forest and Global Change

TYPE Editorial
PUBLISHED 09 February 2023
DOI 10.3389/ffgc.2023.1120987

OPEN ACCESS

EDITED BY
Aaron Shiels,
Animal and Plant Health Inspection Service (USDA), United States

REVIEWED BY
John Robert Healey,
Bangor University, United Kingdom

*CORRESPONDENCE
Francesco Ripullone
✉ Francesco.ripullone@unibas.it

SPECIALTY SECTION
This article was submitted to Forest Disturbance, a section of the journal Frontiers in Forests and Global Change

RECEIVED 10 December 2022
ACCEPTED 26 January 2023
PUBLISHED 09 February 2023

CITATION
Rita A, Ripullone F, Battipaglia G, Camarero JJ and De Micco V (2023) Editorial: Forests under pressure: The need for interdisciplinary approaches to address forest vulnerability to tree mortality in response to drought. *Front. For. Glob. Change* 6:1120987. doi: 10.3389/ffgc.2023.1120987

Editorial: Forests under pressure: The need for interdisciplinary approaches to address forest vulnerability to tree mortality in response to drought

Angelo Rita[1], Francesco Ripullone[2]*, Giovanna Battipaglia[3], J. Julio Camarero[4] and Veronica De Micco[1]

[1]Agricultural Department, University of Naples Federico II, Naples, Italy, [2]School of Agricultural, Forest, Food and Environmental Sciences, University of Basilicata, Potenza, Italy, [3]Department of Environmental, Biological and Pharmaceutical Sciences and Technologies, University of Campania Luigi Vanvitelli, Caserta, Italy, [4]Spanish National Research Council, Pynean Institute of Ecology, Spanish National Research Council, Zaragoza, Spain

KEYWORDS

climate change, drought stress, forest vulnerability, growth decline, hydraulic traits, remote sensing monitoring

Editorial on the Research Topic
Forests under pressure: The need for interdisciplinary approaches to address forest vulnerability to tree mortality in response to drought

Introduction

Extensive tree mortality and widespread forest dieback (i.e., high tree mortality rates at local to regional scales) linked to drought and temperature stress is an emergent concern in many forests that are sensitive to climate change. These dieback episodes highlight how the high vulnerability of forest ecosystems to climatic stressors can manifest as losses in tree vigor (e.g., leaf shedding, canopy and shoot dieback, growth decline, and ultimately tree death). Extended to a larger scale, dieback phenomena may lead to multiple joint effects on biosphere-atmosphere interactions and may play an important role in future water-carbon-cycle feedbacks through complex effects on forest biophysical properties and biogeochemical cycles. The assessment of forest vulnerability and forecasting changes in tree health in the context of climate change are complex issues, with various specific critical ecological, social, and economic thresholds across biomes and countries. Notwithstanding the variety of specific issues to solve, interdisciplinary research and networking are crucial to improve the monitoring of tree mortality and forest dieback. Therefore, this Research Topic of nine papers intends to improve our understanding of how forest ecosystems respond to global warming, especially to drought-induced climate change, covering different aspects, scales, methodologies, and approaches in the study of forest health.

Importance of hydraulic traits

Investigating the causes and mechanisms behind forest mortality is a research priority. The failure of the hydraulic system can be an important contributor to dieback phenomena and was reviewed by Anfodillo and Olson to explore possible links between vulnerability to drought-induced *hydraulic failure* and xylem water-transporting conduit diameter.

Although existing physiological experiments have failed to find a consistent diameter-vulnerability link, the authors maintain caution before rejecting this possibility, as the majority of the studies are from temperate regions. Additionally, there is an absence of experiments examining vulnerability in a wide range of conduit diameters under similar tensions in species adapted to frost-free and drought-prone habitats. Zhao et al. highlighted the importance of *hydraulic traits* in shaping community assembly patterns with different water availability conditions. They tested the difference between economic and hydraulic traits under different conditions of water availability in a large survey experiment of 167 species across two contrasting climatic regions (i.e., semi-arid and humid) in China. Their findings may have significant consequences for predicting plant species responses to drought-induced climate change. Using a dendroecological and process-based growth model approach, Valeriano et al. investigated two *Pinus pinaster* stands with contrasting growth rates and showing recent dieback in north-eastern Spain. They demonstrated that stand vulnerability to drought is contingent on site-specific conditions and highlighted the role of environmental conditions, such as access to soil water or *hydraulic traits,* and suggested their inclusion in process-based growth models to better forecast dieback.

Monitoring forest vulnerability using a remote sensing approach

Satellite-borne remote sensing is a suitable method for monitoring networks that enables the near real-time identification of forests that are subjected to dieback phenomena. Buras et al. created the European Forest Condition Monitor (EFCM), which is a remote-sensing based, freely available, interactive web information tool. Using six specific examples related to spring phenology, drought, late-frost, tree dieback, ice storm, and windthrow, the authors highlighted how the EFCM, by using the remotely sensed forest greenness data, may have the potential to aid in identifying hotspots of forest decline. Furthermore, they discussed the advantages and limitations when monitoring forest conditions at large scales to help guide potential users toward an appropriate interpretation. With freely available cloud computing infrastructures, such as the Google Earth Engine, access to satellite data and high-performance computing resources has become straightforward. Montzka et al. employed Sentinel-2 satellite data for monitoring tree crown transparency in spruce stands of the Northern Eifel region in Germany. They provided interesting insights that showed an increase in damaged trees from 2018 to 2020 in the region and identified sites where forest management may help by transforming spruce monocultures to mixed forests to improve biodiversity and resilience in future negative climate scenarios.

Assessing drought and other disturbance impacts on forests

Drought is considered one of the key drivers of forest dieback but other disturbances, in combination with drought, may also play a relevant role at large and small scales. San-Eufrasio et al. examined how 8-month *Quercus ilex* seedlings from three contrasting Andalusian populations responded to the combined stresses of *Phytoptora cinnamomi* (a widespread soil-borne pathogen causing root rot and cankering) and drought using morphological, physiological, and proteomics data. In all three populations, seedling damage (leaf chlorosis and necrosis) and mortality were greater under combined stresses; however, resilient individuals were also identified, at different percentages, in all the populations, linking variable proteins as putative markers for resilience in *Q. ilex*. Furthermore, Wang et al. applied an attribution approach to quantify the area and potential carbon loss/transfer in the continental US from four types of disturbances (anthropogenic, fire, drought-associated, and other) from 2000 to 2014. Anthropogenic disturbances were the most important drivers, contributing to 58.1%, whereas natural disturbances accounted for ∼41.9% of potential carbon loss/transfer. This result suggests that natural disturbances also played a crucial role in forest carbon turnover, and that these data can be used for evaluating the performances of predictive models of tree mortality under droughts. Shan et al. used extreme climate indices and tree-ring data to investigate the effects of climate events and anthropogenic activities on wild forests. Under the prolonged influence of inappropriate anthropogenic activities, extreme climate events caused the outbreak of pests and diseases resulting in the degeneration of wild forests. Zhang et al. focused on malondialdehyde, a substance produced by membrane lipids, that can be used as a drought indicator to evaluate the degree of plasma membrane damage and the ability of plants to tolerate drought stress. They applied the best malondialdehyde-predicting model to two exotic conifer tree species as plant material exposed to drought stress.

Altogether, these nine contributions to this Research Topic cover several aspects of forest vulnerability and mortality. This collection demonstrates advances in investigating and monitoring forest vulnerability and tree mortality from the local to regional scales. Some of these papers focused on a singular issue related to the mechanisms (i.e., hydraulic traits) involved in dieback phenomena, while other papers in this Research Topic highlighted the importance of remote sensing in detecting forest areas subjected to mortality phenomena. Each of the nine papers identified knowledge gaps and outlined future research directions. Overall, by reading these papers comes out the need to fill the gaps through integrated multi-scale (from cells to plant community), multi-temporal (from xylogenesis to long-term forecasting) and multi-method (from microscopy to satellite applications) approaches.

Author contributions

FR and AR drafted manuscript preparation. All authors reviewed the text and approved the final version of the manuscript.

Acknowledgments

We would like to thank the authors, reviewers, and the Frontiers Editorial Office for their support in creating this special topic, and hope that fellow scientists and grant managers will enjoy reading it as much as we enjoyed editing it.

Conflict of interest

The authors declare that the research was conducted in the absence of any commercial or financial relationships that could be construed as a potential conflict of interest.

Publisher's note

frontiers in Plant Science

ORIGINAL RESEARCH
published: 16 June 2021
doi: 10.3389/fpls.2021.608211

Do Extreme Climate Events Cause the Degradation of *Malus sieversii* Forests in China?

Qianjuan Shan[1,2], Hongbo Ling[1,2,3], Hangzheng Zhao[4], Mengyi Li[5], Zikang Wang[1,2] and Guangpeng Zhang[1,2]*

[1] State Key Laboratory of Desert and Oasis Ecology, Xinjiang Institute of Ecology and Geography, Chinese Academy of Sciences, Urumqi, China, [2] University of Chinese Academy of Sciences, Beijing, China, [3] Xinjiang Aksu Oasis Agro-Ecosystem Observation and Experiment Station, Urumqi, China, [4] School of Chemical and Environmental Engineering, China University of Mining and Technology, Beijing, China, [5] School of Civil Engineering, Tianjin University, Tianjin, China

Frequent extreme climate events have attracted considerable attention around the world. *Malus sieversii* in Xinjiang is the ancestor of cultivated apple, and it is mainly distributed in the Ili river valley at end of the Tianshan Mountains. Wild fruit forests have been degraded, but the cause remains unclear. In order to identify whether extreme climate events caused this degradation reanalysis data and atmospheric circulation indices were used to determine the trends and the reasons for extreme climate changes. Subsequently, we further investigated the effect of extreme climate events on wild fruit forest using characteristics of extreme climate indices and tree-ring chronology. We found increasing trends in both extreme precipitation and warm indices, and decreasing trends in cool indices. Extreme climate events were mainly associated with the Atlantic Multidecadal Oscillation (AMO). Analysis of data of wind and geopotential height field at 500 hPa showed that strengthening wind, increasing geopotential height, cyclone and anti-cyclone circulation drivers contributed to extreme climate events. In the non-degraded region, there were significant positive correlations between tree-ring chronology and both extreme precipitation and extreme warm indices (except for warm spell duration indicator). The other extreme indices (except for heavy rain days) had a large correlation range with tree-rings in a 4–8-year period. These results indicated that extreme precipitation and extreme warm indices intensified *M. sieversii* growth of the non-degraded region on multi-time scales. In contrast, the degraded region showed insignificant negative relationship between tree-ring chronology and both extreme precipitation and extreme warm indices [except for warm spell duration index (WSDI)], and significant negative correlations in a 4–8-year period were detected between tree-ring chronology and most of the extreme precipitation indices, including heavy rain days, very wet days, cold spell duration indicator, simple precipitation intensity index (SDII), and annual total precipitation. Under the long disturbance of inappropriate anthropic activities, extreme climate has caused the outbreak of pests and diseases resulting in the degeneration of wild fruit forest. Our study provides scientific guidance for the ecosystem conservation in wild fruit forest in China, and also across the region.

Keywords: extreme climate indices, atmospheric circulation, anthropogenic impact, dendrochronology of *Malus sieversii* trees, the degraded wild fruit forest

OPEN ACCESS

Edited by:
Angelo Rita,
University of Basilicata, Italy

Reviewed by:
Mario A. Pagnotta,
University of Tuscia, Italy
Irina P. Panyushkina,
University of Arizona, United States

***Correspondence:**
Hongbo Ling
linghb@ms.xjb.ac.cn

Specialty section:
This article was submitted to Plant Abiotic Stress, a section of the journal Frontiers in Plant Science

Received: *19 September 2020*
Accepted: *06 May 2021*
Published: *16 June 2021*

Citation:
Shan Q, Ling H, Zhao H, Li M, Wang Z and Zhang G (2021) Do Extreme Climate Events Cause the Degradation of Malus sieversii Forests in China? Front. Plant Sci. 12:608211. doi: 10.3389/fpls.2021.608211

INTRODUCTION

Global warming has led to increasing of extreme climate events around the world in the past 60 years, such as heat waves, high rainfall and flooding (Powell and Keim, 2015; Sun et al., 2016; Xiao et al., 2016). Extreme climate events have large impact on natural ecosystems and human society (Mullan et al., 2012; Song et al., 2015; Sun et al., 2016), and have characteristics of suddenness, unpredictability and destructiveness (Alexander et al., 2013; Raineri, 2013). Therefore, the majority of researchers suggest that future study of climate change should focus on extreme rather than mean climate change (Shi et al., 2018). Arid and semi-arid areas in northwest China are among the most sensitive areas to climate change, due to vast desert basins, high mountains and being far from the sea (Shi et al., 2007). Extreme weather events occur frequently throughout the arid region of northwest China, such as extreme heat, drought and snowstorms (Li et al., 2019; Han et al., 2020; Pi et al., 2020; Xie et al., 2020). Extreme temperatures are clearly associated with atmospheric circulation, and extreme precipitation shows spatial differences (Wang B. L. et al., 2013; Deng et al., 2014; Han et al., 2016). Notably, the Ili river valley at the western end of the Tianshan Mountains, the world-famous distribution area of wild fruit forest, is not only the vital west water vapor channel in northwest China, but also is the transitional zone of westerly circulation and monsoons (Qian et al., 2001; Shi et al., 2007), which results in frequent extreme weather events there. However, the change characteristics of the extreme climate and its driving mechanism have not been explored, therefore, the first aim in this study is to solve the above scientific problem.

The impact of extreme climate on forest ecosystems has both positive and negative aspects according to previous studies. The negative effects of extreme climate are following expressed by drought, heat waves and wildlife and insect disturbance causing increased tree mortality and dead wood, reduced species diversity and reduced productivity (Ciais et al., 2005; Rammig et al., 2010; Birch, 2014). Extreme high temperature causes lower water use efficiency by accelerating the transpiration of vegetation, and also exacerbates outbreaks of forest pests and diseases (Kolb et al., 2016; Pettit et al., 2020), all of which slow tree growth. Extreme drought results in reduced photosynthesis, which decreases growth and increases mortality of trees (Feldpausch et al., 2016), and also impacts on phenology, such as flowering cycles and end-of-season vegetative growth (Nagy et al., 2013; Cardil et al., 2014). Extreme low temperature such as frost and freezing can impair the extension of leaves (Vanoni et al., 2016), thus reducing photosynthesis and carbon absorption and so slowing tree growth. In contrast, the positive effects of extreme climate follow. Global warming can exacerbate the hydrological cycle leading to changes in rainfall patterns (both spatially and temporally) with extreme wetness and drought becoming more frequent (Min et al., 2011; Cook et al., 2015; Touma et al., 2015; Huang et al., 2016). Extreme precipitation not only satisfies the basic physiological and biochemical processes of vegetation, but also restrains the negative impact of drought on trees caused by high temperature. Compared to extreme drought, extreme wetness compensates for post-drought carbon loss in dry forests, and so enhances tree growth (Jiang et al., 2019). The above extreme climate changes have a significant impact on forest composition and forest main productivity. Therefore, the study of extreme climate change has become an important ecological problem to understand changes in forest growth (Stocker et al., 2013). *Malus sieversii* forest in Xinjiang is one of the major original areas of wild fruit trees worldwide, and includes many wild resources. These include the dominant species of *M. sieversii* confirmed as the ancestor of cultivated apple (Duan et al., 2017) and which has become a Grade II protected plant in China (Archetti, 2009). Following the increasing mortality of *M. sieversii*, the wild fruit forest ecosystem has been seriously damaged and some wild fruit forest region degraded obviously (Fang et al., 2019). One study showed that *M. sieversii* growth was associated with spring precipitation and winter temperature (Panyushkina et al., 2017). However, whether extreme climate change has positive or negative effects on this forest growth has not been determined, and we wonder if the degradation of wild fruit forest may be caused by extreme change, these scientific problems are addressed in this study.

In investigating the above two scientific issues, daily temperature and precipitation data of three meteorological stations were used to calculate extreme climate indices. Identifying the change characteristics of extreme climate and its driving mechanism can be determined using the relationships between extreme climate indices and atmospheric circulation indices. Among many kinds of paleoclimatic substitute data, tree-rings offer a great advantage in research on paleoclimatic information archives with the benefits of accurate annual resolution, a large number of replications, and easy access, long-scale hydrological and climate change chronologies obtained from tree-ring data have unparalleled advantages and great potential in this respect (Fan et al., 2020). Moreover, tree-rings are a sensitive material to reflect the situation of tree growth, and can also record the historic climate and surrounding change (Fritts, 1976). Tree-ring width chronology has been used to reflect the tree growth and the response to changes of surrounding in many studies. Decuyper et al. (2020) indicated that the years of extreme climate (drought and high temperature) resulted in a matching small tree-ring chronology index. In contrast, the tree-ring chronology index is large with the occurrence of extreme wetness (Jiang et al., 2019). Additionally, tree-ring width chronology can also record the response to historic anthropogenic changes (Andrade et al., 2019; Mazza et al., 2020). Human disturbance such as deforestation, pruning and grazing decrease tree growth by reducing photosynthesis, and the resulting tree-ring chronology index is small. In view of the advantages of tree-ring technology, we use it to analyze the change of tree growth, in two regions. We contrastively analyzed the tree-ring chronology of *M. sieversii* in the wild fruit forests in Gongliu County (a non-degraded region) and Xinyuan County (a degraded region) in the Ili river valley (see **Supplementary Table 1** for the classification of degradation degrees), where wild fruit forests are widely distributed. The influence process of extreme climate change on the growth of wild fruit forests was revealed by comparing and analyzing the correlations between extreme climate indices and tree-ring chronology. The reasons

for the degradation of wild fruit forests in Xinjiang, including both extreme climate and human activities, were explored.

MATERIALS AND METHODS

Study Site

Malus sieversii forest in Xinjiang China is the origin of the world's cultivated apples (Wang et al., 2018), and *M. sieversii* is the dominant species in the wild fruit forest mainly distributed on the Tianshan Mountains on both sides of the Ili river valley, China, with a total area of 8,786 km^2. The longitude and latitude ranges are 80°42′52″–83°37′17″E and 43°13′14″–44°26′28″N, and the height above sea level is 1,100–1,700 m. The climate in the study area is a typical temperate continental climate. The water vapor transport in summer and winter comes from the Arctic and Atlantic Oceans, respectively. The average annual precipitation in this area is 260–800 mm, and average annual temperature is 10.4°C (Wang H. et al., 2013; Kong et al., 2017). Compared with cultivated apple, *M. sieversii* has a wider range of adaptation to drought, extreme temperature, and pathogens (Luby et al., 2001; Dzhangaliev, 2002). In order to determine the causes of degradation of wild fruit forests, we selected two wild fruit forest sample points (with similar altitudes of 1,100–1,500 m): in Gongliu County (a non-degraded area) with less human interference, the dead trees represent less than one third of the total trees, and the range of canopy loss is 10–40% in Xinyuan County (a degraded area) with greater human interference, 1/3–3/4 of all trees are dead, and the tree canopy loss exceeds 40%. The soils in the two sampling sites are mainly mountain black brown soils (Lin and Cui, 2000), and the species distributions at the two sampling points were similar (up to 441 species). The distribution of sampling sites in the study area is shown in **Figure 1**.

Data Source

(1) Tree-ring data: Tree-ring width can reflect the radial growth of individual trees, during the vegetation season. In order to avoid being affected by competition, 94 wild apple trees (49 trees in the degraded area, 45 trees in the non-degraded area) were selected from isolated, mature and healthy trees in the two regions, In this way, the selected trees were less affected by the competition of surrounding plants and the growth was more steady. Then, we used Pressler increment borers to extract two radial cores per tree, which were brought back to the laboratory in hollow plastic tubes. (2) Climate data: This study used the daily temperature and precipitation data of meteorological stations including Gongliu, Xinyuan, and Tekesi for calculating the extreme indices for 1961–2017,during which time these stations were not relocated. The water vapor of northwest China is mainly from moisture brought by the westerlies (Chen et al., 2017). To investigate the oceanic influence on the region climate change, we selected four main atmospheric circulation indices including Atlantic Multidecadal Oscillation index (AMO), Atlantic Meridional Mode index (AMM), Pacific Decadal Oscillation index (PDO) and North Atlantic Oscillation index (NAO)[1], which are the main oceanic influence of the climate change in northwest China (Chen et al., 2014, 2017; Steinman et al., 2015; Sun et al., 2020). To quantify the reasons for changes in large-scale atmospheric circulation, monthly mean geopotential height and wind fields at 500 hPa during 1961–2017 were derived from the NCEP/NCAR reanalysis data[2], and the resolution of the reanalysis variables was is 2.5° × 2.5°.

Method

In order to determine whether soil conditions contribute to the difference in tree growth between the two areas, we used *t*-tests in Statistical Product and Service Solutions software (SPSS, IBM Inc., Armonk, NY, United States) to test the two regions soil differences in physical and chemical properties of soil of the two regions. Then, we calculated the required extreme climate indices using climate data and developed the tree-ring width chronologies of the two regions from the tree core samples.

[1]https://www.esrl.noaa.gov/

[2]https://psl.noaa.gov/data/gridded/data.ncep.reanalysis.pressure.html

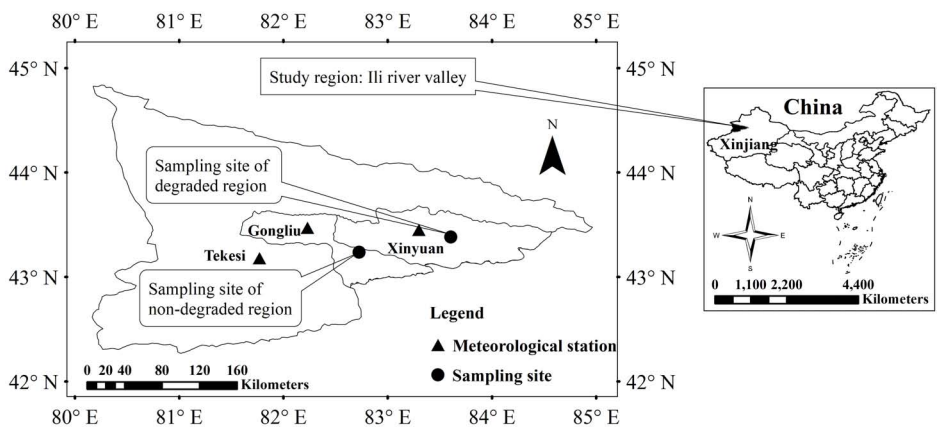

FIGURE 1 | Overview of the study area. The vector map of China was obtained by vectorizing the Chinese map [Approval Number: GS (2016) No. 2893] supervised by the Ministry of Land and Resources of China.

Moreover, characteristic analysis was applied to *M. sieversii* tree-ring chronology and the extreme climate indices series using Mann-Kendall trend tests, Mann–Whitney *U* tests and periodic analysis. Meanwhile, based on the potential impact of climate change in northwest China, we performed Pearson's correlation analysis between the atmospheric circulation indices and extreme climate indices to explore the impact of atmospheric circulation types on extreme climate changes in the study area. Finally, through Pearson's correlation and wavelet coherence analysis of extreme climate indices and tree-ring chronology, we discussed the multi-scale effects of extreme climate events on tree growth in the study area, and analyzed the main reasons for degradation of wild apple forest using the data form the *M. sieversii* forests. The specific flow is shown in **Figure 2**, with the method given in the following.

Sample Processing and Chronology Development

After sampling, core samples were air-dried, before ring-width measurements, all samples were sanded with progressively finer grades of sandpaper (120–1,200) to make the growth ring boundaries more visible. Ring widths were measured with a LINTAB 6 measuring system (Rinntech-Metriwerk GmbH & Co. KG, Heidelberg, Germany) at a precision of 0.01 mm using the tree-ring analysis software TSAP-Win (Rinn, 2003). The COFECHA cross-dating quality control program was used for cross-dating test and calculating moving correlations between each individual series and the mean site series (Holmes, 1983); some cores with small correlation coefficients, short tree age and many singular points were eliminated. In order to get a long time-series, 12 long-core samples to establish the chronology in the non-degraded region (common period: 1955–2017), and 20 core samples in the degraded region (common period: 1965–2017) were used to establish the dendrochronology. The ARSTAN program (calculation of tree-ring chronology) was used to establish the tree-ring chronology of the two study areas on the basis of the accurate cross-dating (Cook, 1985).The growth trend of the tree-ring chronology was fitted using a 25-year step spline function and the tree-ring chronology indices were calculated by dividing the measured value by the fitted value of tree ring width. The chronology statistics are given in **Supplementary Table 3**.

Classification and Definition of Extreme Indices

In this study, we calculated all extreme indices based on mean daily temperature and precipitation data of three stations. Data quality control was performed using RClimDex software[3], which was developed and maintained by Zhang and Yang at the Climate Research Branch of the Meteorological Service of Canada. We selected 17 extreme indices from 27 core indices introduced by the Expert Team on Climate Change Detection and Indices (ETCCDI)[4] (You et al., 2013; Guan et al., 2015; Rahimi and Hejabi, 2018). We grouped the extreme temperature indices into four categories (Choi et al., 2009; Wang et al., 2013). The first category was the indices based on the relative (floating) threshold, abbreviated as the relative indices, we selected the cold days (TX10p: number of days when daily max temperature < 1961–2017 10th percentile) and warm nights (TN90p: number of days when daily min temperature > 1961–2017 10th percentile). The second category was indices based on original observation data and fixed thresholds, abbreviated as the absolute indices, we selected the numbers of hot nights, icing days, and frost days (TR, ID, and FD, respectively). The third category was the highest and lowest daily maximum and minimum temperatures for the

[3]http://etccdi.pacificclimate.org/software.shtml

[4]http://etccdi.pacificclimate.org/

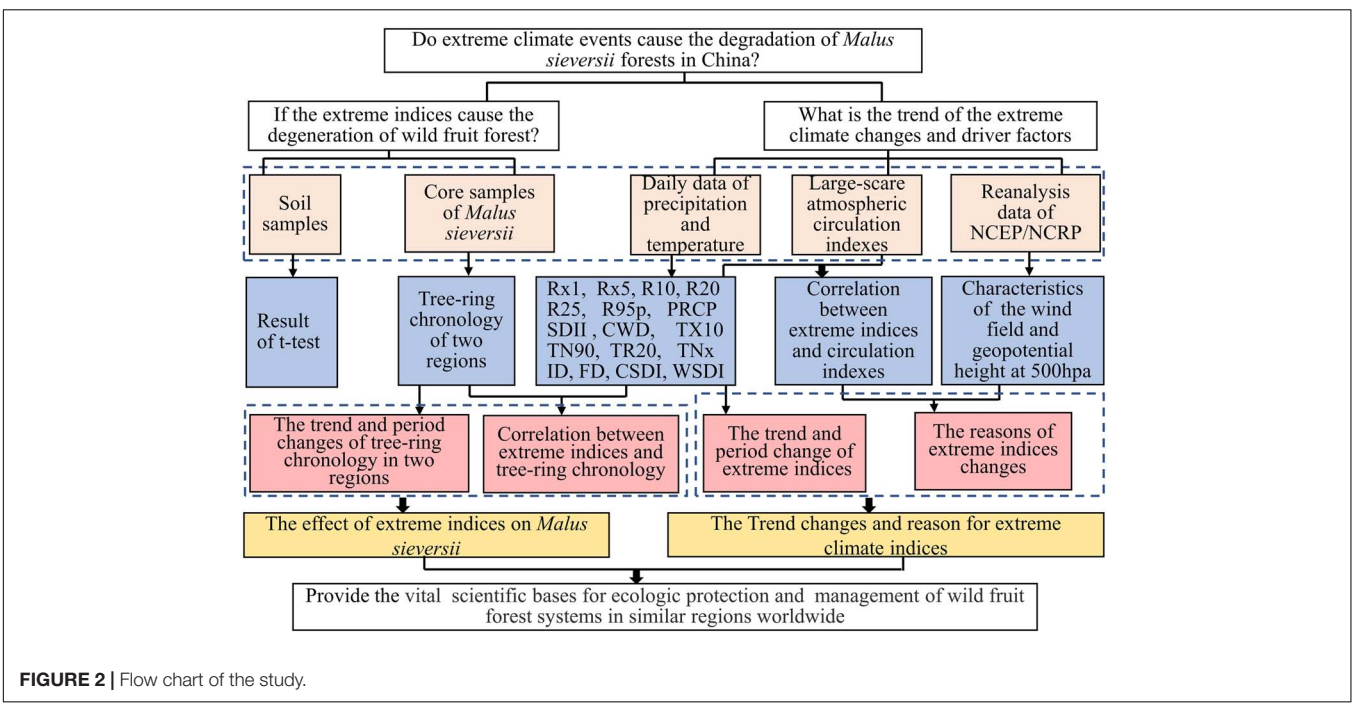

FIGURE 2 | Flow chart of the study.

month, abbreviated as the extreme value indices, we selected the monthly maximum value of daily minimum temperature (TNx). The fourth category was other indices, we selected the WSDI and cold spell duration index (CSDI).

Bonsal's nonparametric scheme was used to determine the threshold of extreme precipitation (Bonsal et al., 2010), the specific calculation follows:

If the number of one climate factor is N, putting these values in ascending order $x_{1,}x_{2},\ldots,x_{m},\ldots,x_{n}$, and the probability that a value is less than or equal to x_m:

$$P = (m - 0.31)/(n + 0.38)$$

where P is the percentile, m is the sequence number of x_m, and n is the number of climate factors.

The percentile threshold method was using to calculate R95 (annual total precipitation when daily total precipitation > 95th percentile). Eight extreme precipitation indices were all calculated by RClimDex software: maximum 1-day precipitation (RX1), maximum 5-day precipitation (RX5), annual count of days when annual total precipitation ≥10, 20, and 25 mm (R10, R20, and R25, respectively), annual total precipitation (PRCP), simple precipitation intensity index (SDII) and consecutive wet days (CWD).

Nonparametric Tests

Mann-Kendall trend test

The Mann-Kendall statistical test is a nonparametric test method. The time series (X_1, X_2, X_3, . . ., X_n) were compared in turn, and the results were recorded as sgn (θ):

$$sgn(\theta) = \begin{cases} 1, & \theta > 0 \\ 0, & \theta = 0 \\ -1, & \theta < 0 \end{cases} \quad (1)$$

The Mann-Kendall statistical calculation result was:

$$s = \sum_{i=1}^{n} \sum_{k=i+1}^{n} sgn(x_k - x_i) \quad (2)$$

where x_k and x_i are random variables and n is the length of the selected data sequence.

The test statistic Z_c was calculated as follows:

$$Z_c = \begin{cases} \frac{s-1}{\sqrt{var(s)}}, s > 0 \\ 0, \quad s = 0 \\ \frac{s+1}{\sqrt{var(s)}}, s < 0 \end{cases} \quad (3)$$

In this equation, $|Z_c| \geq 1.96$ and $|Z_c| \geq 2.58$ indicated that the sample sequence had a significant trend change at $p < 0.05$ and 0.01, respectively, $Z_c > 0$ indicated a rising trend and $Z_c < 0$ indicated a declining trend (Ling et al., 2014).

Mann–Whitney U test

The abrupt-change point should be determined before the abrupt-change test. In this paper, the abrupt-change point was determined according to the trend change of the cumulative anomaly value.

The basic principle of Mann-Kendall test follows:

Suppose the time series is $X = (X_1, X_2, \ldots, X_n)$ and its subsequence $Y = (X_1, X_2, \ldots, X_n)$, and $Z = (X_{n1+1}, X_{n1+2}, \ldots, X_{n1+n2})$. The abrupt-change test is calculated as:

$$Z_c = \frac{\sum_{t=1}^{n_1} r(x_t) - n_1(n_1 + n_2 + 1)/2}{\sqrt{n_1 n_2 (n_1 + n_2 + 1)/12}} \quad (4)$$

In this equation, $r(x_t)$ is the rank of the observed value, n_1 is the number of time series before the abrupt change and n_2 is the number of time series after the abrupt change, then $n_1 + n_2 = n$. If $-Z_{1-a/2} \leq Z_c \leq Z_{1-a/2}$, then the null hypothesis is accepted. Given the test level of a, $Z_{1-a/2}$ is the quantile of the standard normal distribution of 1 – a/2 (Ling et al., 2014).

Analysis of Wavelet Coherence

The wavelet variance represents the strength (energy) of cyclical fluctuation of time series in this scale, and the scale at the corresponding peak value is the main period of this series (Gao and Li, 1993). Therefore, the periodic changes of the climate factors and the tree-ring chronology change were analyzed using wavelet variance.

The wavelet variance is:

$$W_p(a) = W_f(a, b)^2 \quad (5)$$

Wavelet coherence spectrum is used to measure the local correlation degree of two time series in time-frequency space. The wavelet coherence spectrum of two time series X and Y is defined as:

$$R_n^2(s) = \frac{\left|S(s^{-1} W_n^{XY}(s))\right|^2}{S(s^{-1}\left|W_n^X(s)\right|^2) \cdot S(s^{-1}\left|W_n^Y(s)\right|^2)} \quad (6)$$

$$S(W) = S_{scale}(S_{time}(W_n(s))) \quad (7)$$

S_{scale} represents smoothing along the wavelet scaling axis and S_{time} represents smoothing along the wavelet time translation axis.

$$\begin{aligned} S_{time}(W)|_s &= (W_n(s) * c_1^{-t^2/2s^2})|_s \\ S_{scale}(W)|_n &= (W_n(s) * c_2 \textstyle\prod(0.6s))|_n \end{aligned} \quad (8)$$

In this equation, c_1 and c_2 are standardized constants, Π is the rectangular function and the parameter 0.6 is a scale determined based on experience and is related to the solution of the Morlet wavelet wavelength. The significance test of wavelet coherence spectrum adopts the Monte Carlo method. The 95% confidence interval given in this paper is for the wavelet coherence spectrum, and only the phase difference arrow of $R_n^2(s) \geq 0.5$ is marked in the wavelet coherence spectrum.

RESULTS

Extreme Climate Indices

Trend and Periodic Variation of Extreme Precipitation Indices

The extreme precipitation indices for 1961–2017 (**Figure 3**) showed significantly increasing trends ($p < 0.05$) for R25 and

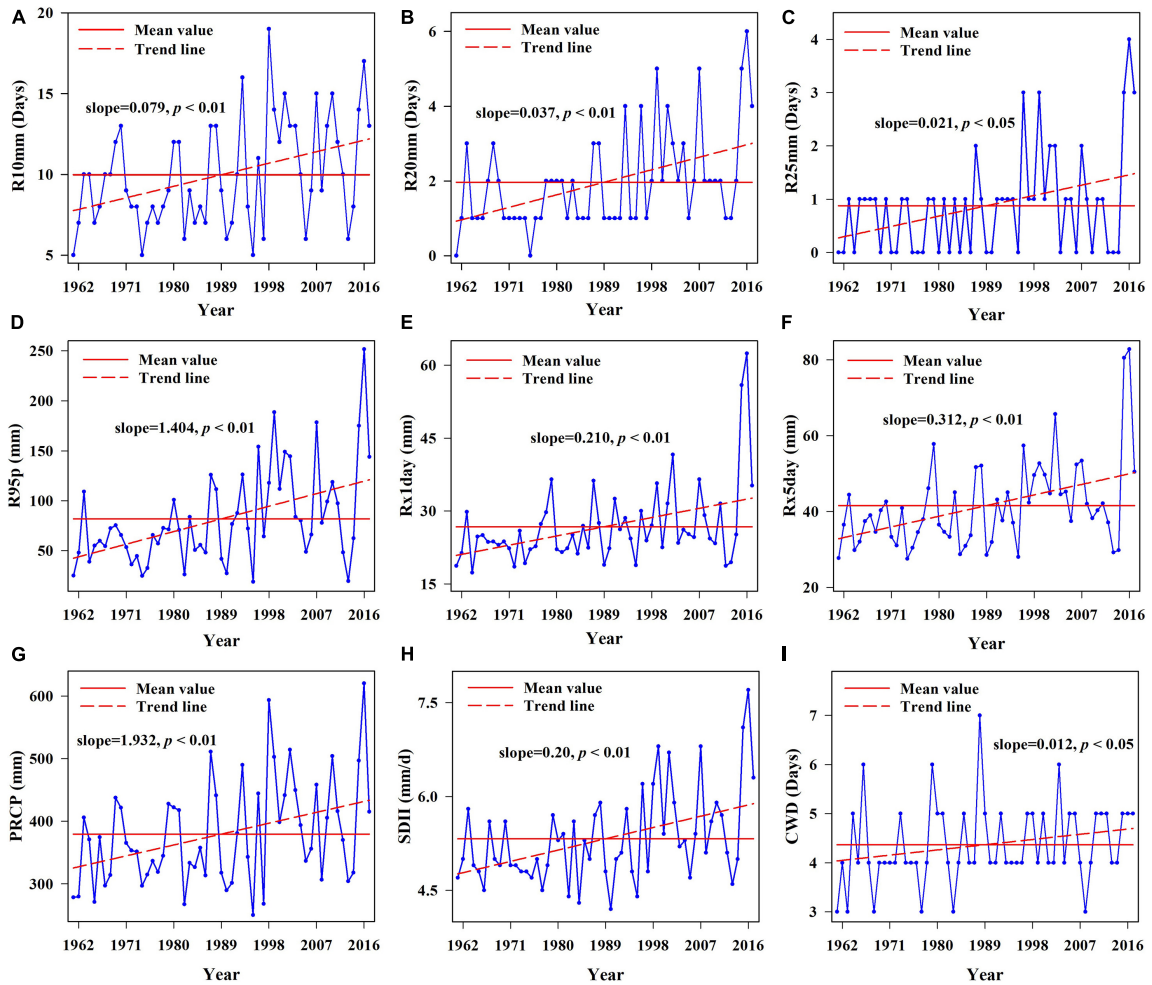

FIGURE 3 | Linear trend charts of annual extreme precipitation indices during 1961–2017. **(A)** Linear trend chart of light rain days, **(B)** linear trend chart of moderate rain days, **(C)** linear trend chart of heavy rain days, **(D)** linear trend chart of very wet days, **(E)** linear trend chart of maximum one-day precipitation, **(F)** linear trend chart of maximum five-day precipitation, **(G)** linear trend chart of annual total precipitation, **(H)** linear trend chart of simple precipitation intensity index, and **(I)** linear trend chart of consecutive wet days.

CWD, and the other extreme precipitation indices showed very significant increasing trends ($p < 0.01$) according to Mann-Kendall trend tests. The number of days of moderate rain, heavy rain and rainfall increased change rates of 0.79, 0.37, and 0.21 d/10 years, respectively (**Figures 3A–C**). Heavy rainfall (R95p) increased at a rate of 14.04 mm/10 years, and heavy rainfall was higher than the average in most years after 1989 (**Figure 3D**). The maximum 1- and 5-d precipitation (R × 1 day, R × 5 day) increased at a rate of 0.21 and 3.12 mm/10 years, respectively. The increase extent was large after 2002 and 2003 (**Figures 3E,F**). The annual total precipitation/snow amount (PRCP)increased at a rate of 19.32 mm/10 years (**Figure 3G**), precipitation intensity (SDII) increased at 2.0 mm/d/10 years (**Figure 3H**) and CWD increased at 0.12 d/10 years, with the fluctuations relatively stable after 1989 (**Figure 3I**). In general, the precipitation intensity was weak before the 1980s, precipitation began to increase in the 1980s and continued to increase after the 1990s, precipitation in the study area showed a continuous increasing trend. The period and abrupt-changes test results showed (**Table 1**) that the R10 and PRCP indices had a very significant increasing abrupt-changes in 1997, CWD had significant increasing abrupt-changes in 1978 and the remaining precipitation indices had very significant increasing abrupt-changes in 1995. From the perspective of wavelet variance, the common period was 13 years, and the period was not significant. Overall, after the 1990s, rainfall in the study area increased significantly.

Trend and Periodic Variation of Extreme Temperature Indices

The warm indices (TN90, TNx, and TR20) significantly increased at rates of 3.51 d/10 years, 0.61°C/10 years, and 0.35 d/10 years, respectively ($p < 0.01$, **Figures 4A–C**). After 1989, most of the values of these indices were higher than the average values, reaching maximum values in 2016, 2015, and 2015, respectively, while WSDI showed an insignificant increasing trend. Compared with the warm indices, CSDI showed a significant decreasing

TABLE 1 | Results of abrupt-change test and period of all extreme indices.

Extreme precipitation	Abrupt-year	|Zc|	H0	Period	Extreme temperature	Abrupt-year	|Zc|	H0	Period
R10 mm	1997	3.49	R	7,12,21	TN90	1996	6.25	R	16,21,25
R20 mm	1995	3.66	R	9,12,21	TNx	1995	5.20	R	9,16,21
R25 mm	1995	2.52	R	8,12,21	TR20	1996	4.75	R	16,21,25
R95p	1995	3.65	R	9,13,21	WSDI	2000	2.99	R	6,14,21
Rx1	1995	2.71	R	9,13,21	FD	2000	4.92	R	16,21,25
Rx5	1995	3.57	R	6,13,21	ID	1994	2.66	R	14,21,25
PRCP	1997	3.14	R	7,13,21	TX10	1994	4.12	R	12,21,25
SDII	1995	3.56	R	9,13,21	CSDI	1988	4.49	R	13,21,25
CWD	1978	2.50	R	8,12,21					

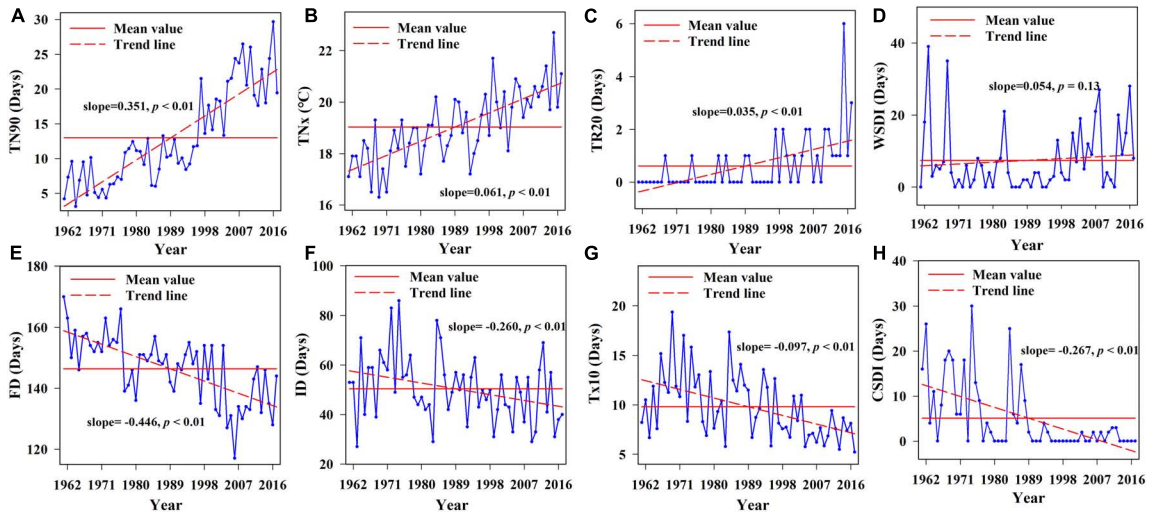

FIGURE 4 | Linear trend charts of annual extreme temperature indices during 1961–2017. **(A)** linear trend chart of warm nights, **(B)** linear trend chart of monthly maximum value of min temperature, **(C)** linear trend chart of hot nights, **(D)** linear trend chart of warm spell duration indicator, **(E)** linear trend chart of frost days, **(F)** linear trend chart of icing days, **(G)** linear trend chart of cold days, and **(H)** linear trend chart of Cold spell duration indicator.

trend at a rate of 2.67 d/10 years ($p < 0.01$). After 1989, the number of cold duration days was lower than average, and most cold duration days were 0 d (**Figure 4D**). Judging from the abrupt-changes test results, except for WSDI and FD which had extremely significant abrupt-changes in 2000, the other temperature indices had extremely significant abrupt-changes in the late 1980s and mid-to-late 1990s (**Table 1**). The periodic changes of extreme temperature indices were insignificant, and all extreme temperature indices did not have a consistent significant period (**Table 1**). Overall, the climate in the study area showed a significant warming trend after the late 1980s.

Tree-Ring Chronology in Two Regions

The tree-ring chronology showed an increasing trend in the non-degraded but a decreasing trend in the degraded regions (**Figure 5**). The abrupt-change year of tree-ring chronology in non-degraded region is 2008, in the degraded region is 1976 and 2001. **Table 2** shows the results of trend and periodic changes of the standardized tree-ring chronology of *M. sieversii* in the two regions. The average tree-ring chronology index of *M. sieversii* was higher in the non-degraded region than the degraded region. The trend test showed an insignificantly decreasing trend of tree-ring chronology in the degraded and insignificantly increasing trend in non-degraded region ($|Z_c| < 1.98, p > 0.05$). The tree-ring chronology in degraded region showed a significant abrupt-changes trend in 1976 ($p < 0.01$), and an insignificant abrupt-changes in 2001. The tree-ring chronology in the non-degraded region showed a very significant increase abrupt-change in 2008 ($p < 0.01$). The results of wavelet variance showed that *M. sieversii* in the non-degraded region had periods of 7, 13, and 21 years, and in the degraded region also had significant periods of 7, 12, and 21 years. The interdecadal cycles of the tree-ring chronology in the two regions were also inconsistent, with the main cycles being 12 and 13 years, respectively.

Relationship Between Extreme Climate Indices and *Malus sieversii* Growth

In arid areas, trees are more sensitive to extreme climates, and climate change has a significant impact on phenology of local vegetation. The interannual correlation coefficients of the tree-ring chronology in non-degraded areas and extreme climate indices are shown in **Figure 6**. Among them, R10, R25, R95P,

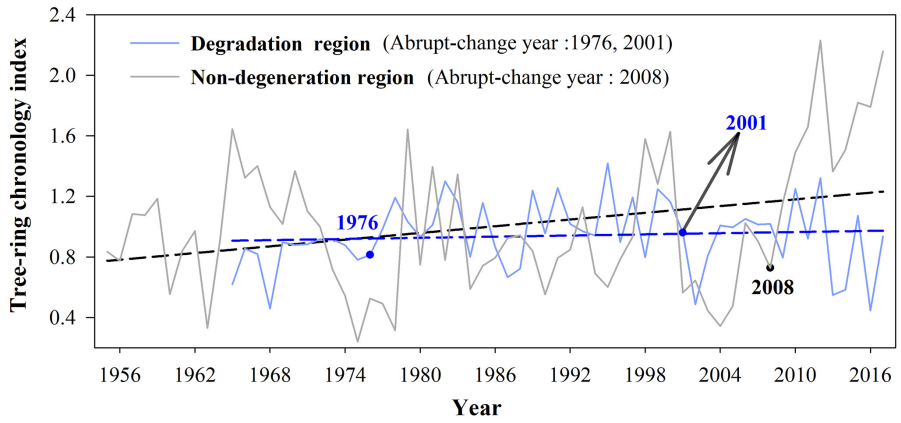

FIGURE 5 | Tendency of tree-ring chronology indices in degraded regions and non-degraded region.

TABLE 2 | Statistics of tree-ring chronology.

Site	Mann–Kendall trend test				Mann–Whitney test			Period
	Mean-value	Z_c	H0	Trend	Abrupt	$\|Z_c\|$	H0	
Degraded region	0.94	–1.37	A	No significant trend	1976	2.9	R	7,12,21
					2001	0.35	A	
Non-degraded region	1.01	1.64	A	No significant trend	2008	4.26	R	7,13,21

Rx1, Rx5, PRCP, SDII, and TR20 were significantly positively correlated with the tree-ring chronology index ($p < 0.01$), and R20, CWD, TN90 and TNx were significantly positively correlated with the tree-ring chronology index ($p < 0.05$). The correlation between WSDI and tree-ring chronology was very low and FD, ID, TX10, and CSDI were insignificantly negatively correlated with tree-ring chronology. Due to the hysteresis and cumulative effects of tree-ring growth in response to climate change, this study further analyzed the multi-scale correlation between extreme climate indices and tree-ring chronology.

We conducted wavelet coherence analysis on nine extreme precipitation indices and three extreme temperature indices with significant correlations between extreme climate indices and tree-ring chronology in non-degraded areas. Among the extreme precipitation indices (**Supplementary Figure 1**), R10, SDII and PRCP had large and significant correlations with tree-ring chronology during the period of the 1980s–1990s, and there were cyclical changes of 4–8 and 12–20 years. Thus, R10, SDII, PRCP and the tree-ring chronology index showed a long-term consistent change, and the phase change direction was the same. Among them, SDII and the tree-ring chronology index also had a large-scale wavelet correlation on an interannual basis. Indices R20 and Rx1 had a small range of opposite phases around the 1970s, indicating that these two extreme climate events were not conducive to the growth of tree rings at this stage. Indices R20, R95p, and Rx1 showed a significant cyclical consistency of 4–8 years in the 1980s–1990s, and Rx5 and the tree-ring chronology index had a significant cyclical consistency of 8–12 years around the 1980s. The number of heavy rain days (R25) and the tree-ring chronology showed a cycle of <4 years in the 1980s, and at other times were insignificant. Thus, among the extreme precipitation indices, SDII, PRCP, and R25 had significant multi-scale correlations with tree-ring chronology in the non-degraded areas.

Among the extreme temperature indices (**Supplementary Figure 2**), the thermal indices (TN90 and TR20) and the tree-ring chronology had significant wavelet correlations in cycles of 4–8 and 8–16 years, respectively. The interdecadal changes of the former mainly occurred in the 1980s and 1990s, and the interannual changes mainly occurred after 2000. The interdecadal changes of the latter were around the 1990s, and the interannual changes were the same as the former. The cold index (TNx) and the tree-ring chronology had a significant wavelet correlation of 2–4-year periods after 2000, and the interdecadal changes were not significant. In general, under the interannual and interdecadal cycles, the cycle consistency between the thermal index and tree-ring chronology was better than for the cold index and tree-ring chronology.

DISCUSSION

Effect of Atmospheric Circulation on Extreme Climate Change

Arid regions in northwest China are sensitive to global warming, and extreme climates occur frequently (Han et al., 2020; Pi et al., 2020; Xie et al., 2020). The extreme warm index in the study area increased significantly, while the extreme cold index decreased in the past 50 years (**Figure 4**). Due to the greater warming in winter than in summer, the increase rate

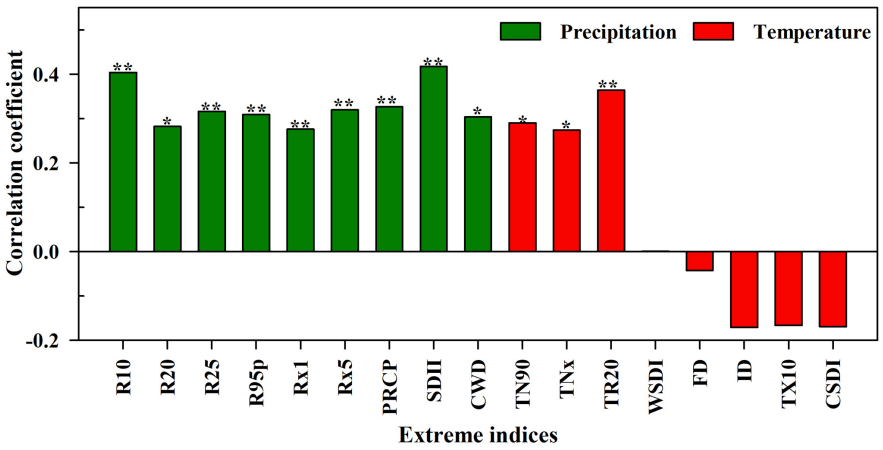

FIGURE 6 | Correlations between extreme climate indices and tree-ring chronology index of *Malus sieversii* in the non-degraded area (*$p < 0.05$, **$p < 0.01$).

of TN90 was the highest. As an important climate factor in the transition from warm and dry to warm and wet in the arid region of northwest China (Zhou and Wu, 2015; Li et al., 2016), all extreme precipitation indices showed a very significant increase trend. These changes were consistent with the trend of extreme climate change throughout the northwest (Wang B. L. et al., 2013). We also found that heavy precipitation increased by 14.04 mm/10 years, while annual total precipitation in the study area increased by 19.32 mm/10 years (**Figure 3**), indicating that extreme precipitation was the main factor affecting the annual total precipitation change. The trend of CWD was consistent with that of PRCP, indicating that extreme precipitation events were more frequent and serious (Wang et al., 2019). In addition, extreme precipitation indices were positively correlated with AMO, AMM and PDO, but insignificantly negatively correlated with NAO (**Figure 7A**). The extreme warming indices were positively correlated with AMO, AMM, and PDO, while WSDI and TN90 were negatively correlated with NAO. In contrast, the extreme cold indices were negatively correlated with AMO, AMM, and PDO, but insignificantly positively correlated with NAO (**Figure 7B**). Thus, AMO, AMM, and PDO had a significant influence on extreme climate change in the study area, and the extreme climate mainly was associated with AMO, consistent with the relationship between climate change and atmospheric circulation in the whole arid area of northwest China (Chen et al., 2017; Sun et al., 2020).

Therefore, change in atmospheric circulation had a significant effect on regional extreme climate change (Shi et al., 2018). The climate warming amplitude was positively correlated with geopotential height at 500 hPa (Tang et al., 2020), and water vapor transport was susceptible to the influence of atmospheric circulation anomalies, for which the variation characteristics of geopotential height field and wind field at 500 hPa in the study area were analyzed. Geopotential height at 500 hPa in the study area had an extremely significant increasing trend, positive anomalies of potential height corresponded to higher temperature and the regional climate clearly showed a trend of increasing extreme warm indices and reducing cold indices (**Figure 8A**). According to the wind field at 500 hPa (**Figure 8B**), a cyclone formed in the south of the Qinghai-Tibet Plateau, and the study area is located in the west of the cyclone. The cyclone strengthened the south wind and promoted water vapor from the north Indian Ocean entered the arid area of northwest China, which was conducive to formation of precipitation. Additionally, there was an anti-cyclone in the southwest direction of Siberia, which promoted the occurrence of extreme precipitation in the study area by strengthening the westerly wind and bringing water vapor from the Arctic Ocean into the study area. The characteristics of geopotential height field and wind field at 500 hPa also indicated that extreme climate change was most strongly related to the AMO. In general, the influence of atmospheric circulation on precipitation and temperature in northwest China was relatively complex. For a better understanding of the relationship between regional extreme climate change and atmospheric circulation, it is particularly important to analyze their changes and relationships using multi-scales in future studies.

Effect of Extreme Climate Change on Tree-Ring Growth

The tree-ring chronology of *M. sieversii* in non-degraded areas showed an increasing trend (**Figure 5**), which had a positive relationship with extreme precipitation indices (**Figure 6**). There was a significant correlation and consistent change in the 1980s–1990s of a 4–8-year period (**Supplementary Figure 1**), indicating that a consistently wet climate increased the radial growth of trees in forests in this arid region. Extreme precipitation promotes the growth of trees. On one hand, sufficient precipitation can promote tree growth by accelerating photosynthesis and carbon storage of tree to improve the effectiveness of trees in the utilization of hydrothermal resources (Sala et al., 2012; Jiang et al., 2019). On the other hand, increasing precipitation can increase decomposition of litter by microorganisms, promoting the growth of trees by improving the effectiveness of nitrogen (Sala et al., 2012). The tree-ring chronology in the non-degraded

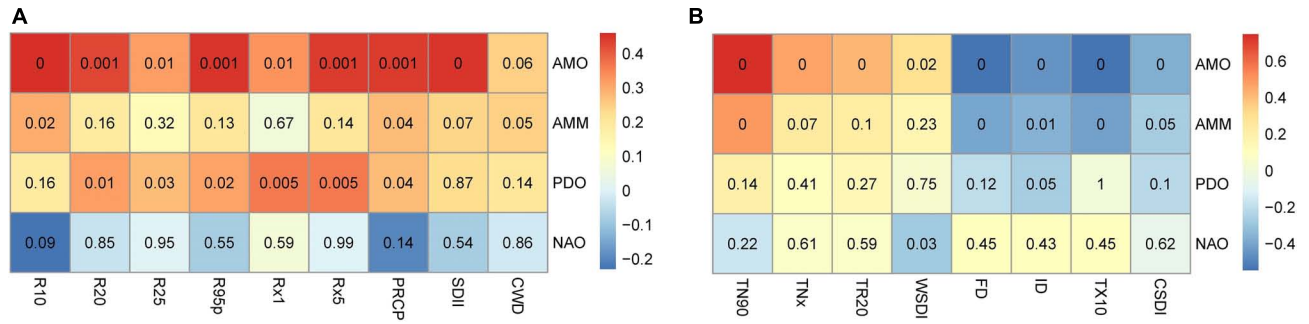

FIGURE 7 | Correlation coefficients (shown in color shading) between atmospheric circulation and extreme climate indices for 1961–2017: **(A)** extreme precipitation and **(B)** extreme temperature (cell numbers are *p*-values).

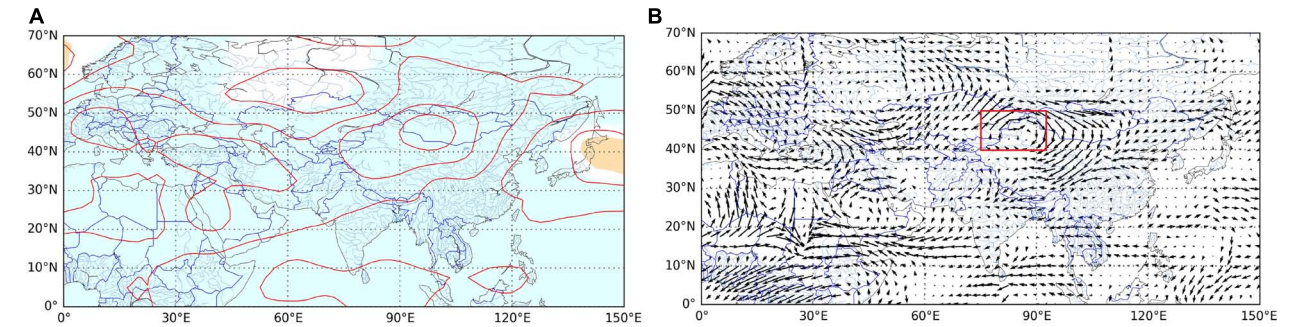

FIGURE 8 | Trends of **(A)** geopotential height and **(B)** wind speed at 500 hPa during 1961–2017 (blue, $p < 0.01$; white, $0.01 < p < 0.05$; yellow, $p > 0.05$).

area was positively correlated with the extreme temperature index and the warm index (TN90, TNx, and TR20), and showed good consistency in 8–16-year period change during the 1980s–1990s. This is because warmer temperatures can close stomates and promote carbon storage in trees, and warmer spring temperatures can promote leaf initiation and tree-ring formation. The positive correlation between tree-ring chronology and WSDI was relatively small in the non-degraded area, possibly due to the adaptability of trees to long-term environmental changes (Drake et al., 2010; Reich et al., 2016). Our study showed that the effect of extreme temperature index was smaller than that of extreme precipitation, and tree-ring chronology was the most sensitive to the change of SDII according to the correlation coefficient values. This was mainly because the study area was located in the arid region of northwest China (Zhou and Wu, 2015; Li et al., 2016). In recent years, the climate has tended to be humid and water resources are the main factors affecting the local vegetation growth. Although temperature in the study area increased year by year and extremely high temperatures and other events were not conducive to tree growth, the fertile soil, and abundant precipitation reversed the negative effect of the extreme high temperature events on tree growth (Scharnweber et al., 2020).

However, the tree-ring chronology of *M. sieversii* in the degraded area was decreasing (**Figure 5**), under insignificant difference between climatic conditions and soil conditions in the two regions (**Supplementary Table 2**). Combining investigation by managers of *M. sieversii* forest with research (Liu et al., 2014; Chen, 2015; Fang et al., 2019), the main difference between the two areas is due to the different levels of human disturbance. The *M. sieversii* forests have experienced minor destruction in the non-degraded region. In contrast, local people began to develop and utilize wild fruit forest resources since 1970. A large number of wild apples were gathered and some trees were cut down by local people in 1970. Local people realized the importance of protecting the *M. sieversii* forests and started to appropriately gather wild apples for making wine since 1980. Since 1990, the utilization of wild apple forest resources has reduced, the protection was strengthened by local inhabitants. In 1995, the new cultivated apple species from China's Shandong Province were introduced into the degraded region, which caused the first detection of *Agrilus mali Matsumura* insects in wild apple trees (Chen, 2015). Local measures of perforating and injecting chemicals to control pests, but the *Valsa ceratosperma* occurred in trees. Local government departments also protected the trees by cutting off diseased branches, and insect control was also carried out through flying control since 2000. Our multi-scale correlation analysis between extreme climatic indexes and tree-ring chronology in the degraded region showed that tree-ring chronology had significant negative correlations with WSDI and CSDI (**Figure 9**). However, the wavelet correlation coefficients between tree-ring chronology and extreme precipitation indices (**Supplementary Figure 3**) showed that in the degraded region, R10, R95p, CWD, SDII, and PRCP were significantly correlated with tree-ring chronology in a 4–8-year period, and tree-ring

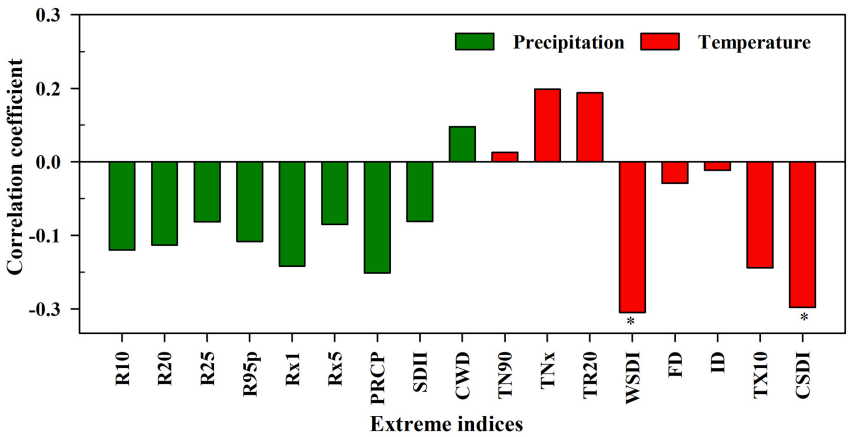

FIGURE 9 | Correlation coefficients of extreme climate indices and the tree-ring chronology of *Malus sieversii* in the degraded region.

chronology was significantly correlated with WSDI and CSDI in a 2–8-year periods (**Supplementary Figure 4**).

The main reasons are as follows. The measures of perforating and injecting chemicals in the early growing season (around April) to control pests promoted the occurrence of *V. ceratosperma*, following extreme precipitation events (mainly in June), which impeded growth of wild apple trees. Extreme high temperature events occur frequently in July in the study region, and are conducive to outbreaks of diseases and insect pests. Human measures of sawing branches further reduced the leaf area of *M. sieversii* trees, resulting in the reduction of photosynthetic production, which hindered the growth of *M. sieversii* trees in the area (Molina et al., 2019). Overall, the occurrence of extreme precipitation and temperature promoted the growth of wild apple tree rings in the degraded area. Moreover, due to unreasonable human activities, such as deforestation, agricultural reclamation and grazing, *M. sieversii* is more vulnerable to climate change, which is not conducive to recovery of *M. sieversii* growth following extreme climate events. As a consequence, the growth of damaged trees would further deteriorate, leading to further degradation of *M. sieversii* forest. Under the conditions of increasing extreme precipitation and extreme warm climate events, growth of trees in the non-degraded area was better, but was worse in the degraded area. These results showed that both unreasonable anthropogenic activities and extreme climate caused outbreaks of pests and diseases, and resulted in degeneration of wild fruit forest. Most studies have focused on the impact of environmental and climate stress (including extreme climate events) on tree growth, while ignoring the human impacts on management and disturbance of tree growth in forests (Julio Camarero et al., 2011; Sidor et al., 2019). In recent years, many trees have been negative growth and even widespread death in the world (Gazol et al., 2015, 2018; Martinez del Castillo et al., 2019; Decuyper et al., 2020). It is necessary to analyze the reasons for changes in tree growth resulting from combined the effects of anthropogenic activities and climate change in future studies.

Ecological Conservation Measures to Adapt to Extreme Climate Change

In dry forest, decayed individuals are able to achieve their pre-drought growth levels following drought, while non-decayed individuals are able to improve further following drought, showing that trees have strong resistance and resilience to short-term drought (Julio Camarero et al., 2018). *M. sieversii* is the ancestor of cultivated apple but has greater ability to resist environmental stress (Wuerdig et al., 2015; Yang et al., 2017, 2019; Wang et al., 2018). Because of their excellent resistance, the vitality of good tree individuals can be strengthened, with poor trees suffering from human disturbance can become worse. For example, improper pruning by humans reduces the water use efficiency of trees (Molina et al., 2019), extreme high temperature exacerbates insect and disease outbreaks, and extreme precipitation can cause outbreaks of *Valsa mali* Miyabe et Yamada. These resulted in the growth of *M. sieversii* showing a decreasing trend, and the correlation between tree-ring chronology in the degraded area and extreme precipitation, and high temperature indices showed negative correlations (**Supplementary Figures 3**, **4** and **Figure 9**). Hence, it is effective to promote tree growth through appropriate pruning after extreme climate events during the growing season. During outbreaks of pests and diseases in wild fruit forests, the control of tree infection by sawing off diseased and dead branches can weaken the resistance of the trees and reduce their ability to cope with extreme climate events. Therefore, it is necessary to strengthen research on pathogenic mechanisms and phenology of *M. sieversii* to enable the use of appropriate chemical control combined with biological control technology. Following extreme weather events, the growth status of trees is related to their previous growth status, and the growth of *M. sieversii* in the non-degraded area showed an increasing trend. Therefore, it is important to strengthen the monitoring of individual tree growth for the timely detection of growth problems and the development of solutions (Hartmann et al., 2018). It is also important to focus on the protection of poor trees in future forest protection and management. In addition,

wild fruit forests are world class wild resource banks. In the process of degradation, many wild species become endangered (Liu et al., 2014). Therefore, the establishment of gene banks for wild resources should be continuously strengthened.

CONCLUSION

In the past 50 years, both the extreme precipitation and extreme warm indices showed an increasing trend while extreme cool indices showed a decreasing trend in the study area. The extreme precipitation indices and extreme warm indices in the study area were positively correlated with the large-scale circulation indices of AMO, AMM and PDO, and negatively correlated with NAO. The geopotential height field and wind field at 500 hPa in the study area showed increasing trends. Changes in both the Siberian anti-cyclone and the Qinghai-Tibet Plateau cyclone near the study area resulted in changes in extreme climate events jointly.

Among the extreme climate indices, the number of days in which extreme cold events occurred tended to decrease in recent years and their effect on tree-ring chronology weakened. Extreme precipitation indices and extreme warmth indices (TN90, TNx, and TR20) showed significantly increasing trends, and were significantly positively correlated with the tree-ring chronology, indicating promoted growth in *M. sieversii* of the non-degraded forest. There were common periods of 12–13 years between tree-ring chronology and both the extreme precipitation, and extreme warm indices, indicating extreme climate events promoted the periodic change in tree-ring chronology of *M. sieversii* in the non-degraded region.

Compared with the increasing growth trend of the non-degraded trees, *M. sieversii* growth in the degraded area showed an insignificant decreasing trend. Pearson's correlation coefficients showed insignificant negative correlations between tree-ring chronology and R10, R95p, CWD, SDII, and PRCP. However, there were significant correlations with tree-ring chronology in a 4–8-year period. Tree-ring chronology in degraded areas was significantly negatively correlated with WSDI and CSDI, and significantly correlated with CSDI in a 2–8-year period. Extreme precipitation and WSDI had a significantly negative effect on the wild fruit forest over a long time-scale. In addition, because of inappropriate anthropogenic disturbance, extreme climate change further aggravated the frequent occurrence of pests and diseases, leading to the degradation of wild fruit forests.

DATA AVAILABILITY STATEMENT

The raw data supporting the conclusions of this article will be made available by the authors, without undue reservation.

AUTHOR CONTRIBUTIONS

QS achieved the analysis of the climate change and tree growth trends, the computation of dendrochronological/climate correlations, and the writing – original manuscript. HL provided the framework, conceptualization, and methodology. HZ and QS calculated the extreme climate index and visualized all results. ML and ZW finished the measurement of tree-ring width, the tree-ring chronology established, and participated in the investigation. GZ finished the formal analysis, and provided conceptualization and methodology. All authors contributed to the article and approved the submitted version.

FUNDING

This work was supported by the National Key Research and Development Program of China (grant number 2016YFC0501500) and The Second Tibetan Plateau Scientific Expedition and Research (STEP) program (grant number 2019QZKK0502).

SUPPLEMENTARY MATERIAL

The Supplementary Material for this article can be found online at: https://www.frontiersin.org/articles/10.3389/fpls.2021.608211/full#supplementary-material

REFERENCES

Alexander, L., Allen, S., and Bindoff, N. L. (2013). *Climate Change 2013: The Physical Science Basis – Summary for Policymakers*. Geneva: IPCC.

Andrade, V. L. C., Flores, B. M., Levis, C., Clement, C. R., Roberts, P., and Schongart, J. (2019). Growth rings of Brazil nut trees (*Bertholletia excelsa*) as a living record of historical human disturbance in Central Amazonia. *PLoS One* 14:e0214128. doi: 10.1371/journal.pone.0214128

Archetti, M. (2009). Evidence from the domestication of apple for the maintenance of autumn colours by coevolution. *Proc. R. Soc. B Biol. Sci.* 276, 2575–2580. doi: 10.1098/rspb.2009.0355

Birch, E. L. (2014). Climate change 2014: impacts, adaptation, and vulnerability. *J. Am. Plann. Assoc.* 80, 184–185.

Bonsal, B. R., Zhang, X., Vincent, L. A., and Hogg, W. D. (2010). Characteristics of daily and extreme temperatures over Canada. *J. Clim.* 14, 1959–1976. doi: 10.1175/1520-0442(2001)014<1959:CODAET>2.0.CO;2

Cardil, A., Molina, D. M., and Kobziar, L. N. (2014). Extreme temperature days and their potential impacts on southern Europe. *Nat. Hazard. Earth Syst.* 14, 3005–3014. doi: 10.5194/nhess-14-3005-2014

Chen, Y. J. (2015). Conservation and recovery of wild apple forest resources in Xinyuan County, Xinjiang. *Beijing Agric.* 632, 98–99.

Chen, Y. N., Deng, H. J., Li, B. F., Li, Z., and Xu, C. C. (2014). Abrupt change of temperature and precipitation extremes in the arid region of Northwest China. *Quat. Int.* 336, 35–43. doi: 10.1016/j.quaint.2013.12.057

Chen, Z., Chen, Y., Bai, L., and Xu, J. (2017). Multiscale evolution of surface air temperature in the arid region of Northwest China and its linkages to ocean oscillations. *Thero. Appl. Climatol.* 128, 945–958. doi: 10.1007/s00704-016-1752-7

Choi, G., Collins, D., Ren, G. Y., Trewin, B., Baldi, M., Fukuda, Y., et al. (2009). Changes in means and extreme events of temperature and precipitation in the Asia-Pacific Network region, 1955-2007. *Int. J. Climatol.* 13, 1906–1925. doi: 10.1002/joc.1979

Ciais, P., Reichstein, M., Viovy, N., Granier, A., Ogee, J., Allard, V., et al. (2005). Europe-wide reduction in primary productivity caused by the heat and drought in 2003. *Nature* 437, 529–533. doi: 10.1038/nature03972

Cook, B. I., Ault, T. R., and Smerdon, J. E. (2015). Unprecedented 21st century drought risk in the American Southwest and Central Plains. *Sci. Adv.* 1, 1–7.

Cook, E. R. (1985). *A Time Series Analysis Approach to Tree Ring Standardization.* Ph. D. Thesis. Tucson, AZ: University of Arizona.

Decuyper, M., Chavez, R. O., Cufar, K., Estay, S. A., Clevers, J. G. P. W., Prislan, P., et al. (2020). Spatio-temporal assessment of beech growth in relation to climate extremes in Slovenia – an integrated approach using remote sensing and tree-ring data. *Agric. Forest Meteorol.* 287:107925. doi: 10.1016/j.agrformet.2020.107925

Deng, H., Chen, Y., Shi, X., Li, W., Wang, H., Zhang, S., et al. (2014). Dynamics of temperature and precipitation extremes and their spatial variation in the arid region of northwest China. *Atmos. Res.* 138, 346–355. doi: 10.1016/j.atmosres.2013.12.001

Drake, B. G., Azcon-Bieto, J., Berry, J., Bunce, J., Dijkstra, P., Farrar, J., et al. (2010). Does elevated atmospheric CO2 concentration inhibit mitochondrial respiration in green plants? *Plant Cell Environ.* 22, 649–657. doi: 10.1046/j.1365-3040.1999.00438.x

Duan, N., Bai, Y., Sun, H., Wang, N., Ma, Y., Li, M., et al. (2017). Genome re-sequencing reveals the history of apple and supports a two-stage model for fruit enlargement. *Nat. Commun.* 8:249.

Dzhangaliev, A. D. (2002). "The wild apple tree of Kazakhstan," in *Horticultural Reviews: Wild Apple and Fruit Trees of Central Asia*, Vol. 29, ed. J. Janick (Hoboken, NJ: John Wiley & Sons, Inc), 63–304. doi: 10.1002/9780470650868.ch2

Fan, Y. T., Shang, H. M., Wu, Y., and Li, Q. (2020). Tree-ring width and carbon isotope chronologies track temperature, humidity, and Baseflow in the Tianshan Mountains, Central Asia. *Forests.* 12, 1308. doi: 10.3390/f11121308

Fang, Z. Y., Li, L. Y., Ai Kebai, Er, Zhou, L., and Lu, B. (2019). Effects of human disturbance on plant diversity of wild fruit forests in Western Tianshan Mountain. *Bull. Soil Water Conserv.* 39, 267–274.

Feldpausch, T. R., Phillips, O. L., Brienen, R. J. W., Gloor, E., Lloyd, J., Lopez-Gonzalez, G., et al. (2016). Amazon forest response to repeated droughts. *Glob. Biogeochem. Cycles* 30, 964–982.

Fritts, H. (1976). *Tree-ring and Climate*. London: Academic Press.

Gao, W., and Li, B. L. (1993). Wavelet analysis of coherent structures at the atmosphere forest interface. *J. Appl. Meteorol. Clim.* 32, 1717–1725. doi: 10.1175/1520-0450(1993)032<1717:waocsa>2.0.co;2

Gazol, A., Julio Camarero, J., Gutierrez, E., Popa, I., Andreu-Hayles, L., Motta, R., et al. (2015). Distinct effects of climate warming on populations of silver fir (*Abies alba*) across Europe. *J. Biogeogr.* 42, 1150–1162. doi: 10.1111/jbi.12512

Gazol, A., Julio Camarero, J., Vicente-Serrano, S. M., Sanchez-Salguero, R., Gutierrez, E., de Luis, M., et al. (2018). Forest resilience to drought varies across biomes. *Glob. Change Biol.* 24, 2143–2158. doi: 10.1111/gcb.14082

Guan, Y., Zhang, X., Zheng, F., and Wang, B. (2015). Trends and variability of daily temperature extremes during 1960-2012 in the Yangtze River Basin, China. *Glob. Planet Change* 124, 79–94. doi: 10.1016/j.gloplacha.2014.11.008

Han, T. T., Guo, X. Y., Zhou, B. T., and Hao, X. (2020). Recent changes in heavy precipitation events in Northern Central China and associated atmospheric circulation. *Asia Pac. J. Atmos. Sci.* 57, 301–310. doi: 10.1007/s13143-020-00195-1

Han, X., Xue, H., Zhao, C., and Lu, D. (2016). The roles of convective and stratiform precipitation in the observed precipitation trends in Northwest China during 1961-2000. *Atmos. Res.* 169, 139–146. doi: 10.1016/j.atmosres.2015.10.001

Hartmann, H., Moura, C. F., Anderegg, W. R. L., Ruehr, N. K., Salmon, Y., Allen, C. D., et al. (2018). Research frontiers for improving our understanding of drought-induced tree and forest mortality. *New Phytol.* 218, 15–28. doi: 10.1111/nph.15048

Holmes, R. L. (1983). Computer-assisted quality control in tree-ring dating and measurement. *Tree Ring Bull.* 43, 69–78.

Huang, J., Yu, H., Guan, X., Wang, G., and Guo, R. (2016). Accelerated dryland expansion under climate change. *Nat. Clim. Change* 6, 247–257.

Jiang, P., Liu, H., Piao, S., Ciais, P., Wu, X., Yin, Y., et al. (2019). Enhanced growth after extreme wetness compensates for post-drought carbon loss in dry forests. *Nat. Commun.* 10, 1–9.

Julio Camarero, J., Bigler, C., Carlos Linares, J., and Gil-Pelegrin, E. (2011). Synergistic effects of past historical logging and drought on the decline of Pyrenean silver fir forests. *Forest Ecol. Manag.* 262, 759–769. doi: 10.1016/j.foreco.2011.05.009

Julio Camarero, J., Gazol, A., Sanguesa-Barreda, G., Cantero, A., Sanchez-Salguero, R., Sanchez-Miranda, A., et al. (2018). Forest growth responses to drought at short- and long-term scales in spain: squeezing the stress memory from tree rings. *Front. Ecol. Evol.* 6:9. doi: 10.3389/fevo.2018.00009

Kolb, T. E., Fettig, C. J., Ayres, M. P., Bentz, B. J., Hicke, J. A., Mathiasen, R., et al. (2016). Observed and anticipated impacts of drought on forest insects and diseases in the United States. *Forest Ecol. Manag.* 380, 321–334. doi: 10.1016/j.foreco.2016.04.051

Kong, T. T., Liu, A. H., and Yue, C. Y. (2017). Entomogenous Fungi of Agrilus mail Matsumura in wild apple trees in Tianshan Mountain. *Northern Hortic.* 1, 138–141.

Li, B., Chen, Y., Chen, Z., Xiong, H., and Lian, L. (2016). Why does precipitation in northwest China show a significant increasing trend from 1960 to 2010? *Atmos. Res.* 167, 275–284. doi: 10.1016/j.atmosres.2015.08.017

Li, X., You, Q. L., Rem, G. Y., Wang, S. Y., and Zhang, Y. Q. (2019). Concurrent droughts and hot extremes in northwest China from 1961 to 2017. *Int. J. Climatol.* 39, 2186–2196. doi: 10.1002/joc.5944

Lin, P. J., and Cui, N. R. (2000). *Wild Fruit Forest Resources in Tianshan Mountains – Comprehensive Research on Wild Fruit Forests in Ili*. Xinjiang: China Forestry Publishing House, 10–13.

Ling, H. B., Xu, H. L., and Fu, J. (2014). Changes in intra-annual runoff and its response to climate change and human activities in the headstream areas of the Tarim River Basin, China. *Quat. Int.* 336, 158–170. doi: 10.1016/j.quaint.2013.08.003

Liu, A. H., Zhang, X. P., Wen, J. B., Yue, C. Y., Alimu, Jiao, S. P., et al. (2014). Preliminary research on the composite damage of *Agrilus mali* Matsumura and *Valsa mali* Miyabe et yamada in wild apple trees in Tianshan Mountain. *Xinjiang Agric. Sci.* 51, 2240–2244.

Luby, J., Forsline, P., Aldwinckle, H., Bus, V., and Geibel, M. (2001). Silk road apples – Collection, evaluation, and utilization of *Malus sieversii* from Central Asia. *Hortscience* 36, 225–231. doi: 10.21273/hortsci.36.2.225

Martinez del Castillo, E., Alberto Longares, L., Serrano-Notivoli, R., Sass-Klaassen, U. G. W., and de Luis, M. (2019). Spatial patterns of climate-growth relationships across species distribution as a forest management tool in Moncayo Natural Park (Spain). *Eur. J. Forest Res.* 138, 299–312. doi: 10.1007/s10342-019-01169-3

Mazza, G., Becagli, C., Proietti, R., and Corona, P. (2020). Climatic and anthropogenic influence on tree-ring growth in riparian lake forest ecosystems under contrasting disturbance regimes. *Agric. Forest Meteorol.* 291, 1–13.

Min, S.-K., Zhang, X., Zwiers, F. W., and Hegerl, G. C. (2011). Human contribution to more-intense precipitation extremes. *Nature* 470, 378–381. doi: 10.1038/nature09763

Molina, A. J., Aranda, X., Llorens, P., Galind, A., and Biel, C. (2019). Sap flow of a wild cherry tree plantation growing under Mediterranean conditions: assessing the role of environmental conditions on canopy conductance and the effect of branch pruning on water productivity. *Agric. Water Manage.* 218, 222–233. doi: 10.1016/j.agwat.2019.03.019

Mullan, D., Favis-Mortlock, D., and Fealy, R. (2012). Addressing key limitations associated with modelling soil erosion under the impacts of future climate change. *Agric. Forest Meteorol.* 156, 18–30. doi: 10.1016/j.agrformet.2011.12.004

Nagy, L., Kreyling, J., Gellesch, E., Beierkuhnlein, C., and Jentsch, A. (2013). Recurring weather extremes alter the flowering phenology of two common temperate shrubs. *Int. J. Biometeorol.* 57, 579–588. doi: 10.1007/s00484-012-0585-z

Panyushkina, I. P., Mukhamadiev, N. S., Lynch, A. M., Ashikbaev, N. A., Arizpe, A. H., O'Connor, C. D., et al. (2017). Wild apple growth and climate change in Southeast Kazakhstan. *Forests* 8, 1–14.

Pettit, J. M., Voelker, S. L., DeRose, R. J., and Burton, J. I. (2020). Spruce beetle outbreak was not driven by drought stress: evidence from a tree-ring iso-demographic approach indicates temperatures were more important. *Glob. Change Biol.* 26, 5829–5843. doi: 10.1111/gcb.15274

Pi, Y. Y., Yu, Y., Zhang, Y. Q., Xu, C. C., and Yu, R. D. (2020). Extreme temperature events during 1960-2017 in the Arid region of Northwest China: spatiotemporal

dynamics and associated large-scale atmospheric circulation. *Sustainability* 12:1198. doi: 10.3390/su12031198

Powell, E. J., and Keim, B. D. (2015). Trends in daily temperature and precipitation extremes for the Southeastern United States: 1948-2012. *J. Clim.* 28, 1592–1612. doi: 10.1175/jcli-d-14-00410.1

Qian, Z. A., Wu, T., Song, M., Ma, X., Cai, Y., and Liang, X. (2001). Arid disaster and advances in arid climate resources over northwest China. *Adv. Earth Sci.* 16, 28–38.

Rahimi, M., and Hejabi, S. (2018). Spatial and temporal analysis of trends in extreme temperature indices in Iran over the period 1960-2014. *Int. J. Climatol.* 38, 272–282. doi: 10.1002/joc.5175

Raineri, R. (2013). Managing the risks of extreme events and disasters to advance climate change adaptation. *Econ. Energy Environ. Pol.* 2, 101–112.

Rammig, A., Jupp, T., Thonicke, K., Tietjen, B., Heinke, J., Ostberg, S., et al. (2010). Estimating the risk of Amazonian forest dieback. *New Phytol.* 187, 694–706. doi: 10.1111/j.1469-8137.2010.03318.x

Reich, P. B., Sendall, K. M., Stefanski, A., Wei, X., Rich, R. L., and Montgomery, R. A. (2016). Boreal and temperate trees show strong acclimation of respiration to warming. *Nature* 531, 633–638. doi: 10.1038/nature17142

Rinn, F. (2003). *TSAP-Win: Time Series Analysis and Presentation for Dendrochronology and Related Applications. Version 0.55 User Reference*. Heidelberg: RINNTECH.

Sala, O. E., Gherardi, L. A., Reichmann, L., Jobbagy, E., and Peters, D. (2012). Legacies of precipitation fluctuations on primary production: theory and data synthesis. *Philos. T. R. Soc. B.* 367, 3135–3144. doi: 10.1098/rstb.2011.0347

Scharnweber, T., Smiljanic, M., Cruz-Garcia, R., Manthey, M., and Wilmking, M. (2020). Tree growth at the end of the 21st century-the extreme years 2018/19 as template for future growth conditions. *Environ. Res. Lett.* 15:074022. doi: 10.1088/1748-9326/ab865d

Shi, J., Cui, L., Ma, Y., Du, H., and Wen, K. (2018). Trends in temperature extremes and their association with circulation patterns in China during 1961-2015. *Atmos. Res.* 212, 259–272. doi: 10.1016/j.atmosres.2018.05.024

Shi, Y., Shen, Y., Kang, E., Li, D., Ding, Y., Zhang, G., et al. (2007). Recent and future climate change in northwest china. *Clim. Change* 80, 379–393. doi: 10.1007/s10584-006-9121-7

Sidor, C. G., Julio Camarero, J., Popa, I., Badea, O., Apostol, E. N., and Vlad, R. (2019). Forest vulnerability to extreme climatic events in Romanian Scots pine forests. *Sci. Total Environ.* 678, 721–727. doi: 10.1016/j.scitotenv.2019.05.021

Song, X., Song, S., Sun, W., Mu, X., Wang, S., Li, J., et al. (2015). Recent changes in extreme precipitation and drought over the Songhua River Basin, China, during 1960-2013. *Atmos. Res.* 157, 137–152. doi: 10.1016/j.atmosres.2015.01.022

Steinman, B. A., Mann, M. E., and Miller, S. K. (2015). Atlantic and Pacific multidecadal oscillations and Northern Hemisphere temperatures. *Science* 347, 988–991. doi: 10.1126/science.1257856

Stocker, T. F., Qin, D., Plattner, G.-K., Tignor, M., Allen, S. K., Boschung, J., et al. (2013). IPCC, 2013: climate change 2013: the physical science basis. contribution of working group I to the Fifth assessment report of the intergovernmental panel on climate change. *Comput. Geom.* 18, 95–123.

Sun, J., Yang, K., Guo, W. D., Wang, Y., He, J., and Lu, H. (2020). Why has the Inner Tibetan Plateau become wetter since the mid-1990s? *J. Clim.* 33, 8507–8522. doi: 10.1175/jcli-d-19-0471.1

Sun, W., Mu, X., Song, X., Wu, D., Cheng, A., and Qiu, B. (2016). Changes in extreme temperature and precipitation events in the Loess Plateau (China) during 1960-2013 under global warming. *Atmos. Res.* 168, 33–48. doi: 10.1016/j.atmosres.2015.09.001

Tang, Xl, Lv, X., and Zhang, Y. (2020). Estimation of future extreme precipitation changes in Xinjiang based on RegCM4.4 simulations. *Nat. Hazards* 102, 201–218. doi: 10.1007/s11069-020-03920-1

Touma, D., Ashfaq, M., Nayak, M. A., Kao, S. C., and Diffenbaugh, N. S. (2015). A multi-model and multi-index evaluation of drought characteristics in the 21st century. *J. Hydrol.* 526, 196–207. doi: 10.1016/j.jhydrol.2014.12.011

Vanoni, M., Bugmann, H., Notzli, M., and Bigler, C. (2016). Drought and frost contribute to abrupt growth decreases before tree mortality in nine temperate tree species. *Forest Ecol. Manag.* 382, 51–63. doi: 10.1016/j.foreco.2016.10.001

Wang, B. L., Zhang, M. J., Wei, J. L., Wang, S. J., Li, S., Ma, Q., et al. (2013). Changes in extreme events of temperature and precipitation over Xinjiang, northwest China, during 1960-2009. *Quat. Int.* 298, 141–151. doi: 10.1016/j.quaint.2012.09.010

Wang, H., Chen, Y., Xun, S., Lai, D., Fan, Y., and Li, Z. (2013). Changes in daily climate extremes in the arid area of northwestern China. *Theor. Appl. Climatol.* 112, 15–28. doi: 10.1007/s00704-012-0698-7

Wang, H., Gao, T., and Xie, L. (2019). Extreme precipitation events during 1960-2011 for the Northwest China: space-time changes and possible causes. *Theor. Appl. Climatol.* 137, 977–995. doi: 10.1007/s00704-018-2645-8

Wang, N., Jiang, S. H., Zhang, Z. Y., Fang, H. C., Xu, H. F., Wang, Y. C., et al. (2018). *Malus sieversii*: the origin, flavonoid synthesis mechanism, and breeding of red-skinned and red-fleshed apples. *Hortic. Res. England* 5:70.

Wang, Z. Y., Zhang, Y. L., Yang, Z. Q., and Wang, X. Y. (2013). Determination of Larval Instars of *Agrilus mali* Matsumura (Coleoptera: Buprestidae). *Forest Res.* 26, 786–789.

Wuerdig, J., Flachowsky, H., Sass, A., Peil, A., and Hanke, M. V. (2015). Improving resistance of different apple cultivars using the Rvi6 scab resistance gene in a cisgenic approach based on the Flp/FRT recombinase system. *Mol. Breed.* 35:95.

Xiao, C., Wu, P., Zhang, L., and Song, L. (2016). Robust increase in extreme summer rainfall intensity during the past four decades observed in China. *Sci. Rep.* 6:38506.

Xie, W. X., Zhou, B. T., You, Q. L., Zhang, Y. Q., and Ullah, S. (2020). Observed changes in heat waves with different severities in China during 1961-2015. *Theor. Appl. Climatol.* 141, 1529–1540. doi: 10.1007/s00704-020-03285-2

Yang, M., Che, S., Zhang, Y., Wang, H., Wei, T., Yan, G., et al. (2019). Universal stress protein in *Malus sieversii* confers enhanced drought tolerance. *J. Plant Res.* 132, 825–837. doi: 10.1007/s10265-019-01133-7

Yang, M., Zhang, Y., Zhang, H., Wang, H., Wei, T., Che, S., et al. (2017). Identification of MsHsp20 gene family in *Malus sieversii* and functional characterization of MsHsp16.9 in heat tolerance. *Front. Plant Sci.* 8:1761. doi: 10.3389/fpls.2017.01761

You, Q., Ren, G., Fraedrich, K., Kang, S., Ren, Y., and Wang, P. (2013). Winter temperature extremes in China and their possible causes. *Int. J. Climatol.* 33, 1444–1455. doi: 10.1002/joc.3525

Zhou, L. T., and Wu, R. (2015). Interdecadal variability of winter precipitation in Northwest China and its association with the North Atlantic SST change. *Int. J. Climatol.* 35, 1172–1179. doi: 10.1002/joc.4047

Conflict of Interest: The authors declare that the research was conducted in the absence of any commercial or financial relationships that could be construed as a potential conflict of interest.

frontiers in Forests and Global Change

ORIGINAL RESEARCH
published: 22 July 2021
doi: 10.3389/ffgc.2021.667151

Sentinel-2 Analysis of Spruce Crown Transparency Levels and Their Environmental Drivers After Summer Drought in the Northern Eifel (Germany)

Carsten Montzka†, Bagher Bayat†, Andreas Tewes†, David Mengen† and Harry Vereecken†*

Institute of Bio- and Geosphere: Agrosphere (IBG-3), Forschungszentrum Jülich, Jülich, Germany

OPEN ACCESS

Edited by:
Francesco Ripullone, University of Basilicata, Italy

Reviewed by:
Martina Pollastrini, University of Florence, Italy
Ahmed Kenawy, Mansoura University, Egypt

***Correspondence:**
Carsten Montzka
c.montzka@fz-juelich.de

†ORCID:
Carsten Montzka
orcid.org/0000-0003-0812-8570
Bagher Bayat
orcid.org/0000-0002-7761-9544
Andreas Tewes
orcid.org/0000-0002-8899-0285
David Mengen
orcid.org/0000-0003-4041-6599
Harry Vereecken
orcid.org/0000-0002-8051-8517

Specialty section:
This article was submitted to Forest Disturbance, a section of the journal Frontiers in Forests and Global Change

Received: *12 February 2021*
Accepted: *11 June 2021*
Published: *22 July 2021*

Citation:
Montzka C, Bayat B, Tewes A, Mengen D and Vereecken H (2021) Sentinel-2 Analysis of Spruce Crown Transparency Levels and Their Environmental Drivers After Summer Drought in the Northern Eifel (Germany). Front. For. Glob. Change 4:667151. doi: 10.3389/ffgc.2021.667151

Droughts in recent years weaken the forest stands in Central Europe, where especially the spruce suffers from an increase in defoliation and mortality. Forest surveys monitor this trend based on sample trees at the local scale, whereas earth observation is able to provide area-wide information. With freely available cloud computing infrastructures such as Google Earth Engine, access to satellite data and high-performance computing resources has become straightforward. In this study, a simple approach for supporting the spruce monitoring by Sentinel-2 satellite data is developed. Based on forest statistics and the spruce NDVI cumulative distribution function of a reference year, a training data set is obtained to classify the satellite data of a target year. This provides insights into the changes in tree crown transparency levels. For the Northern Eifel region, Germany, the evaluation shows an increase in damaged trees from 2018 to 2020, which is in line with the forest inventory of North Rhine-Westphalia. An analysis of tree damages according to precipitation, land surface temperature, elevation, aspect, and slope provides insights into vulnerable spruce habitats of the region and enables to identify locations where the forest management may focus on a transformation from spruce monocultures to mixed forests with higher biodiversity and resilience to further changes in the climate system.

Keywords: Norway spruce, tree crown transparency, Sentinel-2, Eifel, Google Earth Engine

INTRODUCTION

Many parts of the world will suffer increasing tree mortality due to future projected climate change (Dai, 2013; Lausch et al., 2016). However, we are already within this process of higher background tree mortality rates, which have been documented on every vegetated continent and in most bioregions over the past two decades (Anderegg et al., 2013). A large portion of this forest die-off is triggered directly by drought and heat stress or indirectly through infestation-induced mortality, e.g., by the bark beetle (Sproull et al., 2016).

Steinkamp and Hickler (2015) were not able to identify a general drying trend or an increase in extreme drought events in forests globally, but they state that dry forests seem to be affected by decreasing water availability and increasing frequency of droughts. A later study by

Senf et al. (2018) found that canopy mortality increased by 2.4% year^{-1} in Europe, resulting in a doubling of the forest area affected by this phenomenon between 1984 and 2016. Moreover, van Mantgem et al. (2009) reported widespread hydrologic changes for the western United States, such as a declining fraction of precipitation falling as snow, a declining snowpack water content, earlier spring snowmelt, and runoff, and a consequent lengthening of the summer drought. The physiological mechanisms through which drought drives tree death are a rapidly growing research area (Sala et al., 2010), but the impacts of forest die-off remain less well studied.

Even in environments that are not typically considered water-limited, this extensive tree mortality leads to a weakening of the terrestrial carbon sink and provides positive feedback to climate warming (Allen et al., 2010). Moreover, a decline in the sum of plant-level transpiration combined with a reduction of ecosystem photosynthesis leads to a decline in gross primary productivity (Anderegg et al., 2013). Tree mortality events are often "pulsed" due to their links to occasionally but in recent time more frequent drought stress. Two key characteristics determine the magnitude of these impacts, this is the magnitude of the initial "pulse" response and the recovery rate of the ecosystem (Anderegg et al., 2013). Several compensatory mechanisms (e.g., increased resource availability for the remaining trees, niche redundancy and complementarity) explain why substantial tree mortality may not necessarily translate into major changes in ecosystem fluxes (Anderegg et al., 2016).

Tree mortality is a natural ecological process. However, drought- and heat-induced mortality, including associated infestation-related forest die-off, is often a selective force that affects tree species in different ways and rapidly alters the size, age, and spatial structure of forests (Panayotov et al., 2016; Pretzsch et al., 2020). If this increase in mortality persists for a longer period, the average tree age within a forest will be reduced, resulting in a reduced average tree height, stem and crown diameter, and altered forest structure, composition, functioning, architecture, and, consequently, biodiversity and ecosystem service provision (e.g., carbon storage capacity) (van Mantgem et al., 2009; Anderegg et al., 2013). Monitoring and prediction of those tree species that might be most vulnerable are urgently needed to design mitigation strategies (O'Brien et al., 2017).

Spruce is a very fast-growing tree with 15.3 $m^3 ha^{-1}$ a^{-1}. The German National Forest Inventory identified an area of 2.7 Mio. ha covered with spruce in Germany (BMEL, 2015). This is about 25% of the forested area (BMEL, 2020). However, the tendency is decreasing, latest by -4% in the period from 2002 to 2012. The dramatic mortality of spruce is estimated to be about 10.5% in 2020 for North Rhine-Westphalia (NRW) (relation of dead trees to total number of evaluated trees), where other tree species show mortalities of 2.1% (MUNLV, 2020). Not only the severe damage but also the warning level for spruce crown transparency has recently been increased (BMEL, 2020). In addition to the general ecologically driven renunciation tendency in spruce monocultures, heat waves, storm impact, and bark beetle outbreaks are the main reasons. Mezei et al. (2017) call the composition of the latter three aspects *the infernal trio* for spruce stands. However, water limiting conditions may initialize the three aspects (Stadelmann et al., 2014; Netherer et al., 2015).

Earth observation (EO) data, i.e., satellite or ground-based observations and geospatial data, is an important source to monitor changes in forest ecosystems, especially to identify tree mortality (Lausch et al., 2016). Although costly and providing just single snapshots, typically airborne color infrared, multispectral or hyperspectral sensors are used to provide information to the authorities at the state level (Fassnacht et al., 2012; Nielsen et al., 2014; Stovall et al., 2019). For scientific research, more and more spaceborne sensor data is used. For instance, Rao et al. (2019) used passive microwave data and retrievals of vegetation optical depth as an indicator of drought-driven tree mortality at a scale of 0.25°. Latifi et al. (2018) combined coarse (250 m) Moderate Resolution Imaging Spectroradiometer (MODIS) and high resolution (5 m) RapidEye data to identify tree mortality, which they attributed to bark beetle outbreaks. It was possible to relate spectral vegetation indices to local beetle counts. Byer and Jin (2017) demonstrated that MODIS data and two-stage Random Forest models were capable of detecting the spatial patterns and severity of tree mortality with an overall producer's accuracy of 96.3%. By feeding Gaofen-2 and Sentinel-2 data to different machine learning algorithms, Zhan et al. (2020) monitored tree mortality both at the single-tree and forest stand scale. Immitzer and Atzberger (2014) used multispectral WorldView-2 data to identify Norway Spruce mortality. For early detection, the multispectral sensor capabilities are rarely sufficient, but the identification of dead trees performed almost perfectly. Hansen et al. (2013) used the Google Earth Engine for a global assessment of forest loss by Landsat 30 m imagery with good accuracy also at the local scale where clear-cutting is common, and the fire is rare (Linke et al., 2017). Zimmermann and Hoffmann (2020) analyzed Sentinel-2 data to identify bark beetle infestations in German spruce forests, with good results over large areas where the reflectance properties have already been significantly changed. Fleming et al. (2015) used Landsat Thematic mapper data in tandem with forest inventory plot data to provide spatially and temporally explicit estimates of forest carbon stocks. These research examples show the readiness of EO data and related approaches for utilization in tree mortality detection and beyond, however, only little has found its way into the general management of practitioners or governmental monitoring programs in a straightforward operational way. The MODIS-based European forest condition monitor[1] may be considered the first step to get an overview but does not provide the timeliness, and spatial resolution potential users need.

In the Northern Eifel we visually observed an increased mortality of spruce stands in the last years due to climate change. This region, therefore, may serve as an example to study the impact of severe droughts, heatwaves, and bark beetle infestation on spruce mortality using remote sensing.

[1] www.waldzustandsmonitor.de

The intention of this study is to provide a method to quantify and monitor this process. In order to evaluate the severity of spruce damage in the Eifel region, and to support the governmental monitoring program (also to indirectly inform foresters, politicians, timber wood industry, and conservationists, etc.), up-to-date EO data can be used. However, governmental representatives may not be informed about technological innovations from other fields. The aim of this study is to introduce a cloud processing example to locate damaged spruce in the Northern Eifel region, and to evaluate potential environmental conditions for that damage. We focus here on the tree mortality and spruce health analysis after the 2018 summer drought. After an introduction to the area under investigation, it is necessary to explain the special situation of the spruce in this area to understand the environmental and artificial preconditions.

THE SPECIAL SITUATION OF SPRUCE IN THE NORTHERN EIFEL

The area of investigation has been limited to the Northern Eifel region (50.60°–50.80°N, 6.19°–6.53°E, and 532 km^2, see **Figure 1**). More specific, this study focuses on the Rureifel, which encompasses the Eifel/Lower Rhine Valley hydrological observatory (Hasan et al., 2014; Ali et al., 2015; Bogena et al., 2018), a part of the TERrestrial ENvironmental Observatories (TERENO) (Zacharias et al., 2011; Bogena et al., 2018). The main land cover types are forests and grassland. Forest areas are covering the Venn anticline ranging from West to North and the Kermeter in the South East with forested slopes along the Rur and Kall rivers in the National Park Eifel. The elevation increases from the North East to the South West of the area of investigation.

FIGURE 1 | Location of the area under investigation in the Northern Eifel as provided by the GEE.

The geology mainly consists of silt- and mudstone sequences as well as sandstones and graywackes with small cavity and groundwater storage volumes (Montzka et al., 2013). The South East belongs to the so-called Mechernich Trias Triangle, where the Devonian basement is covered by variegated sandstone. The characteristic soils for the Eifel are shallow Cambisols and Leptosols.

Since the 15th century, the Northern Eifel was shaped by a pre-industrialized iron smelting economy, where the tree population provided the energy for the blast furnaces and the rivers the energy for the steel works. Extensive shifting cultivation and livestock farming put additional pressure on the forests. When the iron industry was disrupted in the region in 19th century due to the strong competition to the black coal in the Ruhr area, a large portion of the Eifel forests was cut and heathland dominated. At the Congress of Vienna in 1815, Prussia took over the former French Rhineland, including the Eifel region and started planting fast-growing trees on fallow areas to develop the economy of this poor region. Especially the Norway Spruce (*Picea abies* (L.) H. Karst.), since then known in the region as *Prussian Tree*, was established against initial refusal, which is native from Scandinavia to Northern Russia until the Ural, but also in the Alps and East European mountain ranges. Few generations later the cultivated spruce became the bread (i.e., high-yielding) tree of forestry, able to cover demands for (softwood) timber and to provide pulp for the developing paper industry. During the fierce battles of World War II in the Northern Eifel (Hurtgen Forest), tree stock was severely damaged so that, again, fast-growing spruce was planted in the 1950s to cover the bare hills. When in the 1960s many smallholders quit their business, the government of NRW supported the transfer of grassland and fields, even if not suited, to spruce monoculture. As a result of the major storm disasters of the early 1990s that laid waste to large areas of spruce forests, rethinking began. The latest disturbance to the spruce grown in the Eifel was frequent and severe droughts (see **Figure 2**). This is true especially for the 2018 drought, when a high-pressure system was established over central Europe and persisted nearly continuously from April to October (Buras et al., 2020). For further information about the European drought conditions we refer to the European Drought Observatory reports (Masante and Vogt, 2018).

The growing spruce forests suppressed the understory, and as a consequence, affected the biodiversity of the area. Moreover, the spruce with its shallow root system, is not well prepared for drought conditions, which become also in the Eifel more severe during recent decades. The weakened spruce stands are suffering from bark beetle attacks, the most significant natural mortality agent of mature spruce. That is why the current aim of forestry is to transform non-site-appropriate pure spruce stands into more stable and natural mixed stands or deciduous forest comprising native deciduous trees (Umweltbundesamt, 2019; Holzwarth et al., 2020). Therefore, the increased spruce mortality after the 2018 drought has, on the one hand, tragic impacts on forest management and timber wood prices, but on the other hand provides a chance for fastened forest structure transformation.

FIGURE 2 | Typical situation of a spruce stand in the Northern Eifel in fall 2020. After the 2018 summer drought many spruce stands died and the forest management was not able to quickly remove and substitute the huge amount of affected trees.

GOOGLE EARTH ENGINE FOR CLOUD PROCESSING AND AVAILABLE DATA SETS

An easy way to step into the field of EO application is to use the Google Earth Engine (GEE[2]). The user does not need to download and store large EO data sets, to work with unknown or complex file formats, to check the localization of different data sources, or to care about adequate information technology infrastructure such as high-performance computing facilities (supercomputers). All data is available and accessible to be processed on Google's cloud infrastructure, from local to global geospatial scales. GEE is also designed to support the dissemination of results to other stakeholders or even the general public via Earth Engine Apps (Gorelick et al., 2017). Many solutions based on JavaScript are available, and the number is continuously increasing. Via Application Programming Interfaces (APIs) also Python and R code can be implemented. Small changes in location or time scale make published code easy to apply for own purposes. In this study, we use GEE also to analyze the data and for the preparation of figures.

Sentinel-2 Multispectral Data

The main analysis is based on the multispectral imaging mission Sentinel-2. With four bands at 10 m, six bands at 20 m, and three bands at 60 m spatial resolution Sentinel-2 covers the visible and near-infrared as well as the shortwave infrared regions of the electromagnetic spectrum (Drusch et al., 2012). The mission consists of two satellites launched in June 2015 (Sentinel-2A) and March 2017 (Sentinel-2B), resulting in a revisit time of 2–3 days at mid-latitudes. The data set available at the Earth Engine Data Catalog (S2_SR) is bottom-of-atmosphere surface reflectance (Level 2A) product already corrected for atmosphere, terrain and cirrus impact by sen2cor toolbox (Richter et al., 2012). The image collection was filtered by the cloudy pixel percentage property with values lower than 10% and the median was calculated based on available data in July and August for selected years. Bands B2 (Blue), B3 (Green), B4 (Red), B5 (Red Edge 1), B8 (Near Infra-Red), B11 (Shortwave Infrared 1), and B12 (Shortwave Infrared 2) are used for the analysis by calculating the band-wise temporal median, Bands B4 and B8 of the median were used to calculate the Normalized Difference Vegetation Index (NDVI) (Rouse et al., 1973).

SMAP Soil Moisture Data and Soil Moisture Anomalies

In order to visualize the drought conditions during the summer of 2018 and 2019 in relation to normal years, Soil Moisture Active and Passive (SMAP) satellite soil moisture retrievals were selected. The available data set at the Earth Engine Data Catalog has been developed by the Hydrological Science Laboratory (HSL) at NASA's Goddard Space Flight Center in cooperation with the United Stated Department of Agriculture (USDA) Foreign Agricultural Services and USDA Hydrology and Remote Sensing Lab (Sazib et al., 2018). SMAP is a passive microwave sensor providing spatially enhanced soil moisture estimates at 9 km resolution with overpasses in mid-latitudes of 2–3 days. The product at hand is based on the SMAP Level 3 product which was transferred to a 10 km grid. This data is assimilated into the two-layer Palmer water balance model by a one-dimensional ensemble Kalman filter approach to reduce forcing and observation errors as well as to provide a root zone soil moisture product (Bolten et al., 2010). Here the depth of the effective root zone is defined according to the Food and Agriculture Organization of the United Nations (FAO) digital soil map of the world. The anomalies consider the deviation of the current conditions

[2]https://earthengine.google.com

relative to the average of the available period standardized by the climatological standard deviation, where the climatology values are estimated based on the full data record of the satellite observation period over a 31-day moving window.

Statistical Forest Data of Crown Transparency

The evaluation of the forest conditions in Germany is performed yearly through the national forestry inventory (BMEL, 2020). The vitality of German forests is characterized by a visual inspection of treetops in the months July and August in a systematic 16 km* 16 km sampling grid. This is enhanced (to a 4 km* 4 km scheme) for the federal state of NRW (MUNLV, 2020). Sentinel-2 scenes have been selected during these inspection months.

As tree health cannot be easily characterized, and as multiple definitions exist, the forest inventory makes use of a single indicator, the tree crown transparency. Tree canopies may have been affected by damaging insect pests or fungal pathogens, so that the impact is often manifested through changes in tree crown conditions. In particular the attributes foliage discoloration and crown defoliation are found to provide good indicators of tree health leading to crown transparency (Metzger and Oren, 2001; Borianne et al., 2017).

During national forestry inventory, experts group trees by international standards into 5% steps of crown transparency. These are again grouped into five stages of tree damage, and these again into three groups indicating healthy trees (no increased crown transparency), a warning level (slightly increased crown transparency) and seriously damaged trees (considerably increased crown transparency) (Wellbrock et al., 2018). The standard error of the statistics is given with 2.3% (BMEL, 2020).

Auxiliary Data for Analysis of Mortality-Dependence

Land surface temperature (LST) at daytime has been selected from the Terra LST and Emissivity 8-Day Global 1km data set provided in the Earth Engine Data Catalog. Thermal infrared bands 31 and 32 of MODIS were fed into a generalized split-window LST algorithm, where first-order topographic information (i.e., elevation) is considered in radiative transfer simulations. We analyzed LST data from June to September in 2018 and 2020 with a focus on summer droughts.

In addition, the dependence of crown transparency on precipitation is analyzed. The long-term monthly precipitation of the years 2007–2018 are provided at 1 km in the OpenLandMap data set (Hengl, 2018). The approach behind uses METOP Advanced Scatterometer (ASCAT) soil moisture information fed into the SM2RAIN processor to retrieve precipitation (Brocca et al., 2019). Via cubic splines it has been downscaled to 1 km and averaged between WorldClim, CHELSA, and IMERGE precipitation products. The long-term August precipitation is selected for spatial spruce health analysis here.

Elevation data is taken from the Shuttle Radar Topography Mission (SRTM) V3 C-band product at a resolution of 1 arc-second, i.e., ∼30 m at the equator (Farr et al., 2007). Gaps and voids have been filled by additional data such as the ASTER Global Digital Elevation Model 2 (Fujisada et al., 2012). Aspect and slope were calculated from the elevation data by GEE terrain functions.

APPROACH

The approach makes use of the forest health statistics applied to an analysis of the NDVI obtained by Sentinel-2. Two main assumptions provide the foundation of the analysis: The first assumption considers the spruce health statistics of NRW to be representative also for the spruce stands in the Northern Eifel. Noteworthy spruce stands can be found in the South of NRW only. Next to the Northern Eifel region, especially in the Sauerland and to a lower extent the Bergisches Land and the Weserbergland have spruce coverage. Those regions have comparable elevations (100–600 m), similar geology being German low mountain ranges developed in Devon and Trias, and with this comparable soil genesis. I.e., the environmental conditions are similar to the Northern Eifel. If more specific spruce crown transparency level data for the region of interest is available, this can be implemented similarly. Second, it is assumed that the tree health continuously increases with NDVI. With the previously mentioned crown transparency damage levels and their related foliage discoloration and crown defoliation, a reduction in chlorophyll content can be observed. Therefore, the

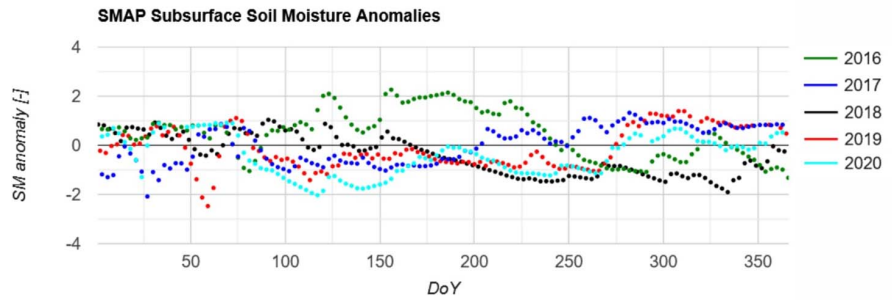

FIGURE 3 | SMAP subsurface soil moisture anomalies for the years 2016–2020 averaged over the area of investigation. Anomalies were calculated with respect to the reference period 2015–2020. Due to the non-continuous 2–3 day acquisitions of SMAP it is shown as a point diagram.

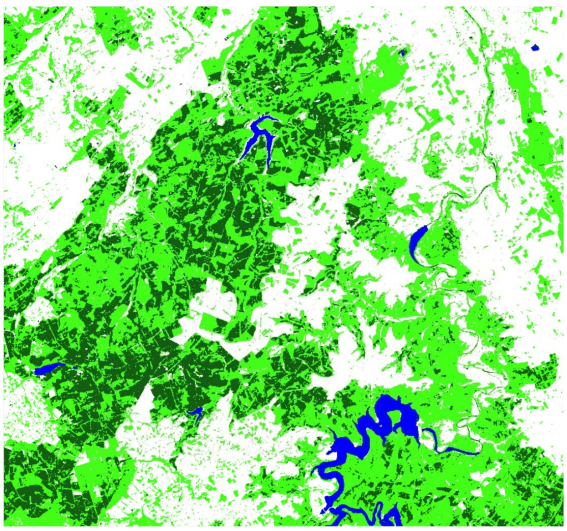

FIGURE 4 | Support Vector Machine (SVM) classification result of the Sentinel-2 2018 median composite of the Northern Eifel (dark green, spruce; light green, other forest; blue, water; and white, other).

assumption of reduced NDVI with increasing tree damage is in general valid and supported by many studies (Lausch et al., 2013; Misurec et al., 2016; Spruce et al., 2019; Gomez et al., 2020; Bryk et al., 2021).

Based on these preconditions, our simple approach evaluates the NDVI of the reference year and identifies NDVI thresholds for the groups *damaged spruce* and *spruce at warning level*. Applying the same thresholds to the target year instead of the reference one, data can be classified accordingly. In this study, we selected 2018 as the reference year and 2020 as the target year. All data is clipped to the area of interest to provide the regional statistics. Without this selection, the analysis can also be applied to larger scales, but the statistics calculation in GEE is limited to a certain number of pixels. A workaround is to reduce the spatial resolution of the analysis.

First, for the reference year the median Sentinel-2 data was classified by a supervised support vector machine (SVM) method. Training polygons were provided for the classes *spruce*, *other forest*, *water* and *others*. The last class includes polygons for built-up areas, grassland and agriculture. The Radial Basis Function (RBF) kernel is used to solve non-linear problems with intermediate hyperplane (gamma of 0.5) and margin (cost of 10) parameters (Cortes and Vapnik, 1995). Our classification approach has been employed before, for instance, Wessel et al. (2018) successfully implemented a similar method for tree species classification using Sentinel-2 data. The area of the resulting *spruce* class for the reference year is then further analyzed, the other classes are neglected. All spruce class NDVI values are used to calculate the histogram and the related CDF. In correspondence with the forest statistics indicating the percentage of damaged (warning level) spruce, the NDVI threshold for the specific percentage of pixels is retrieved. The CDF in the physical NDVI domain provides the probability that the NDVI is below the threshold value for damaged spruce ($NDVI_D$). Here for the reference year 2018 the NRW forest statistics indicate that 37% of the spruce is damaged:

$$P\left(x \leq NDVI_D\right) = \int_{-1}^{NDVI_D} t\, dt = 0.37 \tag{1}$$

Similarly, the statistics indicate that 36% of the spruce forest in 2018 has reached the warning level. This level is used to retrieve the respective threshold $NDVI_W$:

$$P\left(NDVI_D \leq x \leq NDVI_W\right) = \int_{NDVI_D}^{NDVI_W} t\, dt = 0.36 \tag{2}$$

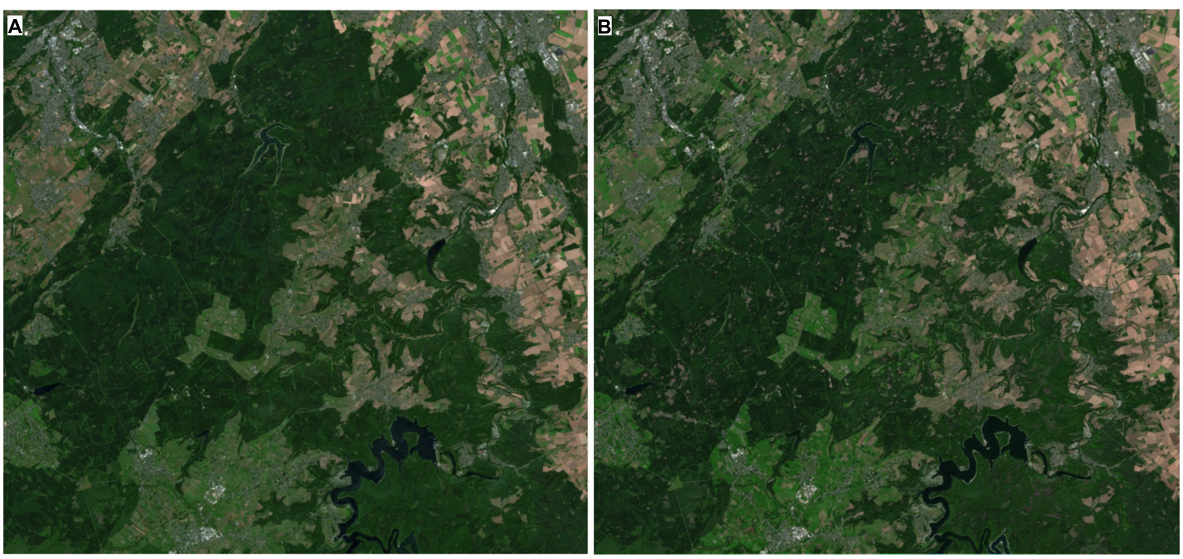

FIGURE 5 | Sentinel-2 July/August median composite (RGB = B4, B3, and B2) **(A)** for the year 2018, and **(B)** for the year 2020 (CDF-matched).

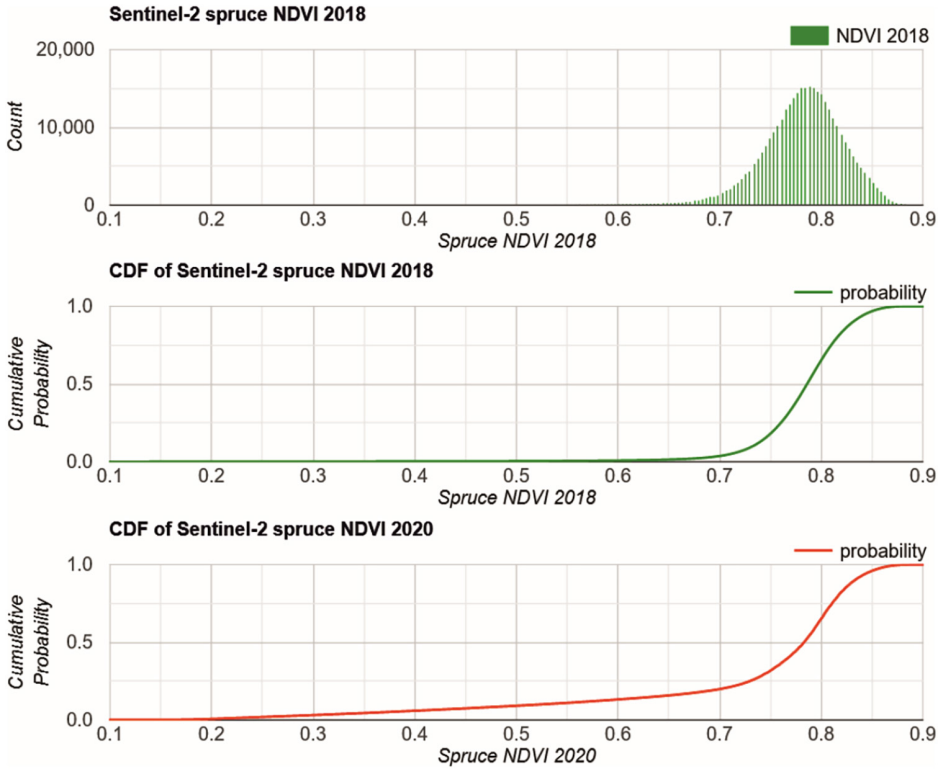

FIGURE 6 | GEE histogram (top) and CDF (center) of spruce NDVI 2018 and CDF (bottom) of spruce 2020. The CDF 2018 is used to identify the NDVI threshold for damaged and warning level spruce according to the forest statistics.

Due to the large number of pixels and histogram bins we omitted fitting a CDF function and used the original spruce NDVI CDF, i.e., the empirical CDF, instead with a negligible error. Once $NDVI_D$ and $NDVI_W$ have been retrieved based on the reference year, with a random selection of respective pixels (here 10% of each level) in the three levels, a supervised SVM was trained based on the reference year Sentinel-2 median composite bands. The same parameters for the classification into spruce transparency levels were used as in the previous SVM application for the land cover classification. In addition to the classes provided in the forest statistics, we wanted to separately identify removed spruce stands. The SVM was trained on representative areas of the 2020 Sentinel-2 data. This information is then applied to classify the 2020 target year Sentinel-2 median composite. However, intermediate results showed significant differences in the reflectance values of the median composites of the reference and target years. The calculation of the median was not able to fully compensate for that. Therefore a CDF matching approach was applied for each median composite band to correct for biases and to map a target image pixel value to a corresponding value in the reference CDF that has the equivalent cumulative probability value. This approach ensures full comparability of Sentinel-2 data from different years, where atmospheric conditions were not fully corrected, or where observation angles or illumination conditions were different. Note that this CDF matching was applied to the full median image and not for the spruce class only.

The area fractions of the three classes of spruce health conditions are calculated for the target year. In addition, the classes are evaluated regarding their frequency in specific levels of LST, elevation, slope, and aspect. The processing of the Sentinel-2 data is performed at 20 m scale for performance reasons. The histogram analysis related to the mentioned environmental preconditions is performed at 50 m resolution.

RESULTS AND DISCUSSION

Drought Conditions

The root zone soil moisture anomalies (dating back to 2015) spatially averaged for the Northern Eifel region are presented in **Figure 3**. They indicate the relative differences between the years to rate the relative dryness during the seasons. Whereas 2016 had a very wet summer and 2017 was a normal year, the recent years exhibit serious drought conditions. In late May 2018 the significant drought began and lasted until the end of the year. During the winter 2018/2019 rainfall was not sufficient to restore the soil water storage capacity. Already in March 2019 soil moisture conditions were slightly lower than the average, but here the specific preconditions from 2018 and the long duration of 7 months was a challenge for some ecosystems. The year 2020 was characterized by a very dry spring separated by few precipitation events from a dry summer.

This illustrates that in recent years 2018–2020 several ecosystems affected by dry weather conditions. In addition, the spruce stands were placed on the barren Eifel regions with shallow soils (Montzka et al., 2008a,b), which were even less

TABLE 1 | Fractions of classified spruce health conditions by the forest statistics and by the proposed remote sensing approach.

	Damaged (%)	Warning level (%)	Healthy (%)
2018 forest statistics	37	36	27
2020 forest statistics	45	29	26
2020 remote sensing	38.3 (13.8% rem.+24.5% dam.)	33.3	28.4

productive for agriculture. The shallow soils over the bedrock have a very low total water storage capacity so that longer dry periods cannot be bridged. These two corresponding factors lead to the increased spruce mortality in the Northern Eifel. Another driver is bark beetle infestation, e.g., Netherer et al. (2019) report for Austrian forests that dry and shallow soil conditions are typically less affected, but acute drought proved to raise the probability of bark beetle attacks. As the low soil depth is not adequately reflected by the higher resolution soil information provided by the Earth Engine Data Catalog, e.g., the OpenLandMap soil texture map, a more detailed analysis may provide misleading results within GEE. Interested analysts may implement the NRW soil map 1:50.000 for this purpose.

Identification of the Area Covered by Spruce

The SVM classification results of the reference year 2018 were evaluated with independent validation samples. The kappa coefficient (Hudson and Ramm, 1987) for the classification is given with 0.965. The confusion matrix indicates that only the class *other* has misclassifications, the class *spruce* was perfectly classified. The separability of *spruce* is remarkable, especially when using the full potential of the Sentinel-2 bands. Visual inspection of the classification results indicate minor spruce misclassifications at the coastlines of the lakes, where the spectral signature of mixed pixels and the re-greening of fallen dry areas after the summer period is closest to the *spruce* class. The classification is shown in **Figure 4**, in line with the multispectral Sentinel-2 data of 2018 and 2020 (**Figure 5**).

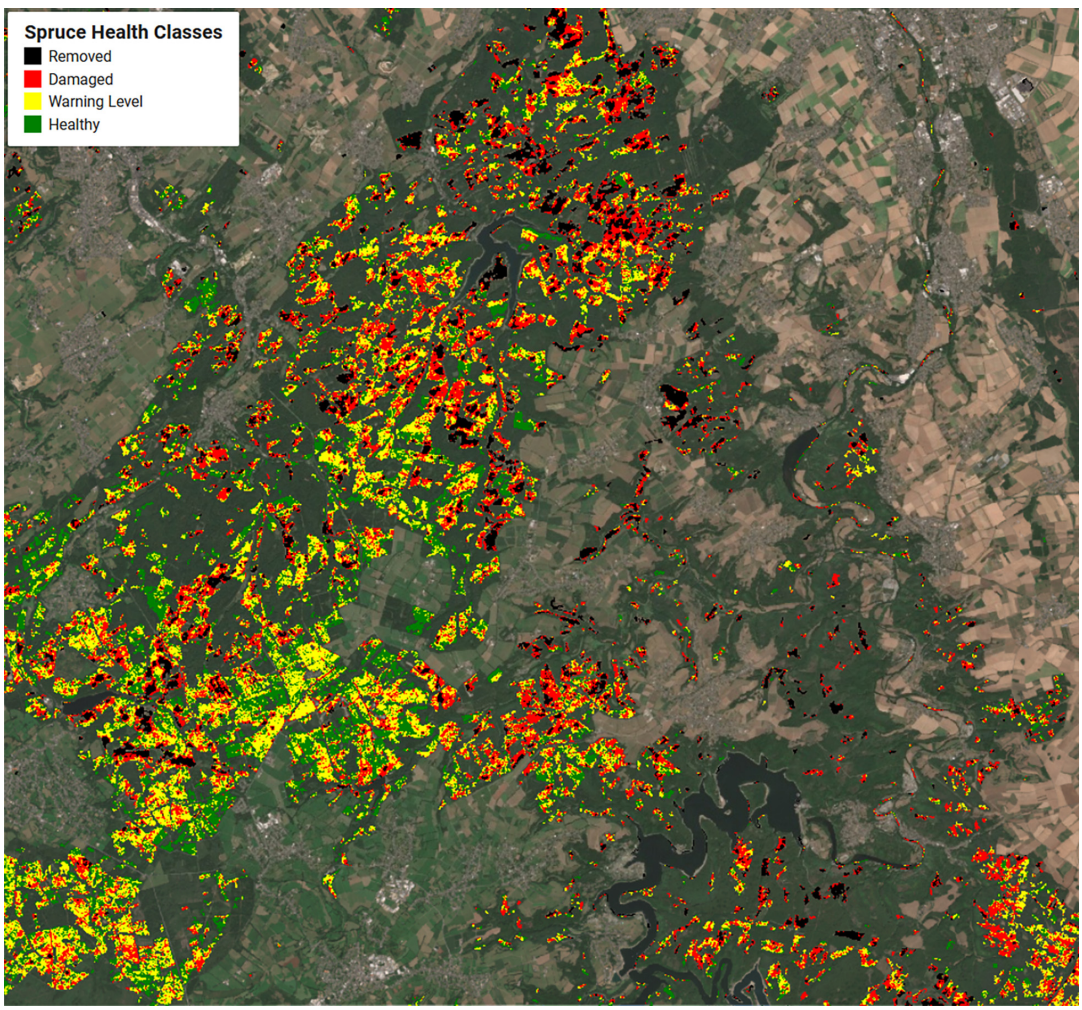

FIGURE 7 | 2020 spruce health classes removed (black), damaged (red), warning level (yellow), and healthy (green) estimated by this study in respect to the CDF matched Sentinel-2 median composite of 2020. The region of interest covers an area of 533 km^2.

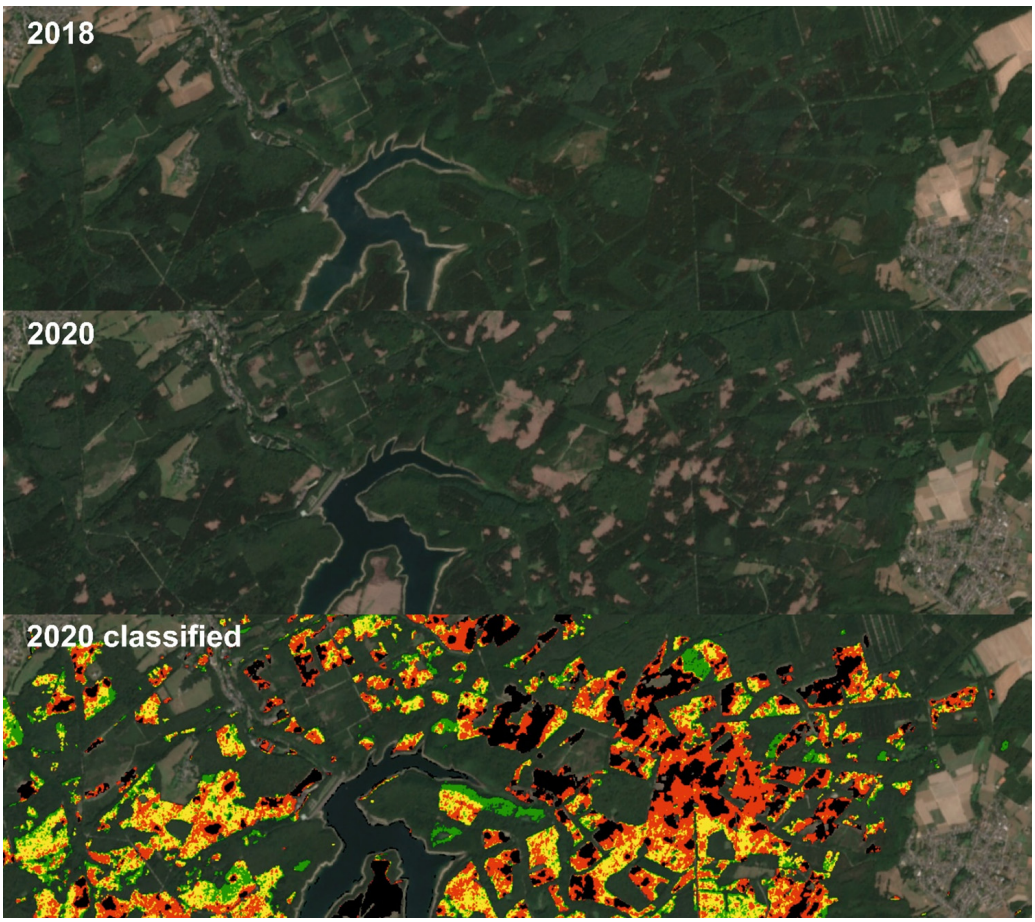

FIGURE 8 | Sentinel-2 data (RGB = B4, B3, and B2) of the Wehe dam area in the Venn anticline for 2018 (top), 2020 (middle, CDF matched), and estimated spruce health classes in 2020 (bottom, removed = black, damaged = red, warning level = yellow, and healthy = green).

Quantifying Tree Health Classes

From the 2018 forest statistics, the damaged and warning level percentages for spruce (i.e., 37% and 36%, respectively) were applied to the NDVI CDF to obtain the threshold values to differentiate between the three treetop transparency levels. The corresponding 2018 histogram and CDF are presented in **Figure 6**. The spruce NDVI histogram for 2018 is close to Gaussian with a mean of 0.78, but slightly skewed with a tail to lower NDVI. The CDF provides the resulting thresholds $NDVI_D$ and $NDVI_W$ with 0.774 and 0.808, respectively. This is in line with other studies evaluating spruce health or bark beetle outbreaks (Lastovicka et al., 2020; Zimmermann and Hoffmann, 2020).

In 2020, the CDF delivered a different picture (**Figure 6**). Here, the CDF is continuously increasing from 0.15, where removed spruce stands are characterized with low NDVI. After the 2018 drought and later tree removal the NDVI is increasing in some locations according to the occasional re-greening of the understory.

After identification of the spruce health levels based on the CDF matched Sentinel-2 median composite for 2020, their fractions were calculated (**Table 1**). The estimation of the area fraction falling into the *healthy* class was close to that of the forest statistics, i.e., 28.4% and 26%, respectively. The class *warning level* is overestimated and the class *damaged* is underrepresented in the remote sensing estimation, i.e., the high amount of 45% of damaged spruce is not fully captured with an area fraction of 38.3%. In this class, the damaged and removed spruce stands are combined. 13.8% of the spruce can be considered damaged as they have been already removed.

The band-wise CDF matching of the target year Sentinel-2 data to the reference year is very important. Otherwise, not adequately compensated atmospheric conditions may impact the threshold application and, therefore the relative area fractions of the three main classes. Here, advanced atmospheric correction methods, e.g., using pseudo-invariant features (Schott et al., 1988) or the iteratively re-weighted multivariate alteration detection (Canty and Nielsen, 2008), may improve the accuracy of the method applied.

Figure 7 shows the spatial extent of the spruce health levels in the Northern Eifel. The *removed* and *damaged* classes appear more compact than the *warning level* and *healthy* classes. For *removed* this is clearly related to the forest management activities typically applied at larger patches, whereas for the *damaged* class this might be an indication for the environmental preconditions

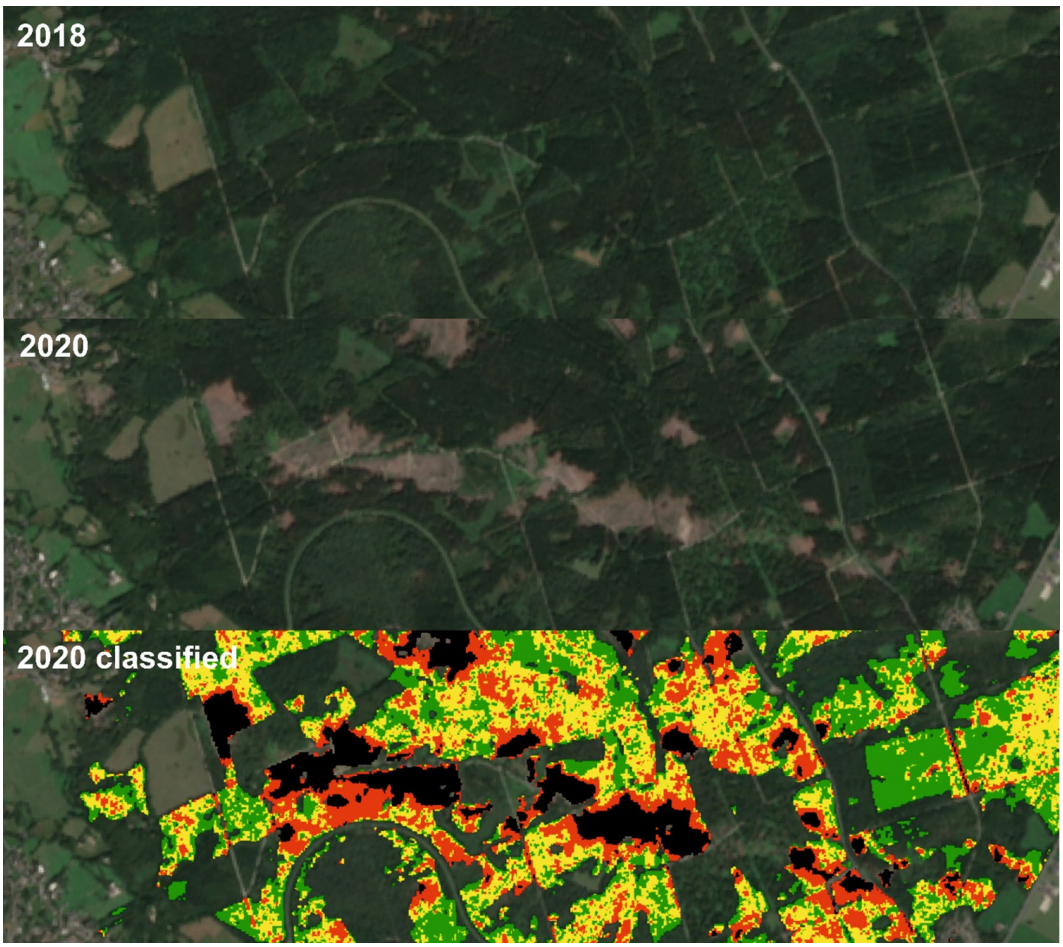

FIGURE 9 | Sentinel-2 median composite (RGB = B4, B3, and B2) for the year 2018 before the tornado (top), 2020 after the tornado (middle, CDF matched), and estimated spruce health classes in 2020 (bottom, removed = black, damaged = red, warning level = yellow, and healthy = green).

on spruce vitality. **Figure 7** and the visual inspection of the landscape, such as in **Figure 2** suggest that no single trees are affected, but large patches of spruce monocultures. In addition to the genotype of the spruce stand in a parcel, which may show a specific resilience to droughts, also common factors such as soil water storage capacity or precipitation levels may affect a parcel of spruce as a whole. Further analysis of these environmental preconditions is provided in section **"The Dependency of Spruce Health on Environmental Conditions."** The division between the *warning level* and *healthy* classes is not that clearly localized, and gradually draws through the parcels. Here, more research is needed if the NDVI is the adequate vegetation index to identify transparency levels of still dense spruce canopies.

In **Figure 8** we show a detailed example for the period July to August in 2018 and 2020. The upper panel depicts Sentinel-2 median composite for the reference year 2018 and the changes after two years for the same period of the year (middle and lower panel). First, the two RGB images appear very similar as a result of the CDF matching. This is not only the case for the bands B2–B4 used to construct the RGB, but also for the other bands including B8 which has been selected for calculating the NDVI (B4 and B8). Second, the cleared patches in 2020 are very prominent, and by comparing with the classification at the bottom, it is indeed the spruce that has been removed only. Those locations are very well captured by the procedure presented before. Moreover, the severely damaged spruce sites are dominating in the Eastern part of this section, originating from both the lower elevated area with generally less precipitation and the lee side to the prevailing West winds, with relatively dryer downward oriented air masses. The relationships of the spruce vitality levels toward environmental conditions is discussed in section **"The Dependency of Spruce Health on Environmental Conditions"**.

Foresters confirm that the main reason for the spruce mortality in the Northern Eifel is the drought conditions in recent years. Earlier studies in German spruce forests already reported the impact at dryer sites, where crown transparency was higher in years following hot summers (Seidling et al., 2012). However, small fractions are also affected by windfall, which may not be directly considered by the forest statistics

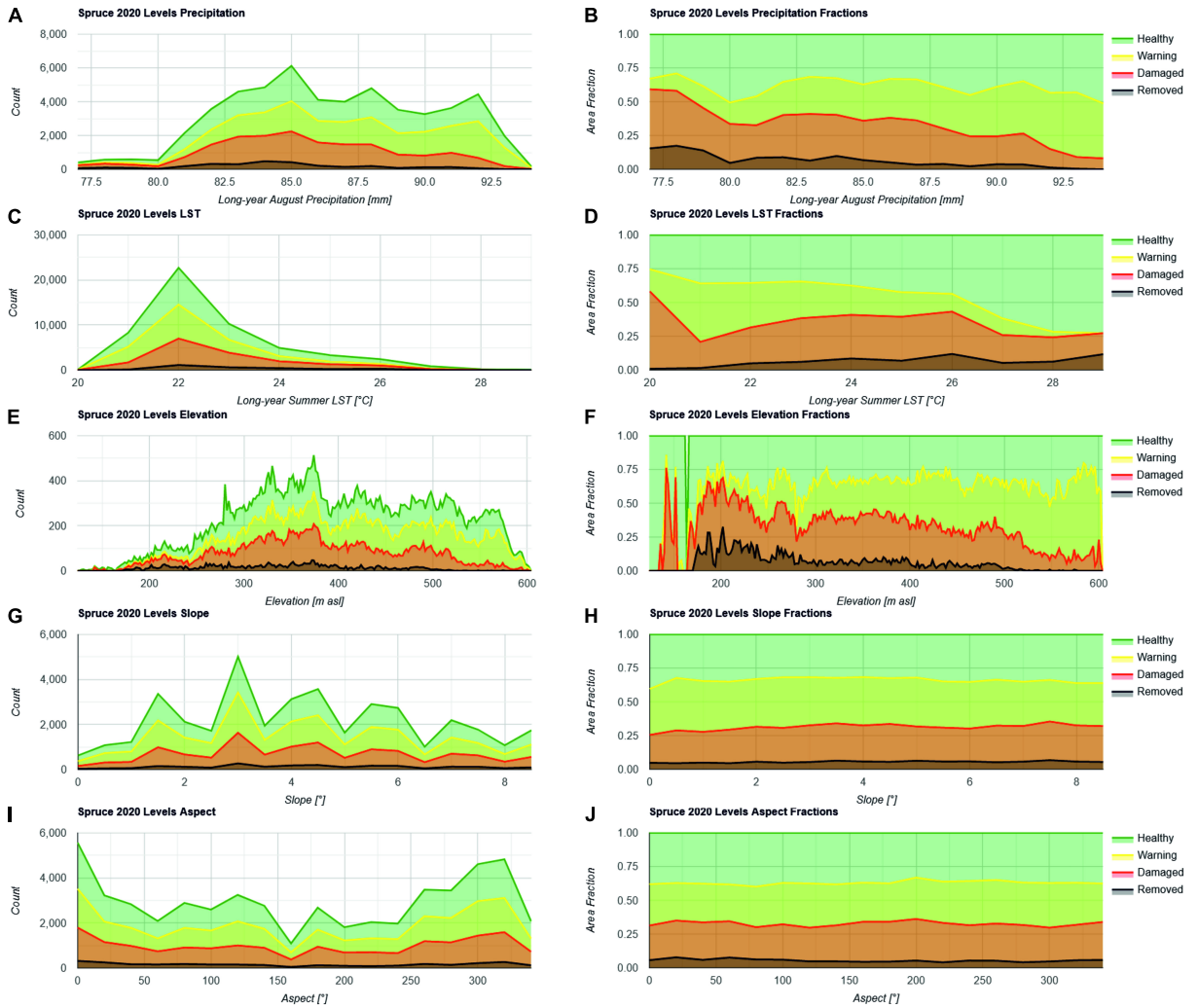

FIGURE 10 | Histograms of spruce health levels expressed in number of pixels showing a specific health level for 2020 in relation to the environmental conditions such as precipitation in August **(A,B)** summer land surface temperature from June to September 2018–2020 **(C,D)** elevation **(E,F)** slope **(G,H)** and aspect **(I,J)**. Both absolute pixel counts (left) and relative spruce area fractions (right) are shown.

applied here. A special incidence may support this interpretation: On March 13, 2019 a tornado devastated houses and forests close to the village of Roetgen in the South West of the investigated area. **Figure 9** shows the conditions before and after the tornado and the corresponding spruce health classification for 2020. The damages within the tornado track is clearly visible in the 2020 Sentinel-2 scene, but a 4 km sampling scheme of the forest statistics would not be able to identify the full dimension.

The Dependency of Spruce Health on Environmental Conditions

The different levels of Norway Spruce vitality in the Northern Eifel were analyzed with respect to their dependency on precipitation, LST, elevation, slope, and aspect. **Figure 10** shows both the absolute pixel counts at 50 m resolution in the function of these factors as well as the relative fractions normalized by total spruce.

Figure 10A shows the typical August precipitation (*X*-axis) ranging between 77 and 93 mm (panels A and B). The importance of precipitation with respect to spruce vitality was already demonstrated with its related soil moisture in **Figure 3**. The *Y*-axis shows the absolute pixel counts classified as spruce. Most spruce trees receive precipitation between 82 and 92 mm. **Figure 10B** shows that there is a clear trend in increasing fractions of *removed* and *damaged* spruce with lower precipitation. This indicates that precipitation (deficit) might be considered as one of the main drivers of spruce mortality, and that dryer areas require higher attention for transforming a monoculture spruce forest into a resilient mixed broadleaved forest. However, wetter areas are classified in the *warning level* already predicting further impacts of anticipating changes in the climate system.

The analysis of the summer LST distribution over the spruce locations shown in **Figures 10C,D** has been performed in order to clarify the impact of relative energy portions through insolation and a loss in transpirable water for plant cooling. This yields that most spruce forests receive a LST of 22°C. When ignoring the few stands with summer LST < 21°C and >26°C, also a trend becomes visible. Increasing mortality is documented with increasing summer LST. Similar to precipitation, the spruce at warning level is evenly distributed over the area, predicting that also lower summer LST may not help to reduce mortality in the future.

Figures 10E,F supports the hypothesis that removed and damaged trees can be increasingly found with lower elevations from 600 m to 200 m asl. The general perception in **Figure 7** is that the negative impact increases from South West to North East, which may be in line with a general decrease in elevation. This hypothesis is supported by **Figure 10**. It is obvious that the same patterns arise from elevation and from summer precipitation and LST, which coincide in the area of investigation.

The distribution of spruce vitality levels according to the steepness of slopes shown in **Figures 10G,H** has its origin in the assumption, that soils at steeper hangs are shallower than soils in flat areas due to gravity forces and erosion. Those shallow soils above bedrock may have lower water holding capacity indicating a lower resilience of the cultivated trees to drought conditions. With slopes up to 8° in the Northern Eifel according to the 1 arc-second resolution SRTM elevation model, no trend is visible. Damaged spruce might be slightly increasing with slope, but this is not significant.

Figures 10I,J shows the relation between the orientation of the hillslope toward the sun expressed in degrees counting clockwise with 0° and 360° being North and the various health levels. Examining this relationship foots on the assumption that the direction toward direct solar radiation relatively modifies evapotranspiration and, therefore, the soil water storage. Here, no significant trend is visible, but there is a small tendency of damaged spruce showing higher fractions at 160–200°, i.e., the orientation toward South.

In summary, there is evidence for trends in the spatial distribution of impact on spruce stands, where precipitation and the corresponding LST and elevation dependencies are most significant. A smaller trend is visible for the aspect according to the insolation, but the slope does not seem to have an effect.

CONCLUSION AND OUTLOOK

In this study, we presented an approach that allows to transfer forest monitoring statistics of a reference year (2018) to Sentinel-2 data to identify different spruce crown transparency levels. We made use of the spruce vegetation index CDF to identify parcels with severe crown transparency and a warning level where the tree health was already affected. In addition, their area fraction was estimated for a target year (2020) as well to support the statistical evaluation and reporting. Within two years, in the Northern Eifel region 14% of the spruce had to be removed, as they fell victim to the extreme drought conditions in recent years. The fraction of trees with severe crown transparency has increased to 38.3% (by including those of removed ones), which shows the dramatic situation in the typical Norway Spruce monocultures in the area. Only 28.3% remains in good condition. The area fractions are supported by the recent forest statistics of 2020. Against the background that the Norway Spruce is not endemic in the Eifel, current and future forest management needs to move toward alternative species such as Chestnut and American Red Oak.

An extension or transfer of the study to Federal State level or further Central European spruce areas such as the Thuringian Forest, the Erzgebirge, Hunsrück, Taunus, Westerwald, Rothaargebirge, Harz or the Southern regions of the Eifel is possible by selecting few adequate training data. Conducting the statistical evaluation of the results on GEE, however, is a limiting factor for selecting the region size. Besides that, also national-scale evaluations of the spruce health are feasible to identify spruce locations under pressure. The utilization of the so-called Level II environmental monitoring sites for forest vitality for that purpose could lead to a standardized spruce monitoring tool (Seidling, 2004). Similarly, machine learning approaches may be trained by data obtained at the 4×4 km sampling grid to predict actual spruce vitality levels.

Although it was the interest to provide a robust tool to evaluate the spruce health conditions in German low mountain ranges, several improvements are still possible. For example, while the NDVI is a robust metric, it may have problems with saturation and non-linearity with forest canopies (Stone and Mohammed, 2017). Alternative vegetation indices may improve the results at hand and may better differentiate affected and non-affected spruce stands by overcoming NDVI saturation effects. Red-edge dependent indices, water-related indices involving a SWIR band, or a combination of multiple indices may improve the method's performance (see e.g., Hawrylo et al., 2018; Abdullah et al., 2019; Lastovicka et al., 2020). Our approach was to support the statistical evaluation of tree health, so that the timing of the observations was aligned to the *in situ* survey. However, Solberg (2004) discussed the causal mechanisms of Norway spruce crown conditions and droughts and observed that the defoliation resulted from increased needle-fall in the autumn after dry summers. Therefore, postponing the *in situ* and remote observations may identify the most recent effects of droughts on spruce stands. Moreover, technical improvements such as the implementation of the Python API instead of JavaScript application would increase the flexibility of the tool in terms of data processing as well as the secondary analysis of the environmental preconditions.

In this study a significant dependency of cut and damaged spruce was reported to precipitation and elevation, a clear sign for the limited resilience of the Norway spruce to increasing drought conditions and a climate change. The spruce mortality stands as well as their environmental conditions identified here can be used to develop a variety of transformation scenarios (Hilmers et al., 2020) and to predict potential secondary infestation (Lausch et al., 2013). The proposed method may support the *in situ* forest evaluation as well as governmental monitoring programs in order to prioritize management practices or to identify highly vulnerable spruce stands. The approach

implemented for the Northern Eifel case study may serve as a blueprint for similar analyses in spruce forests affected by climate change.

CODE AVAILABILITY

The GEE tool can be accessed and the JavaScript code can be tested and implemented for own purposes via the following link: https://code.earthengine.google.com/cde6a13b3c35a72a5d6bf0c3e5a3ea7a.

DATA AVAILABILITY STATEMENT

The original contributions presented in the study are included in the article/supplementary material, further inquiries can be directed to the corresponding author.

AUTHOR CONTRIBUTIONS

CM: conceptualization, methodology, implementation, visualization, and initial draft. BB, AT, DM, and HV: review and editing the manuscript. All authors contributed to the article and approved the submitted version.

FUNDING

We acknowledge support from the German Federal Ministry of Economics and Technology for the AssimEO project under the grant 50EE1914A, the German Federal Ministry of Education and Research for the Agricultural Systems of the Future project DAKIS (grant 031BO729F), and from the Helmholtz research infrastructure Modular Observation Solutions for Earth Systems (MOSES).

REFERENCES

Abdullah, H., Skidmore, A. K., Darvishzadeh, R., and Heurich, M. (2019). Sentinel-2 accurately maps green-attack stage of European spruce bark beetle (*Ips typographus*, L.) compared with Landsat-8. *Remote Sens. Ecol. Con.* 5, 87–106. doi: 10.1002/rse2.93

Ali, M., Montzka, C., Stadler, A., Menz, G., Thonfeld, F., and Vereecken, H. (2015). Estimation and validation of rapideye-based time-series of leaf area index for winter wheat in the rur catchment (Germany). *Remote Sens. Basel.* 7, 2808–2831. doi: 10.3390/Rs70302808

Allen, C. D., Macalady, A. K., Chenchouni, H., Bachelet, D., McDowell, N., Vennetier, M., et al. (2010). A global overview of drought and heat-induced tree mortality reveals emerging climate change risks for forests. *For. Ecol. Manag.* 259, 660–684. doi: 10.1016/j.foreco.2009.09.001

Anderegg, W. R. L., Kane, J. M., and Anderegg, L. D. L. (2013). Consequences of widespread tree mortality triggered by drought and temperature stress. *Nat. Clim. Change* 3, 30–36. doi: 10.1038/nclimate1635

Anderegg, W. R. L., Martinez-Vilalta, J., Cailleret, M., Camarero, J. J., Ewers, B. E., Galbraith, D., et al. (2016). When a tree dies in the forest: scaling climate-driven tree mortality to ecosystem water and carbon fluxes. *Ecosystems* 19, 1133–1147. doi: 10.1007/s10021-016-9982-1

BMEL (2015). *Bundeswaldinventur*. Bonn: Federal Ministry of Food and Agriculture (BMEL).

BMEL (2020). *Ergebnisse der Waldzustanderhebung 2019*. Bonn: Federal Ministry of Food and Agriculture (BMEL).

Bogena, H. R., Montzka, C., Huisman, J. A., Graf, A., Schmidt, M., Stockinger, M., et al. (2018). The TERENO-rur hydrological observatory: a multiscale multi-compartment research platform for the advancement of hydrological science. *Vadose Zone J.* 17:55. doi: 10.2136/vzj2018.03.0055

Bolten, J. D., Crow, W. T., Zhan, X. W., Jackson, T. J., and Reynolds, C. A. (2010). Evaluating the utility of remotely sensed soil moisture retrievals for operational agricultural drought monitoring. *IEEE J. Select. Top. Appl. Earth Observ. Rem. Sens.* 3, 57–66. doi: 10.1109/Jstars.2009.2037163

Borianne, P., Subsol, G., and Caraglio, Y. (2017). Automated efficient computation of crown transparency from tree silhouette images. *Comput. Electron. Agr.* 133, 108–118. doi: 10.1016/j.compag.2016.12.011

Brocca, L., Filippucci, P., Hahn, S., Ciabatta, L., Massari, C., Camici, S., et al. (2019). SM2RAIN-ASCAT (2007-2018): global daily satellite rainfall data from ASCAT soil moisture observations. *Earth Syst. Sci. Data* 11, 1583–1601. doi: 10.5194/essd-11-1583-2019

Bryk, M., Kolodziej, B., and Pliszka, R. (2021). Changes of norway spruce health in the bialowie(z) over dota forest (CE Europe) in 2013-2019 during a bark beetle infestation, studied with landsat imagery. *Forests* 12:10034. doi: 10.3390/f12010034

Buras, A., Rammig, A., and Zang, C. S. (2020). Quantifying impacts of the 2018 drought on European ecosystems in comparison to 2003. *Biogeosciences* 17, 1655–1672. doi: 10.5194/bg-17-1655-2020

Byer, S., and Jin, Y. F. (2017). Detecting drought-induced tree mortality in sierra nevada forests with time series of satellite data. *Remote Sens. Basel.* 9:ARTN929. doi: 10.3390/rs9090929

Canty, M. J., and Nielsen, A. A. (2008). Automatic radiometric normalization of multitemporal satellite imagery with the iteratively re-weighted MAD transformation. *Remote Sens. Environ.* 112, 1025–1036. doi: 10.1016/j.rse.2007.07.013

Cortes, C., and Vapnik, V. (1995). Support-vector networks. *Mach. Learn.* 20, 273–297. doi: 10.1023/A:1022627411411

Dai, A. G. (2013). Increasing drought under global warming in observations and models (vol 3, pg 52, 2013). *Nat. Clim. Change* 3, 171–171. doi: 10.1038/Nclimate1811

Drusch, M., Del Bello, U., Carlier, S., Colin, O., Fernandez, V., Gascon, F., et al. (2012). Sentinel-2: ESA's optical high-resolution mission for GMES operational services. *Remote Sens. Environ.* 120, 25–36. doi: 10.1016/j.rse.2011.11.026

Farr, T. G., Rosen, P. A., Caro, E., Crippen, R., Duren, R., Hensley, S., et al. (2007). The shuttle radar topography mission. *Rev. Geophys.* 45:RG2004. doi: 10.1029/2005rg000183

Fassnacht, F. E., Latifi, H., and Koch, B. (2012). An angular vegetation index for imaging spectroscopy data-preliminary results on forest damage detection in the Bavarian National Park, Germany. *Int. J. Appl. Earth Obs.* 19, 308–321. doi: 10.1016/j.jag.2012.05.018

Fleming, A. L., Wang, G. X., and McRoberts, R. E. (2015). Comparison of methods toward multi-scale forest carbon mapping and spatial uncertainty analysis: combining national forest inventory plot data and landsat TM images. *Eur. J. For. Res.* 134, 125–137. doi: 10.1007/s10342-014-0838-y

Fujisada, H., Urai, M., and Iwasaki, A. (2012). Technical Methodology for ASTER Global DEM. *IEEE Transact. Geosci. Remote Sens.* 50, 3725–3736. doi: 10.1109/Tgrs.2012.2187300

Gomez, D. F., Ritger, H. M. W., Pearce, C., Eickwort, J., and Hulcr, J. (2020). Ability of remote sensing systems to detect bark beetle spots in the southeastern US. *Forests* 11:1167.

Gorelick, N., Hancher, M., Dixon, M., Ilyushchenko, S., Thau, D., and Moore, R. (2017). Google earth engine: planetary-scale geospatial analysis for everyone. *Remote Sens. Environ.* 202, 18–27. doi: 10.1016/j.rse.2017.06.031

Hansen, M. C., Potapov, P. V., Moore, R., Hancher, M., Turubanova, S. A., Tyukavina, A., et al. (2013). High-resolution global maps of 21st-century forest cover change. *Science* 342, 850–853. doi: 10.1126/science.1244693

Hasan, S., Montzka, C., Rüdiger, C., Ali, M., Bogena, H., and Vereecken, H. (2014). Soil moisture retrieval from airborne L-band passive microwave using high resolution multispectral data. *ISPRS J. Photogram. Remote Sens.* 91, 59–71.

Hawrylo, P., Bednarz, B., Wezyk, P., and Szostak, M. (2018). Estimating defoliation of scots pine stands using machine-learning methods and vegetation indices of Sentinel-2. *Eur. J. Remote Sens.* 51:194. doi: 10.1080/22797254.2018.1469337

Hengl, T. (ed.). (2018). *Monthly Precipitation in mm at 1 km Resolution Based on SM2RAIN-ASCAT 2007-2018, IMERGE, CHELSA Climate and WorldClim*. Castellon: OpenLandMap.

Hilmers, T., Biber, P., Knoke, T., and Pretzsch, H. (2020). Assessing transformation scenarios from pure Norway spruce to mixed uneven-aged forests in mountain areas. *Eur. J. For. Res.* 139, 567–584. doi: 10.1007/s10342-020-01270-y

Holzwarth, S., Thonfeld, F., Abdullahi, S., Asam, S., Da Ponte Canova, E., Gessner, U., et al. (2020). Earth observation based monitoring of forests in Germany: a review. *Remote Sens. Basel* 12:3570.

Hudson, W., and Ramm, C. W. (1987). Correct formation of the kappa coefficient of agreement. *Photogram. Eng. Remote Sens.* 53, 421–422.

Immitzer, M., and Atzberger, C. (2014). Early detection of bark beetle infestation in norway spruce (*Picea abies*, L.) using WorldView-2 data. *Photogram. Fernerk.* 14, 351–367. doi: 10.1127/1432-8364/2014/0229

Lastovicka, J., Svec, P., Paluba, D., Kobliuk, N., Svoboda, J., Hladky, R., et al. (2020). Sentinel-2 data in an evaluation of the impact of the disturbances on forest vegetation. *Remote Sens. Basel.* 12:1914. doi: 10.3390/rs12121914

Latifi, H., Dahms, T., Beudert, B., Heurich, M., Kubert, C., and Dech, S. (2018). Synthetic RapidEye data used for the detection of area-based spruce tree mortality induced by bark beetles. *Gisci. Remote Sens.* 55, 839–859. doi: 10.1080/15481603.2018.1458463

Lausch, A., Erasmi, S., King, D. J., Magdon, P., and Heurich, M. (2016). Understanding forest health with remote sensing -part IA review of spectral traits, processes and remote-sensing characteristics. *Remote Sens. Basel.* 8:1029. doi: 10.3390/rs8121029

Lausch, A., Heurich, M., Gordalla, D., Dobner, H. J., Gwillym-Margianto, S., and Salbach, C. (2013). Forecasting potential bark beetle outbreaks based on spruce forest vitality using hyperspectral remote-sensing techniques at different scales. *For. Ecol. Manag.* 308, 76–89. doi: 10.1016/j.foreco.2013.07.043

Linke, J., Fortin, M. J., Courtenay, S., and Cormier, R. (2017). High-resolution global maps of 21st-century annual forest loss: independent accuracy assessment and application in a temperate forest region of Atlantic Canada. *Remote Sens. Environ.* 188, 164–176. doi: 10.1016/j.rse.2016.10.040

Masante, D., and Vogt, J. (2018). *Drought in Central-Northern Europe – August 2018. JRC European Drought Observatory (EDO)*, ed. EDO Analytical Report. Available online at: http://edo.jrc.ec.europa.eu/documents/news/EDODroughtNews201808_Central_North_Europe.pdf (accessed June 14, 2019).

Metzger, J. M., and Oren, R. (2001). The effect of crown dimensions on transparency and the assessment of tree health. *Ecol. Appl.* 11, 1634–1640.

Mezei, P., Jakus, R., Pennerstorfer, J., Havasova, M., Skvarenina, J., Ferencik, J., et al. (2017). Storms, temperature maxima and the Eurasian spruce bark beetle Ips typographus-An infernal trio in Norway spruce forests of the Central European High Tatra Mountains. *Agr. For. Meteorol.* 242, 85–95. doi: 10.1016/j.agrformet.2017.04.004

Misurec, J., Kopackova, V., Lhotakova, Z., Campbell, P., and Albrechtova, J. (2016). Detection of Spatio-temporal changes of norway spruce forest stands in ore mountains using landsat time series and airborne hyperspectral imagery. *Remote Sens. Basel.* 8:92. doi: 10.3390/rs8020092

Montzka, C., Bogena, H. R., Weihermüller, L., Jonard, F., Bouzinac, C., Kainulainen, J., et al. (2013). Brightness temperature and soil moisture validation at different scales during the SMOS validation campaign in the Rur and Erft catchments, Germany. *IEEE Transact. Geosci. Remote Sens.* 51, 1728–1743. doi: 10.1109/TGRS.2012.2206031

Montzka, C., Canty, M., Kreins, P., Kunkel, R., Menz, G., Vereecken, H., et al. (2008a). Multispectral remotely sensed data in modelling the annual variability of nitrate concentrations in the leachate. *Environ. Model. Softw.* 23, 1070–1081. doi: 10.1016/j.envsoft.2007.11.010

Montzka, C., Canty, M., Kunkel, R., Menz, G., Vereecken, H., and Wendland, F. (2008b). Modelling the water balance of a mesoscale catchment basin using remotely sensed land cover data. *J. Hydrol.* 353, 322–334. doi: 10.1016/j.jhydrol.2008.02.018

MUNLV (2020). *Waldzustandsbericht 2020. Ministerium für Umwelt, Landwirtschaft, Natur- und Verbraucherschutzdes Landes Nordrhein-Westfalen, Düsseldorf*. Düsseldorf: MUNLV.

Netherer, S., Matthews, B., Katzensteiner, K., Blackwell, E., Henschke, P., Hietz, P., et al. (2015). Do water-limiting conditions predispose Norway spruce to bark beetle attack? *New Phytol.* 205, 1128–1141. doi: 10.1111/nph.13166

Netherer, S., Panassiti, B., Pennerstorfer, J., and Matthews, B. (2019). Acute drought is an important driver of bark beetle infestation in austrian norway spruce stands. *Front. Glob. Chang.* 2:39. doi: 10.3389/ffgc.2019.00039

Nielsen, M. M., Heurich, M., Malmberg, B., and Brun, A. (2014). Automatic mapping of standing dead trees after an insect outbreak using the window independent context segmentation method. *J. For.* 112, 564–571. doi: 10.5849/jof.13-050

O'Brien, M. J., Engelbrecht, B. M. J., Joswig, J., Pereyra, G., Schuldt, B., Jansen, S., et al. (2017). A synthesis of tree functional traits related to drought-induced mortality in forests across climatic zones. *J. Appl. Ecol.* 54, 1669–1686. doi: 10.1111/1365-2664.12874

Panayotov, M., Kulakowski, D., Tsvetanov, N., Krumm, F., Barbeito, I., and Bebi, P. (2016). Climate extremes during high competition contribute to mortality in unmanaged self-thinning Norway spruce stands in Bulgaria. *For. Ecol. Manag.* 369, 74–88. doi: 10.1016/j.foreco.2016.02.033

Pretzsch, H., Grams, T., Haberle, K. H., Pritsch, K., Bauerle, T., and Rotzer, T. (2020). Growth and mortality of Norway spruce and European beech in monospecific and mixed-species stands under natural episodic and experimentally extended drought. Results of the KROOF throughfall exclusion experiment. *Trees Struct. Funct.* 34, 957–970. doi: 10.1007/s00468-020-01973-0

Rao, K., Anderegg, W. R. L., Sala, A., Martinez-Vilalta, J., and Konings, A. G. (2019). Satellite-based vegetation optical depth as an indicator of drought-driven tree mortality. *Remote Sens. Environ.* 227, 125–136. doi: 10.1016/j.rse.2019.03.026

Richter, R., Louis, J., and üller-Wilm, U. M. (2012). *Sentinel-2 MSI—Level 2A Products Algorithm Theoretical Basis Document*. Darmstadt: Telespazio VEGA Deutschland GmbH.

Rouse, J. W., Haas, R. H., Schell, J. A., and Deering, D. W. (1973). *Monitoring the Vernal Advancement and Retrogradation (Green Wave Effect) of Natural Vegetation*. College Station, TX: Remote Sensing Centre, Texas A&M University.

Sala, A., Piper, F., and Hoch, G. (2010). Physiological mechanisms of drought-induced tree mortality are far from being resolved. *New Phytol.* 186, 274–281. doi: 10.1111/j.1469-8137.2009.03167.x

Sazib, N., Mladenova, I., and Bolten, J. (2018). Leveraging the google earth engine for drought assessment using global soil moisture data. *Remote Sens. Basel.* 10:1265. doi: 10.3390/rs10081265

Schott, J. R., Salvaggio, C., and Volchok, W. J. (1988). Radiometric scene normalization using pseudoinvariant features. *Remote Sens. Environ.* 26, 1–16. doi: 10.1016/0034-4257(88)90116-2

Seidling, W. (2004). Crown condition within integrated evaluations of level II monitoring data at the German level. *Eur. J. For. Res.* 123, 63–74. doi: 10.1007/s10342-004-0014-x

Seidling, W., Ziche, D., and Beck, W. (2012). Climate responses and interrelations of stem increment and crown transparency in Norway spruce, Scots pine, and common beech. *For. Ecol. Manag.* 284, 196–204. doi: 10.1016/j.foreco.2012.07.015

Senf, C., Pflugmacher, D., Zhiqiang, Y., Sebald, J., Knorn, J., Neumann, M., et al. (2018). Canopy mortality has doubled in Europe's temperate forests over the last three decades. *Nat. Commun.* 9:4978. doi: 10.1038/s41467-018-07539-6

Solberg, S. (2004). Summer drought: a driver for crown condition and mortality of Norway spruce in Norway. *For. Pathol.* 34, 93–104. doi: 10.1111/j.1439-0329.2004.00351.x

Sproull, G. J., Adamus, M., Szewczyk, J., Kersten, G., and Szwagrzyk, J. (2016). Fine-scale spruce mortality dynamics driven by bark beetledisturbance in Babia Gora National Park, Poland. *Eur. J. For. Res.* 135, 507–517. doi: 10.1007/s10342-016-0949-8

Spruce, J. P., Hicke, J. A., Hargrove, W. W., Grulke, N. E., and Meddens, A. J. H. (2019). Use of MODIS NDVI products to map tree mortality levels in forests affected by mountain pine beetle outbreaks. *Forests* 10:811. doi: 10.3390/f10090811

Stadelmann, G., Bugmann, H., Wermelinger, B., and Bigler, C. (2014). Spatial interactions between storm damage and subsequent infestations by the European spruce bark beetle. *For. Ecol. Manag.* 318, 167–174. doi: 10.1016/j.foreco.2014.01.022

Steinkamp, J., and Hickler, T. (2015). Is drought-induced forest dieback globally increasing? *J. Ecol.* 103, 31–43. doi: 10.1111/1365-2745.12335

Stone, C., and Mohammed, C. (2017). Application of remote sensing technologies for assessing planted forests damaged by insect pests and fungal pathogens: a review. *Curr. Rep.* 3, 75–92. doi: 10.1007/s40725-017-0056-1

Stovall, A. E. L., Shugart, H., and Yang, X. (2019). Tree height explains mortality risk during an intense drought. *Nat. Commun.* 10:4385. doi: 10.1038/s41467-019-12380-6

Umweltbundesamt (2019). *Monitoringbericht 2019 zur Deutschen Anpassungsstrategie an den Klimawandel*. Bonn: Umweltbundesamt.

van Mantgem, P. J., Stephenson, N. L., Byrne, J. C., Daniels, L. D., Franklin, J. F., Fule, P. Z., et al. (2009). Widespread increase of tree mortality rates in the western United States. *Science* 323, 521–524. doi: 10.1126/science.1165000

Wellbrock, N., Eickenscheidt, N., Hilbrig, L., Dühnelt, P.-E., Holzhausen, M., Bauer, A., et al. (2018). . *Leitfaden und Dokumentation zur Waldzustandserhebung in Deutschland. Thünen Working Paper*. Braunschweig: Johann Heinrich von Thünen-Institut, 97.

Wessel, M., Brandmeier, M., and Tiede, D. (2018). Evaluation of different machine learning algorithms for scalable classification of tree types and tree species based on sentinel-2 data. *Remote Sens. Basel.* 10:1419. doi: 10.3390/rs10091419

Zacharias, S., Bogena, H., Samaniego, L., Mauder, M., Fuss, R., Putz, T., et al. (2011). A network of terrestrial environmental observatories in Germany. *Vadose Zone J.* 10, 955–973. doi: 10.2136/Vzj2010.0139

Zhan, Z. Y., Yu, L. F., Li, Z., Ren, L. L., Gao, B. T., Wang, L. X., et al. (2020). Combining GF-2 and sentinel-2 images to detect tree mortality caused by red turpentine beetle during the early outbreak stage in North China. *Forests* 11:172. doi: 10.3390/f11020172

Zimmermann, S., and Hoffmann, K. (2020). Evaluating the capabilities of Sentinel-2 data for large-area detection of bark beetle infestation in the Central German Uplands. *J. Appl. Remote Sens.* 14:024515. doi: 10.1117/1.Jrs.14.024515

Conflict of Interest: The authors declare that the research was conducted in the absence of any commercial or financial relationships that could be construed as a potential conflict of interest.

frontiers in Forests and Global Change

PERSPECTIVE
published: 16 August 2021
doi: 10.3389/ffgc.2021.704670

Tree Mortality: Testing the Link Between Drought, Embolism Vulnerability, and Xylem Conduit Diameter Remains a Priority

Tommaso Anfodillo[1] *and Mark E. Olson*[2]*

[1] *Department Territorio e Sistemi Agro-Forestali, University of Padova, Legnaro, Italy,* [2] *Instituto de Biologia, Universidad Nacional Autonoma de Mexico, Mexico City, Mexico*

Global climate change-induced droughts are provoking events of forest mortality worldwide, with loss of tree biomass and consequent ecosystem services. Ameliorating the effects of drought requires understanding the causes of forest mortality, with failure of the hydraulic system being an important contributor. Comparative anatomical data strongly suggest that, all else being equal, wider conduits are more vulnerable to drought-induced embolism than narrow ones. However, physiology experiments do not provide consistent support for such a link. If a vulnerability-diameter link exists, though, it would contribute not only to explaining and predicting forest mortality but also to interventions to render individual trees more drought resistant. Given that xylem conduits scale with plant height, taller plants have wider conduits. If there is a vulnerability-diameter link, then this would help explain why taller plants are often more vulnerable to climate change-induced drought. Links between conduit diameter, plant height, and vulnerability would also provide guidance for standardizing sampling of hydraulic variables across individuals and suggest that selecting for relatively narrow conduits at given height from the tree top could produce more drought resistant varieties. As a result, given current ambiguities, together with the potential importance of a link, it is important to maintain the vulnerability-diameter link as a research priority.

Keywords: hydraulic architecture, tree height, tip-to-base xylem conduit widening, comparative anatomical data, climate change

OPEN ACCESS

Edited by:
Giovanna Battipaglia, University of Campania Luigi Vanvitelli, Italy

Reviewed by:
Sabine Rosner, University of Natural Resources and Life Sciences Vienna, Austria
Robert Muscarella, Uppsala University, Sweden

***Correspondence:**
Mark E. Olson
molson@ib.unam.mx

Specialty section:
This article was submitted to Forest Disturbance, a section of the journal Frontiers in Forests and Global Change

Received: *03 May 2021*
Accepted: *07 July 2021*
Published: *16 August 2021*

Citation:
Anfodillo T and Olson ME (2021) Tree Mortality: Testing the Link Between Drought, Embolism Vulnerability, and Xylem Conduit Diameter Remains a Priority. Front. For. Glob. Change 4:704670. doi: 10.3389/ffgc.2021.704670

INTRODUCTION

A major effort is underway to understand the causes of death of millions of trees worldwide under climate change-induced drought (Breshears et al., 2013, 2018; Allen et al., 2015; Anderegg et al., 2015, 2016; Adams et al., 2017; Choat et al., 2018; Trugman et al., 2018, 2021; Brodribb et al., 2020). These studies reveal a multitude of factors involved in forest mortality, from the failure of water transport in the wood, to insect or fungal attack and fire. Identifying the ways mechanisms at the individual level result in the death of trees across the landscape requires integration factors

across multiple scales. We wish to highlight that robust integration between experimental data on plant hydraulic function-- xylem physiology-- with comparative anatomical data-- morphological variation across species-- would provide better direction for research and more robust explanations than for comparative and experimental workers to continue research largely independently. The key point we focus on here is the possible link between vulnerability to drought-induced hydraulic failure and xylem water-transporting conduit diameter. If such a link exists, then it has a potentially very important role to play in explaining forest mortality events on large scales. Testing this possibility requires squaring comparative anatomical, across-species, data with the experimental results of xylem physiology studies.

EXPERIMENTAL DATA ARE INCONSISTENT WITH REGARD TO THE LINK

Physiology experiments have so far failed to find a consistent link between vulnerability to drought-induced embolism and conduit diameter, and likely as a result, recent reviews of the causes of forest mortality do not mention a possible vulnerability-conduit diameter link at all, suggesting that the link is not regarded as a significant potential player (Anderegg et al., 2015, 2016; Adams et al., 2017; Breshears et al., 2018; Stovall et al., 2019; Liang et al., 2020; Trugman et al., 2021). Some physiology experiments show a strong correlation, with the widest vessels in a given stem segment clearly being the first to embolize (Hargrave et al., 1994; Cai and Tyree, 2010). Others suggest that the link is sheer experimental error, known as the "open vessel artifact" (Martin-StPaul et al., 2014; Rockwell et al., 2014; Torres-Ruiz et al., 2015). Other studies examine situations in which the open vessel artifact would seem impossible and even so still fail to recover a vulnerability-diameter link (Cochard et al., 2015; Choat et al., 2016; Brodersen et al., 2018; Bouda et al., 2019; Jacobsen et al., 2019). These include minimally invasive techniques such as micro-computed x-ray tomography, which unlike traditional techniques do not require cutting stems into segments and deranging water columns under tension. Most such studies do not provide striking evidence that wider conduits are more vulnerable than narrow ones (Cochard et al., 2015; Choat et al., 2016; Brodersen et al., 2018; Bouda et al., 2019). At least one micro-ct study, though, suggests that vessels with larger volumes are indeed more susceptible to embolism (Jacobsen et al., 2019). Since conduits widen predictably from the tips of plant twigs to the trunk base and into the roots (Lechthaler et al., 2020; Olson et al., 2021), all else being equal (including xylem tension), roots should be more vulnerable than stems but this result is not always reported (Rodriguez-Dominguez et al., 2018; Wu et al., 2020). Thus, experimental evidence for the link is currently contradictory.

Moreover, there is not even a clear theoretical reason to expect a vulnerability-diameter link. This is in contrast to freezing-induced embolism, which has a consistent and well-understood relationship with conduit diameter (Cavender-Bares and Holbrook, 2001; Pittermann and Sperry, 2003, 2006; Cavender-Bares, 2005; Sevanto et al., 2012; Savage and Cavender-Bares, 2013). Failure of water transport under drought is certain to involve multiple factors, from wood density and pit membrane characteristics to internal conduit sculpture, the types of conductive cells present in the xylem and where gas exists in the xylem (Dalla-Salda et al., 2011; Sano et al., 2011; Li et al., 2016; Guan et al., 2021; Kaack et al., 2021). But all else being equal, wider conduits tend to be longer than narrow conduits, with a higher number of pits, which are often wider and with wider membrane pores (Martínez-Vilalta et al., 2002; Jacobsen et al., 2012, 2019). These traits should facilitate the spread of embolism in wider conduits. If wider conduits are also longer, then embolism propagation will occupy a greater volume in wider conduits (Comstock and Sperry, 2000; Jacobsen et al., 2012). If pit area is uniform across conduits, then conduits with larger volumes will have greater pit area. Greater pit area would offer more opportunity for air-seeding to adjacent conduits. So, even in the absence of a direct link between vulnerability and diameter, there are plausible reasons to suspect that natural selection could favor narrower conduits in situations of drought vulnerability. Yet studies fail to recover the predicted pit area-vulnerability relationships (Lens et al., 2011). Presumably it is on the basis of such inconsistent results regarding a link between vulnerability to drought-induced embolism and xylem conduit diameter that recent treatments of the causes of drought-induced mortality do not mention conduit diameter. And yet, if there were a link, it would contribute to explaining so much about forest mortality and plant adaptation in general.

WHAT IS AT STAKE: WHAT THE VULNERABILITY-DIAMETER LINK WOULD EXPLAIN IF THERE WERE ONE

Testing the link between drought-induced embolism vulnerability and conduit diameter remains a priority because of the explanatory reach it would have if such a link existed, and that it is consistent with comparative anatomical evidence often spanning hundreds or thousands of species (Olson, 2020). We now briefly turn to some examples relevant to studies of forest mortality and drought adaptation.

Why Taller Individuals Are More Vulnerable to Drought

Taller trees are often more vulnerable to drought than their smaller conspecifics (Lindenmayer and Laurance, 2016, 2017; Olson et al., 2018; Stovall et al., 2019; McGregor et al., 2020; Swemmer, 2020). Because death of large trees has disproportionate ecological consequences, explaining the higher vulnerability of large individuals is a focus of plant scientists (Bennett et al., 2015; Stovall et al., 2019; Bartholomew et al., 2020; McGregor et al., 2020). For example, within a community the tallest trees make up a disproportionate part of total aboveground biomass (Lutz et al., 2018; Enquist et al., 2019), making protecting old-growth forests key for forest carbon storage (Körner, 2017). Scientists have suggested that tall trees are

more vulnerable because of the effects of gravity and resistance on their long hydraulic pathlengths, the higher vapor pressure deficit of the canopy, higher xylem demands for leaf-produced photosynthates, or that larger trees are simply more at risk of being pushed over by wind (Niklas, 1998; Koch et al., 2004; Givnish et al., 2014; McDowell and Allen, 2015; Trugman et al., 2018). The vulnerability-diameter link could be added to this list.

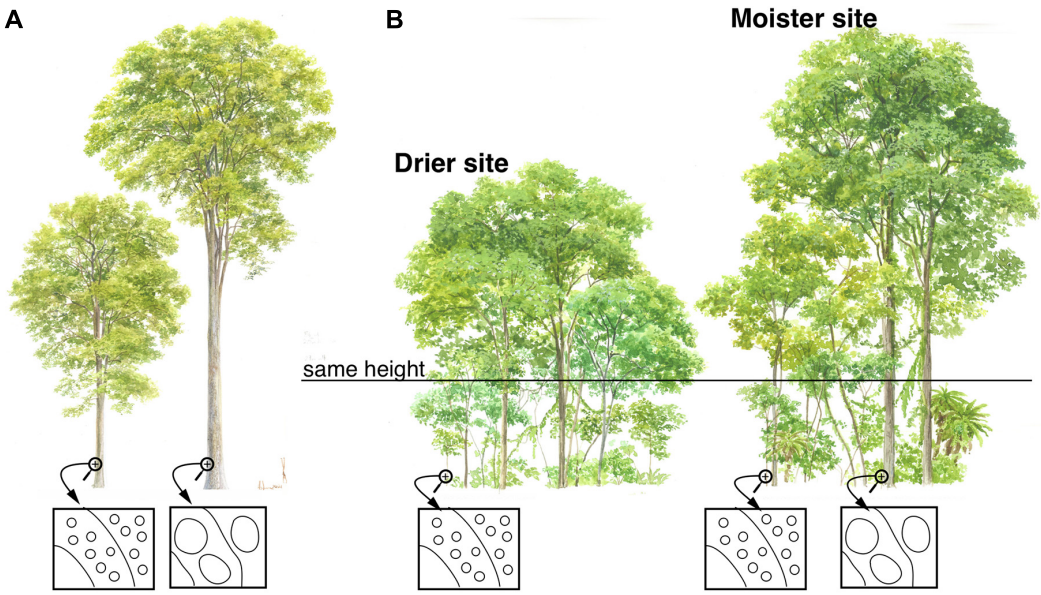

FIGURE 1 | Conduit diameter scales predictably with plant height. The figure shows trees of differing heights, with schematic xylem cross-sections in boxes. The ellipses in the schematics represent vessels. The arcs represent successive layers of xylem produced concentrically by the vascular cambium. **(A)** Natural selection favors widening of conduits as trees grow taller, thus maintaining conductance to the leaves even though conductive pathlength becomes longer and therefore resistance potentially higher. This predictable widening means that when an individual is small, it has narrower conduits in the outermost wood than when it is tall. **(B)** Similar-sized plants have, on average, similar mean conduit diameters, regardless of climate. Similar-sized plants in dry sites have similar mean conduit diameters as similar-sized plants in moist areas. Because maximum and therefore mean height is taller in moist as compared to dry areas, community mean conduit diameter is wider in areas with higher moisture availability.

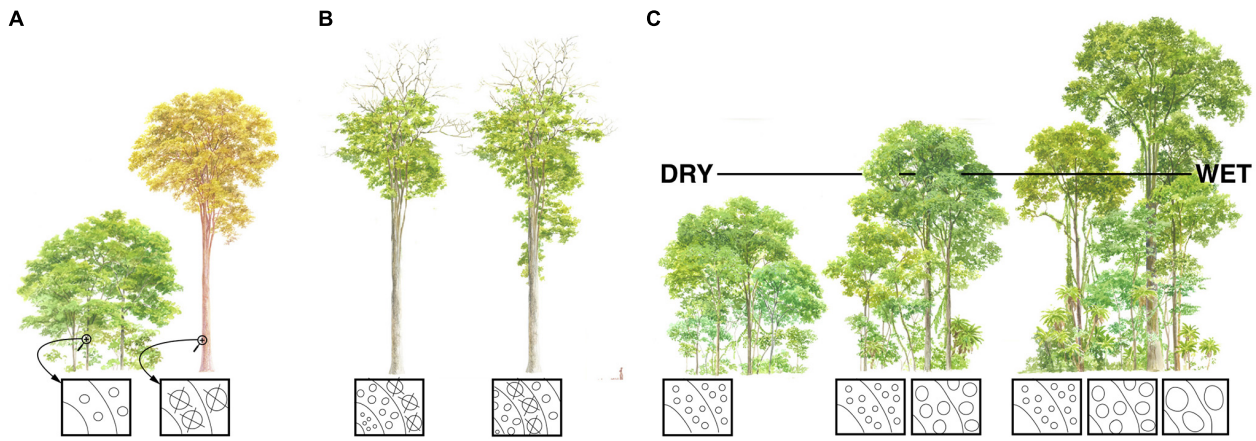

FIGURE 2 | Conduit diameter scaling with plant height, the putative vulnerability-diameter link, and forest mortality. Symbology as for **Figure 1**; "X"s represent embolized vessels. **(A)** Large trees tend to be more vulnerable to drought induced mortality. Because taller trees have wider conduits, if wider conduits are more vulnerable to drought-induced embolism than narrow ones, then this would help explain why larger individuals are more susceptible to mortality than smaller conspecifics at the same locality. **(B)** If wider conduits are more vulnerable to drought induced embolism, it could help explain treetop dieback as an adaptation. If climates become drier, then trees find themselves at heights that are too tall, and therefore conduits too wide, for current drier conditions. Sacrificing terminal branches and resprouting at a lower height would lead to narrower, more embolism-resistant conduits better suited to current conditions. **(C)** Maximum plant height is taller in moister communities. If climate change-induced drought tends to kill the tallest individuals of a species because of their wide, embolism-vulnerable conduits, then mean forest height will become lower.

Taller plants have predictably wider conduits (**Figure 1**), and if wider conduits are more vulnerable to embolism (**Figure 2A**), then this pervasive scaling of conduit diameter with plant height would contribute to explaining the greater vulnerability of taller plants. In all terrestrial vascular plants studied to date, xylem conduits are very narrow in the terminal leaf veins, widening toward the petiole base (Sack et al., 2012; Gleason et al., 2018; Lechthaler et al., 2019, 2020). In the shoot-root system, conduits are narrowest at the twig tips, widening predictably toward the base (Anfodillo et al., 2006; Petit et al., 2009; Koçillari et al., 2021; Olson et al., 2021). Poiseuille's Law shows that if conduits remain the same diameter but become longer, then flow to the leaves will decline in direct proportion to length, that is, the decrease in flow as a linear function of conductive path length.

However, Poiseuille's Law also shows that conductance depends on conduit diameter to the fourth power. This means that small increases in conduit diameter are sufficient to counteract the increase in resistance that increasing conductive path length creates. Given heritable within-species variation, all else being equal, individuals with conduits that widen slowly from the base and so are "too narrow" for a given stem length will have high resistance, low photosynthetic productivity, and low fitness. Those with conduits that widen quickly and so are "too wide" for a given stem length will, if wider conduits are more vulnerable to embolism, have a greater incidence of embolism, higher leaf dehydration and stomatal closure, and low fitness. The "just right" pattern is a hydraulic system made up of conduits that widen enough to overcome the resistance that arises as stems grow longer and conductive pathlength increases, but not so wide as to expose the individual to excessive embolism risk. Accordingly, across species, by far stem length is the variable that best predicts conduit diameter ($r^2 \approx 0.6–0.9$) (Anfodillo et al., 2006; Rosell and Olson, 2014; Olson et al., 2018, 2020b), as well as tip-to-base within individuals ($r^2 \approx 0.8–0.9$) (Anfodillo et al., 2006; Koçillari et al., 2021). As a result of this process of natural selection, taller trees [**Figure 1**; and longer lianas (Rosell and Olson, 2014)] have wider conduits. If wider conduits are more vulnerable to embolism, then this would help explain the greater vulnerability of taller individuals relative to others of the same species subject to the same conditions (**Figure 2A**) (Olson et al., 2018).

Why Some Individuals Die Whereas Others Do Not

Another aspect that a vulnerability-diameter link might help explain is the observation that one individual can die when apparently similar individuals in similar conditions survive (Trugman et al., 2021). A vulnerability-diameter link could help identify vulnerable individuals as those with relatively wide conduits for a given height. Even if the environmental conditions experienced by all individuals are identical, individuals with relatively wide conduits for a given plant height would be more vulnerable than individuals with narrower conduits. If this were the case, it would allow for relatively straightforward screening of populations to identify individuals with relatively wide conduits given height as the most vulnerable. It would allow for selection of more drought tolerant varieties by selecting those with relatively narrow conduits for a given height (Rosner et al., 2016). Additionally, it predicts that pruning in such a way that conductive path length is shortened and thus conduit diameter is narrower, would lower the drought vulnerability of a single individual.

Individual Tree Height

If narrower conduits are more drought resistant, and shorter plants have narrower conduits, then it seems likely that future forests will be shorter, with massive impacts on ecosystem services (Fajardo et al., 2019). If it were possible to select for individuals with slightly narrower conduits in the context of the same height, it might be possible to maintain tree biomass while still increasing drought resistance (cf. Rosner et al., 2016).

A vulnerability-diameter link would help explain the observed patterns of terminal branch dieback and resprouting that are observed in long-lived trees and in trees that survive drought (**Figure 2B**). Dead trunks, often hidden within taller foliage, at the tops of very old trees suggests that their terminal trunks have died and resprouted repeatedly over the centuries (Koch et al., 2004). Moist conditions impose less risk of embolism, permitting wider conduits. Wider conduits in turn permit greater conductive path lengths and thus height. When, over the decades or centuries, conditions become drier, trees can sacrifice their distalmost portions, shortening their total pathlenths. Given a constant rate of tip-to-base conduit widening, then shorter pathlengths lead to narrower conduits. If there is a link between vulnerability and conduit diameter, then these now-narrower conduits are better suited to the novel drier conditions that the trees are now subjected. The return of moister conditions again permits taller growth and the overtopping of the sacrificed trunk, accounting for dead snags in the tops of tall trees.

As with fluctuating heights in ancient trees, a vulnerability-diameter link would also contribute to explaining treetop dieback as an adaptive phenomenon (Rood et al., 2000; Olson et al., 2021). When drought sets in, trees find themselves at heights, and thus conduit diameters, that are excessive given current water availability. In such cases, natural selection favors shedding of terminal branches and re-sprouting at lower heights, allowing narrower, more embolism-resistant conduits better suited to current conditions (**Figure 2B**) (Rood et al., 2000; Olson et al., 2018). If a vulnerability-diameter relationship were to exist, no matter how indirect, it would help explain global patterns of vegetation height limitation, drought vulnerability, and dieback.

Why Maximum Plant Height Is Limited Across Sites of Differing Water Availability

If there were a link between drought-induced embolism vulnerability and conduit diameter, it would also help explain the global tendency for maximum vegetation height to be taller in areas of greater water availability. Minimum plant height tends to be the same across communities (**Figure 2C**). Where variation is most conspicuous is at the upper end of the height range. Drought-prone communities such as frost-free deserts have very

short maximum plant heights (Olson et al., 2020a). In contrast, frost-free rainforests can support trees well above 60 m tall (Adams et al., 2017; Shenkin et al., 2019). If moister conditions permit wider, more embolism-vulnerable conduits, and wider conduits are associated with longer pathlengths, then it helps explain why taller ecological strategies are observed in moister areas (**Figure 2C**).

If there is a link between embolism vulnerability and conduit diameter, then given a constant rate of tip-to-base conduit widening with plant height, a clone planted on a dry site will require a narrow, embolism resistant mean conduit diameter. Because narrow conduits are associated with shorter pathlengths, then clones on a dry microsite will cease growth at a lower height, associated with narrower conduits, than those on moist sites. Clones on moist sites are exposed to lower embolism risk and can produce wider conduits. Wider conduits are associated with longer stems, so the clones planted on moist microsites should grow taller than those on dry ones. The ability to detect embolism risk and adjust conduit diameter and therefore height according to microsite conditions, should be part of the adaptive phenotypic plasticity of all woody plant species. The patterns of variation in plant height globally across communities, as well as within species across microsites, would at least partially seem explicable given a link between drought-induced vulnerability to embolism and conduit diameter (Olson et al., 2018).

Growth Rings in Drought-Prone Plants

The vulnerability-diameter link would also help explain why species with conduit diameters that vary within growth rings in drought-prone, frost-free areas always have wider conduits in earlywood and narrow ones in latewood (Carlquist, 2001; Silva et al., 2019, 2021). Wider conduits are produced early in the growing season when water is abundant and soil water potentials are not highly negative. As the rainy season wanes and drought begins to set it, more highly negative xylem tensions are required to draw water from the soil. These more negative tensions, in turn, require narrower, more embolism-resistant conduits, thus explaining why conduit diameters in dryland species with growth rings go from wide to narrow, and potentially even why tangential diameter might predict dieback better than radial (Rosner et al., 2016). The vulnerability-diameter link thus potentially participates in explaining not only currently puzzling patterns of global tree mortality, but also the action of natural selection in shaping plant hydraulic systems as a function of climate, habitat, microsite, and habit.

THE VITAL INTERDEPENDENCE BETWEEN PHYSIOLOGICAL AND COMPARATIVE ANATOMICAL EVIDENCE OF XYLEM FUNCTION

For inferring xylem function, it is essential for xylem physiologists and comparative anatomists to work together. This is because "function" in biology implies adaptation (Garson, 2016; Olson, 2020). Because adaptation is an evolutionary process reaching into the distant and unobservable past, it requires adducing evidence from as many complementary sources as possible (Olson and Arroyo-Santos, 2015). Two very important sources are xylem physiology experiments and comparative anatomy studies. Both have their weaknesses, which are, happily, largely filled by the strengths of the other. Xylem physiology gains its relevance for inference of function via the assumption that the structure-function relations observed in an experiment are similar even in unobserved individuals, both contemporary and past. The comparative method tests this assumption (Olson et al., 2021). In xylem functional biology the most abundant comparative data are from comparative wood anatomy. For example, experiments show that narrow conifer tracheids are more resistant to freezing-induced embolism (Pittermann and Sperry, 2003, 2006; Sevanto et al., 2012), but these experiments have only covered small parts of a few species. Comparative data spanning hundreds of species are consistent with experimental observations, with conifers in very cold areas, as in plants at or above the treeline, having very narrow tracheids and short stature (e.g., *Podocarpus nivalis*, *Phyllocladus trichomanoides* var. *alpinus*, *Microcachrys*, etc.). In this way, experiments provide mechanistic detail but very limited generality; comparative wood anatomy provides maximal generality but very limited mechanistic detail. As a result, as in all of biology, there is an essential back-and-forth between experimental and comparative data (Mayr, 1982; Olson and Arroyo-Santos, 2015).

CONCLUSION: PERVASIVE PATTERNS REQUIRE EXPLANATION

Optimal tests of the putative link between vulnerability to drought-induced embolism and conduit diameter, examining the vulnerability of a wide range of conduit diameters under similar tensions in species adapted to frost-free, drought-prone habitats, have never been performed. Most physiological data come from temperate zone plants, so adaptation to cold has shaped the conductive systems of these species. As a result, caution is warranted before rejecting outright the possibility of some link existing. The comparative evidence suggesting such a link, e.g., tip-to-base conduit widening, wide-to-narrow conduits in growth rings, wider maximum conduit diameters in moister areas, the wide variance in vessel diameters in lianas (Rosell and Olson, 2014), etc., include without a doubt among the most widespread and pervasive patterns in all of xylem structure. A vulnerability-diameter link would not only contribute to explaining these patterns but also in predicting and potentially mitigating drought-induced damage to forests. Given this explanatory reach, until a plausible alternative explanation is provided for these important comparative patterns, then the vulnerability-diameter link, however, indirect it might be, must remain a research priority for xylem hydraulic biology.

DATA AVAILABILITY STATEMENT

The original contributions presented in the study are included in the article/supplementary material, further inquiries can be directed to the corresponding author.

AUTHOR CONTRIBUTIONS

TA and MO developed the idea and wrote the paper. Both authors contributed to the article and approved the submitted version.

ACKNOWLEDGMENTS

We thank Consejo Nacional de Ciencia y Tecnología project A1-S-26934 and PAPIIT-DGAPA, UNAM, project IN210719 for funding. Illustrations by Aslam Narvaez-Parra.

REFERENCES

Adams, H. D., Zeppel, M. J. B., Anderegg, W. R. L., Hartmann, H., Landhäusser, S. M., Tissue, D. T., et al. (2017). A multi-species synthesis of physiological mechanisms in drought-induced tree mortality. *Nat. Ecol. Evol.* 1, 1285–1291. doi: 10.1038/s41559-017-0248-x

Allen, C. D., Breshears, D. D., and McDowell, N. G. (2015). On underestimation of global vulnerability to tree mortality and forest die-off from hotter drought in the Anthropocene. *Ecosphere* 6, 1–55. doi: 10.1890/ES15-00203.1

Anderegg, W. R. L., Flint, A., Huang, C., Flint, L., Berry, J. A., Davis, F. W., et al. (2015). Tree mortality predicted from drought-induced vascular damage. *Nat. Geosci.* 8, 367–371. doi: 10.1038/ngeo2400

Anderegg, W. R. L., Klein, T., Bartlett, M., Sack, L., Pellegrini, A. F. A., Choat, B., et al. (2016). Meta-analysis reveals that hydraulic traits explain cross-species patterns of drought-induced tree mortality across the globe. *Proc. Natl. Acad. Sci. U.S.A.* 113, 5024–5029. doi: 10.1073/pnas.1525678113

Anfodillo, T., Carraro, V., Carrer, M., Fior, C., and Rossi, S. (2006). Convergent tapering of xylem conduits in different woody species. *New Phytol.* 169, 279–290. doi: 10.1111/j.1469-8137.2005.01587.x

Bartholomew, D. C., Bittencourt, P. R. L., Costa, A. C. L., Banin, L. F., Britto Costa, P., Coughlin, S. I., et al. (2020). Small tropical forest trees have a greater capacity to adjust carbon metabolism to long-term drought than large canopy trees. *Plant Cell Environ.* 43, 2380–2393. doi: 10.1111/pce.13838

Bennett, A. C., McDowell, N. G., Allen, C. D., and Anderson-Teixeira, K. J. (2015). Larger trees suffer most during drought in forests worldwide. *Nat. Plants* 1:15139. doi: 10.1038/nplants.2015.139

Bouda, M., Windt, C. W., McElrone, A. J., and Brodersen, C. R. (2019). *In vivo* pressure gradient heterogeneity increases flow contribution of small diameter vessels in grapevine. *Nat. Commun.* 10:5645. doi: 10.1038/s41467-019-13673-6

Breshears, D. D., Adams, H. D., Eamus, D., McDowell, N. G., Law, D. J., Will, R. E., et al. (2013). The critical amplifying role of increasing atmospheric moisture demand on tree mortality and associated regional die-off. *Front. Plant Sci.* 4:266. doi: 10.3389/fpls.2013.00266

Breshears, D. D., Carroll, C. J. W., Redmond, M. D., Wion, A. P., Allen, C. D., Cobb, N. S., et al. (2018). A dirty dozen ways to die: metrics and modifiers of mortality driven by drought and warming for a tree species. *Front. For. Glob. Change* 1:4. doi: 10.3389/ffgc.2018.00004

Brodersen, C. R., Knipfer, T., and McElrone, A. J. (2018). *In vivo* visualization of the final stages of xylem vessel refilling in grapevine (*Vitis vinifera*) stems. *New Phytol.* 217, 117–126. doi: 10.1111/nph.14811

Brodribb, T. J., Powers, J., Cochard, H., and Choat, B. (2020). Hanging by a thread? Forests and drought. *Science* 368, 261–266. doi: 10.1126/science.aat7631

Cai, J., and Tyree, M. T. (2010). The impact of vessel size on vulnerability curves: data and models for within-species variability in saplings of aspen, *Populus tremuloides* Michx. *Plant Cell Environ.* 33, 1059–1069. doi: 10.1111/j.1365-3040.2010.02127.x

Carlquist, S. (2001). *Comparative Wood Anatomy*, 2 Edn, Berlin: Springer.

Cavender-Bares, J. (2005). "Impacts of freezing on long distance transport in woody plants," in *Vascular Transport in Plants*, eds N. M. Holbrook and M. A. Zwieniecki (San Diego, CA: Academic Press), 401–424. doi: 10.1016/B978-012088457-5/50021-6

Cavender-Bares, J., and Holbrook, N. M. (2001). Hydraulic properties and freezing-induced cavitation in sympatric evergreen and deciduous oaks with contrasting habitats. *Plant Cell Environ.* 24, 1243–1256. doi: 10.1046/j.1365-3040.2001.00797.x

Choat, B., Badel, E., Burlett, R., Delzon, S., Cochard, H., and Jansen, S. (2016). Noninvasive measurement of vulnerability to drought-induced embolism by x-ray microtomography. *Plant Physiol.* 170, 273–282. doi: 10.1104/pp.15.00732

Choat, B., Brodribb, T. J., Brodersen, C. R., Duursma, R. A., López, R., and Medlyn, B. E. (2018). Triggers of tree mortality under drought. *Nature* 558, 531–539. doi: 10.1038/s41586-018-0240-x

Cochard, H., Delzon, S., and Badel, E. (2015). X-ray microtomography (micro-CT): a reference technology for high-resolution quantification of xylem embolism in trees: a reference method for xylem embolism. *Plant Cell Environ.* 38, 201–206. doi: 10.1111/pce.12391

Comstock, J. P., and Sperry, J. S. (2000). Theoretical considerations of optimal conduit length for water transport in vascular plants. *New Phytol.* 148, 195–218.

Dalla-Salda, G., Martinez-Meier, A., Cochard, H., and Rozenberg, P. (2011). Genetic variation of xylem hydraulic properties shows that wood density is involved in adaptation to drought in Douglas-fir (*Pseudotsuga menziesii* (Mirb.)). *Ann. For. Sci.* 68, 747–757. doi: 10.1007/s13595-011-0091-1

Enquist, B. J., Abraham, A. J., Harfoot, M. B. J., Malhi, Y., and Doughty, C. E. (2019). On the importance of the megabiota to the functioning of the biosphere. *EcoEvoRxiv* [Preprint]. doi: 10.32942/osf.io/hn9xs

Fajardo, A., McIntire, E. J. B., and Olson, M. E. (2019). When short stature is an asset in trees. *Trends Ecol. Evol.* 34, 193–199. doi: 10.1016/j.tree.2018.10.011

Garson, J. (2016). *A Critical Overview of Biological Functions,* Berlin: Springer.

Givnish, T. J., Wong, S. C., Stuart-Williams, H., Holloway-Phillips, M., and Farquhar, G. D. (2014). Determinants of maximum tree height in *Eucalyptus* species along a rainfall gradient in Victoria, Australia. *Ecology* 95, 2991–3007. doi: 10.1890/14-0240.1

Gleason, S. M., Blackman, C. J., Gleason, S. T., McCulloh, K. A., Ocheltree, T. W., and Westoby, M. (2018). Vessel scaling in evergreen angiosperm leaves conforms with Murray's law and area-filling assumptions: implications for plant size, leaf size and cold tolerance. *New Phytol.* 218, 1360–1370. doi: 10.1111/nph.15116

Guan, X., Pereira, L., McAdam, S. A. M., Cao, K., and Jansen, S. (2021). No gas source, no problem: Proximity to pre-existing embolism and segmentation affect embolism spreading in angiosperm xylem by gas diffusion. *Plant Cell Environ.* 44, 1329–1345. doi: 10.1111/pce.14016

Hargrave, K. R., Kolb, K. J., Ewers, F. W., and Davis, S. D. (1994). Conduit diameter and drought-induced embolism in *Salvia mellifera* Greene (Labiatae). *New Phytol.* 126, 695–705. doi: 10.1111/j.1469-8137.1994.tb02964.x

Jacobsen, A. L., Brandon Pratt, R., Venturas, M. D., Hacke, U. G., and Lens, F. (2019). Large volume vessels are vulnerable to water-stress-induced embolism in stems of poplar. *IAWA J.* 40, 4–22. doi: 10.1163/22941932-40190233

Jacobsen, A. L., Pratt, R. B., Tobin, M. F., Hacke, U. G., and Ewers, F. W. (2012). A global analysis of xylem vessel length in woody plants. *Am. J. Bot.* 99, 1583–1591. doi: 10.3732/ajb.1200140

Kaack, L., Weber, M., Isasa, E., Karimi, Z., Li, S., Pereira, L., et al. (2021). Pore constrictions in intervessel pit membranes provide a mechanistic explanation for xylem embolism resistance in angiosperms. *New Phytol.* 230, 1829–1843. doi: 10.1111/nph.17282

Koch, G. W., Sillett, S. C., Jennings, G. M., and Davis, S. D. (2004). The limits to tree height. *Nature* 428, 851–854. doi: 10.1038/nature02417

Koçillari, L., Olson, M. E., Suweis, S., Rocha, R. P., Lovison, A., Cardin, F., et al. (2021). The widenened pipe model of plant hydraulic evolution. *Proc. Natl. Acad. Sci. U.S.A.* 118:e2100314118.

Körner, C. (2017). A matter of tree longevity. *Science* 355, 130–131.

Lechthaler, S., Colangeli, P., Gazzabin, M., and Anfodillo, T. (2019). Axial anatomy of the leaf midrib provides new insights into the hydraulic architecture and cavitation patterns of *Acer pseudoplatanus* leaves. *J. Exp. Bot.* 70, 6195–6201. doi: 10.1093/jxb/erz347

Lechthaler, S., Kiorapostolou, N., Pitacco, A., Anfodillo, T., and Petit, G. (2020). The total path length hydraulic resistance according to known anatomical patterns: what is the shape of the root-to-leaf tension gradient along the plant longitudinal axis? *J. Theor. Biol.* 502:110369. doi: 10.1016/j.jtbi.2020.110369

Lens, F., Sperry, J. S., Christman, M. A., Choat, B., Rabaey, D., and Jansen, S. (2011). Testing hypotheses that link wood anatomy to cavitation resistance and hydraulic conductivity in the genus *Acer*. *N. Phytol.* 190, 709–723. doi: 10.1111/j.1469-8137.2010.03518.x

Li, S., Klepsch, M., Jansen, S., Schmitt, M., Lens, F., Karimi, Z., et al. (2016). Intervessel pit membrane thickness as a key determinant of embolism resistance in angiosperm xylem. *IAWA J.* 37, 152–171. doi: 10.1163/22941932-20160128

Liang, X., Ye, Q., Liu, H., and Brodribb, T. J. (2020). Wood density predicts mortality threshold for diverse trees. *New Phytol.* 229, 3053–3057. doi: 10.1111/nph.17117

Lindenmayer, D. B., and Laurance, W. F. (2016). The ecology, distribution, conservation and management of large old trees: ecology and management of large old trees. *Biol. Rev.* 92, 1434–1458. doi: 10.1111/brv.12290

Lindenmayer, D. B., and Laurance, W. F. (2017). The ecology, distribution, conservation and management of large old trees. *Biol. Rev.* 92, 1434–1458. doi: 10.1111/brv.12290

Lutz, J. A., Furniss, T. J., Johnson, D. J., Davies, S. J., Allen, D., Alonso, A., et al. (2018). Global importance of large-diameter trees. *Glob. Ecol. Biogeogr.* 27, 849–864. doi: 10.1111/geb.12747

Martin-StPaul, N. K., Longepierre, D., Huc, R., Delzon, S., Burlett, R., Joffre, R., et al. (2014). How reliable are methods to assess xylem vulnerability to cavitation? The issue of 'open vessel' artifact in oaks. *Tree Physiol.* 34, 894–905. doi: 10.1093/treephys/tpu059

Martínez-Vilalta, J., Prat, E., Oliveras, I., and Piñol, J. (2002). Xylem hydraulic properties of roots and stems of nine Mediterranean woody species. *Oecologia* 133, 19–29.

Mayr, E. (1982). *The Growth Of Biological Thought: Diversity, Evolution, and Inheritance*. Cambridge, MA: Belknap Press.

McDowell, N. G., and Allen, C. D. (2015). Darcy's law predicts widespread forest mortality under climate warming. *Nat. Clim. Chang.* 5, 669–672. doi: 10.1038/nclimate2641

McGregor, I. R., Helcoski, R., Kunert, N., Tepley, A. J., Gonzalez-Akre, E. B., Herrmann, V., et al. (2020). Tree height and leaf drought tolerance traits shape growth responses across droughts in a temperate broadleaf forest. *New Phytol.* 231, 601–616. doi: 10.1111/nph.16996

Niklas, K. J. (1998). The influence of gravity and wind on land plant evolution. *Revi. Palaeobot. Palynol.* 102, 1–14. doi: 10.1016/S0034-6667(98)00011-6

Olson, M. E. (2020). From Carlquist's ecological wood anatomy to Carlquist's Law: why comparative anatomy is crucial for functional xylem biology. *Am. J. Bot.* 107, 1328–1341. doi: 10.1002/ajb2.1552

Olson, M. E., Anfodillo, T., Gleason, S. M., and McCulloh, K. A. (2021). Tip-to-base xylem conduit widening as an adaptation: causes, consequences, and empirical priorities. *New Phytol.* 229, 1877–1893. doi: 10.1111/nph.16961

Olson, M. E., Anfodillo, T., Rosell, J. A., and Martínez-Méndez, N. (2020a). Across climates and species, higher vapor pressure deficit is associated with wider vessels for plants of the same height. *Plant Cell Environ.* 43, 3068–3080. doi: 10.1111/pce.13884

Olson, M. E., and Arroyo-Santos, A. (2015). How to study adaptation (and why to do it that way). *Q. Rev. Biol.* 90, 167–191. doi: 10.1086/681438

Olson, M. E., Rosell, J. A., Martínez-Pérez, C., León-Gómez, C., Fajardo, A., Isnard, S., et al. (2020b). Xylem vessel diameter-shoot length scaling: ecological significance of porosity types and other traits. *Ecological Monographs* 90:e01410 doi: 10.1002/ecm.1410

Olson, M. E., Soriano, D., Rosell, J. A., Anfodillo, T., Donoghue, M. J., Edwards, E. J., et al. (2018). Plant height and hydraulic vulnerability to drought and cold. *Proc. Natl. Acad. Sci. U.S.A.* 115, 7551–7556. doi: 10.1073/pnas.1721728115

Petit, G., Anfodillo, T., and De Zan, C. (2009). Degree of tapering of xylem conduits in stems and roots of small *Pinus cembra* and *Larix decidua* trees. *Botany* 87, 501–508. doi: 10.1139/B09-025

Pittermann, J., and Sperry, J. (2003). Tracheid diameter is the key trait determining the extent of freezing-induced embolism in conifers. *Tree Physiol.* 23, 907–914.

Pittermann, J., and Sperry, J. S. (2006). Analysis of freeze-thaw embolism in conifers. The interaction between cavitation pressure and tracheid size. *Plant Physiol.* 140, 374–382. doi: 10.1104/pp.105.067900

Rockwell, F. E., Wheeler, J. K., and Holbrook, N. M. (2014). Cavitation and its discontents: opportunities for resolving current controversies. *Plant Physiol.* 164, 1649–1660. doi: 10.1104/pp.113.233817

Rodriguez-Dominguez, C. M., Carins Murphy, M. R., Lucani, C., and Brodribb, T. J. (2018). Mapping xylem failure in disparate organs of whole plants reveals extreme resistance in olive roots. *New Phytol.* 218, 1025–1035. doi: 10.1111/nph.15079

Rood, S. B., Patiño, S., Coombs, K., and Tyree, M. T. (2000). Branch sacrifice: cavitation-associated drought adaptation of riparian cottonwoods. *Trees* 14, 248–257. doi: 10.1007/s004680050010

Rosell, J. A., and Olson, M. E. (2014). Do lianas really have wide vessels? Vessel diameter–stem length scaling in non-self-supporting plants. *Perspect. Plant Ecol. Evol. Syst.* 16, 288–295. doi: 10.1016/j.ppees.2014.08.001

Rosner, S., Světlík, J., Andreassen, K., Børja, I., Dalsgaard, L., Evans, R., et al. (2016). Novel hydraulic vulnerability proxies for a boreal conifer species reveal that opportunists may have lower survival prospects under extreme climatic events. *Front. Plant Sci.* 7:831. doi: 10.3389/fpls.2016.00831

Sack, L., Scoffoni, C., McKown, A. D., Rawls, M., Havran, J. C., Tran, H., et al. (2012). Developmentally based scaling of leaf venation architecture explains global ecological patterns. *Nat. Commun.* 3, 1–10. doi: 10.1038/ncomms1835

Sano, Y., Morris, H., Shimada, H., Ronse De Craene, L. P., and Jansen, S. (2011). Anatomical features associated with water transport in imperforate tracheary elements of vessel-bearing angiosperms. *Ann. Bot.* 107, 953–964. doi: 10.1093/aob/mcr042

Savage, J. A., and Cavender-Bares, J. (2013). Phenological cues drive an apparent trade-off between freezing tolerance and growth in the family *Salicaceae*. *Ecology* 94, 1708–1717. doi: 10.1890/12-1779.1

Sevanto, S., Holbrook, N. M., and Ball, M. C. (2012). Freeze/thaw-induced embolism: probability of critical bubble formation depends on speed of ice formation. *Front. Plant Sci.* 3:107. doi: 10.3389/fpls.2012.00107

Shenkin, A., Chandler, C. J., Boyd, D. S., Jackson, T., Disney, M., Majalap, N., et al. (2019). The world's tallest tropical tree in three dimensions. *Front. For. Glob. Change* 2:32. doi: 10.3389/ffgc.2019.00032

Silva, M., dos, S., Funch, L. S., and da Silva, L. B. (2019). The growth ring concept: seeking a broader and unambiguous approach covering tropical species. *Biol. Rev.* 94, 1161–1178. doi: 10.1111/brv.12495

Silva, M. dos S., Funch, L. S., Silva, L. B., and Cardoso, D. (2021). A phylogenetic and functional perspective on the origin and evolutionary shifts of growth ring anatomical markers in seed plants. *Biol. Rev.* 96, 842–876. doi: 10.1111/brv.12681

Stovall, A. E. L., Shugart, H., and Yang, X. (2019). Tree height explains mortality risk during an intense drought. *Nat. Commun.* 10:4385. doi: 10.1038/s41467-019-12380-6

Swemmer, A. (2020). Locally high, but regionally low: the impact of the 2014–2016 drought on the trees of semi-arid savannas, South Africa. *Afr. J. Range Forage Sci.* 37, 31–42. doi: 10.2989/10220119.2020.1723696

Torres-Ruiz, J. M., Jansen, S., Choat, B., McElrone, A. J., Cochard, H., Brodribb, T. J., et al. (2015). Direct X-ray microtomography observation confirms the induction of embolism upon xylem cutting under tension. *Plant Physiol.* 167, 40–43. doi: 10.1104/pp.114.249706

Trugman, A. T., Anderegg, L. D. L., Anderegg, W. R. L., Das, A. J., and Stephenson, N. L. (2021). Why is tree drought mortality so hard to predict? *Trends Ecol. Evol.* 36, 520–532. doi: 10.1016/j.tree.2021.02.001

Trugman, A. T., Detto, M., Bartlett, M. K., Medvigy, D., Anderegg, W. R. L., Schwalm, C., et al. (2018). Tree carbon allocation explains forest drought-kill and recovery patterns. *Ecol. Lett.* 21, 1552–1560. doi: 10.1111/ele.13136

Wu, M., Zhang, Y., Oya, T., Marcati, C. R., Pereira, L., and Jansen, S. (2020). Root xylem in three woody angiosperm species is not more vulnerable to embolism than stem xylem. *Plant Soil* 450, 479–495. doi: 10.1007/s11104-020-04525-0

Conflict of Interest: The authors declare that the research was conducted in the absence of any commercial or financial relationships that could be construed as a potential conflict of interest.

Publisher's Note: All claims expressed in this article are solely those of the authors and do not necessarily represent those of their affiliated organizations, or those of the publisher, the editors and the reviewers. Any product that may be evaluated in this article, or claim that may be made by its manufacturer, is not guaranteed or endorsed by the publisher.

frontiers in Plant Science

ORIGINAL RESEARCH
published: 19 August 2021
doi: 10.3389/fpls.2021.722802

Effect and Response of *Quercus ilex* subsp. *ballota* [Desf.] Samp. Seedlings From Three Contrasting Andalusian Populations to Individual and Combined *Phytophthora cinnamomi* and Drought Stresses

Bonoso San-Eufrasio[1], *María Ángeles Castillejo*[1], *Mónica Labella-Ortega*[1], *Francisco J. Ruiz-Gómez*[2], *Rafael M. Navarro-Cerrillo*[2], *Marta Tienda-Parrilla*[1], *Jesús V. Jorrín-Novo*[1] *and María-Dolores Rey*[1]*

[1] *Agroforestry and Plant Biochemistry, Proteomics and Systems Biology, Department of Biochemistry and Molecular Biology, University of Córdoba, Córdoba, Spain,* [2] *Evaluation and Restoration of Agronomic and Forest Systems ERSAF, Department of Forest Engineering, University of Córdoba, Córdoba, Spain*

OPEN ACCESS

Edited by:
Angelo Rita,
University of Basilicata, Italy

Reviewed by:
José Javier Peguero-Pina,
Aragon Agrifood Research and Technology Center (CITA), Spain
Lorenzo Ferroni,
University of Ferrara, Italy

***Correspondence:**
María-Dolores Rey
b52resam@uco.es

Specialty section:
This article was submitted to Plant Abiotic Stress, a section of the journal Frontiers in Plant Science

Received: *09 June 2021*
Accepted: *22 July 2021*
Published: *19 August 2021*

Citation:
San-Eufrasio B, Castillejo MÁ, Labella-Ortega M, Ruiz-Gómez FJ, Navarro-Cerrillo RM, Tienda-Parrilla M, Jorrín-Novo JV and Rey M-D (2021) Effect and Response of Quercus ilex subsp. ballota [Desf.] Samp. Seedlings From Three Contrasting Andalusian Populations to Individual and Combined Phytophthora cinnamomi and Drought Stresses. Front. Plant Sci. 12:722802. doi: 10.3389/fpls.2021.722802

Quercus ilex L. is the dominant species in the Mediterranean forest and agrosilvopastoral ecosystem "*dehesa*." Currently, this forest species is threatened by natural and anthropogenic agents, especially by the decline syndrome, which is caused by *Phytophthora cinnamomi* and drought periods. Although the morphological and physiological responses of *Q. ilex* to combined stress (*P. cinnamomi* and drought) have been examined already, little is known at the molecular level. In this study, we studied the effect and response of 8-month seedlings from three contrasting Andalusian populations (Seville [Se], Granada [Gr], and Almeria [Al]) to the individual and combined stresses of *P. cinnamomi* and drought from morphological, physiological, biochemical, and proteomics data. Whereas, seedling damage (leaf chlorosis and necrosis) and mortality were greater under the combined stresses in the three populations, the effect of each individual stress was population-dependent. Resilient individuals were found in all the populations at different percentages. The decrease in leaf chlorophyll fluorescence, photosynthetic activity, and stomatal conductance observed in undamaged seedlings was greater in the presence of both stresses, the three populations responding similarly to drought and *P. cinnamomi*. Biochemical and proteomic analyses of undamaged seedlings from the two most markedly contrasting populations (Se and Al) revealed the absence of significant differences in the contents in photosynthetic pigments, amino acids, and phenolics among treatments. The Se and Al populations exhibited changes in protein profile in response to the different treatments, with 83 variable proteins in the former population and 223 in the latter. Variable proteins belonged to 16 different functional groups, the best represented among which were protein folding, sorting and degradation, carbohydrate, amino acid, and secondary metabolism, photosynthesis, and ROS scavenging. While photosynthetic proteins were mainly downaccumulated, those of stress-responsive were upaccumulated. Although no treatment-specific response was observed in any functional

group, differences in abundance were especially marked under the combined stresses. The following variable proteins are proposed as putative markers for resilience in *Q. ilex*, namely, aldehyde dehydrogenase, glucose-6-phosphate isomerase, 50S ribosomal protein L5, and α-1,4-glucan-protein synthase [UDP-forming].

Keywords: holm oak, decline syndrome, climate change, combined stress, proteomics, molecular markers

INTRODUCTION

Holm oak (*Quercus ilex* L.) is the dominant species in Mediterranean basin forests and also in the long-established agrosilvopastoral oak open woodlands called *dehesas* in Spain and *montados* in Portugal (Ruiz de la Torre, 2006; Camilo-Alves et al., 2013). This species possesses a high environmental and ecological importance (Guzmán-Álvarez, 2016). It adapts well to arid and semiarid regions, where it plays a key biological role against desertification (Quero et al., 2006). In recent decades, however, increasing tree defoliation and mortality in large areas of the western Iberian Peninsula are endangering holm oak forests along the Mediterranean basin (Brasier, 1996; Jung et al., 2000; Natalini et al., 2016; Sánchez-Cuesta et al., 2021). Tree mortality is associated with both natural and anthropogenic factors such as overexploitation and poor regeneration or livestock management, and also with the severe effect of external biotic and abiotic factors such as attack by soilborne pathogens, extreme temperatures, heavy rainfall episodes, and extended drought periods, which in combination result in the so-called "oak decline syndrome" (Brasier, 1992; Camilo-Alves et al., 2013; Corral-Ribera et al., 2018; Surová et al., 2018).

Holm oak decline is a complex syndrome usually triggered by extreme climate events such as drought and high temperatures or invasive pathogens such as oomycetes (Sánchez et al., 2004; Sghaier-Hammami et al., 2013; Valero-Galván et al., 2013; Ruiz-Gómez et al., 2018). However, there is solid evidence that drought and root rot by the effect of *Phytophthora cinnamomi* Rands. are the two main factors triggering strong tree death episodes (Brasier, 1996; Sánchez et al., 2004; Corcobado et al., 2014, 2017; Ruiz-Gómez et al., 2018, 2019; Gea-Izquierdo et al., 2021). *P. cinnamomi* is one of the worst invasive alien pathogens around the world (Burgess et al., 2016), and its spectrum of hosts includes more than 5,000 different species (Hardham, 2005). This oomycete is heterothallic (i.e., it has two different mating types, of which only type A2 is present in the Iberian Peninsula). The pathogen reproduces asexually by sporulating motile zoospores that can be carried by soil water to find new roots and spread easily under the typical conditions of Mediterranean climate (*viz.*, short episodes of heavy rainfall, intermittent flooding, and heavy runoff) (Brasier, 1992, 1996; Hardham, 2005). The geographical origin of *P. cinnamomi* is not clearly established. It is an introduced species in Europe, which probably comes from Taiwan or the islands of Papua New Guinea in the south-western Pacific Ocean (Sena et al., 2018). Although in some places *P. cinnamomi* seems to be a relatively new threat, in other parts it has been established for many decades. In Europe, *P. cinnamomi* was identified in chestnuts causing ink disease in the last of the 19th century (Brasier, 1996), and in the Iberian Peninsula, since the end of the last century *P. cinnamomi* has been associated with oak declining (Brasier et al., 1993).

The previous studies have shown drought to increase the susceptibility of *Q. ilex* seedlings to *P. cinnamomi* root rot (Corcobado et al., 2014, 2017; Ruiz-Gómez et al., 2018). This finding is supported by the fact that plants are weakened under environmental cues (Agrios, 2005; Desprez-Loustau et al., 2006). The combined effects of biotic and abiotic stresses on *Q. ilex* seedlings have so far been studied in phenotypic, physiological, and biochemical terms (Corcobado et al., 2014; Ruiz-Gómez et al., 2018, Colangelo et al., 2018). Thus, the presence of *P. cinnamomi* is known to trigger unspecific defense responses, such as the accumulation of phenolics, thickening of cell walls, and accumulation of callose (Ruiz Gómez et al., 2014; Redondo et al., 2015). Under drought, the presence of *P. cinnamomi* results in substantial changes in biomass allocation such as a decrease in root biomass and also in physiological activity-related parameters such as CO_2 assimilation, stomatal conductance, and leaf chlorophyll fluorescence (Ruiz-Gómez et al., 2018). These changes must, no doubt, reflect at the molecular level, but how it does remains largely unknown to date. Recently, Ruiz-Gómez et al. (2018) examined changes in a *Q. ilex* population in Arenas del Rey (Granada, Andalusia, Spain) under stress from both *P. cinnamomi* and drought. However, the high interpopulation and intrapopulation variability of this species (San-Eufrasio et al., 2020) requires comparing various populations in order to better elucidate the response of holm oak to the conditions causing the decline syndrome. Also, molecular studies using the most recent tools available for this purpose could be useful to gain further insight into variability in this species and also to help identify key genes and gene products involved in the response to the syndrome (Rey et al., 2019).

In this study, we studied the effect of exposure of *Q. ilex* to drought and attack by a pathogen (*P. cinnamomi*) individually and in combination from a physiological, biochemical, and proteomic perspective. For this purpose, we examined the response to and tolerance of *P. cinnamomi* and drought in three contrasting Andalusian *Q. ilex* populations (Seville [Se], Granada [Gr], and Almeria [Al]). Elucidating the molecular mechanisms behind resilience to both stresses in *Q. ilex* from physiological and molecular data allowed us to put forward several putative gene markers for use in breeding actions in the framework of conservation and afforestation programs.

MATERIALS AND METHODS

Plant Material

Acorns were collected by staff of the Department of Forestry Engineering of the University of Cordoba from three different *Q. ilex* populations in Andalusia, namely, Almaden de la Plata, Se; Gr); and Al) (**Table 1**; **Supplementary Figure 1**).

Healthy acorns were selected after surface cleaning with 5% HCl and suspension in water, with floating acorns being discarded. In January 2019, acorns were pregerminated in a wet bed and sown in black plastic pots (3 L, 14.5 × 14.5 × 22 cm) containing perlite from Gramoflor GmbH and Co. (Vechta, Germany). Pots were placed in a temperature-controlled greenhouse at a mean temperature of 25°C, 60 ± 10% relative humidity, PPFD of 900 μmol m^{-2} s^{-1}, and natural photoperiod (11/13 h, light/dark) located in Cordoba (Andalusia, Southern Spain; 37°54′46″ N, 4°43′15″ O). During the experiment, the maximum temperature did not exceed of 39°C and did not fall below 13°C. The experiment was started in October 2019, when seedlings were ∼15 cm tall. Seedlings were irrigated every 2 days with tap water (200 ml) and once a week with Hoagland nutrient solution up to the start of the experiment (Hoagland and Arnon, 1950).

Experimental Design and Inoculation

The experimental design (**Supplementary Figure 2**) encompassed four different treatments, namely, (1) irrigation to field capacity in the absence of *P. cinnamomi* (control treatment); (2) no irrigation and no *P. cinnamomi* (drought treatment); (3) irrigation and *P. cinnamomi* inoculation (inoculation treatment); and (4) *P. cinnamomi* inoculation and no irrigation (combined treatment). The treatments were performed as described by Ruiz-Gómez et al. (2018) and Sghaier-Hammami et al. (2013). The experiment was conducted according to a completely randomized design with 20 seedlings per treatment (80 seedlings per population) and a duration of 35 days.

Phytophthora cinnamomi (P90), previously isolated from *Q. ilex* roots in Puebla de Guzmán (Huelva, Andalusia, Spain), was reactivated by using root cuts inoculated in a PARPBH selective medium containing piramicin, amplicilin, rifamycin, pentachloronitrobenzene, benomyl, and hymexazol (Jeffers, 1986; Ruiz-Gómez et al., 2018). The inoculation protocol used was that of Ruiz-Gómez et al. (2018) except that the root system was brought into contact with the pathogen by immersion in Carror–Agar (CA) liquid inoculum (Sghaier-Hammami et al., 2013) at a concentration of 39 chlamydospores/μL (Ruiz-Gómez et al., 2018). Control seedlings were also immersed in CA liquid inoculum but containing no *P. cinnamomi*. After inoculation, seedlings were transplanted into pots filled with fresh perlite. All pots were flooded for 48 h, excess water being removed before the experiment. In the drought treatment, water was withheld according to San-Eufrasio et al. (2020). Control and inoculated seedlings were irrigated to field capacity throughout. The presence of *P. cinnamomi* in the root system was checked on days 19 and 32 by using fine roots from each seedling as described by Ruiz-Gómez et al. (2018). Briefly, three pieces of fine roots per seedling (< 2 mm thick, ∼1 cm long) were randomly selected and immersed in 70% ethanol, washed in sterilized–deionized water, and placed in 9-cm Petri dishes containing PARPBH selective medium. The pathogen was identified morphologically by conventional light microscopy (Erwin and Ribeiro, 1996).

TABLE 1 | Location and environmental features of the three Andalusian *Quercus ilex* populations.

	Location	Altitude	Coordinates	T_{max}	T_{min}	P
More Eastern	Sierra María (Al)	890	37°42′ N 2°07′ W	18.0	5.8	411.0
↓	Arenas del Rey (Gr)	892	36°57′ N 3°54′ W	24.7	11.5	489.3
More Western	Almaden de la Plata (Se)	482	37°52′ N 6°05′ W	26.4	9.5	722.1

Altitude (meters above sea level, MASL), ETRS89 coordinates, the average temperature of the coldest month (T_{min}, °C), the average temperature of the warmest month (T_{max}, °C), and average annual rainfall (P, mm) (Navarro-Cerrillo et al., 2018).

Perlite Water Content and Matric Potential

Both the perlite water content (PWC, %) and the matric potential (Ψ_m, kPa) were estimated according to San-Eufrasio et al. (2020) throughout the experiment. The former parameter was calculated as follows:

$$PWC_t(\%) = [PWW_t - (PDW/PWW_0) - PDW] \times 100$$

where PWW denotes pot wet weight; PDW pot dry weight; and t time, in days, with 0 corresponding to the initial and maximum values.

Damage Symptoms and Seedling Mortality

Damage symptoms (*viz.*, leaf chlorosis and wilting) resulting from the presence of *P. cinnamomi* and/or drought were evaluated visually in all seedlings and registered by taking photographs of all seedlings with a digital camera. When all leaves exhibited severe drought symptoms (*viz.*, a dry-yellow appearance throughout) and quantum yield of photosystem II (Qy) was near 0, the number of dead seedlings was also recorded.

Physiological Measurements

Relative leaf water content (RLWC) was calculated on day 32 from fresh (FW), turgid (TW), and dry (DW) weights, as previously described by San-Eufrasio et al. (2020). RLWC (%) was calculated as [(FW–DW)/(TW – DW)] × 100. The Qy was measured with a FluorPen FP100 portable leaf fluorimeter from Photon Systems Instruments (Drasiv, Czech Republic) at 3-day intervals throughout the experiment (San-Eufrasio et al., 2020). Measurements were always performed on the same three youngest fully expanded leaves in each seedling, using three seedlings per treatment per population (36 seedlings per measurement) throughout the experiment. All measurements were performed in the early morning when the leaves were adapted to darkness throughout the night (dark-adapted leaves) according to Strasser et al. (2000). Net photosynthesis (A, μmol CO_2 m^{-2} s^{-1}), stomatal conductance (Gs, mol H_2O m^{-2} s^{-1}), and F_v'/F_m' (maximal Qy photochemistry for the light-adapted state, arbitrary units) were measured once a week on a

light-adapted fully expanded leaf in five seedlings per treatment per population, using a portable IR CO_2 gas analyzer (IRGA) equipped with a light source integrated in a leaf chamber fluorometer and CO_2 injector system (LiCor Li6400XT, Li-Cor, Inc.; Lincoln, NE, USA). The measurements were taken fixing a CO_2 concentration of 400 ppm and PPFD of 1,000 μmol (photons) m^{-2} s^{-1}. Relative humidity was setup to environmental RH (15.5+- 0.2 mmol H_2O mol air^{-1}), and the length of measurements was controlled by the saturation of the A and G curves, establishing a minimum run time of 30 s. All measurements were performed between 11:00 and 14:30 UTC (Universal Time Coordinates).

Photosynthetic Pigment and Metabolite Contents

Photosynthetic pigments and metabolites were quantified in asymptomatic leaves from the Se and Al populations. Measurements were performed on day 32, when leaf chlorophyll fluorescence had decreased by 20, 30, and 35% in the drought, inoculation, and combined treatment, respectively, relative to the control seedlings (López-Hidalgo et al., 2021). Three biological replicates per treatment per population were used for this purpose. Leaves from each seedling were collected, washed with distilled water, and immersed in liquid nitrogen prior to grinding in a precooled mortar. Leaf tissue (30–50 mg dry weight) was extracted with 80% (v/v) ethanol, the crude extract being centrifuged, and the resulting supernatant collected to quantify photosynthetic pigments (chlorophyll a and b, and carotenoids) and metabolites (total free amino acids, soluble sugars, total phenolics, and total flavonoids) on an Evolution 201 UV–Vis spectrophotometer from Thermo Fischer Scientific (Waltham, MA, USA) (López-Hidalgo et al., 2021). The resulting pellet was extracted with perchloric acid to quantify starch (López-Hidalgo et al., 2021) by measuring the absorbance at 595 nm of the supernatant against a hydrolyzed starch standard (Viles and Silverman, 1949; Rose et al., 1991). The absorbance of the supernatants containing chlorophyll a, chlorophyll b, and carotenoids was recorded at 664, 649, and 470 nm, respectively, and was used to calculate the respective contents, all in micrograms per milliliter, as follows: chlorophyll a = $13.36 \cdot A_{664}$ - $5.19 \cdot A_{649}$; chlorophyll b = $27.43 \cdot A_{649} - 8.12 \cdot A_{664}$; carotenoids = [(1000·$A_{470}$ – 2.13·chlorophyll a – 97.63·chlorophyll b)/209] (Lichtenthaler, 1987). The supernatants were used to calculate the content of free amino acids, soluble sugars, total phenolics, and total flavonoids as follows: For total free amino acids, the crude extract was mixed thoroughly with a commercial (2:1 v/v) ninhydrin reagent (Starcher, 2001) and the absorbance was measured at 450 nm using a standard of (1:1) proline–glycine; for soluble sugars, the crude extract was mixed thoroughly with (1:16 v/v) anthrone reagent (Thayumanavan and Sadasivam, 1984) and the absorbance was measured at 595 nm using a standard of (1:1) glucose; for total phenolics, the supernatants were mixed thoroughly with 10% (1:2 v/v) Folin–Ciocalteu reagent followed by the addition of (3:8 v/v) sodium carbonate (Viles and Silverman, 1949) and the absorbance measured at 720 nm using a standard of (1:1) gallic acid; and for flavonoids, the crude extract was mixed thoroughly with 10% (10:1) (v/v) aluminum chloride, 1 M potassium acetate, and (22:35 v/v) methanol (Mammen and Daniel, 2012), with the absorbance measured at 415 nm by using a standard of (1:1) quercetin.

Protein Extraction and Quantification

Proteomic runs were also performed on the Se and Al populations. Protein extracts were obtained from 300 mg of fresh leaf tissue from asymptomatic seedlings using the TCA/acetone–phenol protocol (Wang et al., 2006). Proteins were extracted from three independent biological replicates under each set of experimental conditions and dissolved in a solution containing 7 M urea, 2 M thiourea, 4% (w/v) CHAPS {3-[(3-cholamidopropyl)dimethylammonium]-1-propanesulphonate}, 0.5% (w/v) Triton X-100, and 100 mM DTT. Protein contents were quantified with the Bradford method using bovine serum albumin (BSA) as the standard (Bradford, 1976).

Gel-Based Proteomic Analysis (SDS-PAGE)

The proteins extracted from each sample (80 μg of BSA protein equivalent) were separated by sodium dodecyl sulfate polyacrylamide gel electrophoresis (SDS-PAGE) on 12% polyacrylamide gel (Laemmli, 1970), using the Protean II-XL (20 × 20 cm) system from Bio-Rad (Hercules, CA, USA) with a voltage run of 80 V until the dye reached the bottom of the gel. Gels were stained with Coomassie Brilliant Blue R-250 (Neuhoff et al., 1988), and images were acquired with a GS-900 Calibrated Densitometer from Bio-Rad. Images were analyzed with the software ImageLab^{TM} 5.2.1, also from Bio-Rad, bands being automatically detected and confirmed by visual inspection. The optical density (OD) of each band was normalized against the combination of all bands for each sample. Band molecular masses were calculated by comparing mobilities with those of protein standard markers (SDS Molecular weight standards, Broad range, Bio-Rad).

Shotgun Proteomic Analysis (LC–MS/MS)

Extracted proteins (80 μg) were subjected to SDS-PAGE in a 12% polyacrylamide gel Mini-PROTEAN 8.6 × 6.7 cm^2 cell from Bio-Rad. The gel was run at 80 V and stopped when Bromophenol Blue had advanced 0.5 cm into the resolving gel. The gel was stained with Coomassie Brilliant Blue R-250. The resulting unique band was removed with a scalpel, cut into pieces smaller than 1 mm^3, and transferred individually to 1.5 ml tubes for digestion with 12.5 ng μL^{-1} sequencing-grade trypsin from Promega (Madison, WI, USA) (Castillejo et al., 2015). Peptides were desalinated by passage through a C18 resin microcolumn from Scharlau (Barcelona, Spain), eluted with 70% acetonitrile (AcN) containing 0.1% trifluoroacetic acid, and dried in a SpeedVac apparatus. The resulting peptides were resuspended in 4% (v/v) AcN containing 0.25% (v/v) formic acid (FA) (López-Hidalgo et al., 2018; Romero-Rodríguez et al., 2019). Peptides were charged to 0.4 μg/μl by injection into a one-dimensional nanoflow [i.e., liquid chromatography with tandem mass spectrometry (LC–MS/MS system)] from Thermo Fisher Scientific (Gómez-Gálvez et al., 2020). A monolithic C18 Acclaim PepMap column 15 cm long × 75 μm inner diameter, also from Thermo Fisher Scientific, was used. Peptides were separated at 40°C in all runs. Solvent A contained 0.1% FA, and solvent B consisted of 80% AcN containing 0.1% FA. Samples

were separated by using a gradient from 95% solvent A to 80% solvent B at a controlled flow rate of 400 nL/min for 120 min. LC was coupled to MS *via* a nanoelectrospray ionization source. MS analyses were carried out on a trihybrid Thermo Orbitrap Fusion mass spectrometer from Thermo Scientific operated in the positive ion mode. The specific settings used in the LC–MS/MS analysis are described elsewhere (Castillejo et al., 2020).

Raw data were processed with the software MaxQuant (https://www.maxquant.org/). MS2 spectra were searched by using the Andromeda engine against the FASTA *Quercus*_Database obtained from the translation of *Q. ilex* transcriptome (Guerrero-Sanchez et al., 2017, 2019). Trypsin was set as the proteolytic enzyme, and a maximum of two missed cleavages were used in all the searches. Precursor mass tolerance was set at 10 ppm, fragment ion mass tolerance at 0.1 Da, and charge states at +2 or greater. Peptides were classified into proteins according to the law of parsimony and filtered to a 1% false discovery rate (FDR). Identification confidence was set to a minimum score of 2, proteins with two or more peptides matched at least 15% of sequence coverage. Proteins were quantified in relative terms from the peak areas for precursor ions (the average of the three strongest peptide ion signals) from the identified peptides. Then, they were categorized by function from their FASTA sequences using the software Mercator v.3.6 (MapMan) (Lohse et al., 2014; http://www.plabipd.de/portal/mercator-sequence-annotation/, accessed January 2021). Uncharacterized proteins were subjected to gene ontology (GO) enrichment (http://pantherdb.org/, accessed March 2021). MS proteomics raw data were deposited with dataset identifier PXD025704 in the ProteomeXchange Consortium *via* the PRIDE partner repository (Perez-Riverol et al., 2019).

Statistical Analyses

The effects of inoculation with *P. cinnamomi* and drought on *Q. ilex* were assessed by using the Kaplan–Meier model, which considers both seedling longevity and status (dead or alive) at the final assessment of survival (Esker et al., 2006; Vivas et al., 2012). This model was used in the previous studies of tree seedling survival (Solla et al., 2011) and provides an effective tool for identifying survival patterns between treatments where cumulative hazards over time (i.e., hazard functions) are generally proportional. The process involved calculating the area under the Qy curve. Levene's test was previously used to confirm homoscedasticity in the physiological and biochemical variables. Then, the data were subjected to ANOVA at $p \leq 0.05$, which means being separated with the LSD *post hoc* test at $p \leq 0.05$. One-way ANOVA was used to assess the effect of the individual and combined treatments on RLWC; two-way ANOVA to assess the influence of population and treatment as factors in Qy, biochemical parameters, and the total content in proteins as measured with the Bradford method; and three-way ANOVA to evaluate the effects of population, treatment, and time as factors on physiological parameters as determined by IRGA. Physiological data were previously checked for compliance with the normality and variance homoscedasticity conditions (Rohlf and Sokal, 1995). When the latter were not fulfilled, the Kruskal–Wallis test was used. Some conventional biochemical data were transformed for easier handling. Thus, the sugar contents were used in inverted, and the IRGA parameters (F_v'/F_m') were converted into logarithms for A and squared for Gs and Tr.

The ANOVA analyses were carried out with the software Statistix v. 10. A random experimental design with drought and inoculation as main factors was used. Significant ($p \leq 0.05$) one-way interactions were subjected to multiple comparisons by least square analysis of means. The significance of pairwise comparisons was determined by using Tukey's test at $\alpha = 0.05$ (Rohlf and Sokal, 1995). The effect of treatments on measured variables was assessed for significance at the 0.05 confidence level. SDS-PAGE band intensities were expressed in relative form by division into the combined intensity of all bands identified in a replicate. Responses were evaluated with provision for repetitiveness between replicates. Significant differences ($p \leq 0.05$) between bands for different treatments and populations were identified by one-way ANOVA. A PCA was performed with RStudio v. 1.3.1093. Changes in protein abundance were assessed on a heat map using the heatmaply package (Galili et al., 2018) for RStudio v. 4.0.3.

RESULTS

Perlite Water Content, Matric Potential, and Plant Infection

Perlite water contents on day 32 ranged from 57% in watered seedlings (control and inoculation treatments) to 12% in droughted ones (drought and combined treatments). These values corresponded to a matric potential of −15 and −43 kPa, respectively. Seedling infection was evaluated in fine roots from each seedling on days 19 and 32. The presence of *P. cinnamomi* in the roots from the inoculated and combined treatments was identified morphologically (see **Supplementary Figure 3**).

Damage Symptoms and Mortality Rate

The effects of the two stresses were examined by inspecting leaf damage visually and recording the number of dead seedlings throughout the experiment. Leaf damage symptoms caused by both stresses included chlorosis, necrosis, and wilting, which were not observed in control seedlings (**Figure 1**). Damage appeared earlier and was more marked in the presence of both stresses. Thus, damage by the effect of combined stress appeared as early as day 6 in the Al population. Survival at the end of the experiment in the seedlings exposed to *P. cinnamomi* ranged from 50% in inoculated seedlings in the Se population to 0% in seedlings under double stress in the Al population. Based on Kaplan–Meier estimates, survival differed significantly among populations and also among treatments ($p < 0.001$ in both cases; **Figure 2**). The Al population had the smallest number of living seedlings, followed by the Se and Gr populations. Also, the combined treatment led to the lowest survival, followed by the inoculation, drought, and control treatment in this sequence.

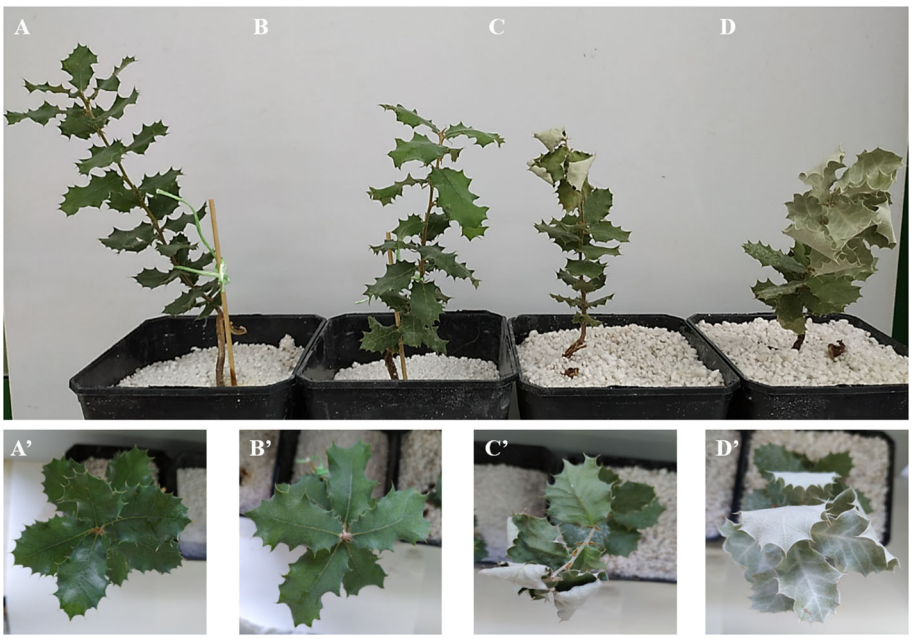

FIGURE 1 | Visually identified damage in *Q. ilex* seedlings from the Seville population Treatments: control (**A,A**'), drought (**B,B**'), *P. cinnamomi* (**C,C**'), and drought × *P. cinnamomi* (**D,D**').

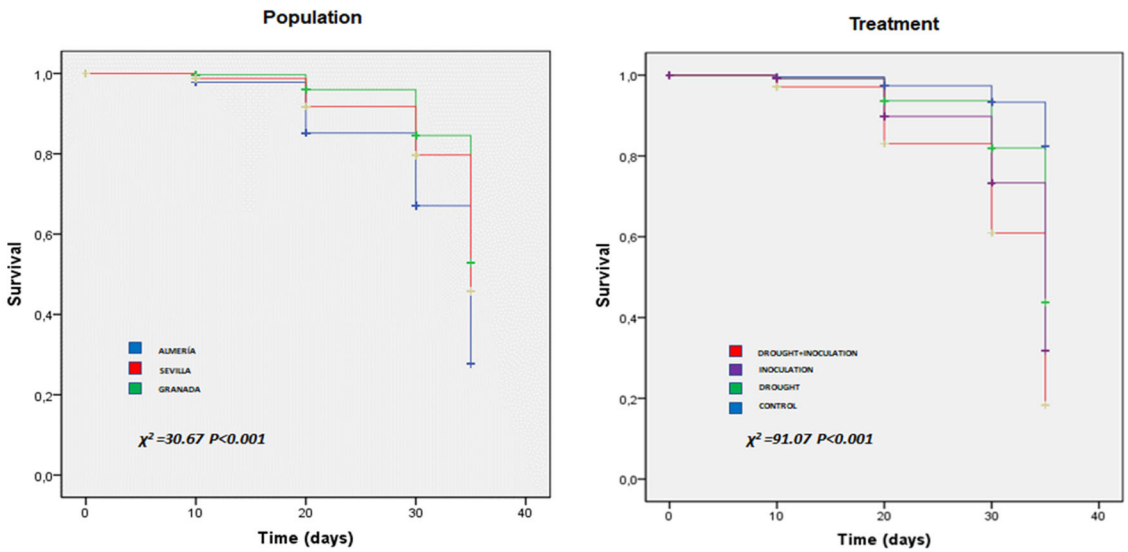

FIGURE 2 | Survival plots for the three *Q. ilex* populations (Almeria, Granada, and Seville) under the individual and combined effects of inoculation with *P. cinnamomi* and drought as determined with the Kaplan–Meier model. The units of the *x*- and *y*-axis are days and seedling survival rate, respectively.

Physiological Parameters

Mean RLWC at the end of the experiment (day 35) ranged from 101.74% with the control treatment in the Se population to 44.22% with the combined treatment in the Al population (**Supplementary Figure 4**). However, no significant differences among populations ($p = 0.3037$) were observed. RLWC was significantly decreased ($p < 0.001$) by both the inoculation (65–70%) and combined treatments (44–76%), followed by the drought (75–85%) and control treatments (90–100%) (**Supplementary Figure 4**).

The Qy in the control seedlings as determined in the dark remained nearly constant at 0.60–0.80 throughout the experiment (**Figure 3**). By contrast, Qy decreased gradually in the seedlings under the drought treatment. The pathogen, both by itself and in combination with drought, resulted in a marked decrease in Qy until day 13, after which the Qy leveled off at

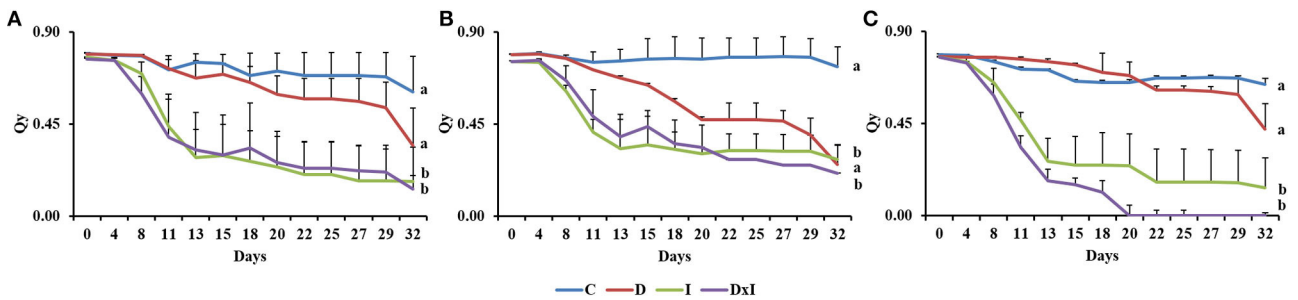

FIGURE 3 | Quantum yield of photosystem II (Qy) in the dark of adapted leaves from the three *Q. ilex* populations (**A**, Seville; **B**, Granada; **C**, Almeria) under the control (C), drought (D), inoculation (I), and combined treatment (D×I). Values are mean ± SE for three biological replicates. Different letters, calculated from the area under the Qy curve, denote significant differences among treatments ($p < 0.05$).

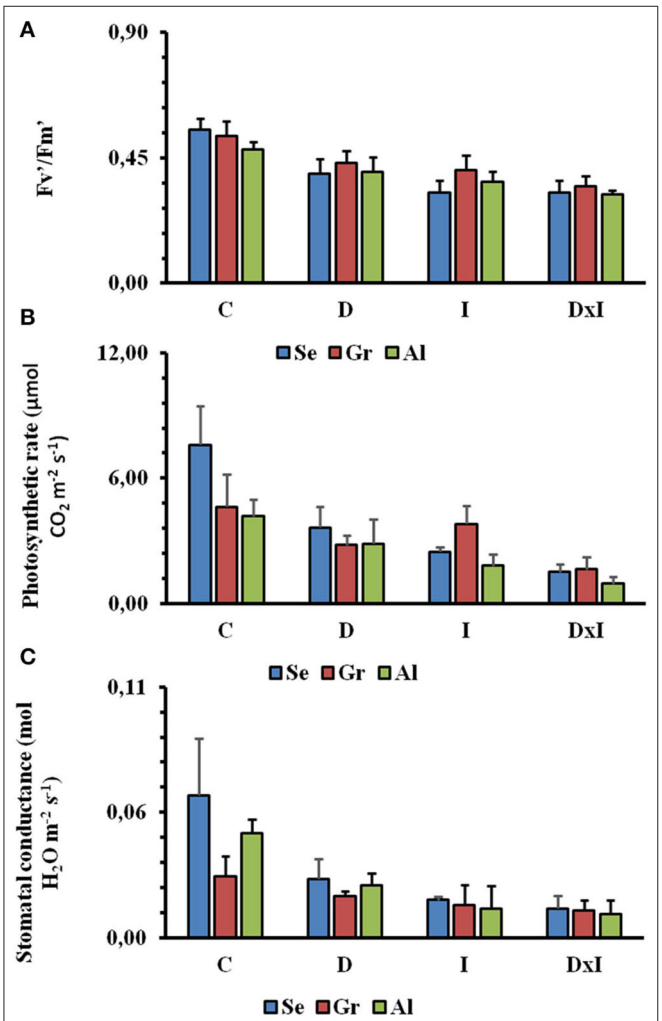

FIGURE 4 | Mean values of F_v'/F_m' **(A)**, net photosynthesis rate **(B)**, and stomatal conductance **(C)** in the Seville (Se), Granada (Gr), and Almeria (Al) populations from day 8 to day 32. Treatments: control (C), drought (D), inoculation (I), and combined (D×I). Different letters denote significant differences among treatments ($p < 0.05$).

~0.19. There were significant differences ($p < 0.001$) in this respect among treatments, the highest Qy levels corresponding to the inoculation and combined treatments. Also, although no significant differences among populations were observed ($p = 0.5032$), Al seedlings under the combined treatment behaved differently in this respect from Se and Gr seedlings, with near-zero Qy mean values by day 20.

Regarding photosynthetic activity determined on the IRGA analyzer, Fv'/F_m', a measure of photosynthetic efficiency in light-adapted leaves, was reduced by about 63% in the control seedlings from day 8 to day 32 (**Figure 4A**). There were, however, no statistically significant differences among populations or measurement times ($p = 0.958$). The decrease in F_v'/F_m' was found to significantly depend on the particular treatment ($p < 0.001$), the combined effect being greater than those of the individual stresses. Reductions in the other photosynthetic parameters (A and Gs) were similar from day 8 to day 32 (**Figures 4B,C**). Thus, A was decreased from 5.47 to 1.37 µmol CO_2 m^{-2} s^{-1} and Gs from 0.05 to 0.01 mol H_2O m^{-2} s^{-1} over the period from day 8 to day 32. The low values of gas exchange in control seedlings were due to the low values of light intensity (900 µmol m^{-2} s^{-1}) through the experiment. Again, there were no statistically significant differences among populations or times. The two stresses, both individually and in combination, significantly decreased the previous parameters ($p < 0.001$). The effect, however, was especially marked with the inoculation of the pathogen.

Changes in Photosynthetic Pigments and Metabolites

The results of **Figures 2**, **3** led us to subject seedlings from the Se and Al populations, which were the most contrasting among the three, to biochemical and proteomic analyses. The determinations included photosynthetic pigments and metabolites (viz., amino acids, sugars, starch, phenolics, and flavonoids) in leaves on day 32. As can be seen from **Figure 5**, the contents in photosynthetic pigments of the control seedlings in the Se population exceeded those in the Al population. The

respective contents in chlorophyll a, in milligrams per gram of dry weight, were 1.56 ± 0.41 and 0.84 ± 0.06; and those in chlorophyll b 0.92 ± 0.28 and 0.43 ± 0.05. There were no statistically significant differences in chlorophyll a ($p = 0.5572$) or chlorophyll b contents ($p = 0.5431$) among treatments. An identical trend was observed in amino acids, with higher contents in the Se population and no significant differences among treatments ($p = 0.3451$). Sugar contents were higher in the Al population than in the Se population; also, although all treatments increased them, the effect was more marked with inoculation alone than with drought alone or the combined treatment. Conversely, starch content was more abundant in the Al population, its highest contents corresponding to the drought, inoculation, and combined treatments. By contrast, none of the treatments changed the contents in phenolics and flavonoids.

Proteomic Analysis

The total amount of proteins extracted with TCA/acetone–phenol and quantified with the Bradford method were similar (0.6–0.9 mg/g FW) in the Se and Al populations irrespective of treatment. 1-D SDS-PAGE electrophoresis resolved up to 37 bands that were present in seedlings from both populations, whichever the treatment (**Supplementary Figure 5**). Twenty-four bands differed statistically among treatments, nine differing within each population and six in both. Most of the resolved bands (11 in total) were more abundant with the combined treatment in at least one population (**Supplementary Table 1**). Based on the PCA results, PC1, which explained 40.5% of the variability in the Se population, discriminated the control and drought treatments on the one hand, and the inoculation and combined treatment on the other. In the Al population, however, PC1, which explained 37.5% of variability, only discriminated the combined treatment (**Supplementary Figure 5**).

Proteins differing between populations and/or treatments were identified by using shotgun analysis, a powerful proteomics platform. The results are summarized in **Table 2**. Filtering the original dataset (3,412 and 2,600 positive matches in the Se and Al population, respectively) for confident matches (≥ 2 peptides, ≥ 2 score, and ≥ 15% coverage, only those proteins consistently present in the three biological replicates, standard deviation < 50%) provided 414 confidence proteins in the Se population and 734 in the Al population, 318 being shared by the two. Statistical analysis for variable proteins reduced the original dataset to 83 in Se and 223 in Al, 25 being shared by the two populations. The whole dataset of confident proteins was categorized in functional terms by using MERCATOR, which established 17 groups (**Supplementary Figures 6, 7**). The best represented groups were carbohydrate metabolism (78 proteins in Se and 116 in Al); folding, sorting, and degradation (75 and 141, respectively); energy metabolism (31 and 67); amino acid metabolism (37 and 53); secondary metabolism (29 and 45); ROS scavenging (24 and 18); cellular processes (19 and 31); and defense (12 and 27) (**Supplementary Figure 6**).

Variable proteins fell in 15 groups in Se and 16 in Al, the best represented groups being folding, sorting, and degradation (17 and 41, respectively); carbohydrate metabolism (14 and 40); energy metabolism (10 and 15); amino acid metabolism (8 and 23); ROS scavenging (5 and 9); and secondary metabolism (4 and 7) (**Supplementary Figure 6**). All functional groups present in the dataset of variable proteins included more upaccumulated proteins—by exception, the energy metabolism group comprised more downaccumulated proteins in both populations (**Figure 6**).

TABLE 2 | Summary of proteins identified by the shotgun–MS/MS analysis in the two populations and their combination.

	Seville	Almeria	Both
Raw data	3,412	2,600	2,484
Confidence parameters (≥ 2 Peptides, Score ≥ 2, Coverage ≥ 15%)	2,447	2,214	2,175
Consistent proteins	1,110	1,214	1,015
Standard deviation < 50% between replicates	414	734	318
Statistically significant ($p \leq 0.05$)	83	223	25

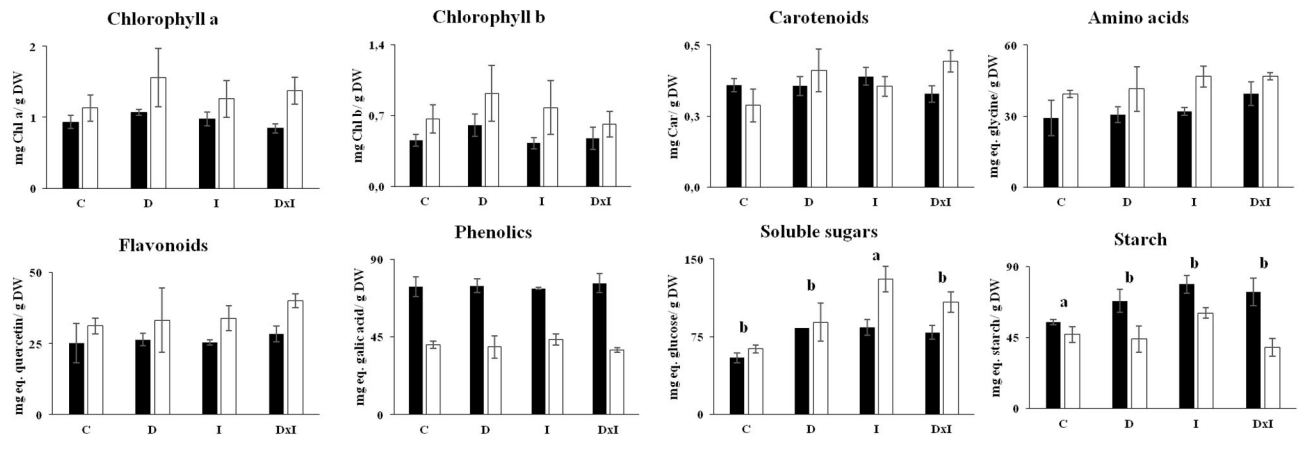

FIGURE 5 | Contents in photosynthetic pigments (chlorophyll a, chlorophyll b, and carotenoids) and metabolites (amino acids, flavonoids, phenolics, soluble sugars, and starch) in leaves of *Q. ilex* seedlings from the Seville (white bars) and Almeria populations (black bars). Values are mean ± SE of three biological replicates on day 32. Different letters denote significant differences among treatments ($p < 0.05$).

Based on the number of variable proteins, the proteome was more markedly affected by the treatments in Al than it was in Se (173 vs. 45 specific proteins). No treatment-related qualitative differences were observed; however, in any case, the combined treatment induced more proteome changes than did the individual stresses in the Se population; also, the presence of *P. cinnamomi*, both individually and in combination with drought, led to more marked changes in the Al population (**Supplementary Table 1**).

The previous datasets were simplified by PCA. Using the whole set of confidence proteins did not allow separation among populations or treatments with either PC1 or PC2, which accounted for 26.00% and 15.20% of the variability in the data (**Supplementary Figure 8**). Differences among treatments in each population were exposed by subjecting the dataset of variable proteins to PCA (**Figure 7**). In Se, PC1 (46.80% variability) discriminated the control and drought treatments from the inoculation and combined treatments, while PC2 (20.40% variability) discriminated the latter two. In Al, PC1 (51.40%) discriminated the control treatment from all others and PC2 (17.40%) discriminated drought from the pathogen. The variable proteins most markedly contributing to PC1 and PC2 are listed by the functional group in **Table 3** and **Supplementary Table 2**. In both populations, the greatest positive loadings were those of the carbohydrate metabolism, and folding, sorting, and degradation groups. On the other hand, the majority of the proteins related to energy metabolism that most markedly contributed to both PC were involved in photosynthesis, such as photosystem

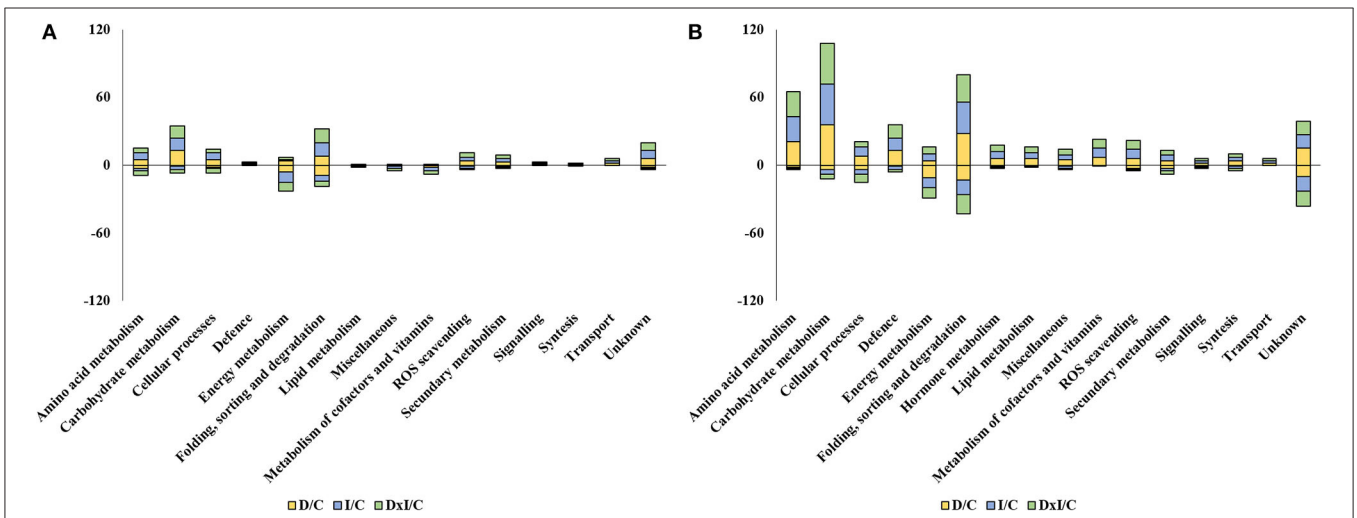

FIGURE 6 | Number of up- and down-accumulated variable proteins whose abundance in the drought (D), inoculation (I), and combined (D×I) treatments was greater or less than with the control treatment (C) in the Seville **(A)** and Almeria **(B)** populations. The numbers of up- and down-accumulated proteins are shown as positive and negative values, respectively.

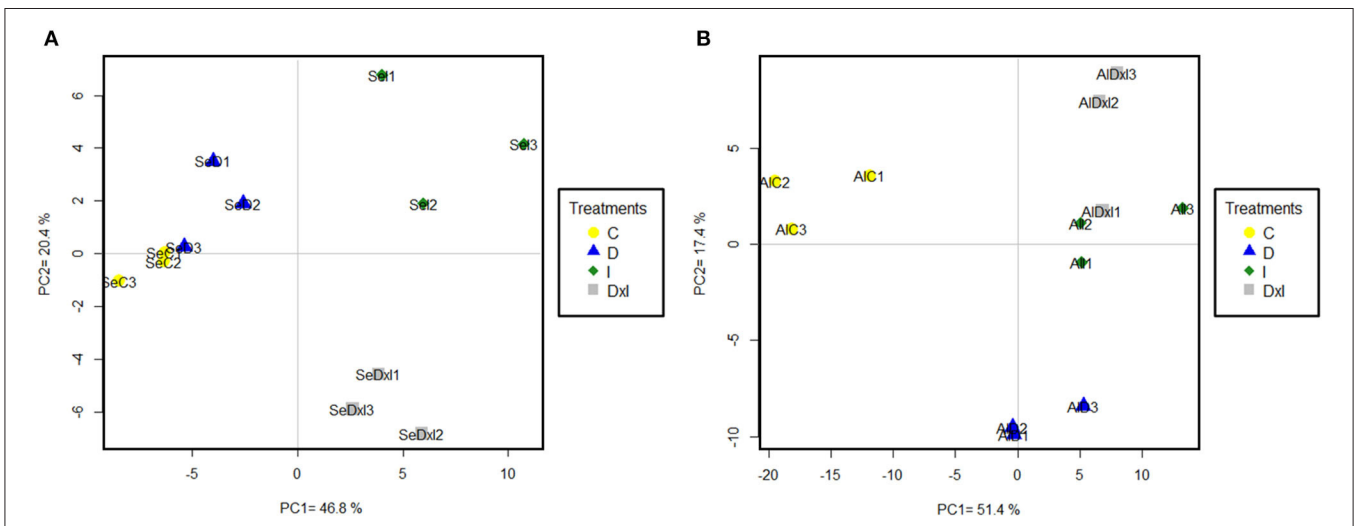

FIGURE 7 | Principal component analysis of variable proteins identified in the Seville **(A)** and Almeria **(B)** populations. Treatments: C control; D drought; I inoculation; D×I combined. Numbers indicate biological replicates for each treatment.

TABLE 3 | First 20 proteins with positive loadings contributing to PC1 and PC2 in the Seville (Se) and Almeria (Al) populations as classified by functional group.

Functional group	Protein	Up-accumulated	Loadings
Se POPULATION			
PC1			
Amino acid metabolism	Cysteine synthase	I	0.134671201
	Alanine–glyoxylate aminotransferase 2 homolog 1, mitochondrial	I; D×I	0.138725675
Carbohydrate metabolism	6-phosphogluconate dehydrogenase, decarboxylating	I; D×I	0.138255713
	Citrate synthase	I	0.146813054
	Aldehyde dehydrogenase, mitochondrial	I; D×I	0.150395963
Cellular processes	Putative reversibly glycosylatable polypeptide	I	0.145130599
	α-1,4-glucan-protein synthase [UDP-forming] 2	I; D×I	0.148753876
Folding, sorting, and degradation	Proline iminopeptidase	I	0.128417337
	Eukaryotic translation initiation factor 3 subunit F	I	0.133480073
	ATP-dependent Clp protease proteolytic subunit-related protein 1, chloroplastic	I	0.138556079
	40S ribosomal protein S5	I	0.139542434
	Translocase of chloroplast	D×I	0.145884352
ROS scavenging	FrnE protein-like	I; C	0.133528064
Secondary metabolism	NADPH-dependent codeinone reductase	D×I	0.141369245
	NADPH:protochlorophyllide oxidoreductase porA	I; D×I	0.142549926
Signaling	Trans-2-enoyl-CoA reductase, mitochondrial	I; D×I	0.130723221
Transport	V-type proton ATPase subunit C	I	0.143391600
Unknown	Outer envelope pore protein 37, chloroplastic	I	0,134589518
	BnaA01g04430D protein	I; D×I	0,138201036
	Carboxylate clamp-tetratricopeptide repeat protein	I; D×I	0,138579354
PC2			
Amino acid metabolism	Glyoxalase I	C; D; I	0.203639693
	Arginine biosynthesis bifunctional protein ArgJ	I	0.204108147
Carbohydrate metabolism	Fructokinase	I	0.120840694
	α-amylase	I	0.134587804
	HMG aldolase	C; D; I	0.191073158
Cellular processes	Cell division protein FtsZ	C	0.121972298
	Patatin	I	0.130841894
	Cell division protein FtsZ homolog 1, chloroplastic	C; D; I	0.153978976
	Harpin binding protein 1	C; D; I	0.215407463
Energy metabolism	Photosystem II subunit P-1	C	0.114099595
Folding, sorting, and degradation	Translocase of chloroplast	I	0.136243712
	Mitochondrial processing peptidase	I	0.163693915
	Mitochondrial processing peptidase subunit beta	I	0.170347898
	Peptidyl-prolyl *cis-trans* isomerase	C; D; I	0.173743165
	Clone PI4869 proteasome inhibitor-like protein mRNA	I	0.214512684
Miscellaneous	Oxidoreductase, putative	I	0.200450416
Secondary metabolism	Caffeic acid *O*-methyltransferase	I	0.121922782
Unknown	Cysteine synthase	I	0,119390920
	Fructose-bisphosphate aldolase	I	0,129593872
	Lysine 6-aminotransferase	I	0,173751918
Al POPULATION			
PC1			
Carbohydrate metabolism	Glucose-6-phosphate 1-dehydrogenase, cytoplasmic isoform 2	D×I	0.083620512
	Aldehyde dehydrogenase	D×I; I; D	0.083884994
	Serine hydroxymethyltransferase	D×I	0.083941959
	Malic enzyme	D×I; I	0.084150059
	NADH dehydrogenase [ubiquinone] flavoprotein 2, mitochondrial	D×I; I; D	0.084854012

(Continued)

TABLE 3 | Continued

Functional group	Protein	Up-accumulated	Loadings
	ATP synthase subunit alpha, mitochondrial	D×I; I; D	0.085624630
	Formate dehydrogenase	D×I; I; D	0.085695392
	Malic enzyme	D×I; I	0.086636987
	Glucose-1-phosphate adenylyltransferase large subunit, chloroplastic/amyloplastic	I	0.086639036
	Malate dehydrogenase	D×I; I; D	0.088034545
Cellular processes	UDP-D-apiose/UDP-D-xylose synthase	I	0.084723943
	α-1,4-glucan-protein synthase [UDP-forming] 2	D×I; I; D	0.086561347
Energy metabolism	Fructose-bisphosphate aldolase	D×I; I; D	0.086927615
Folding, sorting, and degradation	Heat shock protein 60	D×I; I; D	0.085004175
	T-complex protein 1 subunit zeta 1	D×I; I; D	0.089137549
Hormone metabolism	Aluminum-induced protein with YGL and LRDR motifs	D×I; I; D	0.084157903
	Probable aldo–keto reductase 1	D×I; I; D	0.085397904
Lipid metabolism	Acyl-[acyl-carrier-protein] desaturase	I	0.087659507
Miscellaneous	Dynamin-related protein 1E	D×I; I	0.086364345
ROS scavenging	Monothiol glutaredoxin-S17	D×I; I; D	0.083444644
PC2			
Amino acid metabolism	Ornithine carbamoyltransferase, chloroplastic	I; D×I	0.067037801
	Methionine synthase	D×I	0.086406313
Carbohydrate metabolism	Aldehyde dehydrogenase, mitochondrial	D×I	0.069051721
	Glucose-6-phosphate isomerase 1, chloroplastic	D×I	0.089556889
	Serine hydroxymethyltransferase	D×I	0.094407201
	Carbonate dehydratase	D×I	0.105989354
Defense	BURP domain protein RD22	D×I	0.086388976
Energy metabolism	Ferredoxin–NADP reductase	D×I	0.102371216
	Serine–glyoxylate aminotransferase	D×I	0.123546721
Folding, sorting, and degradation	40S ribosomal protein S19	D×I	0.068660324
	AMPP	D×I	0.075187168
	50S ribosomal protein L5, chloroplastic	D×I	0.087674819
	60S ribosomal protein L17-2	D×I	0.104318614
Hormone metabolism	12-oxophytodienoate reductase 1	I; D×I	0.068398959
Miscellaneous	CTF2A-like oxidoreductase	D×I	0.098176129
Nucleotide metabolism	Adenylate kinase	I; D×I	0.102221691
ROS scavenging	Catalase	I; D×I	0.109176303
	Catalase	I; D×I	0.118027832
Secondary metabolism	Aminotransferase	I; D×I	0.073624373
Signaling	Sulphite reductase 1 [ferredoxin], chloroplastic	D×I	0.099056469

C, D, I, and D×I indicate control, drought, inoculation, and combined treatment, respectively.

II subunit P-1, ferredoxin–NADP reductase, postillumination chlorophyll florescence increase protein, 33 kDa oxygen-evolving protein of photosystem II, phosphoglycolate phosphatase 1A, PsbP domain-containing protein 3, and sedoheptulose-1,7-biphosphatase (**Supplementary Table 2**).

DISCUSSION

In nature, plants are simultaneously exposed to a combination of biotic and abiotic stresses (Ramegowda and Senthil-Kumar, 2015; Pandey et al., 2017; Teshome et al., 2020). In a previous study, our group used molecular methods to investigate the individual effects of *P. cinnamomi* and drought, which are the two main stresses leading to oak decline (Jorge et al., 2006; Echevarría-Zomeño et al., 2009; Sghaier-Hammami et al., 2013; Valero-Galván et al., 2013; Simova-Stoilova et al., 2015, 2018; San-Eufrasio et al., 2020), on *Q. ilex* seedlings and their response to these two stresses. In this work, we went one step forward by exploring the combined effects of abiotic (water withholding) and biotic stress (*P. cinnamomi* inoculation) on *Q. ilex* seedlings from three contrasting Andalusian populations (Se, Gr, and Al). Only one study of the effects of combined stress on seedling traits and physiology in holm oak had previously been reported which, however, failed to examine metabolic changes or consider the potential influence of plant variability (Ruiz-Gómez et al., 2018). The high interpopulation and intrapopulation variability

of *Q. ilex* (Valero-Galván et al., 2011; San-Eufrasio et al., 2020) led us to compare several Andalusian populations of this species to gain further insight into the response of holm oak to *P. cinnamomi* and drought.

The effects of stresses and the ensuing response are known to depend on stress intensity and duration. In this work, infection of seedlings was confirmed by isolating the pathogen and identifying it under a light microscope at the end of an experiment where seedlings were placed under severe drought conditions (see San-Eufrasio et al., 2020).

Plant Mortality and Physiological Response

The effect and the level of tolerance to the stresses were assessed here through the visual inspection of the damage symptoms and the number of dead seedlings, which differed among populations and treatments. As regards variability in resilience among populations or individuals within populations, the combined effects of *P. cinnamomi* attack and drought are more damaging to survival than are those of the two stresses in isolation (Desprez-Loustau et al., 2006; Sherwood et al., 2015; Ghanbary et al., 2017, 2020; Ruiz-Gómez et al., 2018). Response to an attack by *P. cinnamomi* drought stress was first observed in the Al population, which is located in the eastern part of Andalusia. This population is in the farthest region to the place where *P. cinnamomi* root rot was first observed, which was seemingly the southwest of the Iberian Peninsula (Brasier, 1996). This is consistent with the increased susceptibility to *P. cinnamomi* of eastern Andalusian populations previously reported by Sghaier-Hammami et al. (2013). On the other hand, *Q. ilex* populations located in the eastern part were previously found to be more tolerant of drought than those in the western part (Valero-Galván et al., 2013; Navarro-Cerrillo et al., 2018), the combination of both stresses having a greater impact on Al than on the other two populations studied here. In turn, the Se and Gr populations exhibited a similar response to *P. cinnamomi* and drought in terms of damage symptoms and mortality, the earliest symptoms of seedling damage being observed on day 6 in both populations. The Gr population responded more effectively to the individual and combined effects of the two factors; in fact, it was the Gr population that exhibited the highest seedling survival at the end of the experiment.

The effects of both stresses and the response of *Q. ilex* to them were also assessed in physiological terms through water status and photosynthetic activity, as previously carried out by Sghaier-Hammami et al. (2013) and Valero-Galván et al. (2013) in studying individual sources of stress. RLWC was significantly decreased by drought and *P. cinnamomi*, both individually and in combination, relative to the control seedlings, the effect of the pathogen attack being especially marked (De Pascali et al., 2019). However, undamaged *Q. ilex* seedlings maintained their leaf moisture levels, which suggest that they succeeded in holding leaf turgor after 35 days under stressing conditions (Forner et al., 2018). The maximum PSII photochemical efficiency (Qy) and conversion efficiency of PSII open reaction centers (F_v'/F_m') are measures of photochemical activity, commonly used as parameters of response to stress in plants (Bolhàr-Nordenkampf and Öquist, 1993; Filella et al., 1998; Peguero-Pina et al., 2009; Murchie and Lawson, 2013; Sancho-Knapik et al., 2018; Jia et al., 2019). Photosynthetic activity decreased throughout the experiment but differences among populations were not significant (San-Eufrasio et al., 2020). This indicates that the PSII reaction site in *Q. ilex* leaves was affected by the two stresses, which inhibited photosynthesis in the seedlings. Also, the fact the combined treatment led to the lowest chlorophyll fluorescence values at the end of the experiment in the Al population is suggestive of an especially synergistic effect of the two stresses on photosynthesis in this population.

An early, fast decrease in A) and Gs) was observed in seedlings under the individual and combined action of *P. cinnamomi* and drought in all populations, which exhibited low values of the two parameters throughout the experiment (Maurel et al., 2001; Sghaier-Hammami et al., 2013; Corcobado et al., 2014; Merilo et al., 2014; Ruiz-Gómez et al., 2018). Early quick stomatal closure in response to *P. cinnamomi* and drought may have reduced water losses and carbon dioxide uptake (Lawlor and Cornic, 2002; Merilo et al., 2014). The quantitative response of these physiological parameters to the individual stresses and their combination was population-independent; in any case, there was a stronger, but not statistically different, response to combined stress (Ruiz-Gómez et al., 2018). Unlike previously found by Ruiz-Gómez et al. (2018), infection by *P. cinnamomi* had more marked effects than drought, possibly as a consequence of the pathogen damaging the root system and reducing water uptake as a result (Crombie and Tippett, 1990; Corcobado et al., 2013). This reduction in turn may have increased water deficiency, thereby decreasing physiological parameters in the seedlings (Maurel et al., 2001; Robin and Desprez-Loustau, 2001). Overall, the physiological response of *Q. ilex* to attack by *P. cinnamomi* and drought, whether individually or in combination, was quite similar among populations, the photosynthetic apparatus of the seedlings being affected mainly by the combination of the two stresses.

Biochemical Parameters in Undamaged Seedlings

The fact that the contents in photosynthetic pigments of undamaged seedlings under stress from drought and *P. cinnamomi* inoculation were similar to those of the control seedlings suggests that the photosynthetic apparatus was altered by neither source of stress (Gallé et al., 2007; San-Eufrasio et al., 2020). Thus, neither amino acids nor phenolics nor flavonoids among other biomolecules were altered in their contents under the stress conditions. The contents in soluble sugars and starch increased markedly in seedlings under both sources of stress, followed by those under drought alone. Abiotic and biotic stresses are known to increase the soluble sugar contents of leaves by regulating expression in genes involved in photosynthesis, osmolyte synthesis, and sucrose metabolism (Holland et al., 2016; Khan et al., 2020). Beyond its role as a source of carbon and energy *via* fermentative or aerobic pathways, soluble sugars promote water uptake to maintain cell volume while avoiding wilting (Manes et al., 2006; Holland et al., 2016). In this work, we found increased starch accumulation with

all treatments relative to the control seedlings, the starch content being especially high in Al seedlings under the inoculation or combined treatment. Starch, phenolic compounds, and other defense-related substances were previously found to accumulate in xylem and protoxylem cells in the roots of inoculated plants (Ruiz Gómez et al., 2014; Redondo et al., 2015). This is consistent with the results of Sghaier-Hammami et al. (2013), who found an increased abundance of proteins involved in starch biosynthesis in response to an attack by *P. cinnamomi*. Therefore, although our seedlings responded more strongly to the pathogen than to drought, their metabolism was not imbalanced as a result. In conclusion, the seedlings succeeded in maintaining cellular homeostasis beyond physiological disturbances even under severe stress conditions.

Alteration of the Protein Profile by Drought and *P. cinnamomi*

The proteomic techniques used (1D and shotgun-MS/MS analysis) allowed the identification and quantification of a large set of proteins in *Q. ilex* seedling leaves altered by inoculation with *P. cinnamomi* and/or drought. Based on the number of 1D SDS-PAGE bands and their intensity, the combined treatment had a stronger effect than all others; also, the Al population was more markedly affected than the Se population, which is quite consistent with the previous results. Based on the shotgun results, the Al population exhibited more changes in both confidence and variable proteins than did the Se population. This was a consequence of the above-described results as regards damage symptoms and mortality and suggests that the most susceptible population was that undergoing the greatest proteomic changes. The differences in the abundance of proteomic changes were found to be dependent on the particular population. Thus, the two populations differed in the number of proteins but not in the functional categories. The largest groups of confidence and variable upaccumulated proteins in the two populations were those of amino acid metabolism; carbohydrate metabolism; folding, sorting, and degradation; ROS scavenging; and secondary metabolism (Sghaier-Hammami et al., 2013; Valero-Galván et al., 2013; Hildebrandt, 2018; San-Eufrasio et al., 2021). In contrast, the largest number of downaccumulated proteins in both populations, which contributed more to the variability, was that of the photosynthesis (Kapoor et al., 2020), which is in line with the above-described results for physiological parameters. Multivariate analysis revealed a different response to *P. cinnamomi* and drought in the two populations. PCA allowed effective discrimination of the inoculation and combined treatments from the drought and control treatments in the Se population, and also of the control treatment from the individual and combined treatments in the Al population. In addition, PCA clearly discriminated between drought and *P. cinnamomi*, the latter individually or in combination. Therefore, proteins in both populations were more markedly affected by *P. cinnamomi* attack than they were by drought.

Putative Markers of Resilience to Stress

Those proteins that were consistently found in the three biological replicates from both populations contributed markedly to variability in the PCA and were more abundant in the combined treatment were taken to be putative molecular markers. The specific proteins considered were aldehyde dehydrogenase, glucose-6-phosphate isomerase, 50S ribosomal protein L5, and α-1,4-glucan-protein synthase [UDP-forming]. Aldehyde dehydrogenase levels are known to be raised by both abiotic and biotic stresses (Tola et al., 2021). Thus, plants under stress produce increased amounts of ROS that in turn boost aldehyde production by cells through stress-induced lipid peroxidation (Bartels and Sunkar, 2005; Tola et al., 2021). Aldehyde dehydrogenase detoxifies aldehydes by oxidizing them to carboxylic acids (Tola et al., 2021). Sunkar et al. (2003) found overexpression of aldehyde dehydrogenase under Arabidopsis conditions to increase tolerance of dehydration. The 50S ribosomal protein L5 is a chloroplast ribosomal protein that is upregulated in response to abiotic stress by boosting the synthesis of chloroplast-encoded proteins to offset damage in photosynthesis proteins caused by abiotic stress (Zhu et al., 2021). α-1,4-Glucan-protein-synthase, which is involved in the biogenesis or degradation of cell walls, has been identified in response to drought conditions (Fadoul et al., 2018; Dugasa et al., 2021). UDP-forming protein is associated with the formation of cell walls as physical barriers against pathogens (Shoresh and Harman, 2008). Glucose-6-phosphate isomerase (also called "phosphoglucose isomerase"), a glycolytic enzyme that interconverts glucose-6-phosphate and fructose-6-phosphate, is a drought stress-related protein whose synthesis is boosted under water-deficient conditions (Khanna et al., 2014). This enzyme has been deemed a promoter of starch synthesis by leaves (Backhausen et al., 1997; Yu et al., 2000). Therefore, all the proteins proposed as markers of resilience to combined biotic and abiotic stress, and hence to the decline syndrome in *Q. ilex* are responsive to adverse environmental conditions, their increased production being a part of the survival mechanisms of this species under restrictive conditions.

CONCLUSIONS

The presence of stress from *P. cinnamomi* and drought was found to have a synergistic effect on *Q. ilex* seedlings from three contrasting populations in Andalusia, southern Spain. There were no qualitative, but only quantitative differences in the effects and responses to the individual or combined stresses, the Al population being the most markedly affected by the combined treatment, and hence the theoretically most vulnerable to the decline syndrome. As regards individual stresses, drought had a more marked effect than *P. cinnamomi* on the Se and Gr populations, whereas the opposite held for the Al population. Even so, a variable proportion of seedlings from each population responded effectively to stress, with no visible symptoms of leaf damage at any time during the experiment. Those asymptomatic seedlings responded differently to the individual stresses and

their combination. Thus, despite the reduced moisture content and photosynthetic activity, their levels were still high enough for cellular homeostasis to be maintained and differences in the contents of key biomolecules such as photosynthetic pigments, amino acids, and phenolics to be insubstantial. The protein functional groups undergoing the greatest changes were folding, sorting, and degradation; carbohydrate metabolism; amino acid metabolism; ROS scavenging and secondary metabolism (upaccumulated); and energy metabolism (downaccumulated). The reduction in photosynthetic activity may have arisen from an increase in heterotrophic catabolism. Also, stress-related proteins were more abundant in the Al population than they were in the other two. The following proteins are proposed as putative markers of resilience to the decline syndrome in *Q. ilex*: aldehyde dehydrogenase, glucose-6-phosphate isomerase, 50S ribosomal protein L5, and α-1,4-glucan-protein synthase [UDP-forming].

DATA AVAILABILITY STATEMENT

The original contributions presented in the study are publicly available. This data can be found at: MS proteomics raw data were deposited with dataset identifier PXD025704 in the ProteomeXchange Consortium via the PRIDE partner repository (Perez-Riverol et al., 2019).

AUTHOR CONTRIBUTIONS

JJ-N and M-DR conceived and designed the experiments. BS-E and M-DR performed the experiments. FR-G supplied the *P. cinnamomi* strain, provided the acorns, and helped with the greenhouse measurements. BS-E, MC, JJ-N, RN-C, and M-DR analyzed the data. JJ-N and M-DR wrote the manuscript. All authors read and approved the final manuscript.

FUNDING

This work was supported by grant ENCINOMICS-2 PID2019-10908RB-100 from the Spanish Ministry of Economy and Competitiveness as well as grant UCO_FEDER-18-12575795R from the Junta de Andalucia.

ACKNOWLEDGMENTS

MÁ-C and M-DR are grateful for the award of a Ramón y Cajal (RYC-2017-23706) and a Juan de la Cierva Incorporación (IJC2018-035272-I) contract, respectively, by the Spanish Ministry of Science, Innovation and Universities. The authors thank Roberto J. Cabrera-Puerto for his help during the collection of the acorns and the staff of the Central Service for Research Support (SCAI) at the University of Cordoba for technical support in the identification of proteins. FR-G was supported by a postdoctoral fellowship of the Andalusian Regional Government (Spain) and the European Social Fund 2014-2020 Program (DOC_0055).

SUPPLEMENTARY MATERIAL

The Supplementary Material for this article can be found online at: https://www.frontiersin.org/articles/10.3389/fpls.2021.722802/full#supplementary-material

REFERENCES

Agrios, G. (2005). *Plant Pathology. 5th edition*. London: Elsevier Academic Press.

Backhausen, J. E., Jöstingmeyer, P., and Scheibe, R. (1997). Competitive inhibition of spinach leaf phosphoglucose isomerase isoenzymes by erythrose 4-phosphate. *Plant Sci.* 130, 121–131. doi: 10.1016/s0168-9452(97)00208-2

Bartels, D., and Sunkar, R. (2005). Drought and salt tolerance in plants. *CRC Crit. Rev. Plant Sci.* 24, 23–58. doi: 10.1080/07352680590910410

Bolhàr-Nordenkampf, H. R., and Öquist, G. (1993). "Chlorophyll fluorescence as a tool in photosynthesis research," in *Photosynthesis and Production in a Changing Environment* (Dordrecht: Springer), 193–206. doi: 10.1007/978-94-010-9626-3_12

Bradford, M. M. (1976). A rapid and sensitive method for the quantitation of microgram quantities of protein utilizing the principle of protein-dye binding. *Anal. Biochem.* 72, 248–254. doi: 10.1016/0003-2697(76)90527-3

Brasier, C. (1996). *Phytophthora cinnamomi* and oak decline in southern Europe. Environmental constraints including climate change. *Ann. Sci. Forest.* 53, 347–358. doi: 10.1051/forest:19960217

Brasier, C. M. (1992). Oak tree mortality in Iberia. *Nature* 360, 539–539. doi: 10.1038/360539a0

Brasier, C. M., Robredo, F., and Ferraz, J. F. P. (1993). Evidence for *Phytophthora cinnamomi* involvement in Iberian oak decline. *Plant Pathol.* 42, 140–145. doi: 10.1111/j.1365-3059.1993.tb01482.x

Burgess, T. I., Scott, J. K., Mcdougall, K. L., Stukely, M. J. C., Crane, C., Dunstan, W. A., et al. (2016). Current and projected global distribution of *Phytophthora cinnamomi*, one of the world's worst plant pathogens. *Glob. Change Biol.* 23, 1661–1674. doi: 10.1111/gcb.13492

Camilo-Alves, C. S. P., Clara, M. I. E., and Ribeiro, N. M. C. A. (2013). Decline of Mediterranean oak trees and its association with *Phytophthora cinnamomi*: a review. *Eur. J. For. Res.* 132, 411–432. doi: 10.1007/s10342-013-0688-z

Castillejo, M. Á., Bani, M., and Rubiales, D. (2015). Understanding pea resistance mechanisms in response to *Fusarium oxysporum* through proteomic analysis. *Phytochemistry* 115, 44–58. doi: 10.1016/j.phytochem.2015.01.009

Castillejo, M. Á., Fondevilla-Aparicio, S., Fuentes-Almagro, C., and Rubiales, D. (2020). Quantitative analysis of target peptides related to resistance against ascochyta blight (*Peyronellaea pinodes*) in Pea. *J. Proteome Res.* 19, 1000–1012. doi: 10.1021/acs.jproteome.9b00365

Colangelo, M., Camarero, J. J., Borghetti, M., Gentilesca, T., Oliva, J., Redondo, M.-A., et al. (2018). Drought and *Phytophthora* are associated with the decline of oak species in southern Italy. *Front. Plant Sci.* 9:1595. doi: 10.3389/fpls.2018.01595

Corcobado, T., Cubera, E., Juárez, E., Moreno, G., and Solla, A. (2014). Drought events determine performance of *Quercus ilex* seedlings and increase their susceptibility to *Phytophthora cinnamomi*. *Agric. For. Meteorol.* 192–193, 1–8. doi: 10.1016/j.agrformet.2014.02.007

Corcobado, T., Cubera, E., Moreno, G., and Solla, A. (2013). *Quercus ilex* forests are influenced by annual variations in water table, soil water deficit and fine root loss caused by *Phytophthora cinnamomi*. *Agric. For. Meteorol.* 169, 92–99. doi: 10.1016/j.agrformet.2012.09.017

Corcobado, T., Miranda-Torres, J. J., Martín-García, J., Jung, T., and Solla, A. (2017). Early survival of *Quercus ilex* subspecies from different populations after infections and co-infections by multiple *Phytophthora* species. *Plant Pathol.* 66, 792–804. doi: 10.1111/ppa.12627

Corral-Ribera, M., Hijano, C. F., and Vázquez, B. P. (2018). *Factores ambientales en la distribución de la seca en la encina (Quercus ilex subsp. ballota). Espacio Tiempo y Forma*. Serie VI, Geografía. doi: 10.5944/etfvi.11.2018.21777

Crombie, D. S., and Tippett, J. T. (1990). A comparison of water relations, visual symptoms, and changes in stem girth for evaluating impact of *Phytophthora cinnamomi* dieback on *Eucalyptus marginata*. *Can. J. For. Res.* 20, 233–240. doi: 10.1139/x90-032

De Pascali, M., Vergine, M., Sabella, E., Aprile, A., Nutricati, E., Nicol,ì, F., et al. (2019). Molecular Effects of *Xylella fastidiosa* and drought combined stress in olive trees. *Plants* 8:437. doi: 10.3390/plants8110437

Desprez-Loustau, M.-L., Marçais, B., Nageleisen, L.-M., Piou, D., and Vannini, A. (2006). Interactive effects of drought and pathogens in forest trees. *Ann. For. Sci.* 63, 597–612. doi: 10.1051/forest:2006040

Dugasa, M. T., Feng, X., Wang, N.-H., Wang, J., and Wu, F. (2021). Comparative transcriptome and tolerance mechanism analysis in the two contrasting wheat (*Triticum aestivum* L.) cultivars in response to drought and salinity stresses. *Plant Growth Regul.* 94, 101–114. doi: 10.1007/s10725-021-00699-4

Echevarría-Zomeño, S., Ariza, D., Jorge, I., Lenz, C., Campo, A. D., Jorrín, J. V., et al. (2009). Changes in the protein profile of *Quercus ilex* leaves in response to drought stress and recovery. *J. Plant Physiol.* 166, 233–245. doi: 10.1016/j.jplph.2008.05.008

Erwin, D. C., and Ribeiro, O. K. (1996). *Phytophthora Diseases Worldwide*. St. Paul, MN: APS Press.

Esker, P. D., Gibb, K. S., Padovan, A., Dixon, P. M., and Nutter Jr, F. W. (2006). Use of survival analysis to determine the postincubation time-to-death of papaya due to yellow crinkle disease in Australia. *Plant Dis.* 90, 102–107. doi: 10.1094/PD-90-0102

Fadoul, H. E., Siddig, M. A. E., Abdalla, A. W. H., and Hussein, A. A. E. (2018). Physiological and proteomic analysis of two contrasting *Sorghum bicolor* genotypes in response to drought stress. *Aust. J. Crop. Sci.* 12, 1543–1551. doi: 10.21475/ajcs.18.12.09.pne134

Filella, I., Llusi,à, J., Piñol, J., and Peñuelas, J. (1998). Leaf gas exchange and fluorescence of *Phillyrea latifolia*, Pistacia lentiscus and *Quercus ilex* saplings in severe drought and high temperature conditions. *Environ. Exp. Bot.* 39, 213–220. doi: 10.1016/s0098-8472(97)00045-2

Forner, A., Valladares, F., and Aranda, I. (2018). Mediterranean trees coping with severe drought: Avoidance might not be safe. *Environ. Exp. Bot.* 155, 529–540. doi: 10.1016/j.envexpbot.2018.08.006

Galili, T., O'Callaghan, A., Sidi, J., and Sievert, C. (2018). Heatmaply: an R package for creating interactive cluster heatmaps for online publishing. *Bioinformatics* 34, 1600–1602. doi: 10.1093/bioinformatics/btx657

Gallé, A., Haldimann, P., and Feller, U. (2007). Photosynthetic performance and water relations in young pubescent oak (*Quercus pubescence*) trees during drought stress and recovery. *New Phytol.* 174, 799–810. doi: 10.1111/j.1469-8137.2007.02047.x

Gea-Izquierdo, G., Natalini, F., and Cardillo, E. (2021). Holm oak death is accelerated but not sudden and expresses drought legacies. *Sci. Total Environ.* 754:141793. doi: 10.1016/j.scitotenv.2020.141793

Ghanbary, E., Kouchaksaraei, M. T., Mirabolfathy, M., Sanavi, S. A. M. M., and Rahaie, M. (2017). Growth and physiological responses of *Quercus brantii* seedlings inoculated with *Biscogniauxia mediterranea* and *Obolarina persicaunder* drought stress. *For. Pathol.* 47:e12353. doi: 10.1111/efp.12353

Ghanbary, E., Kouchaksaraei, M. T., Zarafshar, M., Bader, K. F. M., Mirabolfathy, M., and Ziaei, M. (2020). Differential physiological and biochemical responses of *Quercus infectoria* and *Q. libani* to drought and charcoal disease. *Physiol. Plant* 168, 876–892. doi: 10.1111/ppl.13027

Gómez-Gálvez, I., Sánchez-Lucas, R., San-Eufrasio, B., De Francisco, L. E. R., Maldonado-Alconada, A. M., Fuentes-Almagro, C., et al. (2020). "Optimizing shotgun proteomics analysis for a confident protein identification and quantitation in orphan plant species: the case of holm oak (*Quercus ilex*)," in *Methods in Molecular Biology in Plant Proteomics,* ed J.V. Jorrín-Novo (New York, NY: Springer Nature). doi: 10.1007/978-1-0716-0528-8_12

Guerrero-Sanchez, V. M., Maldonado-Alconada, A. M., Amil-Ruiz, F., and Jorrin-Novo, J. V. (2017). Holm oak (*Quercus ilex*) transcriptome. *De novo* sequencing and assembly analysis. *Front. Mol. Biosci.* 4:70. doi: 10.3389/fmolb.2017.00070

Guerrero-Sanchez, V. M., Maldonado-Alconada, A. M., Amil-Ruiz, F., Verardi, A., Jorrín-Novo, J. V., and Rey, M. D. (2019). Ion Torrent and lllumina, two complementary RNA-seq platforms for constructing the holm oak (*Quercus ilex*) transcriptome. *PLoS ONE* 14:210356. doi: 10.1371/journal.pone.0210356

Guzmán-Álvarez, J. R. (2016). The image of a tamed landscape: Dehesa through History in Spain. *Cult. Hist. Digit. J.* 5:e003. doi: 10.3989/chdj.2016.003

Hardham, A. R. (2005). *Phytophthora cinnamomi*. *Mol. Plant Pathol.* 6, 589–604. doi: 10.1111/j.1364-3703.2005.00308.x

Hildebrandt, T. M. (2018). Synthesis versus degradation: directions of amino acid metabolism during *Arabidopsis* abiotic stress response. *Plant Mol. Biol.* 98, 121–135. doi: 10.1007/s11103-018-0767-0

Hoagland, D. R., and Arnon, D. I. (1950). *The Water-Culture Method for Growing Plants Without Soil*. Berkeley, CA: California Agricultural Experiment Station.

Holland, S. C., Artier, J., Miller, N. T., Cano, M., Yu, J., Ghirardi, M. L., et al. (2016). Impacts of genetically engineered alterations in carbon sink pathways on photosynthetic performance. *Algal Res.* 20, 87–99. doi: 10.1016/j.algal.2016.09.021

Jeffers, S. N. (1986). Comparison of two media selective for *Phytophthora* and *Pythium* species. *Plant Dis.* 70:1038. doi: 10.1094/pd-70-1038

Jia, X.-M., Wang, H., Svetla, S., Zhu, Y.-F., Hu, Y., Cheng, L., et al. (2019). Comparative physiological responses and adaptive strategies of apple *Malus halliana* to salt, alkali and saline-alkali stress. *Sci. Hortic.* 245, 154–162. doi: 10.1016/j.scienta.2018.10.017

Jorge, I., Navarro, R. M., Lenz, C., Ariza, D., and Jorrín-Novo, J. V. (2006). Variation in the holm oak leaf proteome at different plant developmental stages, between provenances and in response to drought stress. *Proteomics* 6, S207–S214. doi: 10.1002/pmic.200500364

Jung, T., Blaschke, H., and Osswald, W. (2000). Involvement of soilborne *Phytophthora* species in Central European oak decline and the effect of site factors on the disease. *Plant Pathol.* 49, 706–718. doi: 10.1046/j.1365-3059.2000.00521.x

Kapoor, D., Bhardwaj, S., Landi, M., Sharma, A., Ramakrishnan, M., and Sharma, A. (2020). The impact of drought in plant metabolism: how to exploit tolerance mechanisms to increase crop production. *Appl. Sci.* 10:5692. doi: 10.3390/app10165692

Khan, N., Ali, S., Zandi, P., Mehmood, A., Ullah, S., Ikram, M., et al. (2020). Role of sugars, amino acids and organic acids in improving plant abiotic stress tolerance. *Pak. J. Bot.* 52:24. doi: 10.30848/pjb2020-2(24)

Khanna, S. M., Taxak, P. C., Jain, P. K., Saini, R., and Srinivasan, R. (2014). Glycolytic enzyme activities and gene expression in *Cicer arietinum* exposed to water-deficit stress. *Appl. Biochem. Biotechnol.* 173, 2241–2253. doi: 10.1007/s12010-014-1028-6

Laemmli, U. K. (1970). Cleavage of Structural Proteins during the Assembly of the Head of Bacteriophage T4. *Nature* 227, 680–685. doi: 10.1038/227680a0

Lawlor, D. W., and Cornic, G. (2002). Photosynthetic carbon assimilation and associated metabolism in relation to water deficits in higher plants. *Plant Cell Environ.* 25, 275–294. doi: 10.1046/j.0016-8025.2001.00814.x

Lichtenthaler, H. K. (1987). Chlorophylls and carotenoids: Pigments of photosynthetic biomembranes. *Meth. Enzymol.* 148, 350–382. doi: 10.1016/0076-6879(87)48036-1

Lohse, M., Nagel, A., Herter, T., May, P., Schroda, M., Zrenner, R., et al. (2014). Mercator: a fast and simple web server for genome scale functional annotation of plant sequence data. *Plant Cell Environ.* 37, 1250–1258. doi: 10.1111/pce.12231

López-Hidalgo, C., Guerrero-Sánchez, V. M., Gómez-Gálvez, I., Sánchez-Lucas, R., Castillejo-Sánchez, M. A., Maldonado-Alconada, A. M., et al. (2018). A multi-omics analysis pipeline for the metabolic pathway reconstruction in the orphan species *Quercus ilex*. *Front. Plant Sci.* 9:935. doi: 10.3389/fpls.2018.00935

López-Hidalgo, C., Meijón, M., Lamelas, L., and Valledor, L. (2021). The rainbow protocol: A sequential method for quantifying pigments, sugars, free amino acids, phenolics, flavonoids and MDA from a small amount of sample. *Plant Cell Environ.* 44, 1977–1986. doi: 10.1111/pce.14007

Mammen, D., and Daniel, M. (2012). A critical evaluation on the reliability of two aluminum chloride chelation methods for quantification of flavonoids. *Food Chem.* 135, 1365–1368. doi: 10.1016/j.foodchem.2012.05.109

Manes, F., Vitale, M., Donato, E., Giannini, M., and Puppi, G. (2006). Different ability of three mediterranean oak species to tolerate progressive water stress. *Photosynthetica* 44, 387–393. doi: 10.1007/s11099-006-0040-7

Maurel, M., Robin, C., Capron, G., and Desprez-Loustau, M. L. (2001). Effects of root damage associated with *Phytophthora cinnamomi* on water

relations, biomass accumulation, mineral nutrition and vulnerability to water deficit of five oak and chestnut species. *For. Pathol.* 31, 353–369. doi: 10.1046/j.1439-0329.2001.00258.x

Merilo, E., Jõesaar, I., Brosché, M., and Kollist, H. (2014). To open or to close: species-specific stomatal responses to simultaneously applied opposing environmental factors. *New Phytol.* 202, 499–508. doi: 10.1111/nph.12667

Murchie, E., and Lawson, T. (2013). Chlorophyll fluorescence analysis: a guide to good practice and understanding some new applications. *J. Exp. Bot.* 64, 3983–3998. doi: 10.1093/jxb/ert208

Natalini, F., Alejano, R., Vázquez-Piqu,é, J., Cañellas, I., and Gea-Izquierdo, G. (2016). The role of climate change in the widespread mortality of holm oak in open woodlands of Southwestern Spain. *Dendrochronologia* 38, 51–60. doi: 10.1016/j.dendro.2016.03.003

Navarro-Cerrillo, R. M., Ruiz Gómez, F. J., Cabrera-Puerto, R. J., Sánchez-Cuesta, R., Rodríguez, G. P., and Pérez, J. L. Q. (2018). Growth and physiological sapling responses of eleven *Quercus ilex* ecotypes under identical environmental conditions. *For. Ecol. Manag.* 415–416, 58–69. doi: 10.1016/j.foreco.2018.01.004

Neuhoff, V., Arold, N., Taube, D., and Ehrhardt, W. (1988). Improved staining of proteins in polyacrylamide gels including isoelectric focusing gels with clear background at nanogram sensitivity using Coomassie Brilliant Blue G-250 and R-250. *Electrophoresis* 9, 255–262. doi: 10.1002/elps.1150090603

Pandey, P., Irulappan, V., Bagavathiannan, M. V., and Senthil-Kumar, M. (2017). Impact of combined abiotic and biotic stresses on plant growth and avenues for crop improvement by exploiting physio-morphological traits. *Front. Plant Sci.* 8:537. doi: 10.3389/fpls.2017.00537

Peguero-Pina, J. J., Sancho-Knapik, D., Morales, F., Flexas, J., and Gil-Pelegrín, E. (2009). Differential photosynthetic performance and photoprotection mechanisms of three Mediterranean evergreen oaks under severe drought stress. *Funct. Plant Biol.* 36:453. doi: 10.1071/fp08297

Perez-Riverol, Y., Csordas, A., Bai, J., Bernal-Llinares, M., Hewapathirana, S., Kundu, D. J., et al. (2019). The PRIDE database and related tools and resources in 2019: improving support for quantification data. *Nucleic Acids Res.* 47, D442–D450. doi: 10.1093/nar/gky1106

Quero, J. L., Villar, R., Marañón, T., and Zamora, R. (2006). Interactions of drought and shade effects on seedlings of four *Quercus* species: physiological and structural leaf responses. *New Phytol.* 170, 819–834. doi: 10.1111/j.1469-8137.2006.01713.x

Ramegowda, V., and Senthil-Kumar, M. (2015). The interactive effects of simultaneous biotic and abiotic stresses on plants: Mechanistic understanding from drought and pathogen combination. *J. Plant Physiol.* 176, 47–54. doi: 10.1016/j.jplph.2014.11.008

Redondo, M. Á., Pérez-Sierra, A., Abad-Campos, P., Torres, L., Solla, A., Reig-Armiñana, J., et al. (2015). Histology of *Quercus ilex* roots during infection by *Phytophthora cinnamomi*. *Trees* 29, 1943–1957. doi: 10.1007/s00468-015-1275-3

Rey, M.-D., Castillejo, M., Sánchez-Lucas, R., Guerrero-Sanchez, V., López-Hidalgo, C., Romero-Rodríguez, C., et al. (2019). Proteomics, holm oak (*Quercus ilex* L.) and other recalcitrant and orphan forest tree species: how do they see each other? *Int. J. Mol. Sci.* 20:692. doi: 10.3390/ijms20030692

Robin, C.;, Capron, G., and Desprez-Loustau, M. L. (2001). Root infection by *Phytophthora cinnamomi* in seedlings of three oak species. *Plant Pathol.* 50, 708–716. doi: 10.1046/j.1365-3059.2001.00643.x

Rohlf, F. J., and Sokal, R. R. (1995). *Statistical Tables*. New York, NY: W.H. Freeman.

Romero-Rodríguez, M. C., Jorrín-Novo, J. V., and Castillejo, M. A. (2019). Toward characterizing germination and early growth in the non-orthodox forest tree species *Quercus ilex* through complementary gel and gel-free proteomic analysis of embryo and seedlings. *J Proteomics* 197, 60–70. doi: 10.1016/j.jprot.2018.11.003

Rose, R., Rose, C. L., Omi, S. K., Forry, K. R., Durall, D. M., and Bigg, W. L. (1991). Starch determination by perchloric acid vs enzymes: evaluating the accuracy and precision of six colorimetric methods. *J. Agric. Food Chem.* 39, 2–11. doi: 10.1021/jf00001a001

Ruiz de la Torre, J. (2006). *Flora Mayor. Organismo Autónomo Parques Nacionales*. Madrid: Dirección General para la Biodiversidad.

Ruiz Gómez, F. J., Navarro-Cerrillo, R. M., Sánchez-Cuesta, R., and Pérez-de-Luque, A. (2014). Histopathology of infection and colonization of *Quercus ilex* fine roots by *Phytophthora cinnamomi*. *Plant Pathol.* 64, 605–616. doi: 10.1111/ppa.12310

Ruiz-Gómez, F., Pérez-De-Luque, A., Sánchez-Cuesta, R., Quero, J., and Cerrillo, R. N. (2018). Differences in the response to acute drought and *Phytophthora cinnamomi* Rands infection in *Quercus ilex* L. seedlings. *Forests* 9:634. doi: 10.3390/f9100634

Ruiz-Gómez, F. J., Pérez-De-Luque, A., and Navarro-Cerrillo, R. M. (2019). The involvement of *Phytophthora* root rot and drought stress in holm oak decline: from ecophysiology to microbiome influence. *Curr. For. Rep.* 5, 251–266. doi: 10.1007/s40725-019-00105-3

Sánchez, M. E., Andicoberry, S., and Trapero, A. (2004). Patogenicidad de *Phytophthora* spp. causantes de podredumbre radical de *Quercus ilex* ssp. *ballota* en viveros forestales. *Bol. San. Veg. Plagas* 30, 385–401.

Sánchez-Cuesta, R., Ruiz-Gómez, F., Duque-Lazo, J., González-Moreno, P., and Navarro-Cerrillo, R. M. (2021). The environmental drivers influencing spatio-temporal dynamics of oak defoliation and mortality in dehesas of Southern Spain. *For. Ecol. Manag.* 485:1189746. doi: 10.1016/j.foreco.2021.118946

Sancho-Knapik, D., Mendoza-Herrer, Ó., Gil-Pelegrín, E., and Peguero-Pina, J. (2018). Chl fluorescence parameters and leaf reflectance indices allow monitoring changes in the physiological status of *Quercus ilex* L. under progressive water deficit. *Forests* 9:400. doi: 10.3390/f9070400

San-Eufrasio, B., Bigatton, E. D., Guerrero-Sánchez, V. M., Chaturvedi, P., Jorrín-Novo, J. V., Rey, M. D., et al. (2021). Proteomics data analysis for the identification of proteins and derived proteotypic peptides of potential use as putative drought tolerance markers for *Quercus ilex*. *Int. J. Mol. Sci.* 22:3191. doi: 10.3390/ijms22063191

San-Eufrasio, B., Sánchez-Lucas, R., López-Hidalgo, C., Guerrero-Sánchez, V. M., Castillejo, M. Á., Maldonado-Alconada, A. M., et al. (2020). Responses and differences in tolerance to water shortage under climatic dryness conditions in seedlings from *Quercus* spp. and *Andalusian Q.* ilex populations. *Forests* 11:707. doi: 10.3390/f11060707

Sena, K., Crocker, E., Vincelli, P., and Barton, C. (2018). *Phytophthora cinnamomi* as a driver of forest change: implications for conservation and management. *For. Ecol. Manag.* 409, 799–807. doi: 10.1016/j.foreco.2017.12.022

Sghaier-Hammami, B., Valero-Galvàn, J., Romero-Rodríguez, M. C., Navarro-Cerrillo, R. M., Abdelly, C., and Jorrín-Novo, J. (2013). Physiological and proteomics analyses of Holm oak (*Quercus ilex* subsp. ballota [Desf.] Samp.) responses to Phytophthora cinnamomi. *Plant Physiol. Biochem.* 71, 191–202. doi: 10.1016/j.plaphy.2013.06.030

Sherwood, P., Villari, C., Capretti, P., and Bonello, P. (2015). Mechanisms of induced susceptibility to Diplodia tip blight in drought-stressed Austrian pine. *Tree Physiol.* 35, 549–562. doi: 10.1093/treephys/tpv026

Shoresh, M., and Harman, G. E. (2008). The molecular basis of shoot responses of maize seedlings to *Trichoderma harzianum* T22 inoculation of the root: a proteomic approach. *Plant Physiol.* 147, 2147–2163. doi: 10.1104/pp.108.123810

Simova-Stoilova, L. P., López-Hidalgo, C., Sánchez-Lucas, R., Valero-Galván, J., Romero-Rodríguez, C., and Jorrín-Novo, J. V. (2018). Holm oak proteomic response to water limitation at seedling establishment stage reveals specific changes in different plant parts as well as interaction between roots and cotyledons. *Plant Sci.* 276, 1–13. doi: 10.1016/j.plantsci.2018.07.007

Simova-Stoilova, L. P., Romero-Rodríguez, M. C., Sánchez-Lucas, R., Navarro-Cerrillo, R. M., Medina-Aunon, J. A., and Jorrín-Novo, J. V. (2015). 2-DE proteomics analysis of drought treated seedlings of *Quercus ilex* supports a root active strategy for metabolic adaptation in response to water shortage. *Front. Plant Sci.* 6:627. doi: 10.3389/fpls.2015.00627

Solla, A., Aguín, O., Cubera, E., Sampedro, L., Mansilla, J. P., and Zas, R. (2011). Survival time analysis of *Pinus pinaster* inoculated with *Armillaria ostoyae*: genetic variation and relevance of seed and root traits. *Eur. J. Plant Pathol.* 130, 477–488. doi: 10.1007/s10658-011-9767-5

Starcher, B. (2001). A ninhydrin-based assay to quantitate the total protein content of tissue samples. *Anal. Biochem.* 292, 125–129. doi: 10.1006/abio.2001.5050

Strasser, R. J., Srivastava, A., and Tsimilli-Michael, M. (2000). "The fluorescence transient as a tool to characterize and screen photosynthetic samples," in *Probing Photosynthesis: Mechanisms, Regulation and Adaptation*, eds M. Yunus, U. Pathre, and P. Mohanty (London: Taylor and Francis), 445–483.

Sunkar, R., Bartels, D., and Kirch, H. H. (2003). Overexpression of a stress-inducible aldehyde dehydrogenase gene from *Arabidopsis thaliana*

in transgenic plants improves stress tolerance. *Plant J.* 35, 452–464. doi: 10.1046/j.1365-313x.2003.01819.x

Surová, D., Ravera, F., Guiomar, N., Sastre, R. M., and Pinto-Correia, T. (2018). Contributions of iberian silvo-pastoral landscapes to the well-being of contemporary society. *Rangel. Ecol. Manag.* 71, 560–570. doi: 10.1016/j.rama.2017.12.005

Teshome, D. T., Zharare, G. E., and Naidoo, S. (2020). The threat of the combined effect of biotic and abiotic stress factors in forestry under a changing climate. *Front. Plant Sci.* 11:601009. doi: 10.3389/fpls.2020.601009

Thayumanavan, B., and Sadasivam, S. (1984). Physicohemical basis for the preferential uses of certain rice varieties. *Plant Foods Hum. Nutr.* 34, 253–259.

Tola, A. J., Jaballi, A., Germain, H., and Missihoun, T. D. (2021). Recent development on plant aldehyde dehydrogenase enzymes and their functions in plant development and stress signaling. *Genes* 12:51. doi: 10.3390/genes12010051

Valero-Galván, J., González-Fernández, R., Navarro-Cerrillo, R. M., Gil-Pelegrín, E., and Jorrín-Novo, J. V. (2013). Physiological and proteomic analyses of drought stress response in holm oak provenances. *J. Proteome Res.* 12, 5110–5123. doi: 10.1021/pr400591n

Valero-Galván, J. V., Valledor, L., Cerrillo, R. M. N., Pelegrín, E. G., and Jorrín-Novo, J. V. (2011). Studies of variability in Holm oak (*Quercus ilex* subsp. ballota [Desf.] Samp.) through acorn protein profile analysis. *J. Proteomics* 74, 1244–1255. doi: 10.1016/j.jprot.2011.05.003

Viles, F. J., and Silverman, L. (1949). Determination of starch and cellulose with anthrone. *Anal. Chem.* 21, 950–953. doi: 10.1021/ac60032a019

Vivas, M., Zas, R., and Solla, A. (2012). Screening of Maritime pine (*Pinus pinaster*) for resistance to *Fusarium circinatum*, the causal agent of Pitch Canker disease. *Forestry* 85, 185–192. doi: 10.1093/forestry/cpr055

Wang, W., Vignani, R., Scali, M., and Cresti, M. (2006). A universal and rapid protocol for protein extraction from recalcitrant plant tissues for proteomic analysis. *Electrophoresis* 27, 2782–2786. doi: 10.1002/elps.200500722

Yu, T. S., Lue, W. L., Wang, S. M., and Chen, J. (2000). Mutation of *Arabidopsis* plastid phosphoglucose isomerase affects leaf starch synthesis and floral Initiation. *Plant Physiol.* 123, 319–326. doi: 10.1104/pp.123.1.319

Zhu, D., Luo, F., Zou, R., Liu, J., and Yan, Y. (2021). Integrated physiological and chloroplast proteome analysis of wheat seedling leaves under salt and osmotic stresses. *J. Proteomics* 234:104097. doi: 10.1016/j.jprot.2020.104097

Conflict of Interest: The authors declare that the research was conducted in the absence of any commercial or financial relationships that could be construed as a potential conflict of interest.

Publisher's Note: All claims expressed in this article are solely those of the authors and do not necessarily represent those of their affiliated organizations, or those of the publisher, the editors and the reviewers. Any product that may be evaluated in this article, or claim that may be made by its manufacturer, is not guaranteed or endorsed by the publisher.

frontiers in Plant Science

ORIGINAL RESEARCH
published: 26 August 2021
doi: 10.3389/fpls.2021.672855

Modeling Climate Impacts on Tree Growth to Assess Tree Vulnerability to Drought During Forest Dieback

*Cristina Valeriano[1,2], Antonio Gazol[1], Michele Colangelo[1,3], Ester González de Andrés[1] and J. Julio Camarero[1]**

[1] Instituto Pirenaico de Ecología (IPE-CSIC), Zaragoza, Spain, [2] Departamento de Sistemas Naturales e Historia Forestal, Universidad Politécnica de Madrid, Madrid, Spain, [3] School of Agricultural, Forest, Food and Environmental Sciences, University of Basilicata, Potenza, Italy

Forest dieback because of drought is a global phenomenon threatening particular tree populations. Particularly vulnerable stands are usually located in climatically stressing locations such as xeric sites subjected to seasonal drought. These tree populations show a pronounced loss of vitality, growth decline, and high mortality in response to extreme climate events such as heat waves and droughts. However, dieback events do not uniformly affect stands, with some trees showing higher symptoms of drought vulnerability than other neighboring conspecifics. In this study, we investigated if trees showing different vulnerabilities to dieback showed lower growth rates (Grs) and higher sensitivities to the climate in the past using dendroecology and the Vaganov-Shashkin (VS) process-based growth model. We studied two *Pinus pinaster* stands with contrasting Grs showing recent dieback in the Iberian System, north-eastern Spain. We compared coexisting declining (D) and non-declining (ND) trees with crown defoliation values above and below the 50% threshold, respectively. The mean growth rate was lower in D than in ND trees in the two stands. The two vigor classes showed a growth divergence prior to the dieback onset and different responsiveness to climate. The ND trees were more responsive to changes in spring water balance and soil moisture than D trees, indicating a loss of growth responsiveness to the climate in stressed trees. Such an interaction between water availability and vigor was reflected by the VS-model simulations, which provided evidence for the observation that growth was mainly limited by low soil moisture in both sites. Such an interaction between water availability and vigor was reflected by the VS-model simulations, which provided evidence for the observation that growth was mainly limited by low soil moisture in both sites. The presented comparisons indicated different stand vulnerabilities to drought contingent on-site conditions. Further research should investigate the role played by environmental conditions and individual features such as access to soil water or hydraulic traits and implement them in process-based growth models to better forecast dieback.

Keywords: climate warming, dendroecology, die-off, growth decline, process-based growth model, *Pinus pinaster*, tree rings

OPEN ACCESS

Edited by:
Ignacio García-González, University of Santiago de Compostela, Spain

Reviewed by:
Martina Pollastrini, University of Florence, Italy
Vladimir V. Shishov, Siberian Federal University, Russia

***Correspondence:**
J. Julio Camarero
jjcamarero@ipe.csic.es

Specialty section:
This article was submitted to Functional Plant Ecology, a section of the journal Frontiers in Plant Science

Received: *10 March 2021*
Accepted: *02 August 2021*
Published: *26 August 2021*

Citation:
Valeriano C, Gazol A, Colangelo M, González de Andrés E and Camarero JJ (2021) Modeling Climate Impacts on Tree Growth to Assess Tree Vulnerability to Drought During Forest Dieback. Front. Plant Sci. 12:672855. doi: 10.3389/fpls.2021.672855

INTRODUCTION

In the last decades, accelerated climate warming has caused a reduction in soil moisture, thereby exacerbating drought stress (Trenberth et al., 2014). Warmer and drier conditions have led to hotter droughts, which negatively impact forests worldwide and subsequently cause forest dieback (Allen et al., 2010, 2015). Such a loss in tree vigor is characterized by crown defoliation and increased mortality rates (Carnicer et al., 2011; Camarero et al., 2015a). Therefore, there is a deep concern for how the forecasted climate warming can expand forest dieback events, thus leading to a weakening of the terrestrial carbon sink and reducing the ability of forests to mitigate climate change (Anderegg et al., 2013). Climate-driven forest dieback is expected to increase in extent and severity in climate-change hotspots such as the Mediterranean Basin region, where seasonal changes in water availability limit tree growth and forest productivity (Vicente-Serrano et al., 2014; Gazol et al., 2018). In this region, climate models have forecasted increases in the frequency and intensity of hotter droughts during the 21st century (Giorgi and Lionello, 2008).

A better understanding of forest dieback processes is needed to identify their climatic causes and ascertain why some individuals are more vulnerable to drought stress than other conspecific, neighboring individuals (McDowell et al., 2008, 2011). Specifically, individual vulnerability may be related to site differences (e.g., soil depth) or intrinsic tree traits such as growth rates (Grs) (Pedersen, 1998). Different studies have found low Grs preceding dieback or tree death (Cailleret et al., 2017) while trying to extract early-warning signals of those radial-growth series (Camarero et al., 2015a; Cailleret et al., 2019). In conifers, declining (D) trees often showed low Grs prior to tree death, and this was associated with hydraulic failure caused by drought and xylem embolism (Choat et al., 2012, 2018; Adams et al., 2017). These results suggest that vulnerability to drought depends on "legacy effects" due to the cumulative impacts of climate stress on tree growth and vigor (Anderegg et al., 2015; Kannenberg et al., 2020).

Long-term, radial growth data allowed the reconstruction of how trees react to successive droughts and respond to such through changes in vigor expressed by differential leaf shedding rates, growth reduction, or tree death (Dobbertin, 2005). Thus, in this study, we compared the Grs and responses to climate variability of trees showing different needle shedding patterns. To delve into the climatic constraints of radial growth dynamics, we used the process-based Vaganov-Shashkin (VS) growth model (VS model hereafter, Vaganov et al., 2006). We argued that mechanistic rather than correlative approaches based on growth models will allow a better understanding of drought-induced dieback and the mortality process (Hendrik and Cailleret, 2017). This mechanistic model determines daily radial Grs as a function of daily climatic conditions by explicitly accounting for non-linear relationships between climate and growth (Tychkov et al., 2019). Relatively simple simulation frameworks such as those provided by the VS model allow the understanding of the major climatic constraints of growth, which is a key question in dieback processes (Sánchez-Salguero et al., 2017, 2020).

In this study, we focused on *Pinus pinaster*, a Mediterranean pine species which exhibits strong variability in response to drought throughout its distribution range in the Western Mediterranean Basin related to local climate conditions and provenance variability (Bogino and Bravo, 2008; Vieira et al., 2009, 2013; Sánchez-Salguero et al., 2018). We hypothesized that: (i) declining (hereafter D) trees will show lower Grs than non-declining (hereafter ND) trees prior to the dieback onset, (ii) D trees will show a higher long-term vulnerability to drought than ND trees, i.e., the radial growth of D trees will be more negatively impacted by dry and warm conditions during the growing season, and (iii) the more pronounced sensitivity of growth to drought stress in D trees, inferred by using the VS model, will explain its preferential dieback.

MATERIALS AND METHODS

Study Site

Two different forests (Orera, Miedes) were studied in the central Iberian System, Aragón, north-eastern Spain (**Table 1**). These are two natural *P. pinaster* Ait. Stands that were subjected to light thinning in the past and now show recent canopy dieback and elevated mortality rates (after 2017), which may account for 22–35% of trees in some places (**Figure 1A**). The Orera site is located in steeper slopes (slope range 15–20°) than the Miedes site (slope range 0–5°). The understory of these forests is formed by *Quercus ilex* L., *Cistus laurifolius* L., and *Arctostaphylos uva-ursi* (L.) Spreng. The climatic conditions are the continental Mediterranean with low precipitation (Prec.) and strong temperature contrasts. The average annual temperature is 12°C, and the annual Prec. is 423 mm with a peak in spring and a secondary maximum in autumn. The period with a water deficit starts in June and may last until October (**Supplementary Figure 1**). The lithology of the zone is dominated by quartzites producing acid, rocky soils with sandy-loamy texture, and being relatively shallow (20–50 cm).

Sampling and Growth Chronologies Building

Sampling was done in 2019 and 2020. We measured the diameter at 1.3 m (Dbh, diameter at breast height) and visually assessed the percent of crown defoliation in pairs of neighboring, dominant trees with different defoliations but similar Dbh (**Table 1**). We considered two groups of vigor based on crown defoliation following Camarero et al. (2015a): D trees with more than 50% of defoliation and ND trees with less than 50% defoliation (refer examples in **Figure 1A**).

We took two cores per tree at 1.3 m using Pressler increment borers (Haglöf Sweden, Sweden). In total, 67 trees were sampled (**Table 2**). The collected cores were air-dried and carefully sanded to distinguish the rings following standard procedures in dendrochronology (Fritts, 1976). Samples were then visually cross-dated, and tree-ring widths (RW) were measured with a 0.001 resolution using scanned images (resolution 2400 dpi) and the CDendro software (Larsson and Larsson, 2018). Tree age at 1.3 m was estimated by counting the number of rings in the cores

TABLE 1 | Main features of the study sites and sampled trees.

Site	Latitude N	Longitude W	Elevation (m)	Tree type	Dbh (cm)	Age at 1.3 m (years)	Defoliation (%)
Orera	41.31	1.45	884	ND	36.0 ± 1.7b	82 ± 3	4.9 ± 2.2a
				D	31.5 ± 1.2a	78 ± 3	94.8 ± 2.2b
Miedes	41.27	1.43	961	ND	26.1 ± 0.9b	92 ± 2	10.7 ± 1.7a
				D	21.3 ± 0.7a	88 ± 2	58.0 ± 3.1b

"ND" and "D" are non-declining and declining trees, respectively. Values are means ± SE. Different letters indicate significant ($p < 0.05$) differences between vigor classes within each site according to Mann–Whitney tests.

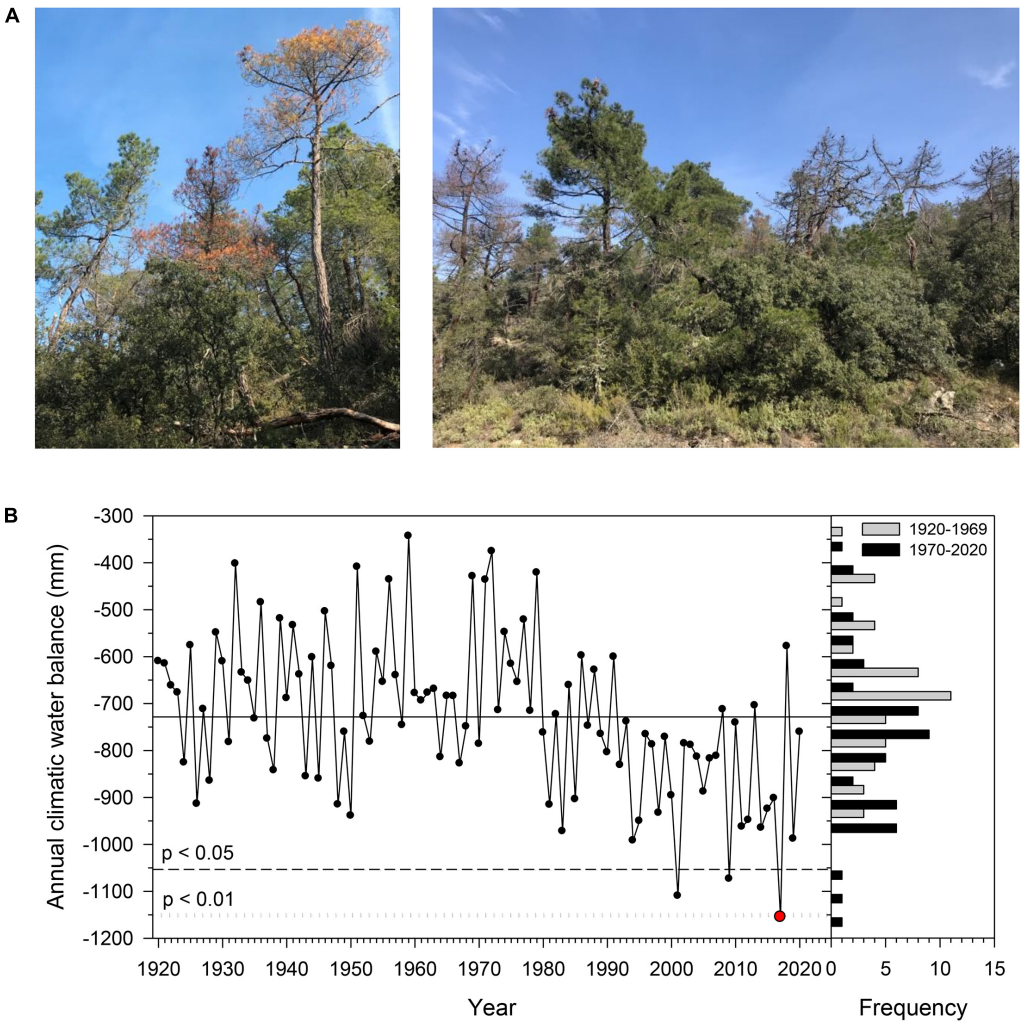

FIGURE 1 | (A) Views of non-declining (ND), declining (D), dying, and recently dead *Pinus pinaster* trees sampled in the Miedes study site. **(B)** Temporal variability of the annual climatic water balance (P-PET) according to the data from the Daroca meteorological station. The dashed and dotted lines show the threshold for considering water balances significantly lower than the long-term mean (period 1920–2020) at the 0.05 and 0.01 significance levels, respectively. The histograms show the distribution of the water balance for the compared 1920–1969 and 1970–2020 periods. The red symbol highlights the 2017 drought.

with pith or with curved inner rings. We also counted latewood intra-annual density fluctuations (IADFs) by inspecting the cores under a binocular microscope (Leyca, Wetzlar, Germany). The visual cross-dating was checked using the software COFECHA (Holmes, 1983).

The RW series were standardized and detrended. First, Friedman's super smoother functions with intermediate smooth values were fitted to individual RW series to obtain ring-width indices (RWI) that preserved high-frequency variability. Second, we removed most first-order autocorrelations by fitting autoregressive models. Third, we obtained the mean series of pre-whitened RWIs or chronologies using bi-weight robust means. These mean series were calculated for D and ND trees in the two study sites separately. These analyses were performed

TABLE 2 | Tree-ring width (RW) data and statistics, first-order autocorrelation (AR1), mean sensitivity (MS), and correlation with mean series of D and ND trees in the Orera and Miedes study sites.

Site	Tree type	No. trees	No. radii	Tree ring width (mm)	AR1	MS	Correlation with mean series
Orera	ND	14	26	1.15 ± 0.08	0.75 ± 0.02	0.40 ± 0.01a	0.82 ± 0.01b
	D	23	46	1.08 ± 0.06	0.69 ± 0.03	0.42 ± 0.01b	0.79 ± 0.01a
Miedes	ND	15	30	0.85 ± 0.04b	0.64 ± 0.03a	0.43 ± 0.01a	0.81 ± 0.01b
	D	15	30	0.73 ± 0.03a	0.74 ± 0.01b	0.46 ± 0.01b	0.73 ± 0.01a

"ND" and "D" are non-declining and declining trees, respectively. Values are means ± SE for the common period 1930–2019. Different letters indicate significant ($p < 0.05$) differences between vigor classes according to Mann–Whitney tests.

using the package dplR (Bunn, 2008) in the R statistical package (R Core Team, 2020). We calculated the Expressed Population Signal (EPS) and the mean interseries correlation (rbar) to assess the coherence and replication of the resulting series (Wigley et al., 1984). We considered the period 1930–2019 with EPS > 0.85 to be well replicated. The rbar was calculated for 20-year intervals that shifted every year.

Climate Data

Climate data were obtained at daily and monthly resolution from the Daroca meteorological station (41°06′54″N, 1°25′0″W, 782 m a.s.l.), which is located 18 km away from the sampling sites. The data series consisted of daily mean temperature (Tm), maximum temperature (Tx), minimum temperature (Tn), and Prec. for the period 1920–2020. Additionally, seasonal Tm and total Prec. were calculated for winter (December to February), spring (March to May), summer (June to August), and autumn (September to November). We also obtained 1.25°-gridded, monthly values of 1-m soil moisture for the period 1970–2016 from the European Centre for Medium-Range Weather Forecasts (ECMWF) Reanalysis (ERA)-Interim reanalysis (Dee et al., 2011). In addition, we also calculated the climatic water balance or difference between Prec. and potential evapotranspiration (P–PET). The PET was calculated using the FAO-56 Penman-Monteith equation (Allen et al., 1998).

VS Growth Model

We focused on inter-annual Grs and calibrated and validated observed series of RW indices by comparing them with simulated series (Tumajer et al., 2017). The VS model (VS-oscilloscope ver.1.362) was used for modeling the Miedes and Orera RWI series of D and ND trees. The VS model is a process-based growth model of intermediate complexity that has been widely applied and validated in conifers (refer, among others, Vaganov et al., 2006; Touchan et al., 2012; Shishov et al., 2016; He et al., 2017; Popkova et al., 2018; Tychkov et al., 2019; Tumajer et al., 2021). The model simulates daily Grs focusing on xylogenesis (enlargement, division, and differentiation of tracheids) and considering the data daily values of air temperature, Prec., and radiation as input. The model parameters defined the integrated Gr and the relative GRs due to soil moisture (Gr_W) or temperature limitations (Gr_T). During the year, days were classified according to the main climatic limitations of growth as: temperature – ($Gr_T < Gr_W$) or moisture-limited ($Gr_W < Gr_T$) and optimal ($Gr_M = Gr_T = 1$).

We used data from daily climate variables (air temperature, Prec., radiation) and the standard RWI series as input data. In total, 18 parameters were used to calibrate the model (refer a description of the model and parameters in **Supplementary Table 1**). The study period was 1930−2019, and it was divided into two sub-periods (1930−1969 and 1970−2019) to calibrate and verify the model predictions, respectively (Cook and Kairiukstis, 1990). The model was adjusted by modifying the parameters until the correlation between the four observed and predicted RWI series reached maximum values. The degree of adjustment between the observed and predicted RWI series was assessed using Pearson correlation coefficients (r) and the root mean squared error (Tychkov et al., 2019).

Statistical Analyses

All analyses were performed in R (R Core Team, 2020). We evaluated the trends of the daily and seasonal climatic variables (Tx, Tn, Prec. and P–PET) with the Mann–Kendall test (τ). Comparisons between years (climate data), variables of sites, or vigor classes (defoliation) were assessed using Mann–Whitney tests.

To assess the differences in growth variability between the two vigor groups, pointer years (Cropper, 1979) and resilience components (Lloret et al., 2011) were calculated using the R package PointRes (van der Maaten-Theunissen et al., 2015). Positive and negative pointer years were calculated considering a 7-year window size, a 0.75 growth deviation, and a minimum percentage of 75% of trees displaying positive or negative event years. Then, the resilience components proposed by Lloret et al. (2011) were calculated using the standard RWI series. We selected the four most severe droughts occurring after the wet-cool 1970s (1983, 2001, 2009, and 2015) because the annual water balance was below the mean in most years of the 1980−2020 period (**Figure 1B**). We considered a 3-year window for pre- and post-disturbance (drought) periods. The resistance index was the ratio between RWIs during drought and the 3-year previous period, and the recovery index was the ratio between the 3-year post-drought period and the drought RWI values. Finally, the resilience index was the ratio between the 3-year RWI values after and before the drought. We compared the individual values of the three resilience indices (resistance, recovery, and resilience) between ND and D trees using Mann–Whitney tests.

Climate-growth relationships were assessed by calculating bootstrapped Pearson correlations between monthly climatic parameters and the mean residual RWI series for the period

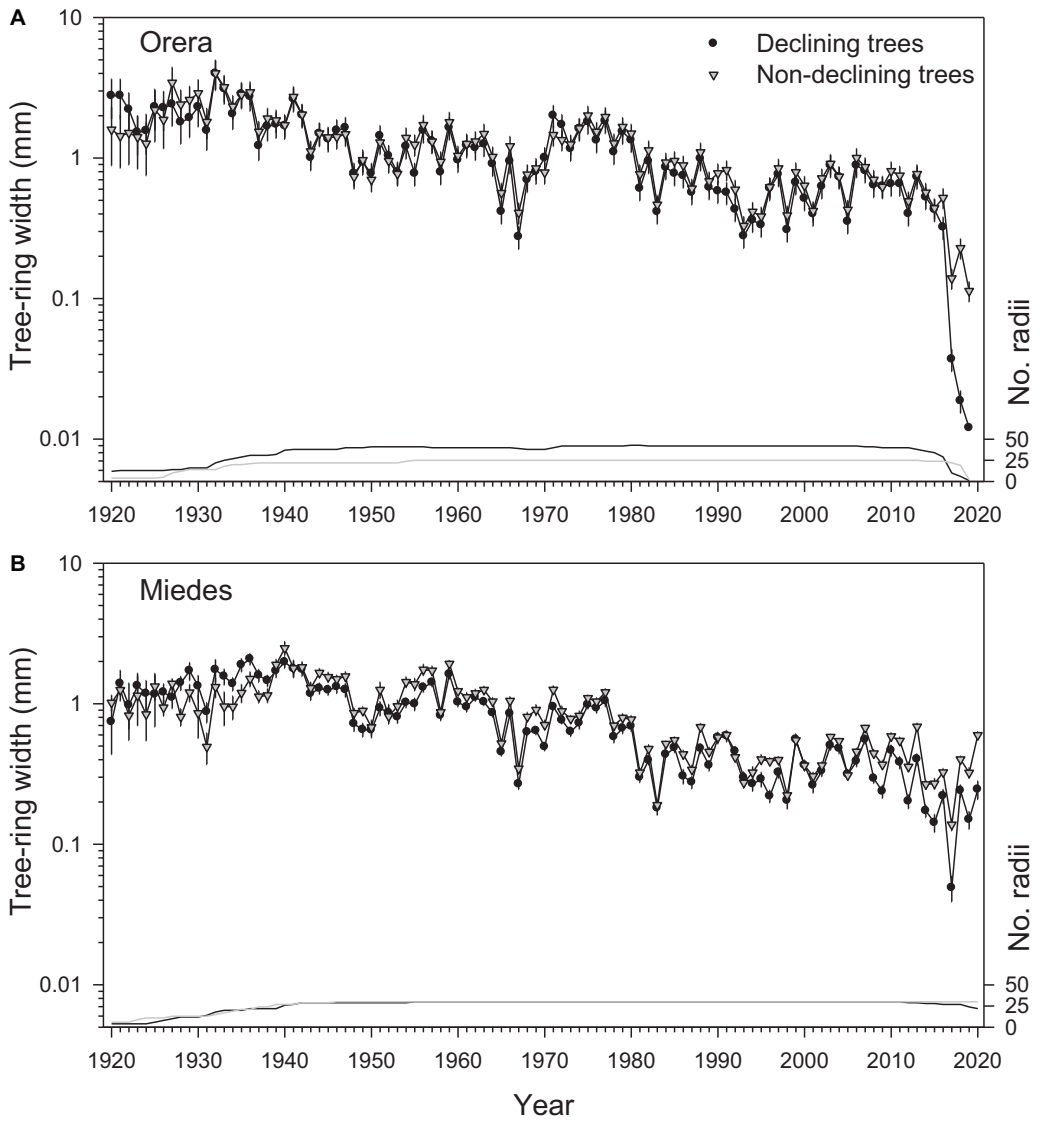

FIGURE 2 | Long-term radial-growth patterns of D (black circles) and ND (gray triangles) trees in the **(A)** Orera and **(B)** Miedes study sites. Values are means SE (note the logarithmic scales in the left *Y*-axis). The number of measured radii (lines) is shown in the right *Y*-axis.

1930–2019. Monthly Tx, Tn, and water balance from the previous September to the current September were included in the windows of analysis. To assess the changes through time in climate-growth associations we also calculated the moving climate-growth relationships for selected climate variables considering the 30-year moving intervals that shifted every year from 1930 to 2019. The calculations were performed for ND and D trees using the R package Treeclim (Zang and Biondi, 2015).

We fitted generalized additive mixed models (GAMMs; Wood, 2017) to study the temporal trends in simulated daily Grs using vigor class and date (DOY, day of year) as explanatory variables. The year was used as a random factor, and a first-order autocorrelation structure (AR1) was introduced to account for temporal autocorrelations within each year. Separate analyses were also performed for the two sub-periods (1930−1969 and 1970−2019). Finally, we fitted GAMMs considering the interaction between the spring (March, April, and May) water balance (P − PET) and DOY to test if the variation in Gr differed between years with different water availabilities. An AR1 was again used to account for temporal autocorrelations. The GAMMs were fitted using the mgcv package (Wood, 2011), and the visreg package (Breheny and Burchett, 2017) was used to visualize regression graphs.

RESULTS

Seasonal Climate Trends and Variability

The mean climatic water balance for the period 1920–2020 was −728 mm with a SD of 167 mm. This variable has shown a

TABLE 3 | Climate-growth relationships of D and ND trees in the Orera and Miedes sites.

Climate variable	Site	Tree type	Month											
			S^{t-1}	O^{t-1}	N^{t-1}	D^{t-1}	J	F	M	A	M	J	J	A	S
Mean maximum temperature (Tx)	Orera	ND	0.02	0.03	−0.04	0.13	−0.12	−0.11	**−0.22**	−0.07	**−0.29**	**−0.21**	−0.13	0.02	0.03
		D	0.05	0.01	−0.06	0.13	**−0.16**	−0.03	−0.12	−0.03	**−0.28**	−0.15	−0.09	−0.06	0.06
	Miedes	ND	−0.07	−0.02	−0.02	0.06	−0.07	−0.10	**−0.25**	−0.04	**−0.31**	**−0.35**	−0.15	−0.07	−0.02
		D	−0.08	−0.08	−0.06	0.06	−0.11	−0.03	**−0.27**	−0.05	**−0.31**	**−0.25**	−0.06	0.01	0.11
Mean minimum temperature (Tn)	Orera	ND	−0.08	−0.08	0.12	0.03	0.18	0.09	0.04	0.17	**−0.27**	**−0.20**	−0.09	−0.15	0.18
		D	−0.02	−0.08	0.15	0.05	0.13	0.11	0.06	0.15	**−0.27**	−0.12	−0.06	−0.14	0.16
	Miedes	ND	−0.09	−0.04	0.17	0.04	**0.20**	0.20	0.07	0.06	**−0.19**	**−0.33**	−0.08	−0.09	−0.04
		D	−0.06	−0.11	0.12	0.04	0.12	**0.19**	0.10	0.11	**−0.23**	**−0.29**	−0.02	−0.12	0.17
Water balance (P-PET)	Orera	ND	−0.06	−0.02	−0.01	0.13	**0.24**	**0.25**	**0.26**	**0.35**	**0.38**	**0.22**	0.21	0.11	**0.23**
		D	−0.08	0.05	0.06	0.15	**0.24**	**0.23**	**0.24**	**0.36**	**0.39**	0.17	0.16	0.15	0.18
	Miedes	ND	0.05	−0.01	−0.01	0.14	0.15	**0.26**	**0.31**	**0.25**	**0.45**	**0.32**	0.17	0.15	**0.20**
		D	0.08	−0.01	−0.01	0.10	0.09	**0.27**	**0.30**	**0.29**	**0.40**	**0.26**	0.12	0.05	0.14

The values are Pearson correlation coefficients calculated by relating the mean series of ring-width indices (RWI) and monthly values of maximum and Tns with water balance. ND and D are non-declining and declining trees, respectively. Correlations were calculated from the prior ($^{t-1}$) to the current September. Significant correlation coefficients are shown as bold values.

negative and significant trend during that period ($\tau = -0.31$, $p < 0.001$) with a mean rate of change of −2.44 mm year^{-1} (**Supplementary Table 2**). The 2017 annual water balance (−1,155 mm) was significantly lower than the long-term mean at the 0.01 significance level due to very low spring (−274 mm) and autumn water balances (−343 mm) (**Figure 1B** and **Supplementary Figure 2**). These two low values correspond to the minimum values of the long-term record for their respective seasons (standardized anomalies of −1.9 and −2.29 in spring and autumn, respectively). The mean Txs of the four seasons significantly increased during the last 100 years, especially in summer ($\tau = -0.41$, $p < 0.001$; **Supplementary Figure 3**).

Growth, Defoliation, and Resilience Indices

The diameter breast height at 1.3 m (Dbh) of D trees was smaller than ND in both sites (**Table 2**). In Miedes, the RW was also significantly lower in D than in ND trees, despite both vigor classes showing similar ages. However, ND trees showed higher first-order autocorrelation and mean sensitivity than D trees in the same site. The ND trees showed a higher mean correlation with the mean RW series than D trees in both study sites (**Table 2**). The mean defoliation rate of sampled trees was significantly lower (Mann–Whitney $U = 389$, $p = 0.022$) in Miedes (mean ± SE, 34.3 ± 4.7%) than in Orera (61.7 ± 7.3%). We observed very high (>90%) defoliation rates in 6.7 and 47.4% of trees sampled in Miedes and Orera, respectively, albeit the growth rate was lower in Miedes.

The long-term pattern of radial growth variability was similar between D and ND trees (**Figure 2** and **Supplementary Figure 4**). Within each site, both ND and D mean series of RWI were significantly correlated during the 1930 − 2019 period (Miedes, $r = 0.79$; Orera, $r = 0.94$; $p < 0.001$ in both cases). Similar strong associations were found between sites either for ND ($r = 0.66$) or D ($r = 0.68$) trees. The coherence in the year-to-year growth variability between sites and vigor classes suggests a similar response to climatic constraints such as water deficits.

We found a clear growth divergence between ND ad D trees in both sites due to a growth reduction of D trees after the 2017 severe drought and after 2008 (about 12 years before the dieback started) in Miedes (**Figure 2**). Trees from the Orera site also presented a reduction in the mean interseries correlation of D trees after the 1990s, which was subsequently reversed in the 2010s (**Supplementary Figure 5**).

The pointer years (Cropper values) were similar in magnitude and direction between D and ND trees (**Supplementary Figure 6**). The most negative pointer years coincided with dry years (e.g., 1983, 2001, 2009, 2015, and 2017). The latewood IADFs were usually observed during wet-cool years (e.g., 1952, 1961, and 1970s) with similar yearly frequencies in D and ND trees (**Supplementary Figure 7**). However, the D trees tended to form fewer IADFs after the 1980s as the climate warmed and dried and their Grs decreased.

The resilience indices were similar between D and ND trees in both sites apart from the 2001 recovery index with lower values in ND trees in the Orera site and the 2009 resistance index

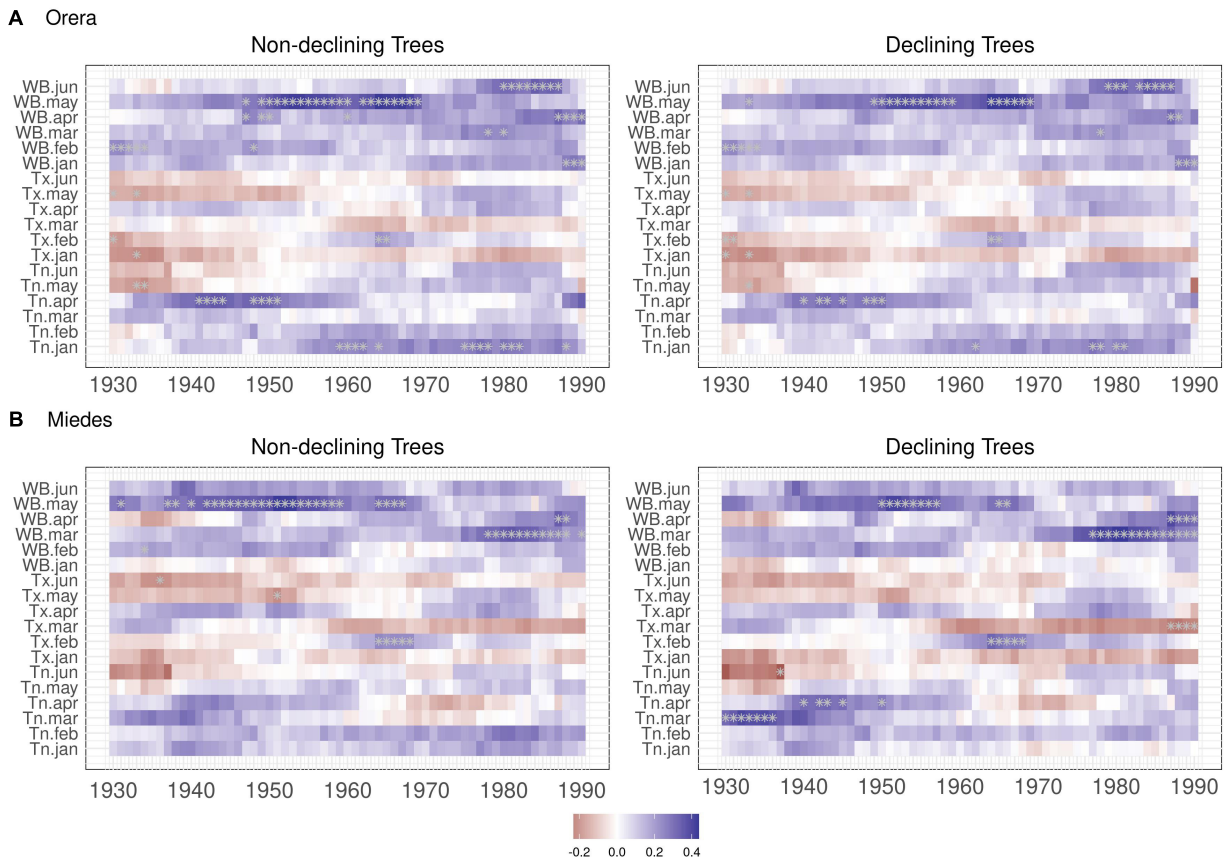

FIGURE 3 | Moving climate-growth correlations of ND and D trees in the **(A)** Orera and **(B)** Miedes study sites. Plots show selected climate variables and their relationships with RWI considering 30-year moving intervals that shifted every year from 1930 to 2019. Values are plotted for the first year of each 30-year interval. Asterisks indicate significant ($p < 0.05$) correlations.

with higher values in ND trees from Miedes (**Supplementary Figure 8**).

In both sites, crown defoliation and recent growth rate (mean RW of the last formed 5 years) were inversely related (**Supplementary Figure 9**).

Growth Responses to Climate: The Importance of Water Balance

Growth was enhanced by cool and wet conditions in May and June (**Table 3**). High water balance values from January to April and September were associated with higher Grs. In Miedes, high Tns from January to February improved growth. The growth responsiveness to climate was similar between ND and D trees apart from the positive influence of September water balance on the growth of ND trees in both sites. These relationships agree with the positive associations found between growth and spring to early summer soil moisture, which were stronger for ND than for D trees in Miedes (**Supplementary Figure 10**).

The moving climate-growth correlations showed that March–April water balance is gaining importance as a major driver of growth in Miedes. Despite this, the May water balance is losing relevance, whereas January–April and June water balances are becoming significant drivers of growth in Orera (**Figure 3**). These changes suggest shifts in the growing season, which we investigated using the VS model.

Shifting Climatic Limitations of Tree Growth

The simulated and observed RWI series of the calibration and verification periods were significantly correlated, indicating robust models (**Supplementary Table 3** and **Supplementary Figure 11**). The Gr values peaked from early May to mid-June (**Figure 4**). A second autumn peak (September) was also observed, suggesting a facultative bimodal growth pattern. The GAMMs showed lower Grs of D than ND trees in both study sites and periods (**Table 4** and **Figure 4**).

Grs increased in years with higher spring water balance. We observed shifts in climatic limitations of growth with optimal conditions in wet-cool periods (e.g., the 1970s) and a trend toward higher importance of water balance and soil moisture as constraints of growth (**Figure 5**). This can be observed by comparing wet-cool with dry-warm periods in the most recent decades (the 2000s to 2010s), which shows simulated

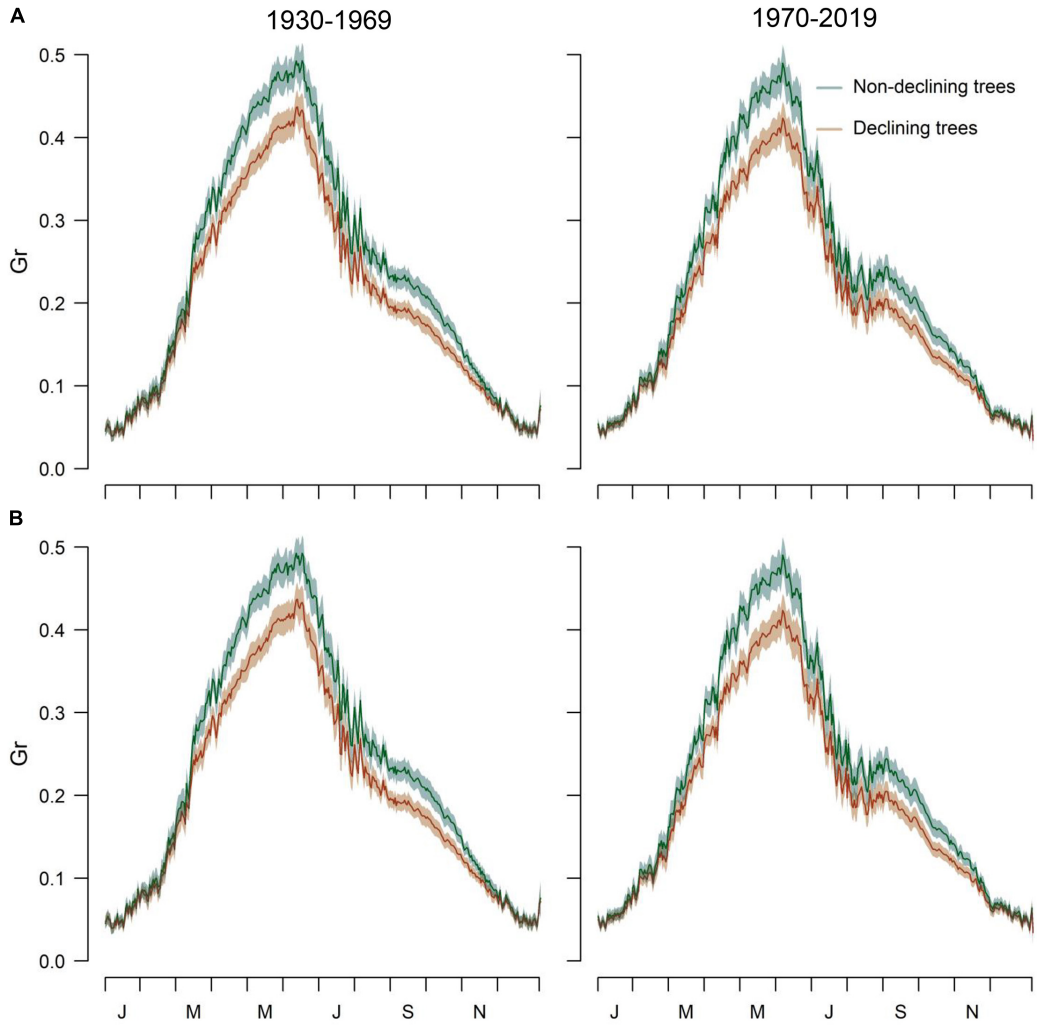

FIGURE 4 | Simulated Grs of the VS model obtained by relating daily climate data and mean series of RWI of D and ND trees in the **(A)** Orera and **(B)** Miedes study sites considering the periods 1930–1969 and 1970–2019. The daily Gr values are means ± SD.

TABLE 4 | Results of the generalized additive mixed models (GAMMs) fitted to study the simulated growth variability (Gr) in *P. pinaster* D and ND in two consecutive periods (1930−1969 and 1970−2019) in Orera and Miedes sites.

Site	Period	Tree type	Edf	*F*	*t*	R^2
Orera	1930−1969	ND	8.68	509.7**	10.35**	0.63
		D	8.57	385.1**		
	1970−2019	ND	8.72	456.7**	9.91**	0.66
		D	8.60	340.3**		
Miedes	1930−1969	ND	8.68	510.9**	10.41**	0.63
		D	8.57	385.1**		
	1970−2019	ND	8.72	457.4**	9.97**	0.59
		D	8.60	340.1**		

*For each model, the degrees of freedom (Edf) and F values associated with the smooth parameter (DOY, day of the year) and their interaction with tree vigor (ND and D trees) are shown. In addition, the significance of the t statistic comparing vigor classes and the R^2 of the model are presented. Significant values ($P < 0.01$) are indicated with **.*

Grs below the soil moisture (sm) threshold for growth (W3, **Figure 6**). There was a significant interaction of spring water balance and DOY on Grs in both sites, indicating a shift in the climatic limitations of growth related to lower soil moisture availability due to a more negative water balance (**Figures 1**, **7** and **Supplementary Table 4**).

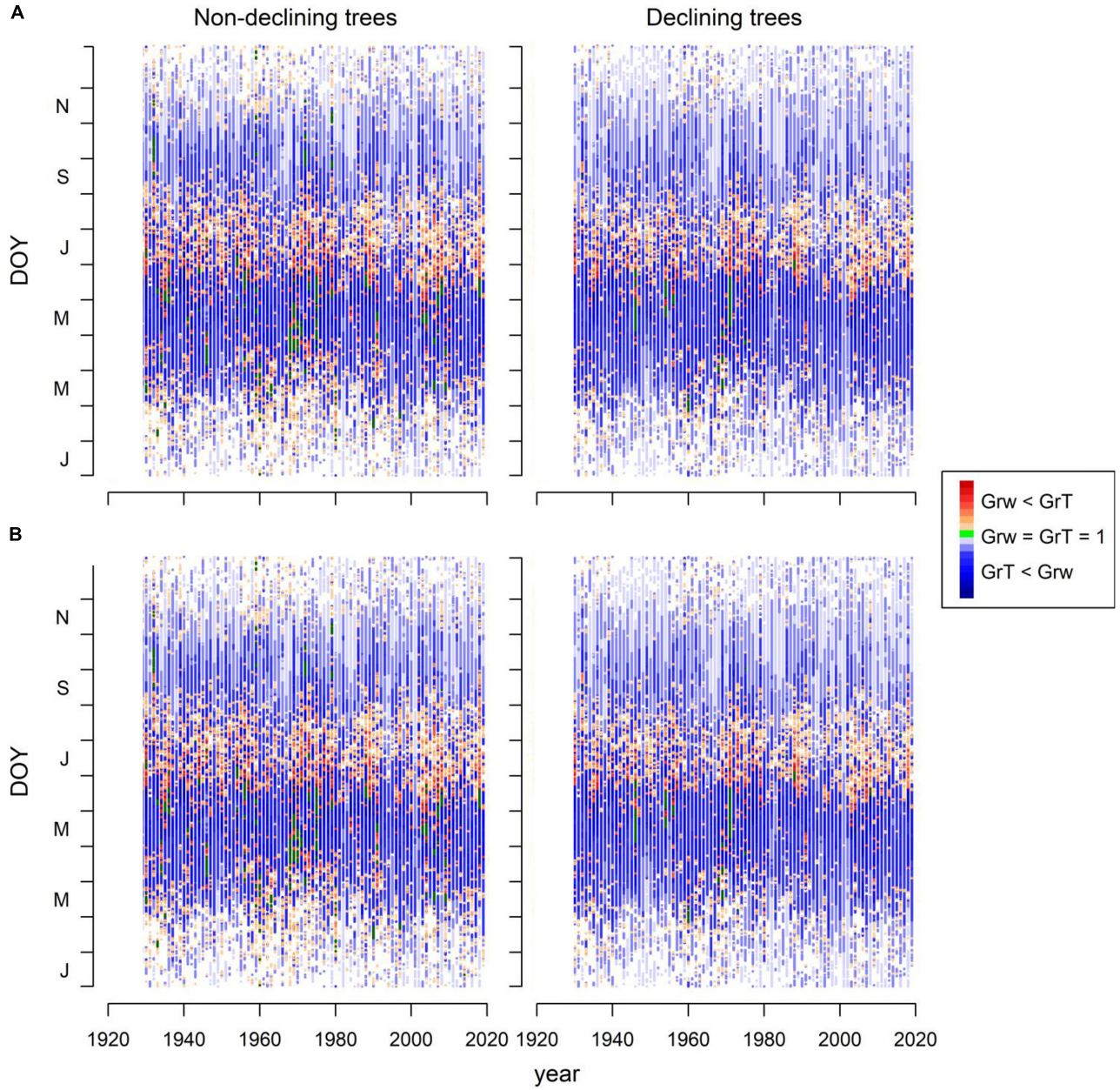

FIGURE 5 | Simulated radial growth rates (Gr) based on the fits of the VS model to mean series of RWI of ND and D trees in the Orera **(A)** and Miedes **(B)** study sites. The graphs show the growth function (Gr) values for each day of the year (DOY, *Y*-axis) and considering the period 1930 – 2019 (*X*-axis). Plotted values are classified according to soil-moisture ($Gr_W < Gr_T$, orange-red symbols) or temperature limitation of growth ($Gr_T < Gr_W$, blue symbols). The green symbols indicate optimal growing conditions ($Gr_T = Gr_W = 1$).

DISCUSSION

The findings contribute to recent research showing how successive and hotter droughts lead to pervasive growth reductions (Cailleret et al., 2017; Camarero et al., 2018) and trigger dieback and mortality in Mediterranean *P. pinaster* forests (Gea-Izquierdo et al., 2019; Férriz et al., 2021). The presented results confirm the first hypothesis that Grs of D trees were lower than ND trees in at least one site (Miedes), but refute the idea of D trees being more vulnerable to drought stress unlike what has been found in other conifer species such as *Abies alba* (Camarero et al., 2015a). We found that the growth of ND and D trees was severely impacted by warm and dry spring conditions and that climate is warming and drying in the study area, with a record spring hot drought found in 2017. In Miedes, ND trees were more responsive to water availability than D trees as confirmed in the correlation analyses with soil moisture. In Miedes, the growth of D trees is uncoupling from

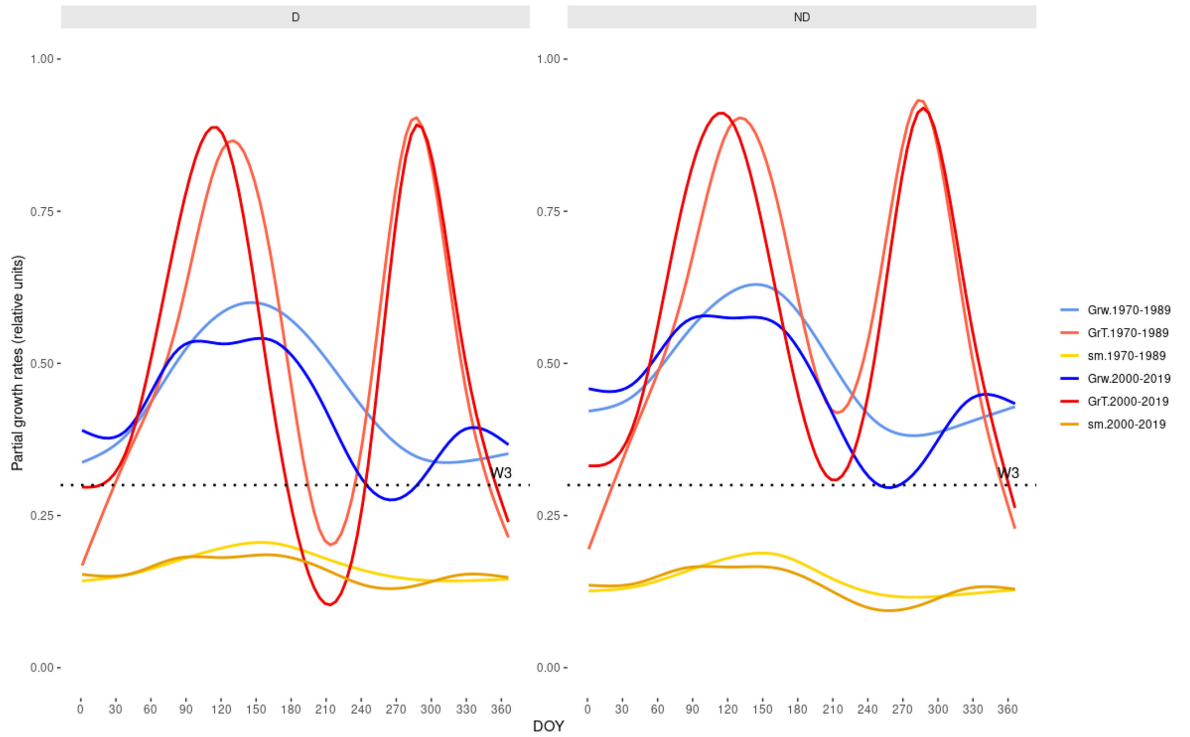

FIGURE 6 | Tree growth is becoming more limited by warmer and drier climate conditions according to the Vaganov-Shashkin (VS) model simulations. The plot shows the partial Grs driven by soil moiture (GrW) or temperture (GrT) limitations of growth, and depending on soil moisture (sm) during the year (*X*-axis shows DOY). We compared wet-cool (1970–1989, mean annual water balance –673 mm) and dry-warm (2000–2019, mean annual water balance –873 mm) periods in the case of the trees from the Miedes site. The W3 is the soil moisture threshold needed for growth (refer **Supplementary Table 1**).

climatic constraints, perhaps because they are presenting legacy or carryover effects (Anderegg et al., 2015) of previous droughts, thus impairing their post-drought recovery.

The growth loss of D trees was recent in Orera, as it started in 2017, but could be dated back to 2008 in Miedes, where ND trees showed higher responsiveness to water availability. The findings are in line with previous studies showing that *P. pinaster* radial growth is very dependent on sufficient water availability and elevated soil moisture from the prior winter to early summer (Bogino and Bravo, 2008; Camarero et al., 2015b). The study species is considered a drought-avoiding conifer (Picon et al., 1996) with rapid stomatal closure in response to mild-water stress which, thereby, reduces photosynthetic rates (Ripullone et al., 2007). These responses could explain the elevated rates of needle shedding observed in D trees in this study and elsewhere (Férriz et al., 2021). Such irreversible canopy defoliation could reflect a hydraulic failure in many shoots and impair carbon uptake leading to dieback (McDowell et al., 2008).

The sensitivity of xylogenesis to inter- and intra-annual changes in water availability is also reflected in its ability to form abundant latewood IADFs and modulate its xylogenesis in seasonally dry sites (Vieira et al., 2009, 2010, 2013). However, this xylem plasticity has limits. This would explain how the extremely hot 2017 drought triggered the recent dieback process. The results suggest that ND trees from Miedes grew more than their D conspecifics and were more sensitive to spring water deficits, which agrees with a recent study (Férriz et al., 2021). The different impacts of drought on conspecific individuals could be caused by differential vulnerabilities to xylem embolism related to greater vulnerabilities to xylem conduit implosion and/or a lower ability to store carbohydrates or show post-drought recovery in D trees (Gaylord et al., 2015; Savi et al., 2020). In contrast, tree-ring data, VS model simulations, and IADFs show that ND and D trees from Orera were similarly stressed by drought. For instance, growth divergence between both vigor classes was only apparent after the severe 2017 drought. The correlation between the mean series of these classes was higher than in Miedes, suggesting a strong coherence in growth between conspecifics regardless of recent defoliation. In Orera, ND trees also produced a low frequency of IADFs since the 1980s, suggesting a drought-constrained or a low ability to show bimodal patterns. Interestingly, the VS model indicated a higher bimodality in ND trees, which responded more to the September Prec. This bimodality was probably more evident during wet-cool periods (the 1960s and 1970s) when growing conditions were less stressful and more IADFs were produced. This different response to climate suggests the higher growth plasticity of ND trees in response to autumn Prec., but this should be further investigated. Differences in growth responsiveness to climate between the two study sites cannot be attributed to genetic origin (cf. Sánchez-Salguero et al., 2018) since they are separated by ca. 5 km, and the two stands belong to the same provenance. Stand structure does not seem

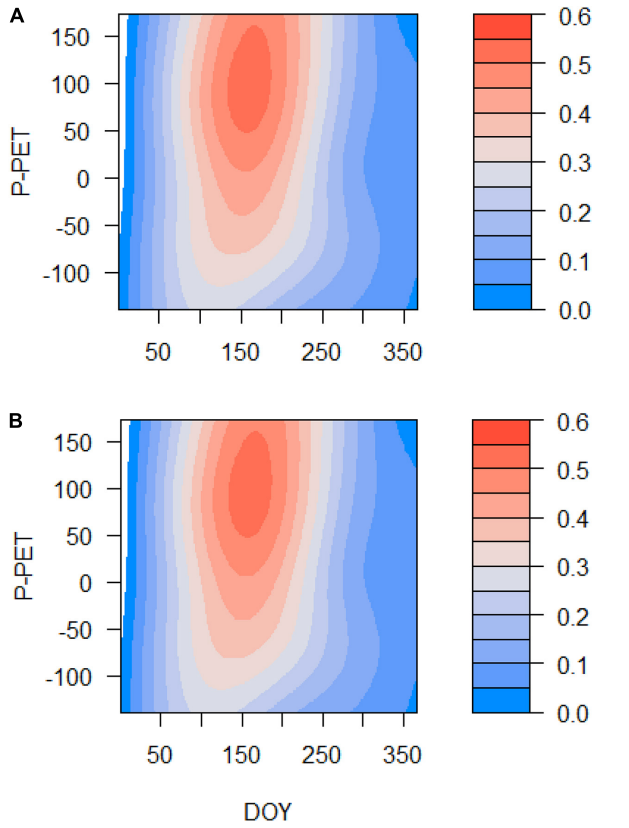

FIGURE 7 | Effects of the DOY, the spring water balance (P – PET, *Y*-axis), and their interaction on the simulated Gr (color scale) in the Orera **(A)** and Miedes **(B)** study sites. The analyses correspond to GAMMs fitted to Gr data for the period 1930–2019.

to explain these differences because, in both cases, we sampled open stands with low to mid densities (J. J. Camarero, personal observation) where competition for soil water was probably low. A potential factor explaining site-contingent responses or different vulnerabilities of neighboring trees may be related to the actual amount of water stored by soil, since Orera trees were growing on steeper slopes that may make them more stressed by warm and dry conditions. In contrast, D trees in Miedes could be growing on sites with shallow, rocky soils or showing intrinsic anatomic or physiological traits that reduce their drought resilience. We did not observe D, less vigorous trees showing significantly lower resilience to drought as has been observed for dying trees in many sites (DeSoto et al., 2020). However, only two vigor classes were considered in this study based on their contrasting crown defoliation. Further studies with larger samples allowing for a more complete classification of defoliation classes may be helpful to advance the understanding of the relationships between canopy defoliation and growth vigor in *P. pinaster*.

Process-based models have not been able to accurately predict drought-induced tree mortality (Hendrik and Cailleret, 2017; Choat et al., 2018), which limits the forecasting capacity of vegetation dynamics in a warmer and drier world. Physiological models explicitly consider hydraulic architecture and carbon allocation processes to simulate drought-induced dieback and tree mortality (Xu et al., 2013), but process-based models such as the VS model could be more easily parameterized to provide growth forecasts (Sánchez-Salguero et al., 2017; Sánchez-Salguero and Camarero, 2020). Such growth models could also be compared with retrospective analyses of hydraulic and carbon-use proxies obtained from RW, such as wood anatomical or isotope discrimination data (Gaylord et al., 2015; Pellizzari et al., 2016).

The modeling approach also has limitations, such as the relative simplicity of the VS model, which focused on carbon sinks (cambium activity) but did not consider physiological processes related to gas and water exchange and how they are linked to hydraulic failure (Plaut et al., 2012) as other more complex models do (Hendrik and Cailleret, 2017). The VS model simulates radial-Grs (RWI) with great accuracy but is not able to produce a series of absolute growth values (e.g., basal area increment), an output generated by other models dealing with carbon allocation (Li et al., 2014). Finally, the modeling framework uses input means and indexed growth series for D and ND trees. Despite this, more realistic approaches should deal with individual growth data to account for the huge growth variability among conspecific, coexisting trees. Such variabilities could be related to differences in soil features (e.g., depth, texture, and water holding capacity) or stand structure (e.g., tree-to-tree competition), which should be considered in further modeling exercises. Interestingly, some of the values used to parametrize the VS model, such as root depth, were realistic enough and produced reliable simulated Grs since *P. pinaster* forms most fine roots in the uppermost 40 cm of the soil in dry sites (Bakker et al., 2006).

CONCLUSION

We studied recent dieback events in two *P. pinaster* stands using a retrospective approach and the process-based VS model. Dieback was characterized by recent growth declines and crown defoliation, which were responses to prior spring droughts. Overall, ND trees presented higher Grs. However, the growth responses to climate were also contingent on on-site conditions, with long and short growth declines prior to the dieback onset in Miedes and Orera sites, respectively. The growth of ND trees from the Miedes sites responded more to water balance and soil moisture, suggesting that D trees from this site were chronically stressed as inferred for all trees from the Orera site. Process-based growth models should be more widely used and refined to characterize the mechanisms of drought-induced dieback and be used as prospective tools to forecast forest dynamics under warmer and drier climate scenarios.

DATA AVAILABILITY STATEMENT

The original contributions presented in the study are included in the article/**Supplementary Material**, further inquiries can be directed to the corresponding author.

AUTHOR CONTRIBUTIONS

CV led the manuscript writing and the sample analyses with contributions from JC and AG. All authors participated in field sampling and data collection, and contributed to the writing of the manuscript and approved its final version.

FUNDING

We acknowledge funding by project RTI2018-096884-B-C31 and by a FPI grant (ref. PRE2019-089800) to CV (Spanish Ministry of Science).

ACKNOWLEDGMENTS

We thank the personnel of the Aragón Govt. (forest technicians and guards) for facilitating the field sampling and providing all required permissions. We also thank the Spanish Climatic Agency (AEMET) for providing climatic data from the Daroca station.

SUPPLEMENTARY MATERIAL

The Supplementary Material for this article can be found online at: https://www.frontiersin.org/articles/10.3389/fpls.2021.672855/full#supplementary-material

REFERENCES

Adams, H. D., Zeppel, M. J., Anderegg, W. R., Hartmann, H., Landhäusser, S. M., Tissue, D. T., et al. (2017). A multi-species synthesis of physiological mechanisms in drought-induced tree mortality. *Nat. Ecol. Evol.* 1, 1285–1291. doi: 10.1038/s41559-017-0248-x

Allen, C. D., Breshears, D. D., and McDowell, N. G. (2015). On underestimation of global vulnerability to tree mortality and forest die off from hotter drought in the Anthropocene. *Ecosphere* 6, 1–55. doi: 10.1890/ES15-00203.1

Allen, C. D., Macalady, A. K., Chenchouni, H., Bachelet, D., McDowell, N., Vennetier, M., et al. (2010). A global overview of drought and heat-induced tree mortality reveals emerging climate change risks for forests. *For. Ecol. Manage.* 259, 660–684. doi: 10.1016/j.foreco.2009.09.001

Allen, R. G., Pereira, L. S., Raes, D., and Smith, M. (1998). *Crop Evapotranspiration: Guidelines for Computing Crop Requirements*. Irrigation and Drainage Paper No. 56. Rome: FAO.

Anderegg, W. R., Kane, J. M., and Anderegg, L. D. L. (2013). Consequences of widespread tree mortality triggered by drought and temperature stress. *Nat. Clim. Chang.* 3, 30–36. doi: 10.1038/nclimate1635

Anderegg, W. R., Schwalm, C., Biondi, F., Camarero, J. J., Koch, G., Litvak, M., et al. (2015). Pervasive drought legacies in forest ecosystems and their implications for carbon cycle models. *Science* 349, 528–532. doi: 10.1126/science.aab1833

Bakker, M. R., Augusto, L., and Achat, D. L. (2006). Fine root distribution of trees and understory in mature stands of maritime pine (*Pinus pinaster*) on dry and humid sites. *Plant Soil* 286, 37–51. doi: 10.1007/s11104-006-9024-4

Bogino, S. M., and Bravo, F. (2008). Growth response of *Pinus pinaster* Ait. To climatic variables in central Spanish forests. *Ann. For. Sci.* 65, 506–506. doi: 10.1051/forest:2008025

Breheny, P., and Burchett, W. (2017). Visualization of regression models using visreg. *R J.* 9, 56–71.

Bunn, A. G. (2008). A dendrochronology program library in R (dplR). *Dendrochronologia* 26, 115–124. doi: 10.1016/j.dendro.2008.01.002

Cailleret, M., Jansen, S., Robert, E. M., DeSoto, L., Aakala, T., Antos, J. A., et al. (2017). A synthesis of radial growth patterns preceding tree mortality. *Glob. Change Biol.* 23, 1675–1690. doi: 10.1111/gcb.13535

Cailleret, M., Vasilis, D., Steven, J., Robert, E. M. R., Aakala, T., Amoroso, M., et al. (2019). Early-warning signals of individual tree mortality based on annual radial growth. *Front. Plant Sci.* 19:1964. doi: 10.3389/fpls.2018.01964

Camarero, J. J., Gazol, A., Sangüesa-Barreda, G., Cantero, A., Sánchez-Salguero, R., Sánchez-Miranda, A., et al. (2018). Forest growth responses to drought at short- and long-term scales in Spain: squeezing the stress memory from tree rings. *Front. Ecol. Evol.* 6:9. doi: 10.3389/fevo.2018.00009

Camarero, J. J., Gazol, A., Sangüesa-Barreda, G., Oliva, J., and Vicente-Serrano, S. M. (2015a). To die or not to die: early warnings of tree dieback in response to a severe drought. *J. Ecol.* 103, 44–57. doi: 10.1111/1365-2745.12295

Camarero, J. J., Gazol, A., Tardif, J. C., and Conciatori, F. (2015b). Attributing forest responses to global-change drivers: limited evidence of a CO_2-fertilization effect in Iberian pine growth. *J. Biogeogr.* 42, 2220–2233. doi: 10.1111/jbi.12590

Carnicer, J., Coll, M., Ninyerola, M., Pons, X., Sánchez, G., and Peñuelas, J. (2011). Widespread crown condition decline, food web disruption, and amplified tree mortality with increased climate change-type drought. *Proc. Natl. Acad. Sci. U.S.A.* 108, 1474–1478. doi: 10.1073/pnas.1010070108

Choat, B., Brodribb, T. J., Brodersen, C. R., Duursma, R. A., López, R., and Medlyn, B. E. (2018). Triggers of tree mortality under drought. *Nature* 558, 531–539. doi: 10.1038/s41586-018-0240-x

Choat, B., Jansen, S., Brodribb, T. J., Cochard, H., Delzon, S., Bhaskar, R., et al. (2012). Global convergence in the vulnerability of forests to drought. *Nature* 491, 752–755. doi: 10.1038/nature11688

Cook, E. R., and Kairiukstis, L. A. (eds) (1990). *Methods of Dendrochronology: Applications in the Environmental Sciences*. Dordrecht: Kluwer. doi: 10.1007/978-94-015-7879-0

Cropper, J. P. (1979). Tree-ring skeleton plotting by computer. *Tree Ring Bull.* 39, 47–59.

Dee, D. P., Uppala, S. M., Simmons, A. J., Berrisford, P., Poli, P., Kobayashi, S., et al. (2011). The ERA-interim reanalysis: configuration and performance of the data assimilation system. *Q. J. R. Meteorol. Soc.* 137, 553–597. doi: 10.1002/qj.828

DeSoto, L., Cailleret, M., Sterck, F., Jansen, S., Kramer, K., Robert, E. M. R., et al. (2020). Low growth resilience to drought is related to future mortality risk in trees. *Nat. Commun.* 11:545. doi: 10.1038/s41467-020-14300-5

Dobbertin, M. (2005). Tree growth as an indicator of tree vitality and of tree reaction to environmental stress: a review. *Eur. J. For. Res.* 124, 319–333. doi: 10.1007/s10342-005-0085-3

Férriz, M., Martin-Benito, D., Cañellas, I., and Gea-Izquierdo, G. (2021). Sensitivity to water stress drives differential decline and mortality dynamics of three co-occurring conifers with different drought tolerance. *For. Ecol. Manage.* 486:118964. doi: 10.1016/j.foreco.2021.118964

Fritts, H. C. (1976). *Tree Rings and Climate*. London: Academic Press.

Gaylord, M. L., Kolb, T. E., and McDowell, N. G. (2015). Mechanisms of piñon pine mortality after severe drought: a retrospective study of mature trees. *Tree Physiol.* 35, 806–816. doi: 10.1093/treephys/tpv038

Gazol, A., Camarero, J. J., Vicente-Serrano, S. M., Sánchez-Salguero, R., Gutiérrez, E., de Luis, M., et al. (2018). Forest resilience to drought varies across biomes. *Glob. Change Biol.* 24, 2143–2158. doi: 10.1111/gcb.14082

Gea-Izquierdo, G., Férriz, M., García-Garrido, S., Aguín, O., Elvira-Recuenco, M., Hernandez-Escribano, L., et al. (2019). Synergistic abiotic and biotic stressors explain widespread decline of *Pinus pinaster* in a mixed forest. *Sci. Total Environ.* 685, 963–975. doi: 10.1016/j.scitotenv.2019.05.378

Giorgi, F., and Lionello, P. (2008). Climate change projections for the Mediterranean region. *Glob. Planet. Change* 63, 90–104. doi: 10.1016/j.gloplacha.2007.09.005

He, M., Shishov, V., Kaparova, N., Yang, B., Bräuning, A., and Grießinger, J. (2017). Process-based modeling of tree-ring formation and its relationships with climate on the Tibetan Plateau. *Dendrochronologia* 42, 31–41. doi: 10.1016/j.dendro.2017.01.002

Hendrik, D., and Cailleret, M. (2017). Assessing drought-driven mortality trees with physiological process-based models. *Agric. For. Meteorol.* 232, 279–290. doi: 10.1016/j.agrformet.2016.08.019

Holmes, R. L. (1983). Computer-assisted quality control in tree-ring dating and measurement. *Tree Ring Bull.* 43, 68–78.

Kannenberg, S. A., Schwalm, C. R., and Anderegg, W. R. (2020). Ghosts of the past: how drought legacy effects shape forest functioning and carbon cycling. *Ecol. Lett.* 23, 891–901. doi: 10.1111/ele.13485

Larsson, L.-A., and Larsson, P. O. (2018). *CDendro and CooRecorder (v. 9.3.1) [Software]*. Saltsjöbaden: Cybis Elektronik and Data AB.

Li, G., Harrison, S. P., Prentice, I. C., and Falster, D. (2014). Simulation of tree-ring widths with a model for primary production, carbon allocation, and growth. *Biogeosciences* 11, 6711–6724. doi: 10.5194/bg-11-6711-2014

Lloret, F., Keeling, E. G., and Sala, A. (2011). Components of tree resilience: effects of successive low-growth episodes in old ponderosa pine forests. *Oikos* 120, 1909–1920. doi: 10.1111/j.1600-0706.2011.19372

McDowell, N. G., Beerling, D. J., Breshears, D. D., Fisher, R. A., Raffa, K. F., and Stitt, M. (2011). The interdependence of mechanisms underlying climate-driven vegetation mortality. *Trends Ecol. Evol.* 26, 523–532. doi: 10.1016/j.tree.2011.06.003

McDowell, N., Pockman, W. T., Allen, C. D., Breshears, D. D., Cobb, N., Kolb, T., et al. (2008). Mechanisms of plant survival and mortality during drought: why do some plants survive while others succumb to drought? *New Phytol.* 178, 719–739. doi: 10.1111/j.1469-8137.2008.02436.x

Pedersen, B. S. (1998). The role of stress in the mortality of midwestern oaks as indicated by growth prior to death. *Ecology* 79, 79–93.

Pellizzari, E., Camarero, J. J., Gazol, A., Sangüesa-Barreda, G., and Carrer, M. (2016). Wood anatomy and carbon-isotope discrimination support long-term hydraulic deterioration as a major cause of drought-induced dieback. *Glob. Change Biol.* 22, 2125–2137. doi: 10.1111/gcb.13227

Picon, C., Guehl, J. M., and Ferhi, A. (1996). Leaf gas exchange and carbon isotope composition response? To drought in a drought-avoiding (*Pinus pinaster*) and a drought-tolerant (*Quercus petraea*) species under present and elevated atmospheric CO_2 concentrations. *Plant Cell Environ.* 19, 182–190. doi: 10.1111/j.1365-3040.1996.tb00239.x

Plaut, J. A., Yepez, E. A., Hill, J., Pangle, R., Sperry, J. S., and Pockman, W. T. (2012). Hydraulic limits preceding mortality in a piñon–juniper woodland under experimental drought. *Plant Cell Environ.* 35, 1601–1617. doi: 10.1111/j.1365-3040.2012.02512.x

Popkova, M. I., Vaganov, E. A., Shishov, V. V., Babushkina, E. A., Rossi, S., Fonti, M. V., et al. (2018). Modeled tracheidograms disclose drought influence on *Pinus sylvestris* tree-rings structure from Siberian forest-steppe. *Front. Plant Sci.* 9:1144. doi: 10.3389/fpls.2018.01144

R Core Team (2020). *R: A Language and Environment for Statistical Computing*. Vienna: R Foundation for Statistical Computing.

Ripullone, F., Guerrieri, M. R., Nolé, A., Magnani, F., and Borghetti, M. (2007). Stomatal conductance and leaf water potential responses to hydraulic conductance variation in *Pinus pinaster* seedlings. *Trees Struct. Funct.* 21, 371–378. doi: 10.1007/s00468-007-0130-6

Sánchez-Salguero, R., and Camarero, J. J. (2020). Greater sensitivity to hotter droughts underlies juniper dieback and mortality in Mediterranean shrublands. *Sci. Total Environ.* 721:137599. doi: 10.1016/j.scitotenv.2020.137599

Sánchez-Salguero, R., Camarero, J. J., Gutiérrez, E., González Rouco, F., Gazol, A., Sangüesa-Barreda, G., et al. (2017). Assessing forest vulnerability to climate warming using a process-based model of tree growth: bad prospects for rear-edges. *Glob. Change Biol.* 23, 2705–2719. doi: 10.1111/gcb.13541

Sánchez-Salguero, R., Camarero, J. J., Rozas, V., Génova, M., Olano, J. M., Arzac, A., et al. (2018). Resist, recover or both? Growth plasticity in response to drought is geographically structured and linked to intraspecific variability in *Pinus pinaster*. *J. Biogeogr.* 45, 1126–1139. doi: 10.1111/jbi.13202

Sánchez-Salguero, R., Colangelo, M., Matías, L., Ripullone, F., and Camarero, J. J. (2020). Shifts in growth responses to climate and exceeded drought-vulnerability thresholds characterize dieback in two Mediterranean deciduous oaks. *Forests* 11:714. doi: 10.3390/f11070714

Savi, T., Casolo, V., Dal Borgo, A., Rosner, S., Torboli, V., Stenni, B., et al. (2020). Drought-induced dieback of *Pinus nigra*: a tale of hydraulic failure and carbon starvation. *Conserv. Physiol.* 7:coz012. doi: 10.1093/conphys/coz012

Shishov, V. V., Tychkov, I. I., Popkova, M. I., Ilyin, V. A., Bryukhanova, M. V., and Kirdyanov, A. V. (2016). VS-oscilloscope: a new tool to parameterize tree radial growth based on climate conditions. *Dendrochronologia* 39, 42–50. doi: 10.1016/j.dendro.2015.10.001

Touchan, R., Shishov, V. V., Meko, D. M., Nouiri, I., and Grachev, A. (2012). Process based model sheds light on climate sensitivity of Mediterranean tree-ring width. *Biogeosciences* 9, 965–972. doi: 10.5194/bg-9-965-2012

Trenberth, K. E., Dai, A., van der Schrier, G., Jones, P. D., Barichivich, J., Briffa, K. R., et al. (2014). Global warming and changes in drought. *Nat. Clim. Chang.* 4, 17–22. doi: 10.1038/nclimate2067

Tumajer, J., Altman, J., Štěpánek, P., Treml, V., Doležal, J., and Cienciala, E. (2017). Increasing moisture limitation of Norway spruce in central Europe revealed by forward modelling of tree growth in tree-ring network. *Agric. For. Meteorol.* 247, 56–64. doi: 10.1016/j.agrformet.2017.07.015

Tumajer, J., Kašpar, J., Kuželová, H., Shishov, V. V., Tychkov, I. I., Popkova, M. I., et al. (2021). Forward modeling reveals multidecadal trends in cambial kinetics and phenology at treeline. *Front. Plant Sci.* 12:32. doi: 10.3389/fpls.2021.613643

Tychkov, I. I., Sviderskaya, I. V., Babushkina, E. A., Popkova, M. I., Vaganov, E. A., and Shishov, V. V. (2019). How can the parameterization of a process-based model help us understand real tree-ring growth? *Trees Struct. Funct.* 33, 345–357.

Vaganov, E. A., Hughes, M. K., and Shashkin, A. V. (2006). *Growth Dynamics of Conifer Tree Rings*. Berlin: Springer-Verlag. doi: 10.1007/3-540-31298-6

van der Maaten-Theunissen, M., van der Maaten, E., and Bouriaud, O. (2015). pointRes: an R package to analyze pointer years and components of resilience. *Dendrochronologia* 35, 34–38. doi: 10.1016/j.dendro.2015.05.006

Vicente-Serrano, S. M., Camarero, J. J., and Azorin-Molina, C. (2014). Diverse responses of forest growth to drought time-scales in the Northern Hemisphere. *Glob. Ecol. Biogeogr.* 23, 1019–1030. doi: 10.1111/geb.12183

Vieira, J., Campelo, F., and Nabais, C. (2009). Age-dependent responses of tree-ring growth and intra-annual density fluctuations of *Pinus pinaster* to Mediterranean climate. *Trees Struct. Funct.* 23, 257–265. doi: 10.1007/s00468-008-0273-0

Vieira, J., Campelo, F., and Nabais, C. (2010). Intra-annual density fluctuations of *Pinus pinaster* are a record of climatic changes in the western Mediterranean region. *Can. J. For. Res.* 40, 1567–1575. doi: 10.1139/X10-096

Vieira, J., Rossi, S., Campelo, F., Freitas, H., and Nabais, C. (2013). Seasonal and daily cycles of stem radial variation of *Pinus pinaster* in a drought-prone environment. *Agric. For. Meteorol.* 180, 173–181. doi: 10.1016/j.agrformet.2013.06.009

Wigley, T. M., Briffa, K. R., and Jones, P. D. (1984). On the average value of correlated time series, with applications in dendroclimatology and hydrometeorology. *J. Clim. Appl. Meteorol.* 23, 201–213. doi: 10.1175/1520-04501984023<0201:OTAVOC>2.0.CO;2

Wood, S. N. (2011). Fast stable restricted maximum likelihood and marginal likelihood estimation of semiparametric generalized linear models. *J. R. Stat. Soc. B* 73, 3–36. doi: 10.1111/j.1467-9868.2010.00749.x

Wood, S. N. (2017). *Generalized Additive Models: An Introduction with R*. Boca Raton, FL: CRC. doi: 10.1201/9781315370279

Xu, C., McDowell, N. G., Sevanto, S., and Fisher, R. A. (2013). Our limited ability to predict vegetation dynamics under water stress. *New Phytol.* 200, 298–300. doi: 10.1111/nph.12450

Zang, C., and Biondi, F. (2015). Treeclim: an R package for the numerical calibration of proxy-climate relationships. *Ecography* 38, 431–436. doi: 10.1111/ecog.01335

Conflict of Interest: The authors declare that the research was conducted in the absence of any commercial or financial relationships that could be construed as a potential conflict of interest.

Publisher's Note: All claims expressed in this article are solely those of the authors and do not necessarily represent those of their affiliated organizations, or those of the publisher, the editors and the reviewers. Any product that may be evaluated in this article, or claim that may be made by its manufacturer, is not guaranteed or endorsed by the publisher.

frontiers in Plant Science

ORIGINAL RESEARCH
published: 18 October 2021
doi: 10.3389/fpls.2021.735275

Prediction and Utilization of Malondialdehyde in Exotic Pine Under Drought Stress Using Near-Infrared Spectroscopy

Yini Zhang, Qifu Luan, Jingmin Jiang and Yanjie Li**

Research Institute of Subtropical Forestry, Chinese Academy of Forestry, Fuyang, China

Drought is a major abiotic stress that adversely affects the growth and productivity of plants. Malondialdehyde (MDA), a substance produced by membrane lipids in response to reactive oxygen species (ROS), can be used as a drought indicator to evaluate the degree of plasma membrane damage and the ability of plants to drought stress tolerance. Still measuring MDA is usually a labor- and time-consuming task. In this study, near-infrared (NIR) spectroscopy combined with partial least squares (PLS) was used to obtain rapid and high-throughput measurements of MDA, and the application of this technique to plant drought stress experiments was also investigated. Two exotic conifer tree species, namely, slash pine (*Pinus elliottii*) and loblolly pine (*Pinus taeda*), were used as plant material exposed to drought stress; different types of spectral preprocessing methods and important feature-selection algorithms were applied to the PLS model to calibrate it and obtain the best MDA-predicting model. The results show that the best PLS model is established *via* the combined treatment of detrended variable–significant multivariate correlation algorithm (DET-sMC), where latent variables (LVs) were 6. This model has a respectable predictive capability, with a correlation coefficient (R^2) of 0.66, a root mean square error (RMSE) of 2.28%, and a residual prediction deviation (RPD) of 1.51, and it was successfully implemented in drought stress experiments as a reliable and non-destructive method to detect the MDA content in real time.

Keywords: model calibration, abiotic stress, NIR spectroscopy, non-destructive, pine tree

OPEN ACCESS

Edited by:
Francesco Ripullone, University of Basilicata, Italy

Reviewed by:
Brian Via, Auburn University, United States
Alessandra Biancolillo, University of L'Aquila, Italy
Agus Arip Munawar, Syiah Kuala University, Indonesia

****Correspondence:***
Qifu Luan
qifu.luan@caf.ac.cn
Yanjie Li
aj7105@gmail.com

Specialty section:
This article was submitted to Plant Abiotic Stress, a section of the journal Frontiers in Plant Science

Received: *02 July 2021*
Accepted: *17 September 2021*
Published: *18 October 2021*

Citation:
Zhang Y, Luan Q, Jiang J and Li Y (2021) Prediction and Utilization of Malondialdehyde in Exotic Pine Under Drought Stress Using Near-Infrared Spectroscopy. Front. Plant Sci. 12:735275. doi: 10.3389/fpls.2021.735275

INTRODUCTION

Slash pine (*Pinus elliottii*) and loblolly pine (*Pinus taeda*) trees were introduced to China in the past century, and due to their high-resin yield, fast growth, and suitably long humid, warm-temperate climatic condition, they are mostly cultivated in the south of the country (Yi et al., 2000; Liu et al., 2013; Lilian et al., 2021). In recent years, both slash and loblolly pine have attained key status in terms of their ecological and economic benefits. The annual yield of resin in China is ca. 0.6 million tons, accounting for 50% of the global turpentine trade (Acosta et al., 2019; McConnell et al., 2021; Yi et al., 2021). However, resin yield and wood quality are affected by biological and abiotic stresses (Towler et al., 2015), and understanding the degree of important stress factors and taking timely measures to effectively avoid their adverse effects on turpentine yield and wood properties is imperative.

Plants incur lipid peroxidation in response to oxidative stress after encountering various forms of adversity or when they undergo senescence, which leads to the destruction and protein lysis of the cell membrane system, thereby impairing plant photosynthesis and respiration, causing the death of plant cells in severe cases (Janku et al., 2019). Malondialdehyde (MDA) is one of the final products of polyunsaturated fatty acid peroxidation in the cells; for this reason, it is a widely used and reliable marker for determining the degree of injury to a stressed plant (Morales and Munné-Bosch, 2019). The more the plant is damaged, the higher its MDA content, as found in studies that focused on plant responses to abiotic and biotic stresses (Alché, 2019). That is to say, plants will generate ROS under abiotic or biotic stress conditions, thereby impairing the production of biomolecules, such as lipids, proteins, and nucleic acids, which increases the MDA content and the permeability of the plasma membrane, leading to extravasation of the content of cells. It is the mechanism by which drought resistance in plants is regulated (Munnik et al., 2000; Kong et al., 2016). Therefore, the MDA content could be used as a robust diagnostic indicator when studying plant growth dynamics, such that predicting the MDA content in plants could be used to know the stress conditions of plants in real-time, enabling corresponding pre-emptive measures against drought to be taken. Still, our understanding of methods and results in membrane lipid peroxidation markers remains limited by several shortcomings (Munnik et al., 2000).

The thiobarbituric acid (TBA) assay has been the most common method used for determining MDA in plants. This mainly relies on the chromogenic reaction of TBA with MDA under acidic conditions to produce reddish-brown 3,5,5-trimethyloxazole-2,4-ditone ($C_6H_9NO_3$), whose absorbance values at 532- and 600-nm wavelengths are compared to calculate the MDA content (Janero, 1990; Hodges et al., 1999). However, this method is susceptible to interference from carbohydrates in plants, which affects the final measurement results (Xu et al., 1993). Furthermore, traditional methods devised to empirically determine these indicators are time-consuming, laborious, and destructive. Hence, it is of great significance to establish a rapid, effective, non-destructive, and non-polluting way to determine MDA for drought resistance of plants.

Near-infrared (NIR) spectroscopy is a highly flexible form of analysis, whose applications began in the 1950s (Pasquini and Celio, 2003; Mohamed et al., 2018; Chu et al., 2020). Since then, through over half a century of development, it has matured and is now widely employed in food, medicine, petrochemical, and other research fields (Mohamed et al., 2018; Guo et al., 2020). In recent years, NIR spectroscopy technology has become increasingly and broadly used in forestry, for example, to estimate photosynthetic characteristics (Dechant et al., 2017), to predict leaf-level nitrogen content (Kokaly, 2001), to distinguish bamboo shoots of different qualities (Tong et al., 2020), and to name a few applications. Partial least squares (PLS) regression, a quick, efficient, and optimal regression method based on covariance, is a widely used chemometric method, one that combines the advantages of multiple linear regression, canonical correlation analysis, and principal component regression (Tenenhaus et al., 2005; Sarker and Nichol, 2011). This approach has been applied to rapidly predict leaf photosynthetic parameters (Meacham et al., 2019), analyze the quantitative of forest biomass (Acquah et al., 2016), among others. It is worth noting that substantial spectral data will contain redundant and complicated information. Therefore, to establish a moderately practical model, it is necessary to preprocess the collected spectral data (Xu et al., 2008).

Preprocessing of NIR spectral data has become a crucial step in chemometric modeling. The target of this preprocessing is to remove physical phenomena, including a specific source of noise and overlapping information, from the spectra so as to improve the subsequent multivariate regression, classification model, or exploratory analysis (Rinnan et al., 2009). Similarly, variable selection is also a critical step in spectral analysis, which can select the most relevant spectral band to improve the overall performance of the model (Yu et al., 2020). Surprisingly, the prediction of MDA in *P. elliottii* and *P. taeda* under drought stress has yet to be reported.

Therefore, this study aimed (1) to derive a technique to reliably estimate and predict MDA of *P. elliottii* and *P. taeda* under different drought stress conditions using NIR technology; (2) to compare the performance of different preprocessing methods and differing feature-variable selection methods; and (3) to evaluate the response of leaf-level MDA in *P. elliottii* and *P. taeda* under drought stress using the NIR-based technique.

MATERIALS AND METHODS

Site and Plants

The experimental site was a greenhouse at the Research Institute of Subtropical Forestry, Chinese Academy of Forestry, located in Hangzhou, Zhejiang Province, China (30°3′N, 119°57′E).

The experiment materials consisted of 1-year-old container seedlings of slash pine and loblolly pine. Watering, fertilizing, and other managements were all implemented according to the growth requirements of both species. The drought stress treatment began after 3 weeks of acclimatization of seedlings to the greenhouse conditions. Two experiments were set up for model calibration and drought stress investigation. In each experiment, the watering regime was set during the seedling tempering period as the normal watering amount (control check), and this watering amount was then reduced into four different drought stress conditions as follows: by 20% (treatment 1), 40% (treatment 2), 60% (treatment 3), and 80% (treatment 4). There are 15 biological replicates per species under each treatment, and in total, 150 samples per experiment were used.

NIR Spectrum Measurements

Near-infrared spectral data were collected in August and September 2020 using a field-based spectrometer (LF-2500, Spectral evolution, USA). For each scan, the fresh needle samples were arranged tightly to minimize other noise pollution, placed on a background board, and scanned directly with a handheld fiber optic contact probe; spectra were averaged after 20 scans per sample, whose values ranged from 1,000 to 2,500 nm with a 6-nm resolution. (1) For the model calibration experiment, three

samples per treatment were selected for NIR data collection and MDA content measurement on days 0, 7, 14, 21, and 27 at 9:00–10:00 a.m. (2) For the same drought stress experiment, all the 150 samples have only been taken NIR spectra on the same day when the NIR data were taken in the model calibration experiment.

MDA Measurement of Conifers

A commercially available detection kit for MDA measurement was used (Suzhou Keming Biotechnology Company). For this, mixed fresh needles were weighed to ca. 0.1 g and then ground into powder with a 1-ml extracting solution. The extraction was centrifuged for 10 min at 8,000 *rcf* at 4°C. Then, 0.2 ml of the supernate was removed and mixed with 0.6 ml of TBA and moderately shaken. These mixed liquids were placed in a 95°C water bath for 30 min and then centrifuged for 10 min at 10,000 *rcf* at 25°C. Each extraction was placed in a spectrophotometer, and its recorded absorption at 532 and 600 nm wavelengths were used to determine the MDA concentration of that sample (Chen and Wang, 2012).

Preprocessing and Variable Selection of NIR

To reduce bias from physical factors and irrelevant variables on the establishment of a stable and reliable model (Liang et al., 2020), six preprocessing methods, namely standard normal variate (SNV), detrended variable (DET, $p = 2$), block scale (BS), block normal (BN), block scale and standard normal variate (BS-SNV), and detrended variable and standard normal variate (DET-SNV), were combined with PLS (Wold et al., 2001). Four variable selection methods were applied as follows: inverse variable elimination (bve) (Eason, 1990), genetic algorithm (ga) (Molajou et al., 2021), regularization elimination (rep) (Mehmood et al., 2012; Molajou et al., 2021), and a significant multivariate correlation (sMC) algorithm (Tran et al., 2014). The calibration set ($n = 80$ samples) was used to develop a calibrated model, and the separate validation set ($n = 20$ samples) was reserved to assess and evaluate the prediction performance of the developed model. Three indicators of internal cross-validation, namely, the correlation coefficient (R^2), root mean square error (RMSE), and residual prediction deviation (RPD), were used to assess model robustness. For that, the closer the R^2 to 1 and the RMSE to 0 and higher values for the RPD, the better the prediction ability of the model is (Yan et al., 2000; Plans et al., 2012). Finally, the optimum number of PLS components (latent variables (LVs)) were selected.

Software Tools

All the data analyses were implemented using R software (v4.0.4). The "pls" (Mevik and Wehrens, 2007) and "enpls" (Xiao et al., 2019) packages of R were used for building the PLS model, and the "prospectr" package (Stevens and Ramirez-Lopez, 2020) was used for manipulation of the NIR spectral data, with the "ggplot2" (Wickham, 2017) package for drawing the plots.

RESULTS

Model Performance

Six spectral preprocessing methods and four kinds of variable selection were used for model calibration, whose results are shown in **Table 1**. Compared with the model without data processing, the accuracy of the model established was improved when using the SNV, DET, DET-SNV, and BS-SNV spectral preprocessing methods. For all models, the average R^2 and RMSE values of the calibration and validation sets were 0.64 (range: 0.63–0.65), 2.30% (range: 2.28–2.33%) and 0.61 (range: 0.61–0.62), 2.98% (range: 2.96–2.99%) respectively. In addition, the average RPD was 1.31 (range: 1.04–1.51). Despite the variable selection methods, the DET processing method yielded the highest accuracy, with R^2 and RMSE values for the calibration set of 0.65 (range: 0.65–0.66) and 2.28% (range: 2.26%−2.28), respectively, and the values of RPD was 1.40 (range: 1.35–1.51). Then, performance was ranked in the following order: DET-SNV, BS-SNV, SNV, BS, and original spectrum (OG) processing methods, followed by BN showing the worst accuracy whose mean values for R^2 and RMSE were 0.64 (range: 0.63–0.64), 2.32% (range: 2.31–2.33%), and 0.61 and 2.97% (range: 2.96–2.98%) for the calibration and validation sets, respectively. Compared with the full spectrum PLS model, the ga, rep, and sMC variable selection methods generated similar results when applied to all preprocessing model types. Among these, the sMC variable selection combined with the DET preprocessing method produced the most accurate MDA prediction model, having R^2 and RMSE values for the calibration set of 0.66 and 2.28%, respectively, and the RPD of DET-sMC was 1.51.

Establishment of MDA Content Prediction Model Based on PLS

The relationships between the MDA content predicted and measured by the PLS model when using the DET-sMC spectra and original full spectra are plotted in **Figure 1**. Although the prediction accuracy of each model differed, their prediction error was still low. The fitting model accuracy after spectral processing is slightly better than that based on original full spectra with only <10% of the full length of spectra. **Figure 2** shows the residuals of the best processing spectral model for the MDA content. The latter tends to be underestimated when the measurement value is small. As the MDA content value increases, the predicted MDA value is more likely to be overpredicted. The residual values of the MDA model are all between −5 and 5%. In contrast, for the model established without any spectral preprocessing, the residual values of the MDA model are all between −5 and 7.5%.

The important variable that was selected by using the sMC variable selection method 100 times in the MDA model on DET-sMC has exhibited in **Figure 3**. Evidently, as selected by 100 random models, the band selected by sMC is stable and robust, featuring several relative spectral regions in the prediction model. The variables at 1,000, 1,240, 1,430, 1,500, 2,130, and 2,450 nm were thus critical for building the MDA prediction model.

TABLE 1 | The calibration and validation results of PLS models for the prediction of MDA content in pine seedlings based on different spectral processing and variable selection methods.

		Calibration				Validation				RPD
		R^2		RMSE		R^2		RMSE		
Pro-processing	Variable selection	Mean	SD	Mean	SD	Mean	SD	Mean	SD	
OG	raw	0.64	0.04	2.31	0.12	0.61	0.00	2.97	0.00	1.30
	ga_sel	0.64	0.04	2.31	0.12	0.61	0.01	2.96	0.03	1.26
	rep_sel	0.64	0.04	2.31	0.12	0.61	0.00	2.97	0.00	1.33
	bve_sel	0.63	0.06	2.33	0.17	0.61	0.01	2.98	0.03	1.05
	sMC_sel	0.64	0.04	2.31	0.12	0.62	0.01	2.96	0.05	1.10
SNV	raw	0.65	0.01	2.28	0.03	0.61	0.00	2.98	0.01	1.42
	ga_sel	0.65	0.01	2.29	0.03	0.61	0.00	2.98	0.01	1.46
	rep_sel	0.65	0.01	2.28	0.03	0.61	0.00	2.97	0.00	1.40
	bve_sel	0.64	0.02	2.30	0.07	0.61	0.01	2.98	0.03	1.32
	sMC_sel	0.65	0.00	2.28	0.01	0.61	0.00	2.98	0.01	1.44
BS	raw	0.64	0.05	2.32	0.14	0.61	0.00	2.97	0.01	1.05
	ga_sel	0.64	0.04	2.32	0.13	0.61	0.00	2.97	0.01	1.06
	rep_sel	0.64	0.05	2.32	0.14	0.61	0.00	2.97	0.01	1.05
	bve_sel	0.64	0.05	2.32	0.15	0.61	0.00	2.98	0.02	1.04
	sMC_sel	0.64	0.02	2.30	0.07	0.61	0.01	2.96	0.03	1.50
BN	raw	0.64	0.04	2.31	0.12	0.61	0.00	2.97	0.00	1.30
	ga_sel	0.64	0.04	2.31	0.12	0.61	0.01	2.96	0.03	1.26
	rep_sel	0.64	0.04	2.31	0.12	0.61	0.00	2.97	0.00	1.33
	bve_sel	0.63	0.06	2.33	0.17	0.61	0.01	2.98	0.03	1.05
	sMC_sel	0.64	0.04	2.31	0.12	0.62	0.01	2.96	0.05	1.10
DET	raw	0.65	0.00	2.28	0.01	0.61	0.00	2.97	0.01	1.40
	ga_sel	0.65	0.01	2.28	0.02	0.61	0.00	2.97	0.00	1.48
	rep_sel	0.65	0.00	2.28	0.00	0.61	0.00	2.97	0.00	1.40
	bve_sel	0.65	0.01	2.28	0.02	0.61	0.02	2.99	0.06	1.35
	sMC_sel	0.66	0.00	2.28	0.00	0.61	0.00	2.97	0.00	1.51
BS_SNV	raw	0.65	0.01	2.28	0.02	0.61	0.00	2.97	0.02	1.40
	ga_sel	0.65	0.01	2.28	0.02	0.61	0.00	2.97	0.01	1.48
	rep_sel	0.65	0.01	2.28	0.02	0.61	0.01	2.97	0.02	1.40
	bve_sel	0.64	0.02	2.30	0.07	0.61	0.00	2.97	0.00	1.35
	sMC_sel	0.65	0.01	2.28	0.02	0.61	0.01	2.97	0.02	1.41
DET_SNV	raw	0.65	0.00	2.28	0.01	0.61	0.00	2.97	0.01	1.38
	ga_sel	0.65	0.01	2.28	0.02	0.61	0.00	2.97	0.00	1.33
	rep_sel	0.64	0.00	2.28	0.00	0.61	0.00	2.97	0.00	1.41
	bve_sel	0.65	0.01	2.29	0.02	0.61	0.02	2.99	0.06	1.19
	sMC_sel	0.65	0.00	2.29	0.00	0.61	0.00	2.97	0.00	1.43

PLS, partial least squares; MDA, malondialdehyde; R^2, correlation coefficient; RMSE, root mean square error; RPD, residual prediction deviation; SNV, standard normal variate; BS, block scale; BN, block normal; DET, detrended variable; BS-SNV, block scale and standard normal variate; DET-SNV, detrended variable and standard normal variate; ga, genetic algorithm; rep, regularization elimination; bve, inverse variable elimination; sMC, significant multivariate correlation.

MDA Variation Under Drought Stress Using the PLS Model

The DET-sMC model was used to predict the MDA content of loblolly and slash pine seedlings under the same treatment. With more days elapsed since the initiation of each treatment, the MDA content of each treatment changed, by first increasing and then decreasing. In the two pine species, one-way ANOVA showed that on day 7 of drought exposure, the treatments entailing a 60% and 80% reduction in watering volume differed significantly from the other treatments (**Figure 4**). However, on day 14, those treatments with a 20 and 40% reduction in watering volume were significantly different from the other treatments. At other time points, the differences among treatments were not significant (**Figure 4**).

DISCUSSION

The purpose of this study was to reveal the applicability of NIR for the detection of MDA in loblolly pine and slash pine. The balance among production, elimination, and signal

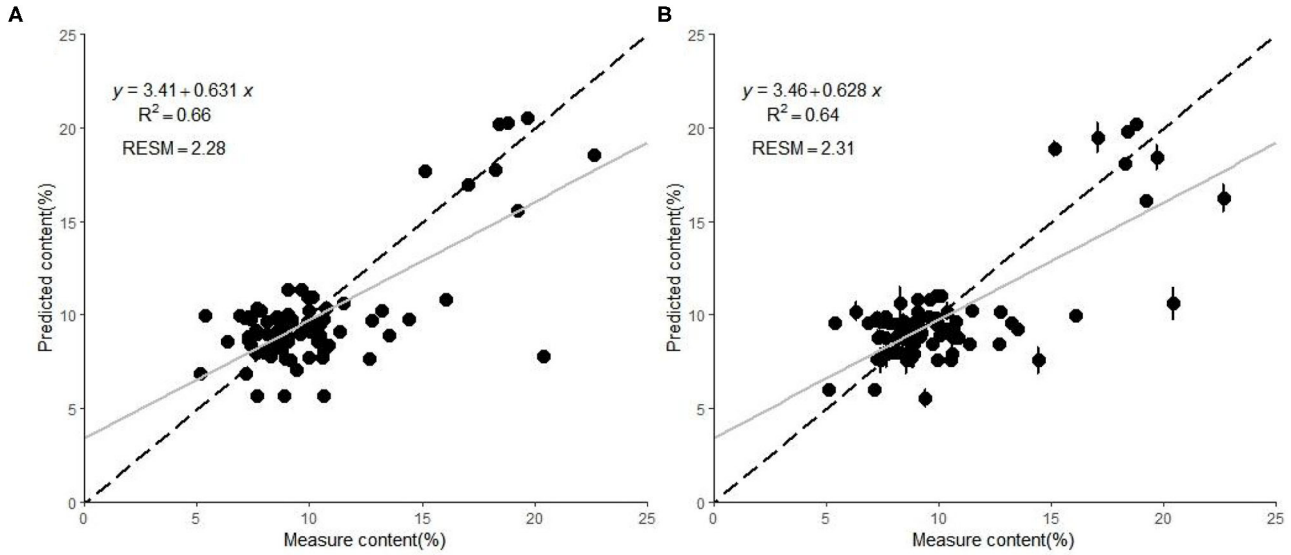

FIGURE 1 | Scatterplots of the malondialdehyde (MDA) in pine seedlings predicted by **(A)** the detrended variable–significant multivariate correlation algorithm (DET-sMC) partial least squares (PLS) model and **(B)** the full-spectrum PLS model. The error bar of each symbol point represents the sample prediction error obtained by 100 random calibration models. The regression line of the model appears in gray; the dotted black line denotes the equality of measured vs. predicted MDA values.

transduction of MDA is an important feature in redox biology and may determine the survival of plants under stress; hence, both enzymatic and non-enzymatic peroxidation processes can foster the formation of MDA and other oxidative peroxidation products in plants (Esterbauer et al., 1991; Morales and Munné-Bosch, 2019). Consequently, a quick and non-destructive method by which to monitor, *in situ*, the MDA content in plants under drought stress is a logistical priority, because it can enable timely and effective interventions by tree or crop managers to restore normal physiological activity. In this study, the relationship between MDA and NIR spectra was explored using seven spectral preprocessing methods and five effective variable selection algorithms. Comparing the results in **Table 1**, the DET preprocessing method coupled with the sMC variable selection method emerged as the optimal prediction model, with R^2 and RMSE of 0.66 and 2.28%, respectively. These values were lower than those reported for predicting the MDA concentration (R^2 = 0.996, RMSE = 2.117) in oilseed rape (*Brassica napus*) fresh leaves (Kong et al., 2016). The reason for this disparity may be leaf morphology. Oilseed rape plants have broad leaves, making the collection of their spectral data easier than for needles of slash or loblolly pine, whose single-leaf surface of a needle is very small and could not always be accurately positioned. This could have introduced relatively more irrelevant information in the collected spectral data, which reduced the modeling accuracy of the MDA content.

One advantage of using NIR spectroscopy is that it can model properties robustly without depending on unique chemical signals by applying statistical methods of chemometrics. Nonetheless, while collecting the NIR spectroscopy data, often high-frequency sounds, personnel operations, the external environment, and irrelevant noises are liable to interfere with this process, so it is vital to select effective spectral information (Guo et al., 2020). Accordingly, implementing appropriate spectral preprocessing and variable selection can improve the accuracy of a fitted model (Zou et al., 2010; Gerretzen et al., 2016). For example, the SNV-SVR model is based on SNV, which reduces particle size noise effects by scaling each spectrum to have an SD of 1.0 and by utilizing accurate prediction performance of both catechins and caffeine as suggested by Wang et al. (Wang et al., 2020); DET can reduce the curvature of each spectrum (Murphy et al., 2021); and BS can balance the effect of the modeled blocks, to avoid any block dominating the model (Mishra et al., 2021). In this study, this exercise shows that the sMC algorithm combined with PLS can efficiently identify the useful informative wavelength to provide a promising and robust correction model for the prediction of MDA. This finding is similar to another study that applied the sMC algorithm to get a robust model for predicting the chlorophyll content of *Sassafras tzumu* (Li et al., 2019). Several important variables that are related to MDA were selected similarly in each model, including those at regions corresponding to 1,000, 1,240, 1,430, 1,500, 2,130, and 2,450 nm. As reported by Kokaly et al., the regions around 1,500–1,600 nm are mainly related to O–H stretching vibration of aldehyde and phenolic compounds (Kokaly and Skidmore, 2015). Residual values are uniformly distributed in the horizontal band, which suggests that the selected model is more suitable, and coupled with a narrower bandwidth, which indicates a better fitting accuracy and implies greater accuracy of the fitted regression equation (Couture et al., 2016). Therefore, in this study, after DET-sMC processing of the spectral data, the range of residual values is smaller, and the model is more accurate.

For a comparative study, we then performed additional experiments for the inversion of the PLS model on the same

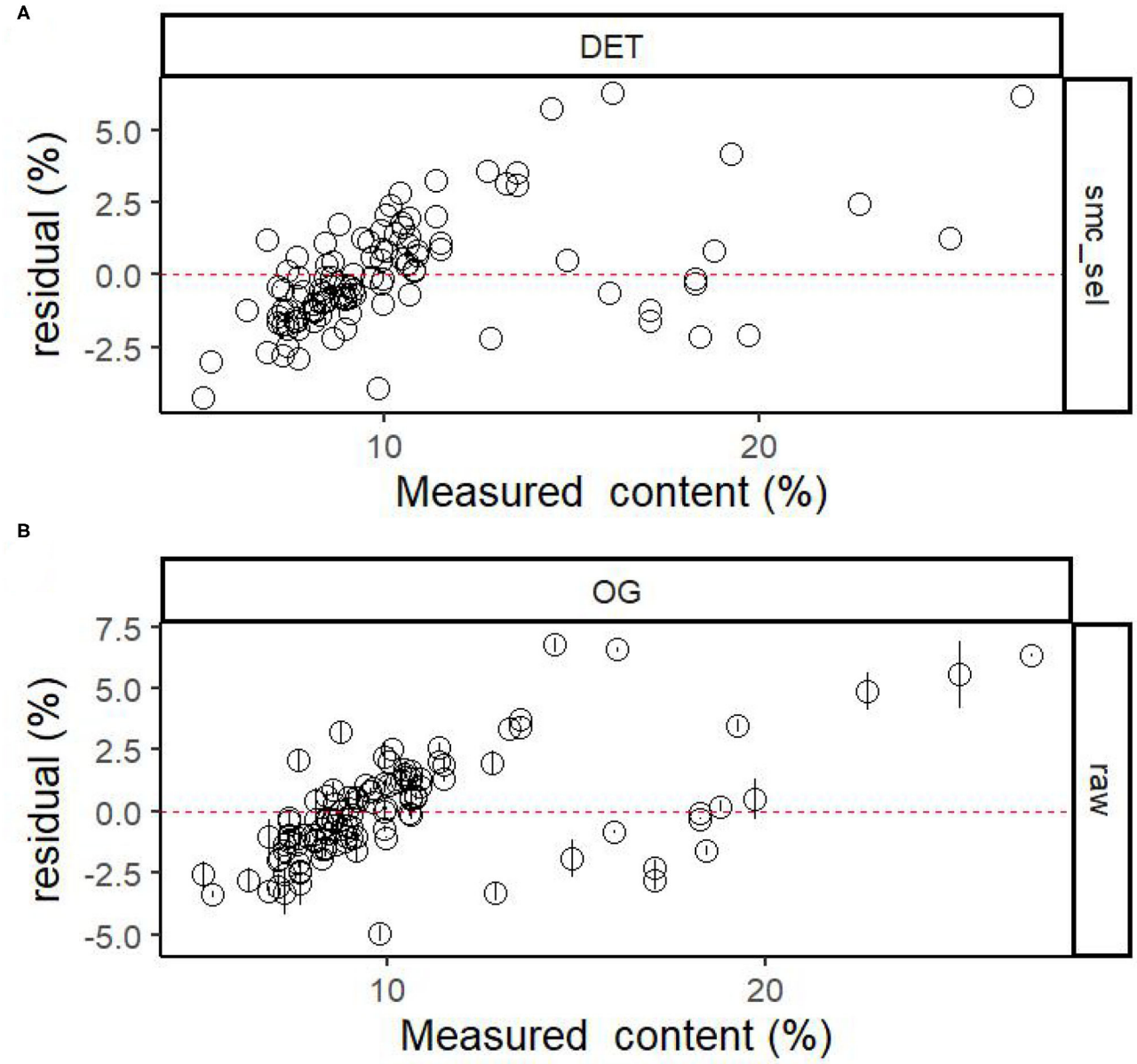

FIGURE 2 | Residuals plotted against the measured MDA in pine seedlings based on **(A)** DET-sMC spectra and **(B)** full length of spectra. Error bars for predicted values represent the SDs obtained from the 100 simulated models.

treated loblolly and slash pine seedlings. In the prediction model results for this experiment, the MDA content increased at first but then decreased, a pattern consistent with the findings reported by Zhu (2014) and Wang et al. (2016), who, respectively, studied the physiological effects of water stress on *Pinus sylvestris* and *Larix gmelinii*. This shows that our optimal PLS model, which can detect the MDA content faster than *via* laboratory measurements, has a certain level of accuracy. However, the changes to the MDA content under the low-stress condition (i.e., treatments 1 and 2) and the high-stress condition (i.e., treatments 3 and 4) were not synchronous. The MDA content reached the maximum on day 7 under high-stress treatments but later on day 14 under the low-stress treatments (**Figure 4**). Previous studies have shown that the activity of lipoxygenase increase may lead to the formation of MDA and other lipid peroxidation products in plants, and that temperature is a critical factor influencing enzyme activity. Furthermore, our experiment was carried out in the hot summer, so that lipoxygenase activity was high, which may have led to the high MDA content detected under low drought stress. Therefore, membrane lipid peroxidation peaked earlier under high drought stress condition than under low stress condition, and seedlings were then adjusted to the

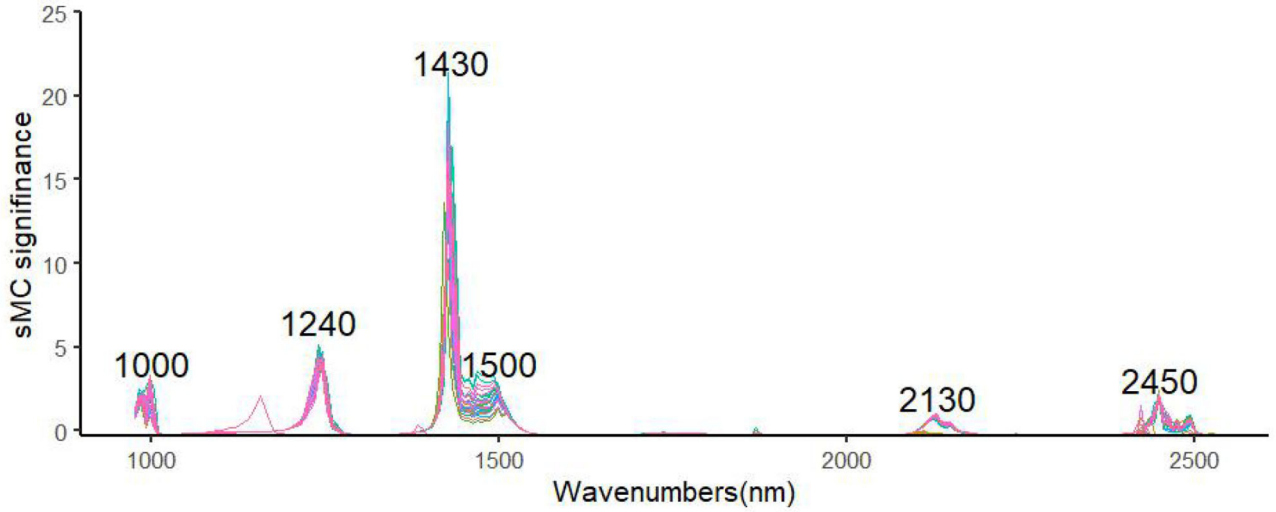

FIGURE 3 | Spectral influence in the MDA models that were randomly run 100 times.

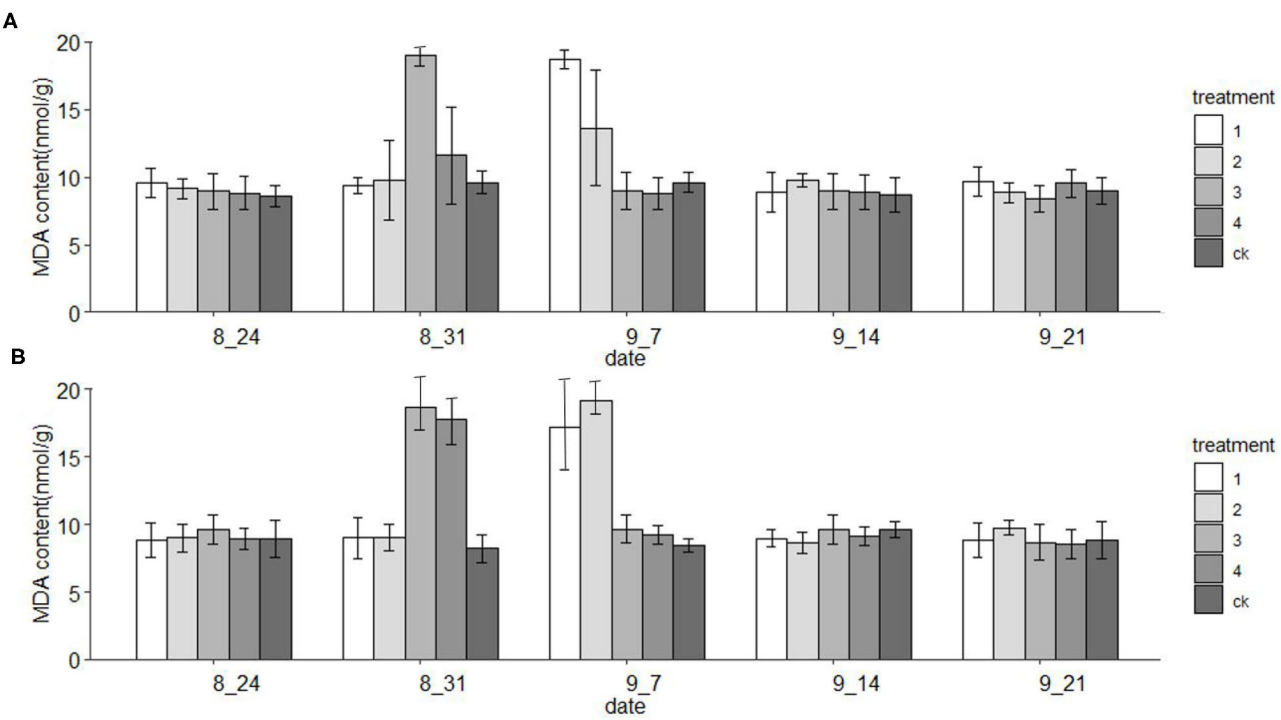

FIGURE 4 | PLS model inversion of MDA composition in **(A)** loblolly pine and **(B)** slash pine.

drought environment. Similarly, with prolonged stress exposure, the MDA content also increased under high temperature and low-stress conditions.

CONCLUSION

Near-infrared spectroscopy combined with PLS modeling provides a reliable and non-destructive way to predict the MDA content of pine trees. Furthermore, the spectral preprocessing methods and variable selection can successfully increase the model prediction accuracy with less variables used. Most importantly, we successfully applied this technology to predict MDA under drought stress in a fast and non-destructive way, thus demonstrating that the NIR-based technique harbors promising prospects for use in future studies of plant stress, especially for trees.

DATA AVAILABILITY STATEMENT

The original contributions presented in the study are included in the article/supplementary material, further inquiries can be directed to the corresponding author/s.

AUTHOR CONTRIBUTIONS

YZ conducted the experiment and wrote the manuscript. YL designed this study, supervised experiments, and performed revisions of the manuscript. QL supervised experiments and performed revisions of the manuscript. JJ supported the data collection and field experiment. All authors read and approved the final manuscript.

FUNDING

This study was supported by the Fundamental Research Funds of CAF (CAFYBB2020SY008), the National Natural Science Foundation of China (31901323), Fundamental Research Funds of Chinese Forestry Academy (CAFYBB2017ZA001-2-1), and Zhejiang Science and Technology Major Program on Agricultural New Variety Breeding (2021C02070-8).

REFERENCES

Acosta, J. J., Fahrenkrog, A. M., Neves, L. G., Resende, M., Christopher, D., and Davis, J. M. (2019). Exome resequencing reveals evolutionary history, genomic diversity, and targets of selection in the conifers Pinus taeda and Pinus elliottii. *Genome Biol. Evol.* 11, 508–520. doi: 10.1093/gbe/evz016

Acquah, G. E., Via, B. K., Fasina, O.O., and Eckhardt, L. G. (2016). Rapid quantitative analysis of forest biomass using fourier transform infrared spectroscopy and partial least squares regression. *J. Anal. Methods Chem.* 183, 95–98. doi: 10.1155/2016/1839598

Alché, J. D. D. (2019). A concise appraisal of lipid oxidation and lipoxidation in higher plants. *Redox Biol.* 23, 101–136. doi: 10.1016/j.redox.2019.101136

Chen, J. X., and Wang, X. F. (2012). Experimental guidance of plant physiology. *South china Univ Techoll.* 12, 348–351. doi: 10.11707/j.1001-7488.20130205

Chu, X. L., Chen, P. L., and Jing, Y. (2020). Progresses and perspectives of near infrared spectroscopy analytical technology. *J. Instr. Anal.* 39,1181–1188. doi: 10.3969/j.issn.1004-4957.2020.10.001

Couture, J. J., Singh, A., Rubert-Nason, K. F., Serbin, S. P., Lindroth, R. L., and Townsend, P. A. (2016). Spectroscopic determination of ecologically relevant plant secondary metabolites. *Methods Ecol. Evol.* 7, 1402–1412. doi: 10.1111/2041-210X.12596

Dechant, B. M., Cuntz, M., Vohland, E., Schulz, and Doktor, D. (2017). Estimation of photosynthesis traits from leaf reflectance spectra: correlation to nitrogen content as the dominant mechanism. *Remote Sens. Environ.* 196, 279–292. doi: 10.1016/j.rse.2017.05.019

Eason, S. (1990). *Backward variable elimination canonical correlation and canonical cross-validation*. Sandra Eason, University of New Orleans, Lakefront, New Orleans, LA 70148.

Esterbauer, H., Schaur, R. J., and Zollner, H. (1991). Chemistry and biochemistry of 4-hydroxynonenal, malonaldehyde and related aldehydes. *Free Radic. Biol. Med.* 11, 81–128. doi: 10.1016/0891-5849(91)90192-6

Gerretzen, J. E., Szymańska, J., Bart, A. N., Davies, H., Manen, E. R., Heuvel, J. J., et al. (2016). Boosting model performance and interpretation by entangling preprocessing selection and variable selection. *Anal. Chim. Acta.* 938, 44–52. doi: 10.1016/j.aca.2016.08.022

Guo, Y., Liu, C., Ye, R., and Duan, Q. (2020). Advances on water quality detection by uv-vis spectroscopy. *Appl. Sci.* 10, 68–74. doi: 10.3390/app10196874

Hodges, M. D., DeLong, M. J., Forney, F. C., and Prange, K. R. (1999). Improving the thiobarbituric acid-reactive-substances assay for estimating lipid peroxidation in plant tissues containing anthocyanin and other interfering compounds. *Planta* 207, 604–611. doi: 10.1007/s004250050524

Janero, D. R. (1990). Malondialdehyde and thiobarbituric acid-reactivity as diagnostic indices of lipid peroxidation and peroxidative tissue injury. *Free Radic. Biol. Med.* 9, 515–540. doi: 10.1016/0891-5849(90)90131-2

Janku, M. L., Luhov, Á., and Petrivalský, M. (2019). On the origin and fate of reactive oxygen species in plant cell compartments. *Antioxidants.* 8:105. doi: 10.3390/antiox8040105

Kokaly, R. F. (2001). Investigating a physical basis for spectroscopic estimates of leaf nitrogen concentration. *Remote Sens. Environ.* 75, 153–161. doi: 10.1016/S0034-4257(00)00163-2

Kokaly, R. F., and Skidmore, A. K. (2015). Plant phenolics and absorption features in vegetation reflectance spectra near 1.66 μm. *Int. J. Appl. Earth Obs. Geoinf.* 43, 55–83. doi: 10.1016/j.jag.2015.01.010

Kong, W., Liu, F., Zhang, C., Zhang, J., and Feng, H. (2016). Non-destructive determination of malondialdehyde (MDA) distribution in oilseed rape leaves by laboratory scale nir hyperspectral imaging. *Sci. Rep.* 6:35393. doi: 10.1038/srep35393

Li, Y. J., Sun, Y., Jiang, J. M., and Liu, J. (2019). Spectroscopic determination of leaf chlorophyll content and color for genetic selection on *Sassafras tzumu*. *Plant Methods.* 15:73. doi: 10.1186/s13007-019-0458-0

Liang, L. L., Wei, G., Fang, F., Xu, Y., Deng, K., Shen, Q., et al. (2020). Prediction of holocellulose and lignin content of pulp wood feedstock using near infrared spectroscopy and variable selection. *Spectrochim. Acta A Mol. Biomol. Spectrosc.* 225:117515. doi: 10.1016/j.saa.2019.117515

Lilian, P. M., Ross, W. W., Georgina, M. S., and Kitt, G. P. (2021). Breeding for climate change resilience: A case study of loblolly pine (*Pinus taeda* L.) in North America. *Front. Plant Sci.* 12:606908. doi: 10.3389/fpls.2021.606908

Liu, C. X., Huang, S. W., Zhong, S. W., and Chen, B. Q. (2013). Growth variation and selection to the progeny of nucleus breeding population of *Pinus taeda*. *Scientia Silvae Sinicae.* 49, 27–32.

McConnell, T. E., Silva, B. K. D., Sun, C.Y., and Tanger, S. M. (2021). Forest to mill timber price trends and volatility for mississippi timber products. *For. Prod. J.* 71, 177–187. doi: 10.13073/FPJ-D-21-00010

Meacham, H. K., Montes, C., Wu, J., Guan, K., Fu, P., and Ainsworth, E. (2019). High-throughput field phenotyping using hyperspectral reflectance and partial least squares regression (PLSR) reveals genetic modifications to photosynthetic capacity. *Remote Sens. Environ.* 231, 111–176. doi: 10.1016/j.rse.2019.04.029

Mehmood, T. J., Warringer, L., Snipen, and Saebo, S. (2012). Improving stability and understandability of genotype-phenotype mapping in Saccharomyces using regularized variable selection in L-PLS regression. *BMC Bioinform.* 13, 1–13. doi: 10.1186/1471-2105-13-327

Mevik, B. H., and Wehrens, R. (2007). The pls Package: Principal component and partial least squares regression in R. *J.stat.software.* 18, 1–24. doi: 10.18637/jss.v018.i02

Mishra, P., Roger, J. M., Rimbaud-Bouveresse, D., Biancolillo, A., Marini, F., Nordon, A., et al. (2021). Recent trends in multi-block data analysis in chemometrics for multi-source data integration. *Trac-trend Anal Chem* 137:116206. doi: 10.1016/j.trac.2021.116206

Mohamed, E. S., Saleh, A. M., Belal, A. B., and Gad, A. A. (2018). Application of near-infrared reflectance for quantitative assessment of soil properties. *Egypt. J. Remote. Sens. Space Sci.* 21, 1–14. doi: 10.1016/j.ejrs.2017.02.001

Molajou, A. V., Nourani, A., Afshar, M., Khosravi, and Brysiewicz, A. (2021). Optimal design and feature selection by genetic algorithm for emotional artificial neural network (EANN) in rainfall-run off modeling. *Water Resour. Manag.* 21:2861. doi: 10.1007/s11269-021-02861-z

Morales, M., and Munné-Bosch, S. (2019). Malondialdehyde: Facts and artifacts. *Plant Physiol.* 180, 1246–1250. doi: 10.1104/pp.19.00405

Munnik, T. W., Ligterink, I. I., Meskiene, O., Calderini, J., Beyerly, A., Musgrave, and Hirt, H. (2000). Distinct osmo-sensing protein kinase pathways are

involved in signalling moderate and severe hyper-osmotic stress. *Plant J.* 20, 381–388. doi: 10.1046/j.1365-313x.1999.00610.x

Murphy, D. J., Brien, B. O., Donovan, M. O., Condon, T., and Murphy, M. D. (2021). A near infrared spectroscopy calibration for the prediction of fresh grass quality on irish pastures. *Inf. Process. Agric.* 4:12. doi: 10.1016/j.inpa.2021.04.012

Pasquini, T., and Celio, R. (2003). Near Infrared Spectroscopy: fundamentals, practical aspects and analytical applications. *J. Braz. Chem. Soc.* 14, 198–219. doi: 10.1590/S0103-50532003000200006

Plans, M., Sim,ó, J., Casañas, F., and Sabat,é, J. (2012). Near-infrared spectroscopy analysis of seed coats of common beans (*Phaseolus vulgaris* L.): a potential tool for breeding and quality evaluation. *J. Agric. Food Chem.* 60, 706–712. doi: 10.1021/jf204110k

Rinnan, A., Berg, V., and Engelsen, F. (2009). Review of the most common pre-processing techniques for near-infrared spectra. *Trac-trend Anal Chem.* 28, 1201–1222. doi: 10.1016/j.trac.2009.07.007

Sarker, L. R., and Nichol, J. E. (2011). Improved forest biomass estimates using alos avnir-2 texture indices. *Remote Sens. Environ.* 115, 968–977. doi: 10.1016/j.rse.2010.11.010

Stevens, A., and Ramirez-Lopez, L. (2020). *An introduction to the prospectr package*. R package Vignette.

Tenenhaus, M., Vinzi, V. E., Chatelin, Y., and Lauro, C. (2005). PLS path modeling. *Comput. Stat. Data Anal.* 48, 159–205. doi: 10.1016/j.csda.2004.03.005

Tong, L., Li, B., Geng, Y. H., Chen, L. J., Li, Y. J., and Cao, R. S. (2020). Spectrometric classification of bamboo shoot species by comparison of different machine learning methods. *Food Anal. Methods.* 14,300–306. doi: 10.1007/s12161-020-01885-2

Towler, M. J., Kim, Y., Wyslouzil, B. E., and Weathers, C. P. J. (2015). Medical cannabis and industrial hemp tissue culture: present status and future potential. *Front. Plant Sci.* 12:627240. doi: 10.3389/fpls.2021.627240

Tran, T. N., Afanador, N. L., Buydens, L., and Blanchet, L. (2014). Interpretation of variable importance in partial least squares with significance multivariate correlation (sMC). *Chemometr. Intell. Lab Syst.* 138, 153–160. doi: 10.1016/j.chemolab.2014.08.005

Wang, Y. J., Li, T. H., Li, L. Q., Ning, J. M., and Zhang, Z. Z. (2020). Micro-nir spectrometer for quality assessment of tea: comparison of local and global models. *Spectrochim. Acta A Mol. Biomol. Spectrosc.* 237:118403. doi: 10.1016/j.saa.2020.118403

Wang, Q. C., Lu, A. J., and Feng, J. (2016). Effects of drought stress on physiological indices of *Japanese Larch*. *J For Res.* 44, 13–18. doi: 10.13759/j.cnki.dlxb.2016.08.003

Wickham, H. (2017). ggplot2: Elegant graphics for data analysis. *J. Stat. Softw.* 17:02. doi: 10.18637/jss.v077.b02

Wold, S. M., Sjöström, T., and Eriksson, L. (2001). PLS-regression: a basic tool of chemometrics. *Chemometr Intell Lab Syst.* 58,109–130. doi: 10.1016/S0169-7439(01)00155-1

Xiao, N., Cao, D., Li, M., and Xu, Q. (2019). *enpls: Ensemble Partial Least Squares Regression.* Available online at: cloud.r-project.org/?package=enpls

Xu, C. C., Zhao, S. J., and Zuo, Q. (1993). Interference in measurement of lipid peroxidation by thiobarbituric acid test in plant tissues. *Plant Physiol. Commun.* 29, 361–363.

Xu, L., Zhou, Y. P., Tang, L. J., Wu, H. L., Jiang, J. H., and Shen, G. L. (2008). Ensemble preprocessing of near-infrared (nir) spectra for multivariate calibration. *Anal. Chim. Acta.* 616, 138–143. doi: 10.1016/j.aca.2008.04.031

Yan, Y. L., Zhao, L. L., and Li, J. H. (2000). Information technology of modern NIR spectral analysis. *Spectroscop. Spectr. Anal.* 20, 777–780.

Yi, M., Jia, T., Dong, L. M., Zhang, L., Leng, C. H., Liu, S. Y., et al. (2021). Resin yield in Pinus elliottii Engelm. is related to the resin flow rate, resin components and resin duct characteristics at three locations in southern China. *Ind. Crops Prod.* 160, 113–141. doi: 10.1016/j.indcrop.2020.113141

Yi, N. J., Han, Z. M., and Yin, D. M. (2000). Genetic variation of RAPD markersin a disease resistant seed orchard of *Pinus elliottii* engelm. *Scientia Silvae Sinicae.* 36, 51–55. doi: 10.3321/j.issn:1001-7488.2000.Z1.007

Yu, H., Zuo, S., Xia, G., Liu, X., Yun, Y., and Zhang, C. (2020). Rapid and non-destructive freshness determination of tilapia fillets by a portable near-infrared spectrometer combined with chemometrics methods. *Food Anal. Methods* 13, 1918–1928. doi: 10.1007/s12161-020-01816-1

Zhu, N. (2014). *Effects of Water Stress on Growth and Physiological Characteristics in Pinus sylvest var. Sylvestriformis*. Jilin Agricultural University.

Zou, X., Zha, J., Povey, M., Holmes, M., and Mao, H. (2010). Variables selection methods in near-infrared spectroscopy. *Anal. Chim. Acta.* 667, 14–32. doi: 10.1016/j.aca.2010.03.048

Conflict of Interest: The authors declare that the research was conducted in the absence of any commercial or financial relationships that could be construed as a potential conflict of interest.

Publisher's Note: All claims expressed in this article are solely those of the authors and do not necessarily represent those of their affiliated organizations, or those of the publisher, the editors and the reviewers. Any product that may be evaluated in this article, or claim that may be made by its manufacturer, is not guaranteed or endorsed by the publisher.

frontiers in Plant Science

ORIGINAL RESEARCH
published: 01 December 2021
doi: 10.3389/fpls.2021.689220

The European Forest Condition Monitor: Using Remotely Sensed Forest Greenness to Identify Hot Spots of Forest Decline

Allan Buras[1]*, *Anja Rammig*[1] and *Christian S. Zang*[1,2]

[1] Land Surface-Atmosphere Interactions, Technische Universität München, Freising, Germany, [2] Forests and Climate Change, Hochschule Weihenstephan-Triesdorf, Freising, Germany

Forest decline, in course of climate change, has become a frequently observed phenomenon. Much of the observed decline has been associated with an increasing frequency of climate change induced hotter droughts while decline induced by flooding, late-frost, and storms also play an important role. As a consequence, tree mortality rates have increased across the globe. Despite numerous studies that have assessed forest decline and predisposing factors for tree mortality, we still lack an in-depth understanding of (I) underlying eco-physiological mechanisms, (II) the influence of varying environmental conditions related to soil, competition, and micro-climate, and (III) species-specific strategies to cope with prolonged environmental stress. To deepen our knowledge within this context, studying tree performance within larger networks seems a promising research avenue. Ideally such networks are already established during the actual period of environmental stress. One approach for identifying stressed forests suitable for such monitoring networks is to assess measures related to tree vitality in near real-time across large regions by means of satellite-borne remote sensing. Within this context, we introduce the European Forest Condition monitor (EFCM)—a remote-sensing based, freely available, interactive web information tool. The EFCM depicts forest greenness (as approximated using NDVI from MODIS at a spatial resolution of roughly 5.3 hectares) for the pixel-specific growing season across Europe and consequently allows for guiding research within the context of concurrent forest performance. To allow for inter-temporal comparability and account for pixel-specific features, all observations are set in relation to normalized difference vegetation index (NDVI) records over the monitoring period beginning in 2001. The EFCM provides both a quantile-based and a proportion-based product, thereby allowing for both relative and absolute comparison of forest greenness over the observational record. Based on six specific examples related to spring phenology, drought, late-frost, tree die-back on water-logged soils, an ice storm, and windthrow we exemplify how the EFCM may help identifying hotspots of extraordinary forest greenness. We discuss advantages and limitations when monitoring forest condition at large scales on the basis of moderate resolution remote sensing products to guide users toward an appropriate interpretation.

Keywords: MODIS NDVI, drought, late frost, phenology, water stress, ice storm, windthrow

OPEN ACCESS

Edited by:
Veronica De Micco,
University of Naples Federico II, Italy

Reviewed by:
Anna Brook,
University of Haifa, Israel
Antonio Gazol,
Superior Council of Scientific Investigations, Spain
Luís Pádua,
National Research Council (CNR), Italy

***Correspondence:**
Allan Buras
allan@buras.eu

Specialty section:
This article was submitted to Plant Abiotic Stress, a section of the journal Frontiers in Plant Science

Received: *31 March 2021*
Accepted: *28 September 2021*
Published: *01 December 2021*

Citation:
Buras A, Rammig A and Zang CS (2021) The European Forest Condition Monitor: Using Remotely Sensed Forest Greenness to Identify Hot Spots of Forest Decline. Front. Plant Sci. 12:689220. doi: 10.3389/fpls.2021.689220

INTRODUCTION

The higher frequency of more extreme climate conditions in course of climate change poses certain threats on forests worldwide (Allen et al., 2010, 2015; Anderegg et al., 2015; Vitasse et al., 2019; Buras et al., 2020; Kannenberg et al., 2020). Among potential direct causes of the resulting forest decline and tree mortality are in particular so-called hotter droughts (Allen et al., 2010, 2015; Buras et al., 2018; Brun et al., 2020; Rita et al., 2020; Schuldt et al., 2020), late-frost (Menzel et al., 2015; Príncipe et al., 2017; Vitasse et al., 2019), periodically water-logged soils after floods and heavy precipitation (Kreuzwieser and Rennenberg, 2014), ice storms (Roženbergar et al., 2020), and winter storms (Valinger et al., 2014). Since extreme environmental conditions often impair tree defense mechanisms, secondary pathogens such as fungi and beetles frequently amplify tree decline and die-back rates (Bigler et al., 2006; Kohler et al., 2010; Spruce et al., 2019).

Although the underlying environmental causes of observed forest decline often can be identified, the individualistic response of trees to extreme environmental conditions remains largely unexplained. Therefore, we currently lack a mechanistic explanation of frequently observed individual growth responses to adverse climatic conditions which may ultimately result in neighboring dying and surviving trees of the same species (Cailleret et al., 2017). Even though first assessments have identified soil properties, stand structure, and micro-climate as influencing factors of forest decline and tree mortality (Lévesque et al., 2013; Rehschuh et al., 2017; Buras et al., 2018), the eco-physiological processes that govern the fate of single trees still need further investigation (Bascietto et al., 2018; D'Andrea et al., 2019; Dox et al., 2020, 2021; Schuldt et al., 2020). One reason for this important research gap is related to the fact that key eco-physiological processes such as sap flow, regulation of leaf water potential, and changes in xylem conductivity cannot be studied retrospectively for dead trees. At the same time, it is difficult to forecast where, when, and which trees are going to die in order to install monitoring equipment prior to death.

An important approach to deepen our knowledge on forest decline is the evaluation of large-scale tree-ring networks which allows for a retrospective analysis of secondary tree growth and its relation to environmental factors. For instance, the effects of droughts on tree growth have been studied using large tree-ring networks, which suggested so-called drought legacies, i.e., prolonged reductions of secondary growth after drought, to render a frequently observed phenomenon (Anderegg et al., 2015; Kannenberg et al., 2018, 2020; Gazol et al., 2020). More specific tree-ring networks targeting both dead and live trees revealed that dying trees often featured decreased growth rates if compared to surviving trees up to several decades prior to death (Camarero et al., 2015; Pellizzari et al., 2016; Cailleret et al., 2017; Buras et al., 2018). Another important source of information within this context comes from long-term ecological monitoring and the evaluation of eddy covariance data from flux towers within large networks [e.g., long-term ecological research (LTER), integrated carbon observation system (ICOS), and FLUXNET] which allow for quantifying declining net biome production under extreme climatic conditions (e.g., Ciais et al., 2005; Bastos et al., 2020; Pastorello et al., 2020).

Despite the value of the aforementioned retrospective investigations, a deeper process-based understanding of forest decline can only be achieved by intensively monitoring stressed and/or dying trees throughout the stress period and the process of death (Bascietto et al., 2018; D'Andrea et al., 2019; Dox et al., 2020, 2021; Scharnweber et al., 2020; Schuldt et al., 2020). As mentioned above, this however requires timely installation of monitoring equipment. Consequently, the majority of our knowledge about tree eco-physiology under extreme conditions is based on experimental treatments of saplings (e.g., Seidel and Menzel, 2016; Seidel et al., 2016; Ruehr et al., 2019; Seo et al., 2020).

To increase the available data for studying forest decline, it is necessary to identify hotspots of forest stress in space and time, ideally, in near real-time to allow for contemporary investigations under stressful conditions. Satellite-borne remote sensing renders a means to obtain such information on a large scale. That is, satellites provide information on vegetation surface reflectance which can be translated into vegetation indices and/or products that serve as proxies for tree condition and productivity (Kogan, 1995; Anyamba and Tucker, 2012; Misra et al., 2016; Rogers et al., 2018; Liu et al., 2019; Spruce et al., 2019; Brun et al., 2020; Buras et al., 2020; Rita et al., 2020; Shekhar et al., 2020). If corresponding satellite imagery is regularly updated and obtained at fairly high spatiotemporal resolution (i.e., high enough to resolve single forest stands at weekly intervals) over decades to provide sufficiently long referencing periods, such data can be used to generate products that allow for a near-real time monitoring of forest condition (but see section Limitations for limitations of this approach).

Within this context, we here introduce a framework for monitoring European forest condition, the European Forest Condition Monitor (EFCM), a freely available web information tool which is based on Terra Moderate Resolution Imaging Spectroradiometer Normalized Difference Vegetation Index (MODIS NDVI, see section Computation of Central Metrics). The EFCM provides relative measures of forest greenness at a spatial resolution of 231.25 × 231.25 m at 16-day intervals. The main purpose of the EFCM is to provide forest researchers, stakeholders, and policy makers with large scale information on forest condition allowing for identifying hotspots of extraordinary canopy greenness. Based on the information provided by the EFCM, additional ground-based investigations and monitoring campaigns may help to elucidate the causes underlying extraordinary canopy greenness, thereby potentially deepening our knowledge on the eco-physiology of trees under stress within a natural setting. In the following, we describe the methodological approach of the EFCM and exemplify its application using specific case studies related to phenology, drought, late-frost, flooding, ice storms, and windthrow.

MATERIALS AND METHODS

Computation of Central Metrics

The EFCM is based on 16-day maximum value composites derived from daily Terra MODIS NDVI observations spanning the period of 2001 to current at a spatial resolution of 231.25 × 231.25 m and covering the area of Europe. We based the EFCM on NDVI since it represents vegetation greenness which reflects tree-species phenology (Misra et al., 2016, 2018) and responds sensitively to drought-stress in trees (Anyamba and Tucker, 2012; Orth et al., 2016; Buras et al., 2018, 2020; Brun et al., 2020; Rita et al., 2020), late-frost damage (Rubio-Cuadrado et al., 2021), tree die-back (Rogers et al., 2018; Liu et al., 2019; Spruce et al., 2019), and has been used to compute vegetation condition indices (e.g., Kogan, 1995). Given its wide application within a forest-decline context, we consider NDVI as a meaningful proxy for actual forest condition which, in case of extreme values, may represent extraordinary phenology (early start of the season and early senescence, e.g., Misra et al., 2016; Brun et al., 2020) or canopy greenness due to atypical environmental conditions such as drought, late-frost, water-logged soils succeeding long-lasting precipitation events, ice storms, and windthrow (e.g., Bascietto et al., 2018; Buras et al., 2020; Rita et al., 2020). NDVI is computed according to Equation 1 (see also Rouse et al., 1974):

$$NDVI = \frac{NIR - RED}{NIR + RED} \quad (1)$$

with NIR representing the surface reflectance in the near infrared spectrum and RED representing the surface reflectance in the red spectrum. Given its computation, NDVI ranges from −1 to 1 with (1) negative values representing clouds, water, and snow, (2) values around zero representing bare rock and soil, while (3) values above 0.5 typically represent densely vegetated surfaces such as forests or crops (Lillesand et al., 2014). NDVI and pixel quality information layers are obtained from the Application for Extracting and Exploring Analysis Ready Samples (AppEEARS)[1]. The preparation of NDVI time series is based on previous studies (Misra et al., 2016, 2018; Buras et al., 2020) and will be described in the following.

For masking MODIS NDVI of non-forest areas, we use the Coordinated Information on the European Environment land cover map (CORINE, Büttner et al., 2004) retrieved from COPERNICUS[2] at a spatial resolution of 100 m and remapped to the MODIS projection using the nearest neighbor method to retain the original classes. The retrieved MODIS layers are masked to only represent pixels which according to the different time-steps of CORINE land-cover since the year 2000 (i.e., 2000, 2006, 2012, and 2018) consistently refer to the land-cover classes of broadleaved forest, coniferous forest, and mixed forest, thereby lowering the probability of artifacts from land-use change.

The MODIS pixel quality layers are used to mask NDVI-pixels of the corresponding time-step that represent poor quality to keep the influence of snow and clouds on NDVI time series as low as possible. Thus, only pixels with good and marginal quality are retained for further analyses. Due to this masking, pixel-specific time series usually contain gaps which are linearly interpolated from the neighboring values. Since the gap-filled time series may still contain pixels with insufficient quality that is usually reflected in extraordinarily low NDVI values, we subsequently identify and remove negative outliers. Outliers are defined as those exceeding two negative standard deviations of standardized differences between interpolated NDVI time series and a corresponding Gaussian-filtered time series whose filter size was chosen to be 80 days, i.e., 5 time steps (Misra et al., 2016). Removed outliers are replaced by the corresponding values of the Gaussian-filtered time series. Eventually, the quality-checked, gap-filled, and outlier-removed NDVI time series is smoothed by applying the same Gaussian filter with a window size of five time steps. The resulting time series are finally detrended individually, i.e., pixel-specific to remove long-term trends that have been reported for vegetation indices (Bastos et al., 2017; Buras et al., 2020).

To represent relative forest condition for specific days of the year (DOYs) over the whole observational period (2001-current), we, for each pixel and time step, computed the corresponding quantile *Q*. That is, each pixel-specific time-series was transformed into quantiles by assigning each value its corresponding rank within all observations of this pixel and dividing it by the number of observations:

$$Q_t = \frac{R(NDVI_t)}{n} - \frac{1}{n \cdot 2} \quad (2)$$

with *R* representing the relative rank of the NDVI at a given time step *t* and *n* being the number of total observations. The subtraction by $1/(n \times 2)$ is applied to center the quantiles around 0.5. Consequently, Q_t values range from $1/(n \times 2)$ to $1–1/(n \times 2)$. While a value of $1/(n \times 2)$ represents the absolutely lowest observation over the period of investigation (currently 2001–2020) for a given DOY at a given pixel, the value $1\text{-}1/(n \times 2)$ indicates the absolutely highest observation. This metric is closely related to the vegetation condition index (VCI, Kogan, 1995). However, it does not have the disadvantage of the VCI to become heavily skewed in case extreme values enter the distribution. That is, since VCI relies on the range of NDVI over the observational period, extraordinarily low or high NDVI values can lead to heavily skewed distributions, whereas the computation of quantiles results in uniformly distributed observations.

In addition, since a rank-based measure as *Q* does not allow for comparing absolute changes in NDVI among pixels, we computed proportional deviations from the median (*PDM*) for each pixel-DOY combination according to Equation 3:

[1]AppEEARS Team (2021). Application for Extracting and Exploring Analysis Ready Samples (AppEEARS). NASA EOSDIS Land Processes Distributed Active Archive Center (LP DAAC), USGS/Earth Resources Observation and Science (EROS) Center, Sioux Falls, South Dakota, USA. Available online at: https://lpdaacsvc.cr.usgs.gov/appeears (accessed September 16, 2021).

[2]COPERNICUS Corine land cover: https://land.copernicus.eu/pan-european/corine-land-cover.

$$PDM_t = \frac{NDVI_t - \overline{NDVI}}{\overline{NDVI}} - 1 \quad (3)$$

With the bar over NDVI indicating the median over all observations. Consequently, *PDM* represents a proportional deviation from the median and thus allows for better comparison among pixels since it is not related to the range of local NDVI observations as is the case with *Q*. Thus, *PDM* can be considered a metric which complements *Q* since it allows for depicting absolute variations in comparison to ranks as is the case with *Q*. We applied these two standardization methods to account for pixel-specific stand characteristics (e.g., tree-species, soil type) that result in pixel-specific statistical properties of NDVI time-series. While doing so, we opted for non-parametric estimates of forest condition since parametric estimates, for instance, a z-transformation, rely on parameter estimates (in case of z-transformation mean and standard deviation) which assume an underlying normal distribution which is not fulfilled for NDVI that features a bounded distribution (Buras et al., 2020). Due to this standardization procedure, differences among pixels regarding their absolute NDVI are masked. Consequently, spatial variations in *Q* and *PDM* should be interpreted as pixel-specific, relative differences in forest greenness over time and not as absolute variations in forest greenness among pixels.

We constrained the visualization of *Q* and *PDM* to the pixel-specific growing season to account for differing lengths of growing seasons across Europe. In order to define the pixel-specific growing season, we used high resolution (1 km²) CHELSA (Climatologies at high resolution for the earth's land surface areas) monthly mean temperature climatologies (Karger et al., 2017) which were remapped to MODIS resolution and linearly interpolated to daily climatologies for each pixel. For each pixel the period with a temporally interpolated mean temperature above 5°C was defined as the growing season. The threshold of 5°C is based on identified thresholds for cambial activity, xylogenesis, and growth (Rossi et al., 2007; Körner, 2015).

For the visualization, we use color charts ranging from red, over orange, yellow, dark-gray, light-blue, and dark blue representing a gradient from low to high values of *Q* and *PDM*, respectively. Thus, while reddish colors represent relatively low forest greenness, blueish colors refer to high greenness. Light-gray colors indicate pixels outside the pixel-specific growing season. For *Q*, the color chart is resolved in steps representing the number of expected quantiles. That is, for the current observation period spanning 20 years (2001–2020), the color-chart is resolved into 21 classes according to 20 breaks ranging from 1/40 to 1–1/40 in steps of 1/20. For *PDM*, we subjectively decided for resolving deviations from below −10% to above +10% in steps of 2.5%. This selection was based on observations of tree dieback following severe drought (Buras et al., 2018), for which corresponding pixels in the year of drought featured deviations between −20 and −5%, and, on average, −10%. Thus, red colors in *PDM* maps relate to deviations for which mortality of individual trees has been observed, which however does not necessarily mean that PDM value in the order of −10% does not necessarily indicate mortality. The threshold of −10% also corresponds well with the steep increase in observed tree-mortality caused by Mountain pine beetles in the Rocky Mountains beyond an NDVI decline of 10% (see Figure 6 in Spruce et al., 2019).

Since *Q* allows for a more systematic color-chart in terms of visualization in comparison to *PDM* for which we subjectively decided on color-chart thresholds, we in our study emphasize on *Q* in the main text while *PDM* is shown in the **Supplementary Information**. Nonetheless, the two metrics can be considered equally meaningful for interpreting variations in forest greenness.

To allow the public to retrieve information based on the EFCM framework, a web-based interactive application has been established at http://interaktiv.waldzustandsmonitor.de/. This Forest Condition Monitor allows for viewing *Q* and *PDM* for the entire European Union for any given date over the monitoring period (2001-now). Users can interactively select which product (*Q* and *PDM*) to display for two different dates, allowing for comparison (e.g., 2003 vs. 2018 as in Buras et al., 2020). *Q* and *PDM* are visualized as colored maps and histograms which allow for quantifying the relative spatial share of specific values of *Q* and *PDM* for the selected dates (the breaks used for the coloration are mentioned above). The underlying data can be downloaded as geo-tiffs. The code underlying the EFCM-viewer has been programmed within the "R-Shiny" environment (Chang et al., 2021) and is provided in the **Supplementary Material** of this article. Due to high computational costs, the monitored period of the EFCM viewer will be updated twice a year, i.e., at peak season (end of July) as well as at the end of the year.

Performance Examples

To exemplify the performance of *Q* and *PDM* under different environmental settings, we first depict the temporal development of peak season NDVI (i.e., end of July, represented by DOY 209) from 2001 to 2020 (section Q and PDM From 2001 to 2020). Secondly, we visualize the performance of specific DOY *Q* or *PDM* for selected regions that represent the onset of the growing season, i.e., land-surface phenology (section Land Surface Phenology), forest condition under extreme drought (section Drought), forest condition succeeding late-frost (section Late-frost), forest condition under water-logged soils (section Water Stress), forest condition following an ice storm (section Ice Storm), and forest condition succeeding windthrow (section Windthrow). The specific selection of locations for these examples was based on the knowledge of extraordinary events by the first author of this article.

For the phenology example, we emphasized on Germany and downloaded phenological observations of budburst in beech, which together with pedunculate and sessile oak represents the most abundant deciduous tree species in Germany. Data were obtained from the German Meteorological Service (DWD) for the period 1951–2020. For each year, we computed the mean DOY of budburst over all stations as a representation for the Germany-wide onset of the growing season. We depict *Q* and *PDM* representative of the first of May for the total area of Germany of the year with the earliest onset (2014) and in addition compute a linear regression between mean *Q* and *PDM* and mean budburst (all averaged over Germany) for the common overlap period, i.e., 2001–2020.

In terms of visualizing forest condition under drought, we selected the extreme drought of 2015 which resulted in increased die-back rates of Scots pine in Franconia, Southern Germany (Buras et al., 2018). Here, we depict *Q* and *PDM* for the study region investigated in Buras et al. (2018) for the first of May 2015 (i.e., before the drought), the 13th of August, 2015 (peak of drought), and the first of May 2016 (after the drought). Based on a tree-species cover map (Brus et al., 2012), we extracted *Q* and *PDM* values that corresponded to pixels dominated by Scots pine (relative share per pixel > 70%) and compared those between the three dates visually and using pairwise Wilcoxon rank sum test.

For the late-frost example, we focused on Bavaria in 2011 where a major late-frost event on May 4th (DOY 124) caused foliage damage in beech-trees over a large area (Menzel et al., 2015; Príncipe et al., 2017). We showed maps of *Q* and *PDM* for DOYS 121 and 153 to represent NDVI prior to the event and 4–5 weeks after the event when affected beech trees were about to rebuild their canopy (Menzel et al., 2015). Besides these two time-slices, we also analyze the behavior of *Q* and *PDM* over several time-slices, beginning at DOY 105 and ending at DOY 217, when beech trees presumably had rebuilt their full canopy (Menzel et al., 2015). Thereby, we emphasized on pixels for which beech cover was larger than 45% according to Brus et al. (2012). The selection of 45% as threshold for beech dominance was a necessary compromise, since only few pixels in Bavaria feature beech cover above 50%. Using 45% as threshold left us with 4,938 pixels for the analyses. We then distinguished between beech-pixels which were likely to have experienced frost on May 4th and those which were unlikely to have experienced frost. Frost's likelihood was indicated by thin-plate spline interpolated daily minimum temperature data from climate stations of the German Meteorological service using a digital elevation model at 30 m resolution (SRTM30, Becker et al., 2009) which was remapped to MODIS resolution. The threshold for frost occurrence was set to −1°C to account for the imprecision of the interpolated data whose difference to absolute observations featured a standard deviation of 0.5. Thus, for pixels below −1°C the likelihood of actually experiencing frost on that day is roughly 97.5 %. This left us with 4,708 and 230 beech dominated pixels that were likely or unlikely, respectively, to have experienced late-frost on May 4, 2011.

To exemplify the performance of *Q* and *PDM* under water-stress, we focused on the Darß-Zingst-peninsula in Northern Germany, which is characterized by forests growing on formerly drained and recently rewetted coastal mires. Due to the establishment of the national park, "Vorpommersche Boddenlandschaft," in 1990, the drainage of mires was gradually stopped over the last decades, wherefore the extremely wet summer of 2011 resulted in waterlogging in large parts of the national park over a period of several months. As a consequence, a remarkable number of trees, mostly alder (*Alnus glutinosa*) and birch (*Betula pubescens*) growing on the formerly drained mires, suffered from water stress and eventually died. To examine how the EFCM mirrors such events, we extracted peak season (DOY 209) *Q* and *PDM* for the years 2010 through 2013 and mapped those for the peninsula. In addition, we extracted *Q* and *PDM* for the two areas that had featured the most remarkable die-back ("Neudarß" and "Sundische Wiesen") for each time step and compared time steps to each other visually along with using pairwise Wilcoxon rank sum test. To visualize how extraordinary precipitation sums were in 2011, we used climate station data from the German Meteorological Service (DWD) of the closest station with a continuous precipitation record since 1970, i.e., "Groß Lüsewitz" ∼40 km south of the peninsula.

For the ice storm example, we focused on the extreme ice storm that hit Slovenia in February 2014 (Roženbergar et al., 2020). Here, we compared the temporal development of *Q* and *PDM* from DOY 97 to DOY 289 (i.e., most of the local growing season) in 2005 for areas that were affected or unaffected by the ice storm, respectively. To identify the corresponding areas, we digitized and georeferenced the map shown in Roženbergar et al. (2020) and applied the resulting shapefile to extract *Q* and *PDM* for the corresponding EFCM maps and categorized the values as either affected or unaffected. Extracted values were statistically compared for each DOY according to the two categories using Wilcoxon rank-sum test.

Regarding the performance of EFCM following windthrow, we focused on the extreme winter storm "Gudrun" which resulted in extraordinary windthrow in southern Sweden in January 2005 (Valinger et al., 2014). For this, we extracted end of June *Q* and *PDM* values for 2005 and grouped them according to maximum wind gust speed, which was downloaded from the Extreme Wind Storms Catalog[3]. We defined groups by subtle storm impact (maximum wind gust < 20 m/s, i.e., <9 Beaufort) and then sequentially increasing storm impact in steps of 5 m/s up to wind gusts stronger than 45 m/s. The resulting groups were compared statistically using a one-sided Wilcoxon rank-sum test comparing subtle storm impacts (gust speed < 20 m/s) with the remaining groups under the assumption that *Q* and *PDM* should decrease with increasing maximum wind gust speed.

All analyses were computed in R (version 4.0.3, R foundation for statistical computing in Vienna, 2021) extended for the packages raster (Hijmans, 2017), rgdal (Keitt et al., 2011), fields (Nychka et al., 2017), and shiny (Chang et al., 2021).

RESULTS

Q and *PDM* From 2001 to 2020

End of July EFCM quantiles *Q* and proportional deviations from the median *PDM* show clear trends over the study period from 2001 until 2020 (**Figure 1**, **Supplementary Figure 1**). Specifically, the amount of low quantiles and negative deviations (red colors in **Figure 1**, **Supplementary Figure 1**) feature an increasing share, which peaks in the years 2018 and 2019. Considering spatiotemporal variations (see **Supplementary Videos 1, 2**), the well-known major drought events of 2003 (central and southern Europe), 2006 (Baltic states), 2012 (south-eastern Europe), 2015 (central and southern Europe), 2017 (Mediterranean region), 2018 (central and northern Europe), and 2019 (southwestern, central, and

[3]Extreme Wind Storm Catalog. Available online at: http://www.europeanwindstorms.org, Copyright Met Office, University of Reading and University of Exeter.

northern Europe) are all reflected by regionally low *Q* and *PDM* values (compare **Figure 1**, **Supplementary Figure 1** with **Supplementary Figure 2**). However, not all the observed extreme values (high and low) are related to drought, as will be shown in Sections Land Surface Phenology, Late-frost, Water Stress, Ice Storm, and Windthrow.

Land Surface Phenology

Early season quantiles featured a significant negative relationship with forest phenology (**Figure 2**). For instance, the year 2014 which featured the earliest observed budburst of beech across Germany in the period 1950–2020 (blue dot in **Figure 2B**) was characterized by a high share of high *Q* and *PDM* values (**Figure 2A**, **Supplementary Figure 3A**). Over the common overlap period, mean DOY of beech budburst explained 48 and 50% of variance ($p < 0.001$) of *Q* and *PDM* on May 1st, respectively (**Figure 2C**, **Supplementary Figure 3C**).

Drought

Comparing *Q* and *PDM* before and after the extreme drought of 2015 in Franconia, Northern Bavaria indicated a clear and negative response of forests to drought. Particularly during the peak of drought in August 2015 (**Figure 3B**, **Supplementary Figure 4B**), large parts of the study area featured extraordinarily low *Q* and *PDM* and overall lower in comparison to the onset of the growing season 2015 (**Figures 3A,D**, **Supplementary Figures 4A,D**). Also, at the onset of the growing season of 2016, *Q* and *PDM* featured significantly lower locations (i.e., the non-parametric mean that is tested for in Wilcoxon rank-sum test) if compared to before the drought (**Figures 3C,D**, **Supplementary Figures 4C,D**).

Late-Frost

Comparing *Q* and *PDM* on DOY 121 in 2011 (just before the late-frost event on DOY 124) to *Q* and *PDM* on DOY 153 revealed a much higher share of low *Q* and *PDM* 4 weeks after the late-frost event (**Figures 4A** vs. **4B**, **Supplementary Figures 5A** vs. **5B**), particularly in the region that experienced freezing temperatures at DOY 124 (**Supplementary Figure 6**). If analyzed over time, pixels representing a high share of beech cover (>45%), featured a specific temporal development of *Q* and *PDM* depending on whether they had experienced minimum temperatures below or above −1°C at DOY 124. For pixels that had experienced below −1°C, *Q* and *PDM* decreased over time, whereas they increased over time for pixels that had experienced higher minimum temperatures (**Figure 4C**, **Supplementary Figure 5C**). Differences between these two groups remained significant until DOY 217, i.e., early in August.

Water Stress

The areas on the Darß-Zingst-peninsula that featured tree die-back due to extraordinary precipitation (**Figure 5F**) and, consequently, flooding during the wet summer of 2011 featured corresponding patterns of *Q* and *PDM*. In particular, peak-season *Q* and *PDM* values of affected areas significantly dropped in 2011 to reach minimum values in 2012 when the die-back occurred and eventually recovered partly in 2013 (**Figures 5A–E**, **Supplementary Figures 7A–E**). Aerial photographs of affected areas are shown in **Supplementary Figures 8, 9**.

Ice Storm

The areas in Slovenia that were affected by the ice storm in February 2014 clearly protruded by, on average, lower *Q* and *PDM* throughout the evaluated period (DOY 97-289, **Figures 6A,B**, **Supplementary Figures 10A,B**). However, not all areas appeared to have been equally affected, as indicated by remaining high *Q* and *PDM* values in the corresponding group. Nonetheless, time-step specific comparisons revealed statistical significance throughout the whole growing season of 2005, i.e., a significant shift to lower greenness in the affected areas (**Figure 6C**, **Supplementary Figure 10C**).

Windthrow

The area in Sweden which was hit by extreme wind gusts during the winter storm "Gudrun" in January 2005 featured comparably lower *Q* and *PDM* relative to regions with less extreme wind gusts (**Figures 7A,B**, **Supplementary Figures 11A,B**). For wind gusts stronger than 40 m/s, a significantly negative effect on *Q* and *PDM* distributions was observed which was most pronounced for wind gusts stronger than 45 m/s (**Figure 7C**, **Supplementary Figure 11C**, Wilcoxon rank-sum test $p < 0.001$ for both *Q* and *PDM*).

DISCUSSION

Using MODIS NDVI to Monitor European Forests

The EFCM relies on Terra MODIS NDVI to map the condition of European forests across space and time. The decision to use Terra MODIS NDVI for monitoring European forests is based on the fact that it is provided at a relatively high spatial resolution (231.25 × 231.25 m) with regularly obtained images (in theory daily images which are used to obtain 16-day maximum value composites) that cover a comparably long reference period (2001–2020). Particularly, the regular imaging of land-surface reflectance over long periods renders an important aspect of forest condition monitoring, allowing for tracing changes in greenness in near real-time and relating those to a relatively long monitoring period. While the spatial resolution is superseded by corresponding sensors of the LANDSAT (30 × 30 m) and Sentinel missions (10 × 10 m) by an order of magnitude, these high-resolution images do not provide data at equal temporal resolution. Despite a revisit frequency of 5 days at the equator for Sentinel 2, pixel quality frequently suffers from cloud coverage, both of which, in combination, lead to comparably longer gaps and thus higher uncertainty in corresponding time series. Regarding the reference period, LANDSAT satellites would allow extending the period of Sentinel 2 (beginning in 2015) further back in time however with the same drawback of comparably larger data gaps in comparison to MODIS. Nevertheless, we intend to extend the product portfolio of the EFCM by high-resolution sensors in the future allowing for a more detailed picture of European forest condition.

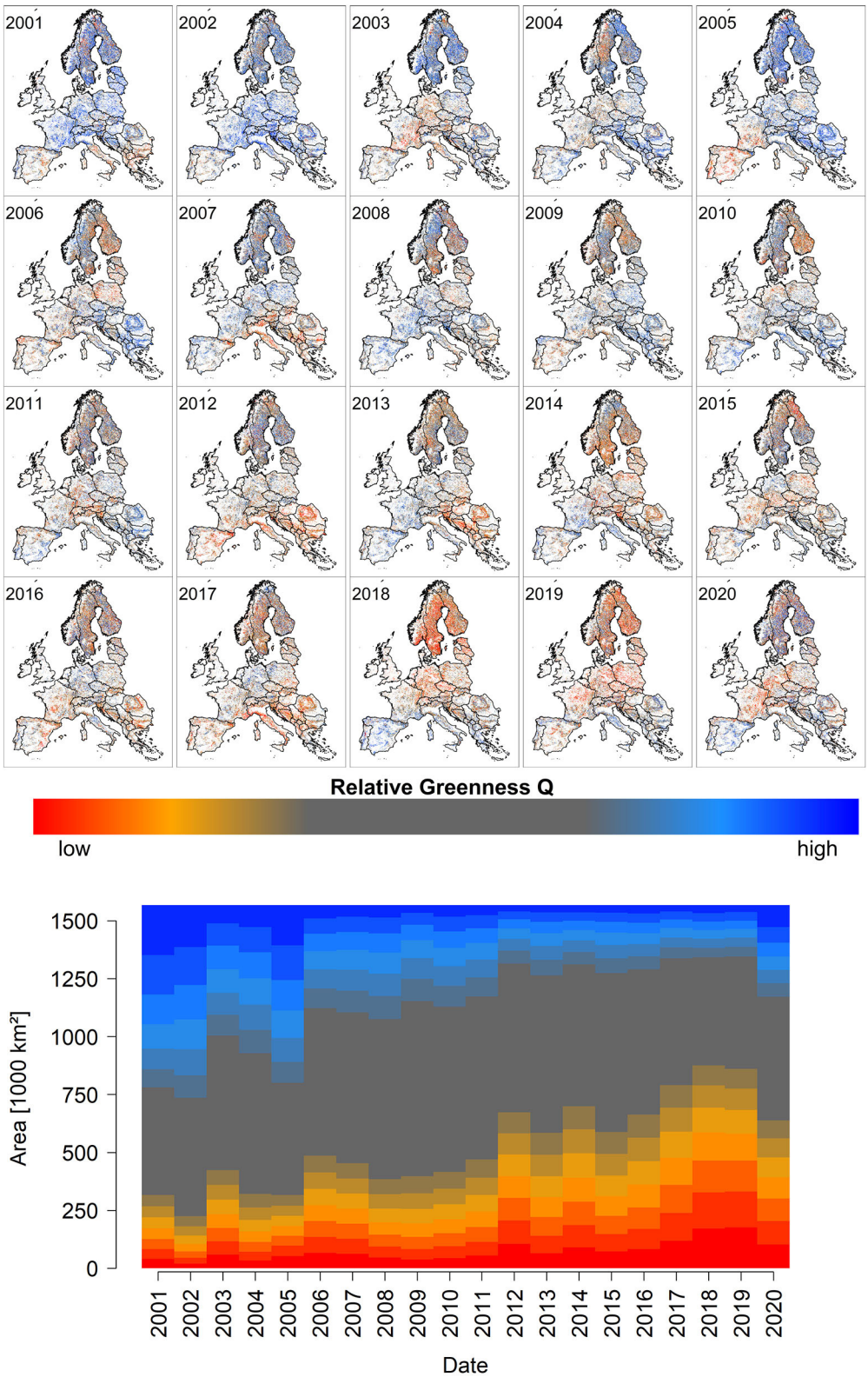

FIGURE 1 | The upper small panels depict the spatiotemporal development of peak season quantiles *Q* over the observational period from 2001 to 2020 (for an animated version with higher resolution please see **Supplementary Video 1**). The lower stacked barplot depicts the spatial share of corresponding quantiles. The value of *Q* increases from dark red over orange, gray, to blue shades. **Supplementary Figure 1** depicts similar information for *PDM*. A video depicting the spatio-temporal variation of *PDM* is shown in the **Supplementary Video 2**).

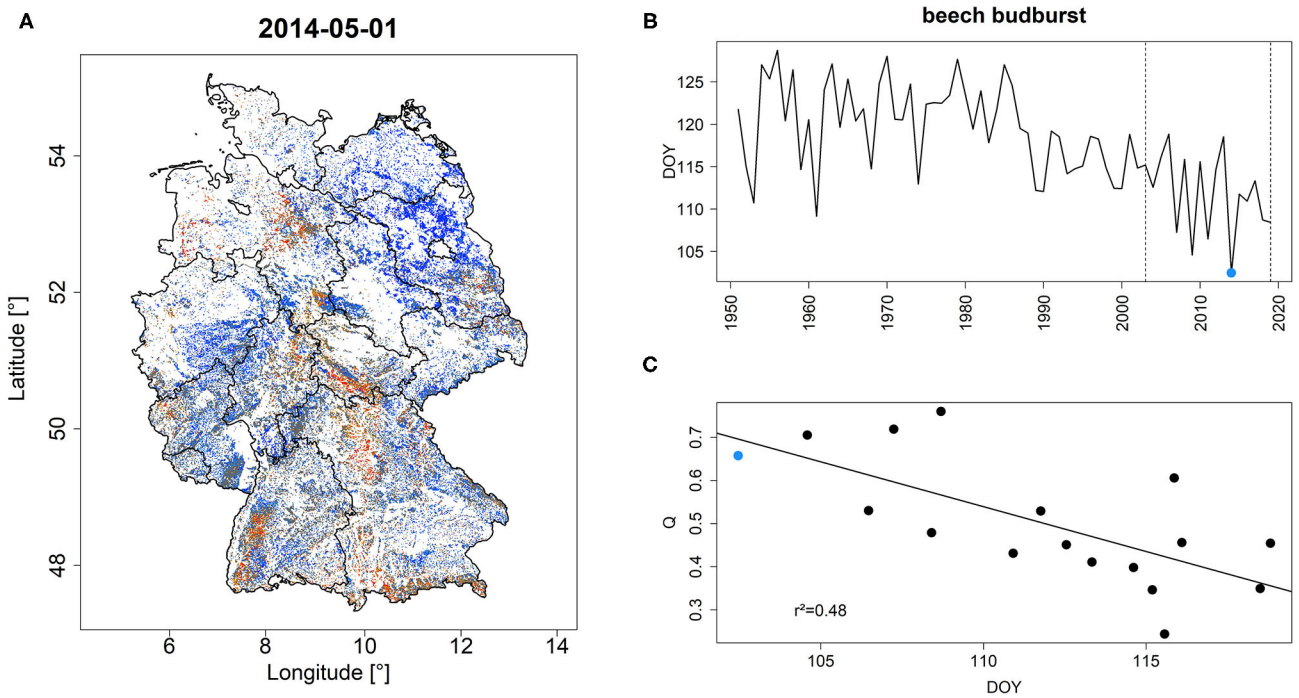

FIGURE 2 | *Q*-values in Germany for May 1, 2014 **(A)** which represents the year with the earliest bud-burst of beech across Germany for the period 1950–2020 **(B)**. *Q* features a significant negative relationship with the average DOY of beech budburst **(C)**. Vertical dashed lines in **(B)** refer to the common overlap period of beech phenology and monitoring period. The blue dot indicates the year 2014 which is depicted in **(A)**. r^2 in **(C)** refers to the explained variance of the depicted regression line. A similar figure but for *PDM* is shown in **Supplementary Figure 3**.

Regarding the choice of the product, we preferred NDVI over other available vegetation indices that have been used to quantify forest condition in the context of climate change. Among candidate vegetation indices are the solar induced chlorophyll fluorescence (SIF) and the enhanced vegetation index (EVI). While SIF was shown to provide a more precise proxy of GPP in comparison to NDVI (Liu et al., 2018; Shekhar et al., 2020), it suffers from relatively coarse spatiotemporal resolution. SIF observations are usually obtained at irregular frequencies with relatively long return periods for a given location and at the same time typically feature relatively coarse spatial resolutions of more than 1 km² which would not allow for forest monitoring on the aspired scale of individual forest stands. For instance, the NASA Orbiting Carbon Observatory provides SIF at a comparably high resolution (1.3 × 2.25 km) which, however, is insufficient to adequately resolve the heterogeneous landscape patterns in Central and Southern Europe. As a consequence, most of the acquired pixels show a mixed signal which makes it difficult to relate observed fluctuations to actual forest condition. Existing model-based gridded SIF products are able to circumvent the problem of irregular spatiotemporal sampling (Zhang et al., 2018), yet they suffer from a too coarse resolution of 0.05°, i.e., roughly 5 × 5 km in Central Europe. In case SIF-products become available at sufficiently high spatiotemporal resolution, extending the EFCM for valuable additional products will be considered. In contrast to SIF, EVI is also available from the MODIS mission and thus, at a similar spatio-temporal resolution as NDVI. Theoretically, the EFCM could therefore also be based on EVI, but we decided for NDVI since both metrics showed similar patterns for the most prominent European drought events, i.e., 2003 and 2018 (Buras et al., 2020) and NDVI, in comparison to EVI, has been used more frequently in the past for monitoring forest decline and die-back (Kogan, 1995; Xu et al., 2011; Anyamba and Tucker, 2012; Orth et al., 2016; Buras et al., 2018; Rogers et al., 2018; Liu et al., 2019; Brun et al., 2020; Rita et al., 2020) thus allowing for better comparability to existing studies. For the future, we intend to extend the product portfolio of the EFCM by additional vegetation indices such as EVI and SIF to provide a more complete picture of European forest condition. In this context, the next step forward would be to implement early-warning indicators which require integrating information over several time-steps based on statistical properties of NDVI time-series (Liu et al., 2019) along with an extensive testing and validation.

The overall development over the monitoring period of 2001–2020 (section Q and PDM From 2001 to 2020) and more specific case studies (sections Land Surface Phenology, Drought, Late-Frost, Water Stress, Ice Storm, and Windthrow) support the use of NDVI quantiles *Q* and proportional deviations from the median *PDM* for monitoring forest condition. Across Europe, the temporal development of *Q* and *PDM* indicates an increasing forest decline over the last two decades which

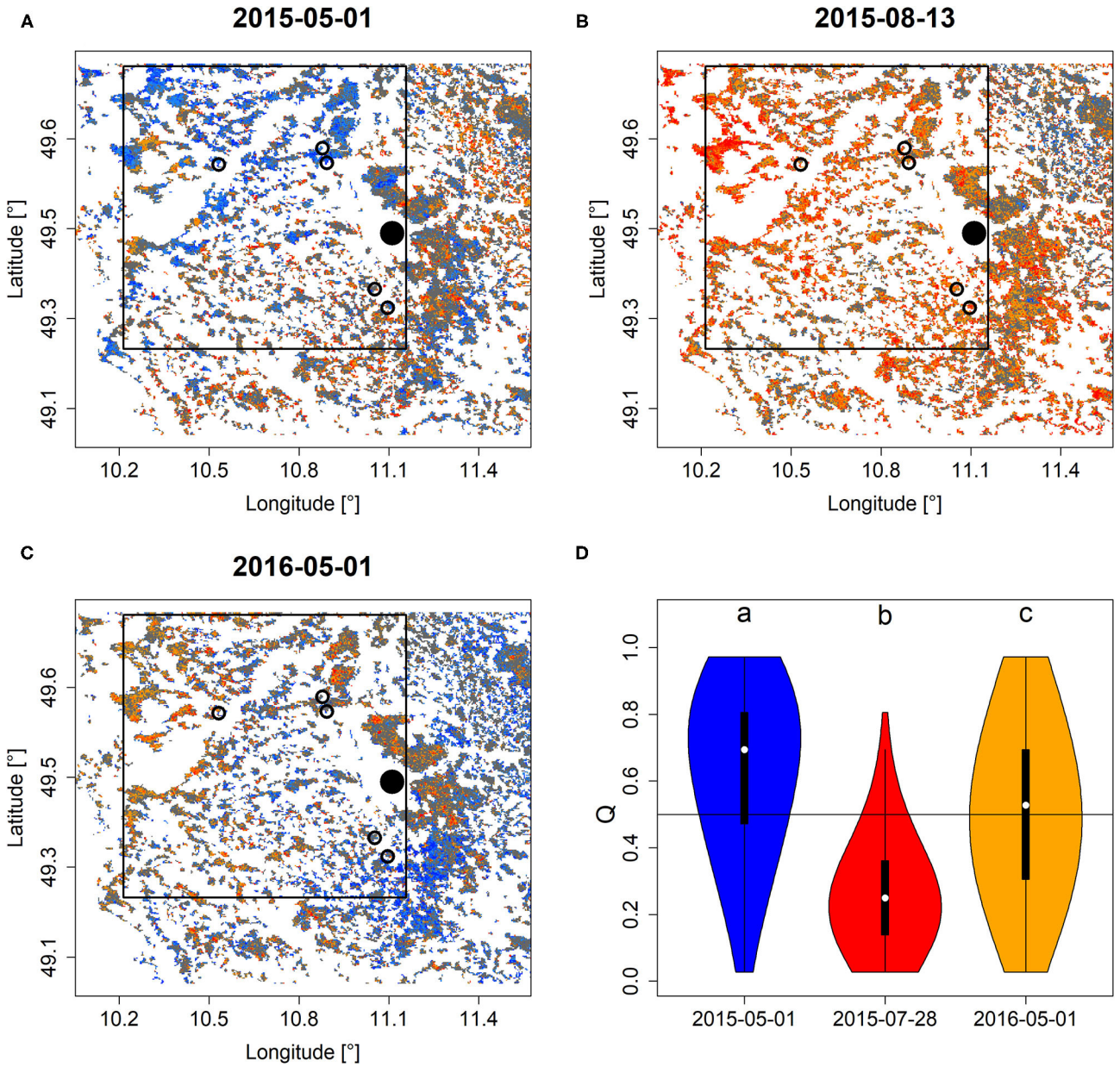

FIGURE 3 | *Q* mapped for the area surrounding Nuremberg (black dot) before **(A)**, during **(B)**, and after **(C)** the extreme drought of 2015. Circles refer to study sites investigated in Buras et al. (2018), in which tree die-back was observed early in 2016. The black rectangle roughly refers to the study area of Buras et al. (2018) for which *Q* was extracted to generate **(D)** which depicts violin plots of *Q*-values of the three corresponding dates of pixels within this rectangle that feature Scots pine cover of more than 70 percent. Minor case letters in **(D)** refer to group-assignments according to Wilcoxon rank-sum test. A similar figure but for *PDM* is shown in **Supplementary Figure 4**.

is in line with the general observation that forests are becoming increasingly stressed in course of climate change (Allen et al., 2010, 2015; Zang et al., 2014; Cailleret et al., 2017; Buras et al., 2018, 2020; Bose et al., 2020; Senf et al., 2020; Shekhar et al., 2020). In comparing clusters of low *Q* and *PDM* (**Figure 1**, **Supplementary Figure 1**) with water availability indices, such as the standardized climatic water balance (**Supplementary Figure 2**), clear similarities of spatial patterns were observed. Finally, spatial patterns of low *Q* and *PDM* mirror reports of well-known major drought events in 2003, 2006, 2012, 2015, 2017, and 2018 (Spinoni et al., 2015; Cindrić et al., 2016; Buras et al., 2018, 2020; Rita et al., 2020; Schuldt et al., 2020). This finding underlines the overarching importance of drought-stress for tree performance and, consequently, mortality. However, as indicated by five of the six presented case studies, extraordinary *Q* and *PDM*

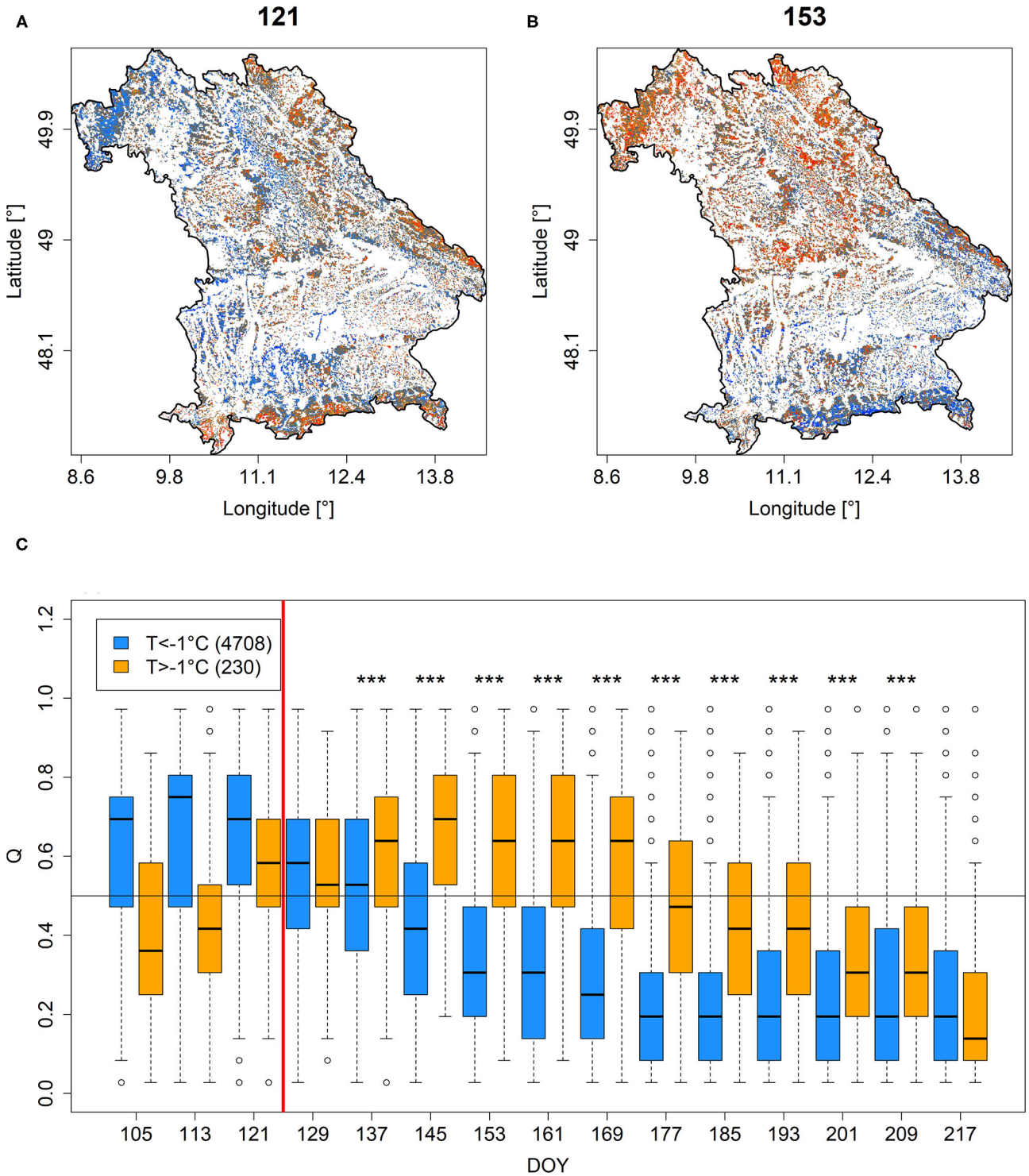

FIGURE 4 | *Q* for DOYs 121 **(A)** and 153 **(B)** in 2011. **(C)** Times-series depicting *Q*-values extracted for each time step between DOY 105 and DOY 217 for pixels featuring more than 45% beech cover and minimum temperatures at DOY 124 (indicated by vertical red line) below (blue) or above (orange)−1°C (for minimum temperature distributions at DOY 124, see **Supplementary Figure 6**). ***Stars indicate significant differences ($p < 0.001$). A similar figure but for *PDM* is shown in **Supplementary Figure 5**.

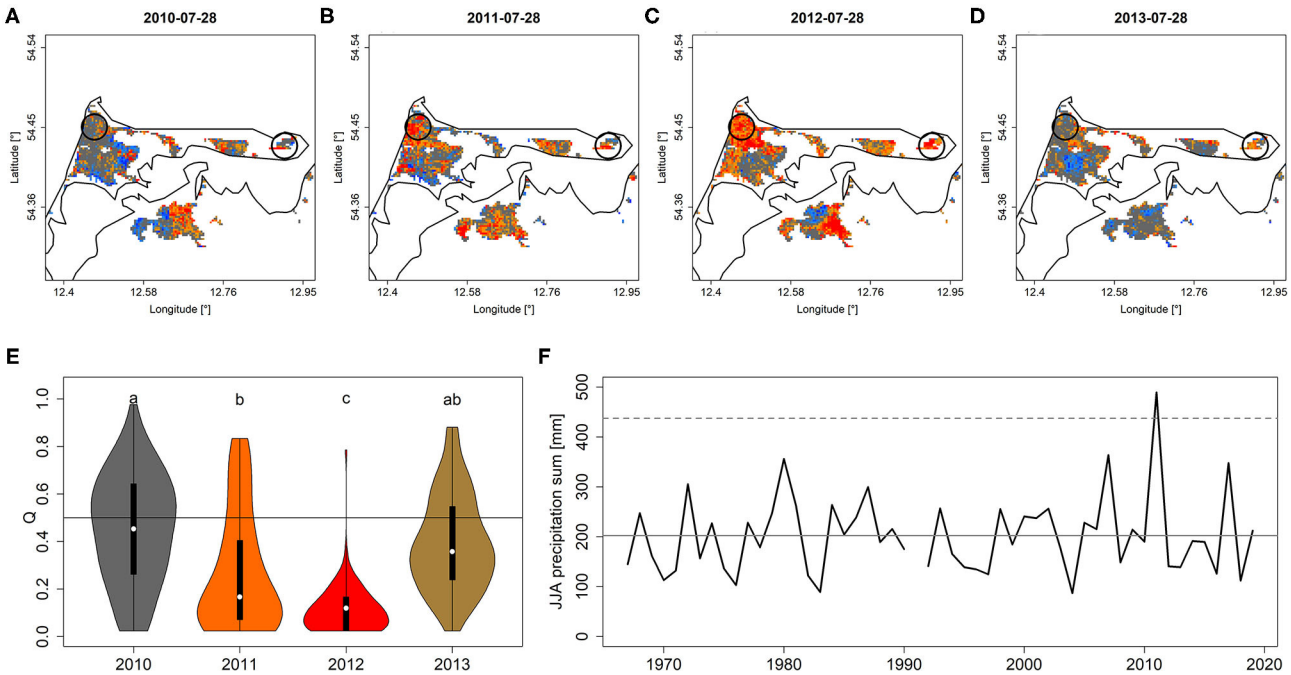

FIGURE 5 | *Q* depicted for peak season (July 28th) for each year from 2010 to 2013 **(A–D)**. Black circles refer to the areas that experienced increased die-back after 2011 (see also **Supplementary Figures 8, 9**) for which *Q*-values were extracted [shown in **(E)**]. **(F)** June-August precipitation sum from a nearby climate station indicates the year 2011 to exceed the 99% confidence interval (dashed line). Minor case letters in **(E)** indicate group-assignment according to pairwise Wilcoxon rank-sum test. Colors in **(E)** refer to colors of mean quantiles per year. The gray vertical line in **(F)** refers to mean JJA precipitation sum. A similar figure but for *PDM* is shown in **Supplementary Figure 7**.

values may also be caused by other extraordinary environmental conditions related to an early start of the growing season (section Land Surface Phenology), late-frost (section Late-Frost), mortality on water-logged soils (section Water Stress), mortality following an ice storm (section Ice Storm), and windthrow (section Windthrow). Thus, variations in *Q* and *PDM* always must be interpreted in a comprehensive context, taking further environmental variables such as climate data and phenological observations into consideration.

Besides the EFCM, other national or international remote sensing based (forest) monitoring platforms exist. For instance, on a national level the Sentinel 2 based German "Forest Watch" from the LUP, Potsdam[4] provides annual updates of the forest condition at a spatial resolution of 10 × 10 m. Thus, while the spatial resolution of Forest Watch is an order of magnitude higher in comparison to the EFCM, it does not allow for resolving different time-steps over the growing season as with the EFCM. Given the comparably shorter reference period of Sentinel 2, Forest Watch only allows for referencing observations against 2017 and, in some regions, 2018 (for details see homepage of Forest Watch). Consequently, the reference period is, to some degree, affected by forest decline (legacies of the drought in 2015, drought in 2018). Moreover, the applied vegetation index is not described in detail, hampering reproducibility and, therefore, comparability with other monitoring tools. Nevertheless, Forest Watch can be considered a complementation to the EFCM with higher spatial, yet lower temporal resolution while interpretations should be undertaken carefully given the rather fixed reference period of one specifically selected year (2017 or 2018). On the international level, the European drought observatory (EDO)[5] provides various drought-related indices amongst other combined drought indicators and anomalies of the fraction of the absorbed photosynthetically absorbed radiation (fAPAR; Cammalleri et al., 2021), specifically for vegetation. While the availability of several indices is an advantage in comparison to the EFCM, and the monitoring and reference period almost match the EFCM (2002-now), products provided by EDO are of coarser spatial resolution (highest spatial resolution is 500 × 500 m, recurrence period is 10 days). Moreover, since EDO does not specifically monitor forests but vegetated areas in general, direct interpretation of forest condition within a certain area (as provided by the histograms in the EFCM) is not possible. EDO can therefore be considered a valuable source of complementary information which may help interpreting the products provided by the EFCM, particularly in the context of drought-stress. In conclusion, the EFCM renders a novel source of information with regards to European forest monitoring which provides an added value in comparison to existing platforms.

[4]Forest Watch, LUP Potsdam, http://forestwatch.lup-umwelt.de/.

[5]Available online at: https://edo.jrc.ec.europa.eu.

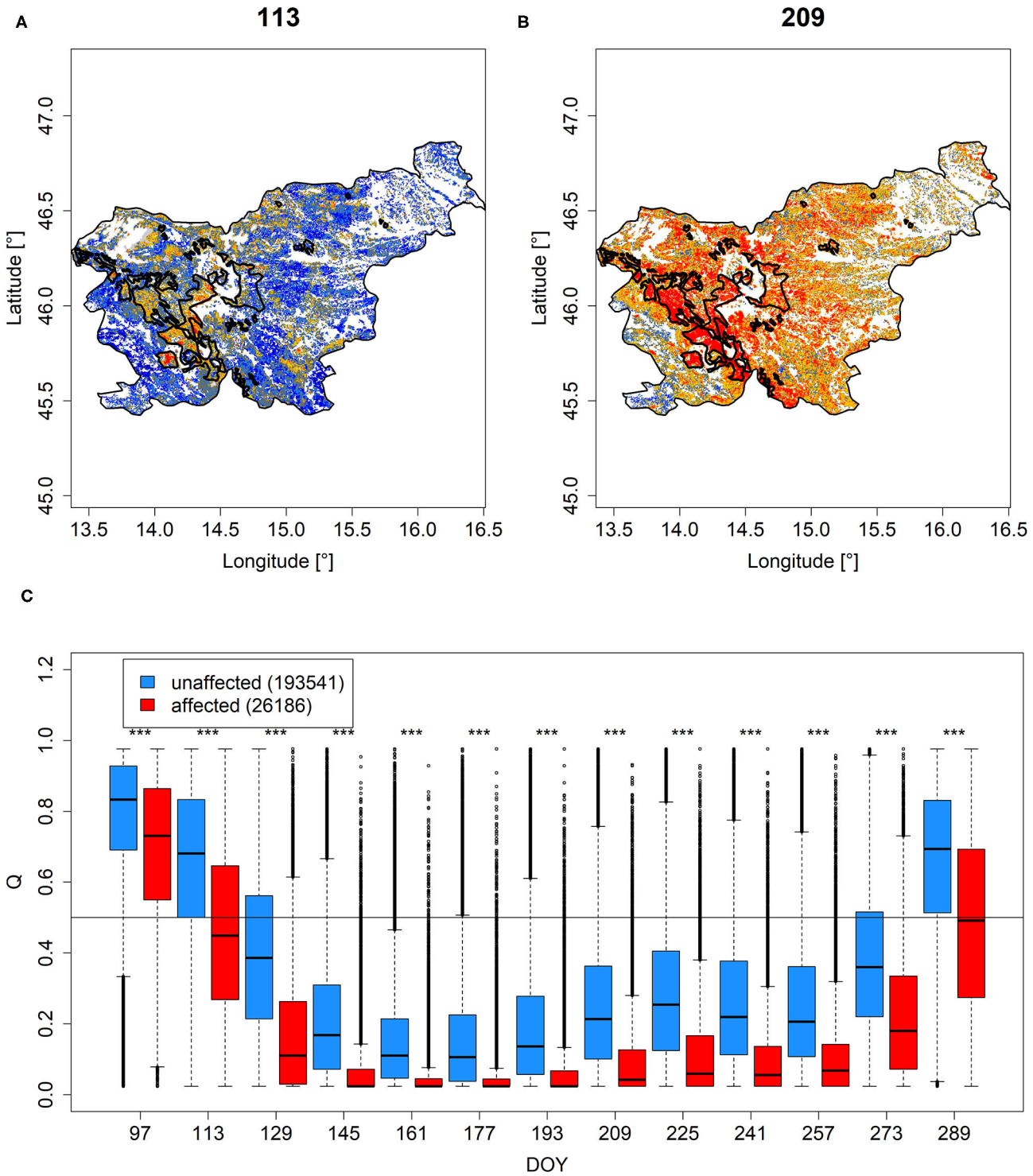

FIGURE 6 | *Q* mapped for Slovenia on DOY 113 **(A)** and 209 **(B)**. The polygons demarcate areas affected by the ice storm according to Roženbergar et al. (2020). Corresponding values grouped according to affectedness from DOY 97 until DOY 289 are shown in **(C)**. The horizontal line in **(C)** demarcates median *Q* values of 0.5. ***Significance stars indicate significant differences between DOY-specific groups according to Wilcoxon rank-sum test. Similar results for *PDM* are shown in **Supplementary Figure 10**.

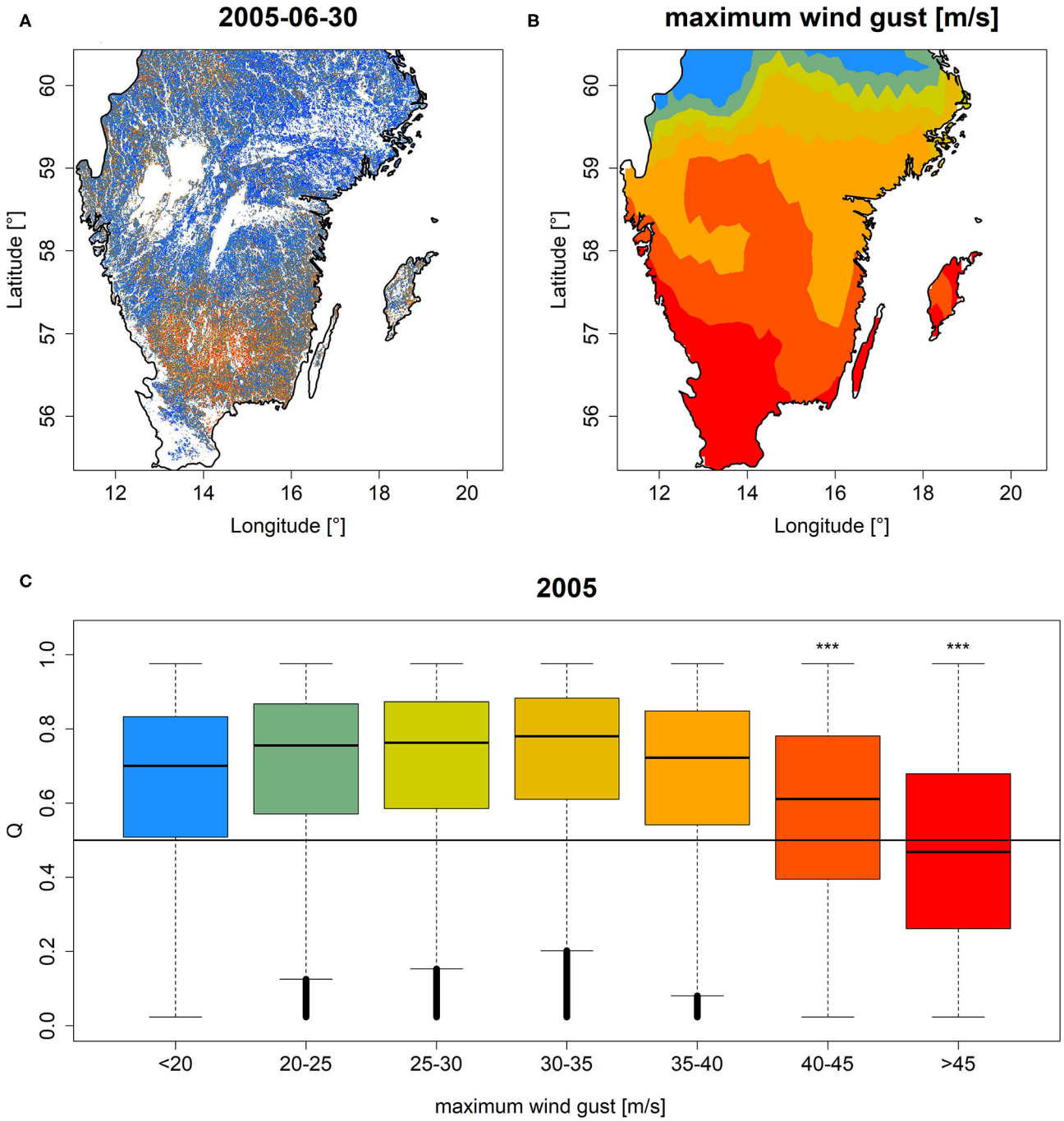

FIGURE 7 | *Q* mapped for southern Sweden on 30th of June, 2005 **(A)** along with maximum wind gust speed during the winter storm "Gudrun" in January 2005 **(B)** and boxplots of *Q* grouped according to different categories of wind gust speed **(C)**. ***Significance stars in **(C)** demarcate a significant ($p < 0.001$) one-sided Wilcoxon rank-sum test between subtle storm impact (gust speed <20 m/s) and the corresponding groups. Colors in **(B,C)** refer to the same wind gust speed categories as indicated on the x-axis of **(C)**. Similar results for *PDM* are shown in **Supplementary Figure 11**.

Evaluating Specific Examples of Forest Monitoring

The observed negative relationships between the two EFCM products and ground-based phenological observations (section Land Surface Phenology) suggest a strong potential to interpret early season *Q* and *PDM* as indicator of land surface phenology. A strong relationship between MODIS NDVI derived land surface phenology and ground observations has been reported earlier (Misra et al., 2016, 2018). However, other factors than the climatically stimulated onset of the growing season may

affect early season NDVI, explaining the circumstance that only roughly 50% of the variance in MODIS NDVI was explained by ground observations of beech budburst (see also below). Particularly, years succeeding extreme droughts may feature comparably low NDVI despite an early start of the season, in case the preceding drought has resulted in prolonged forest decline. For instance, after the extreme drought of 2015, a relatively high share of Scots pine forests in Franconia featured partial tree dieback, which to some degree was reflected in lower *Q* and *PDM* values in early 2016 (**Figure 3**, **Supplementary Figure 4**). Based on tree-rings and remote sensing observations, drought legacies lasting for 1 year have been frequently reported in the scientific literature (Anderegg et al., 2015; Kannenberg et al., 2018, 2020) which, however, do not always translate directly into reduced forest greenness, e.g., if resources are allocated into canopy repair (greening) instead of secondary growth (Kannenberg et al., 2019, see also section Limitations). Another possible influencing factor is late-frost, which, at least for broadleaved tree-species, may result in delayed greening due to the necessity to rebuilt damaged foliage (section Late-Frost). Also, in the year 2014, a moderate late-frost event stroke parts of southern Germany on April 17th (**Supplementary Figure 12**), i.e., DOY 107 while the mean budburst of beech took place around DOY 104 (**Figure 2C**) which may explain some of the red patches observed in **Figure 2A**. Moreover, negative impacts caused by waterlogged soils, ice storms, or winter storms also result in decreasing forest greenness at the onset of the growing season (sections Water Stress, Ice Storm, and Windthrow). Thus, while it seems likely that high *Q* and *PDM* reflect an early start of season, low values of these metrics do not necessarily indicate a late onset of the growing season. As a consequence, when interpreting early season *Q* and *PDM* phenological observations such as those provided by the Pan European Phenological database, PEP725 (Templ et al., 2018) should be considered as an additional source of information. In case that EFCM observations do not match phenological observations, this potentially indicates a stress situation of corresponding forests which would require further investigation. The close relationship between spring phenology and forest greenness also explains the high share of low *Q* and *PDM* values in spring 2021 (see EFCM viewer) due to a southward location of the polar jetstream over Europe which caused temperatures to be much colder than average (COPERNICUS)[6] and, consequently, a delay in forest greening.

The impact of the hotter drought of 2015 was also clearly visible in EFCM products (section Drought). While the area of interest in Northern Bavaria featured relatively high *Q* and *PDM* values at the onset of the 2015 growing season, they strongly declined over the summer period due to a strong precipitation deficit (Buras et al., 2018) and only locally recovered early in 2016. Indeed, the regional forest response to 2015 was very heterogeneous, depending on soil conditions, local precipitation events, and stand structure that modify micro-climate. For instance, the observed dieback of Scots pine early in 2016 was most pronounced at south-facing forest edges which, under long-lasting drought, suffer from a warmer and drier micro-climate in comparison to the forest interior (Buras et al., 2018). The resulting heterogeneous response of forests to drought explains the wide distribution of *Q* and *PDM* in early 2016. That is, while some forests had already recovered in 2016, other stands were still negatively affected. In the context of tree mortality, it is important to stress that given the often observed patchiness of tree die-back, the EFCM will not allow for directly identifying individual tree dieback, since the canopy of single trees on average only contribute around 2 permille to the MODIS pixel (10 × 10 m canopy compared to 231.25 × 231.25 m pixel size). However, since low *Q* and *PDM* values likely indicate stressed trees, the likelihood of tree die-back increases with decreasing *Q* and *PDM*. Consequently, low *Q* and *PDM* values during the peak season may inform study site selection if investigating drought-induced tree mortality which then, however, needs confirmation from ground truthing. Since mostly Scots pine was affected by the die-back after 2015, we want to stress the added value of evaluating *Q* and *PDM* in conjunction with local tree-species abundance, since this may allow for more clearly identifying specifically affected tree species. This is also the reason why we only considered pixels with more than 70% Scots pine abundance for this regional example. Tree-species distribution maps such as the one provided by Brus et al. (2012) provide a meaningful source of information within this context. In addition to the example of Scots pine in Franconia, we want to refer to other studies which reported low NDVI for drought-stressed forests which often resulted in increased die-back rates of individual trees (Brun et al., 2020; Buras et al., 2020; Rita et al., 2020; Schuldt et al., 2020).

Besides droughts, late-frost events may have a significant negative impact on NDVI (section Late-Frost). Particularly for broad-leaved tree-species freezing temperatures after leaf unfolding results in loss of foliage and, consequently, a delay in forest phenology and reductions in GPP and, eventually, nonstructural carbohydrates (Menzel et al., 2015; Príncipe et al., 2017; Bascietto et al., 2018; D'Andrea et al., 2019; Vitasse et al., 2019). Here, we could show a differing temporal NDVI development of beech-covered MODIS pixels with contrasting exposure to freezing temperatures in May 2011. Significant effects were observable until the end of July (DOY 209, see **Figure 4**, **Supplementary Figure 5C**), i.e., well-beyond the time, it took to re-establish a mature canopy in a heavily affected beech-stand in the Bavarian Forest where beech canopies had reestablished around DOY 178 in 2011 (Menzel et al., 2015). This example indicates how the EFCM may allow for quantifying impacts of late-frost events on a large scale, which then can be combined with ground-based observations as derived from tree-rings (Príncipe et al., 2017; Vitasse et al., 2019), eddy covariance flux measurements (Bascietto et al., 2018), or measurements of soluble sugar concentrations and non-structural carbohydrates (D'Andrea et al., 2019) to gain a deeper understanding of intermediate and midterm tree response. Our late-frost example is in line with Bascietto et al. (2018) who also reported a different seasonal development of satellite borne vegetation indices (in their case enhanced vegetation index, EVI) in dependence of late-frost damage. Yet again, care needs to be taken when

[6]COPERNICUS Report on spring 2021: https://climate.copernicus.eu/spring-2021-europe-was-it-really-so-cold.

interpreting the temporal development of *Q* and *PDM* since it may be affected by other environmental conditions as well. For instance, the ongoing decline of *Q* and *PDM* over the growing season 2011 in Bavaria for all beech-covered pixels independent of frost damage is likely related to the extremely wet and relatively cool summer in that year, which in other regions resulted in tree die-back on water-logged soils (section Water Stress). Also, if trees suffer from legacies of preceding droughts (section Drought), late-frost patterns as observed in 2011, which were not affected by preceding drought, may be obscured. Thus, when interpreting late-frost impacts based on the EFCM, additional information from climate station data and phenological observations on budburst of potentially affected tree species needs to be considered, too. As for the drought example, we want to stress the importance of considering species-specific reactions to late frost. It is obvious that evergreen coniferous tree-species are likely less affected by late-frost in comparison to deciduous tree-species. And even among deciduous tree-species, varying vulnerability to late-frost, in dependence of species-specific budburst and defense mechanisms, is likely (Lenz et al., 2013). Therefore, if studying impacts of late-frost on forest performance, we recommend incorporating information on tree-species abundance for the area under study as exemplified here.

In section Water Stress, we have shown that stand-wide die-back of trees is clearly reflected by the EFCM. In course of the extremely wet summer of 2011, formerly drained and recently rewetted coastal mires on the Darß-Zingst peninsula featured water-logged soils during summer 2011, i.e., at a time when trees growing on these mires usually had experienced comparably lower ground-water tables throughout their lifetime. As a consequence, tree roots suffered from anoxia during a period of active photosynthesis which eventually led to die-back of most trees in the affected areas (see **Supplementary Figures 8, 9**). The die-back was clearly reflected in *Q* and *PDM* for 2011 and 2012. While in 2013, the reduction in NDVI compared to 2010 partly recovered to values around the median. We explain this relaxation from low NDVI values by the impact of the forest understory, which established after the die-back and consequently raised the NDVI signal where canopies of dead trees had disappeared. In conclusion, while the EFCM is able to resolve the die-back of complete stands efficiently, the replacement of dead trees by successive vegetation will lead to a recovery of NDVI, which however does not indicate an immediate recovery of forests. The same holds true for other causes of large-scale tree die-back, wherefore recovering NDVI values succeeding extremely low values should always be interpreted carefully. At best, ground-based observations or remote sensing products with a higher spatial resolution are considered to obtain more detailed information on the causes of NDVI recovery (Senf et al., 2020). The observation that the EFCM resembles tree die-back is well in line with previous studies, which reported declining NDVI for forests suffering from bark-beetle calamities and/or drought (Rogers et al., 2018; Liu et al., 2019; Spruce et al., 2019).

Also, tree damage and mortality, because of the Slovenian ice storm in February 2014, was well-captured by the EFCM metrics (section Ice Storm). First, patterns of canopy damage were clearly visible when mapping *Q* and *PDM* (**Figures 6A,B**, **Supplementary Figure 10**). Comparing unaffected areas with affected areas, both *Q* and *PDM* featured significantly lower values for affected pixels over the whole growing season of 2005 (**Figure 7C**, **Supplementary Figure 10**). The observation that some of the presumably affected pixels yet featured relatively high values possibly refers to the specific impact of the ice storm in dependence of tree species and tree size (Roženbergar et al., 2020) but also the varying local impact of the ice storm which was not represented using the digitized shape with a binary classification.

Finally, the windthrow in southern Sweden caused by the extreme winter storm "Gudrun" in February 2005 (Valinger et al., 2014) was spatially well resembled by *Q* and *PDM* (section Windthrow). Particularly, above a maximum wind gust speed of 40 m/s, significantly negative effects on EFCM metrics were observed. Yet, the observation of high values in regions presumably affected by extreme wind gusts was surprising. We hypothesize that this observation is caused by a multitude of factors which affect the critical wind gust speed above which a tree is thrown and variations in local turbulence intensity and wind gust duration which result in heterogeneous, patchy patterns of gust impact that are not represented by interpolated wind gust data (England et al., 2000). Finally, according to Valinger et al. (2014) windthrow in 2005 almost exclusively affected Norway spruce (*Picea abies* L.) wherefore the canopy greenness of other tree species (particularly, broadleaved tree species) likely contributed to the observed heterogeneous signal. To better understand the observed heterogeneous patterns of *Q* and *PDM*, more detailed ground-truthing, for instance, from forest inventories, would be needed. Nevertheless, the windthrow caused by the winter storm in 2005 exemplifies another potential cause of low *Q* and *PDM* which should be taken into consideration when interpreting products from the EFCM.

Limitations

As already pointed out in section Evaluating Specific Examples of Forest Monitoring, interpretations derived from EFCM products should be interpreted carefully and in conjunction with other environmental information to get a more complete picture of potential underlying causes. One specific limitation of the EFCM is related to the spatial resolution of 231.25 × 231.25 m (roughly 5.3 hectares) which is too coarse to resolve single trees and further results in statistical noise in pixels including non-forest areas. Since various environmental conditions may result in extraordinarily low NDVI, it may be difficult to clearly identify the cause of observed effects. To partly overcome these limitations, we recommend additionally considering high-resolution satellite imagery as, e.g., provided by the LANDSAT and Sentinel missions. Based on their finer spatial resolution, they likely allow for canceling out noise caused by non-forest land cover and in case of Sentinel 2 potentially to backtrack low NDVI values to specific tree groups. Moreover, considering ecological climate parameters as derived from climate station data and phenological observations may help to better understand observations of extraordinary

NDVI. As mentioned earlier, we intend to extend the EFCM with additional remote-sensing based vegetation indices from additional sensors, allowing for a more comprehensive picture of forest condition.

We want to stress that EFCM products do not translate directly into forest productivity and vitality. While NDVI and productivity and vitality are linked to some degree, this link may be violated under specific circumstances. For instance, so-called masting events of beech, which result in reduced NDVI due to a high share of beechnuts in the canopy, may lower NDVI while high GPP is maintained. Again, it, therefore, seems mandatory to always interpret EFCM products in the context of other environmental constellations and consider additional measures of productivity such as eddy covariance flux measurements (e.g., Bascietto et al., 2018; Pastorello et al., 2020) and solar induced fluorescence (Liu et al., 2018; Shekhar et al., 2020). In addition, when interpreting *Q* and *PDM* in the context of tree mortality, care needs to be taken. While the likelihood of tree mortality is likely to increase in course of declining canopy greenness (Rogers et al., 2018; Liu et al., 2019; Spruce et al., 2019), trees may yet recover from the causal environmental stressors. Consequently, additional ground truthing is needed to confirm the actual death of trees, which on a larger scale may be derived from satellite-based canopy mortality assessments (Senf et al., 2020).

Within this context, we want to highlight the possible mismatch between measures of secondary growth (e.g., indexed tree-ring width) and canopy greenness as represented by NDVI (Kannenberg et al., 2019). For instance, Kannenberg et al. (2019) observed significantly reduced tree-ring width during drought and in the subsequent year while GPP and NDVI only featured significant reductions during drought but not in the following year. These authors hypothesized this observation to be caused by post-drought photosynthesis upregulation and carbon allocation in favor of canopy repair (recovering NDVI) at the expense of secondary growth (reducing tree-ring width). In another study, the link between NDVI and secondary tree-growth differed between non-drought and drought conditions (Meyer et al., 2020): while tree-ring width was most closely linked with the start of season NDVI under non-drought conditions, peak-season NDVI better reflected secondary growth decline under drought conditions. The link of spring NDVI with tree-growth under normal conditions is probably caused by the overarching effect of spring conditions on secondary growth of trees growing in temperate climates (Buras et al., 2018; Kannenberg et al., 2019), while the link under drought conditions with summer NDVI likely reflects early leaf coloration or senescence which result in reduced ring-widths (Meyer et al., 2020; Schuldt et al., 2020). On the global scale, the relationship between secondary growth and canopy greenness is further modified by tree-species, climate zone, and integration period of the NDVI signal (Vicente-Serrano et al., 2016; Bhuyan et al., 2017). In conclusion, care needs to be taken when translating fluctuations of *Q* and *PDM* into GPP and variations of secondary growth.

Regarding *PDM,* the subjectively chosen steps for the color-charts may be considered a potential weakness. The main reason for adding *PDM* is the complementation of *Q* which does not allow for quantifying the absolute deviation from the long-term median in contrast to *PDM*. Since *PDM* however also requires visualization, we defined the relatively arbitrary thresholds described in section Computation of Central Metrics. While these thresholds are based on forest decline observations made by the first-author after a severe drought in 2015 (Buras et al., 2018), we admit that such thresholds likely are site and tree-species specific. Nevertheless, the chosen lower threshold of −10% is well in line with a sharp increase in tree mortality observed in course of a Mountain pine beetle calamity in the western U.S. (Spruce et al., 2019). Based on the examples shown, the color-chart applied to *PDM* often resulted in a less pronounced impression of forest decline in comparison to *Q*. However, when studying the supplied box and violin-plots, *PDM* generally supported significant results reported for *Q*, although differences again appeared to be less pronounced. This latter impression comes from the fact, that *PDM* in comparison to *Q* does not feature a bounded distribution between 0 and 1, wherefore whiskers of the corresponding plots stretch to more extreme values, thereby affecting the y-axis limits. As a consequence, boxplot comparisons for *PDM* suggested smaller differences in comparison to *Q*, which however was not the case (both metrics are based on the same underlying data). Given these potentially ambiguous effects related to the visualization of *PDM*, we decided to emphasize our performance examples on *Q*. Despite these drawbacks regarding visualization, we consider *PDM* a required complementation to *Q* allowing for quantifying the proportional deviation of forest greenness from the long-term median.

CONCLUSION AND OUTLOOK

Based on an assessment of the overall development of peak season NDVI quantiles and proportional deviations from the median and six local case-studies, we have shown that the framework behind the European Forest Condition Monitor provides meaningful information on forest condition at a continental and local scale (sections Using MODIS NDVI to Monitor European Forests and Evaluating Specific Examples of Forest Monitoring). To understand the causes of observed effects, we recommend consulting additional sources of environmental information such as climate station data, phenological observations, and additional high-resolution satellite imagery to overcome limitations associated with the relatively coarse spatial resolution (section Limitations). If interpreted in conjunction with additional environmental information, the EFCM allows for identifying hotspots of forest decline across Europe since 2001 and may therefore serve as a decision tool for designing forest vulnerability assessments in the context of extreme environmental conditions. The ecologically meaningful performance of the EFCM supports the underlying methodological approach based on MODIS NDVI. An interactive web application that allows for viewing and downloading corresponding images and data of *Q* and *PDM* for any time-step since 2001 across the entire European

Union is available at http://interaktiv.waldzustandsmonitor.de/. Future updates of the EFCM will aim at extending the product portfolio integrating additional vegetation indices (e.g., EVI, SIF) and additional sensors (e.g., Sentinel 2, LANDSAT 8) which in combination provide a better estimate of actual forest condition at a higher spatial resolution. Updates on the further refinement of the EFCM will be posted in the newsfeed of the forest condition monitor homepage at www.waldzustandsmonitor.de.

DATA AVAILABILITY STATEMENT

Publicly available datasets were analyzed in this study. This data can be found at: https://lpdaacsvc.cr.usgs.gov/appeears.

AUTHOR CONTRIBUTIONS

AB invented, conceptualized, and published the forest condition monitor in 2019 and developed the shiny app in 2021. He also designed the research underlying this study, performed all analyses, and drafted the manuscript. AR and CZ provided valuable suggestions on how to improve the visualization of the forest condition monitor and commented on the manuscript draft. All authors contributed to the article and approved the submitted version.

FUNDING

This project was funded by the Bavarian Ministry of Science and the Arts in the context of the Bavarian Climate Research Network (BayKliF).

ACKNOWLEDGMENTS

AR acknowledges additional funding from the ERA-Net Sumforestproject Forests and extreme weather events: Solutions for risk resilient management in a changing climate (FOREXCLIM). We would like to thank the reviewers for their constructive criticism. Finally, we highly appreciate the valuable contributions by Mona Reiß regarding the web-design of the EFCM homepage and the provision of aerial photographs of the Darß-Zingst peninsula by Lutz Storm. We specifically thank Wolfgang Kurtz for help in context of setting up the shiny-server environment.

SUPPLEMENTARY MATERIAL

The Supplementary Material for this article can be found online at: https://www.frontiersin.org/articles/10.3389/fpls.2021.689220/full#supplementary-material

REFERENCES

Allen, C. D., Breshears, D. D., and McDowell, N. G. (2015). On underestimation of global vulnerability to tree mortality and forest die-off from hotter drought in the Anthropocene. *Ecosphere* 6, 1–55. doi: 10.1890/ES15-00203.1

Allen, C. D., Macalady, A. K., Chenchouni, H., Bachelet, D., McDowell, N., Vennetier, M., et al. (2010). A global overview of drought and heat-induced tree mortality reveals emerging climate change risks for forests. *For. Ecol. Manage.* 259, 660–684. doi: 10.1016/j.foreco.2009.09.001

Anderegg, W. R. L., Schwalm, C., Biondi, F., Camarero, J. J., Koch, G., Litvak, M., et al. (2015). Pervasive drought legacies in forest ecosystems and their implications for carbon cycle models. *Science* 349, 528–532. doi: 10.1126/science.aab1833

Anyamba, A., and Tucker, C. J. (2012). "Historical perspective of AVHRR NDVI and vegetation drought monitoring," in *Remote Sensing of Drought: Innovative Monitoring Approaches*, eds B. D. Wardlow, M. C. Anderson, and J. P. Verdin (Boca Raton, FL; London; New York, NY: CRC Press; Taylor and Francis Group), 23.

Bascietto, M., Bajocco, S., Mazzenga, F., and Matteucci, G. (2018). Assessing spring frost effects on beech forests in Central Apennines from remotely-sensed data. *Agric. Forest Meteorol.* 248, 240–250. doi: 10.1016/j.agrformet.2017.10.007

Bastos, A., Ciais, P., Friedlingstein, P., Sitch, S., Pongratz, J., Fan, L., et al. (2020). Direct and seasonal legacy effects of the 2018 heat wave and drought on European ecosystem productivity. *Sci. Adv.* 6:eaba2724. doi: 10.1126/sciadv.aba2724

Bastos, A., Ciais, P., Park, T., Zscheischler, J., Yue, C., Barichivich, J., et al. (2017). Was the extreme Northern Hemisphere greening in 2015 predictable? *Environ. Res. Lett.* 12:044016. doi: 10.1088/1748-9326/aa67b5

Becker, J. J., Sandwell, D. T., Smith, W. H. F., Braud, J., Binder, B., Depner, J., et al. (2009). Global bathymetry and elevation data at 30 arc seconds resolution: SRTM30_PLUS. *Marine Geodesy* 32, 355–371. doi: 10.1080/01490410903297766

Bhuyan, U., Zang, C., Vicente-Serrano, S. M., and Menzel, A. (2017). Exploring relationships among tree-ring growth, climate variability, and seasonal leaf activity on varying timescales and spatial resolutions. *Remote Sens.* 9:526. doi: 10.3390/rs9060526

Bigler, C., Bräker, O. U., Bugmann, H., Dobbertin, M., and Rigling, A. (2006). Drought as an inciting mortality factor in scots pine stands of the Valais, Switzerland. *Ecosystems* 9, 330–343. doi: 10.1007/s10021-005-0126-2

Bose, A. K., Gessler, A., Bolte, A., Bottero, A., Buras, A., Cailleret, M., et al. (2020). Growth and resilience responses of Scots pine to extreme droughts across Europe depend on predrought growth conditions. *Glob. Chang. Biol.* 26, 4521–4537. doi: 10.1111/gcb.15153

Brun, P., Psomas, A., Ginzler, C., Thuiller, W., Zappa, M., and Zimmermann, N. E. (2020). Large-scale early-wilting response of Central European forests to the 2018 extreme drought. *Glob. Chang. Biol.* 26, 7021–7035. doi: 10.1111/gcb.15360

Brus, D. J., Hengeveld, G. M., Walvoort, D. J. J., Goedhart, P. W., Heidema, A. H., Nabuurs, G. J., et al. (2012). Statistical mapping of tree species over Europe. *Eur. J. For. Res.* 131, 145–157. doi: 10.1007/s10342-011-0513-5

Buras, A., Rammig, A., and Zang, C. S. (2020). Quantifying impacts of the 2018 drought on European ecosystems in comparison to 2003. *Biogeosciences* 17, 1655–1672. doi: 10.5194/bg-17-1655-2020

Buras, A., Schunk, C., Zeiträg, C., Herrmann, C., Kaiser, L., Lemme, H., et al. (2018). Are Scots pine forest edges particularly prone to drought-induced mortality? *Environ. Res. Lett.* 13:025001. doi: 10.1088/1748-9326/aaa0b4

Büttner, G., Feranec, J., Jaffrain, G., Mari, L., Maucha, G., and Soukup, T. (2004). The CORINE land cover 2000 project. *EARSeL eProceed.* 3, 331–346. Available online at: http://eproceedings.uni-oldenburg.de/website/vol03%5F3/03%5F3%5Fbuttner2%2Ehtml

Cailleret, M., Jansen, S., Robert, E. M. R., Desoto, L., Aakala, T., Antos, J. A., et al. (2017). A synthesis of radial growth patterns preceding tree mortality. *Glob. Change Biol.* 23, 1675–1690. doi: 10.1111/gcb.13535

Camarero, J. J., Gazol, A., Sangüesa-Barreda, G., Oliva, J., and Vicente-Serrano, S. M. (2015). To die or not to die: early warnings of tree dieback in response to a severe drought. *J. Ecol.* 103, 44–57. doi: 10.1111/1365-2745.12295

Cammalleri, C., Arias-Muñoz, C., Barbosa, P., de Jager, A., Magni, D., Masante, D., et al. (2021). A revision of the Combined Drought Indicator (CDI) used in

the European Drought Observatory (EDO). *Natl. Hazards Earth Syst. Sci.* 21, 481–495. doi: 10.5194/nhess-21-481-2021

Chang, W., Cheng, J., Allaire, J., Sievert, C., Schloerke, B., Xie, Y., et al. (2021). *Shiny: Web Application Framework for R*. Available online at: https://shiny.rstudio.com/reference/shiny/1.4.0/shiny-package.html

Ciais, P., Reichstein, M., Viovy, N., Granier, A., Ogée, J., Allard, V., et al. (2005). Europe-wide reduction in primary productivity caused by the heat and drought in 2003. *Nature* 437, 529–533. doi: 10.1038/nature03972

Cindrić, K., Telišman Prtenjak, M., Herceg-Bulić, I., Mihajlović, D., and Pasarić, Z. (2016). Analysis of the extraordinary 2011/2012 drought in Croatia. *Theor. Appl. Climatol.* 123, 503–522. doi: 10.1007/s00704-014-1368-8

D'Andrea, E., Rezaie, N., Battistelli, A., Gavrichkova, O., Kuhlmann, I., Matteucci, G., et al. (2019). Winter's bite: beech trees survive complete defoliation due to spring late-frost damage by mobilizing old C reserves. *New Phytol.* 224, 625–631. doi: 10.1111/nph.16047

Dox, I., Gričar, J., Marchand, L. J., Leys, S., Zuccarini, P., Geron, C., et al. (2020). Timeline of autumn phenology in temperate deciduous trees. *Tree Physiol.* 40, 1001–1013. doi: 10.1093/treephys/tpaa058

Dox, I., Prislan, P., Gričar, J., Mariën, B., Delpierre, N., Flores, O., et al. (2021). Drought elicits contrasting responses on the autumn dynamics of wood formation in late successional deciduous tree species. *Tree Physiol.* 41, 1171–1185. doi: 10.1093/treephys/tpaa175

England, A. H., Baker, C. J., and Saunderson, S. E. T. (2000). A dynamic analysis of windthrow of trees. *Forestry* 73, 225–238. doi: 10.1093/forestry/73.3.225

Gazol, A., Camarero, J. J., Sánchez-Salguero, R., Vicente-Serrano, S. M., Serra-Maluquer, X., Gutiérrez, E., et al. (2020). Drought legacies are short, prevail in dry conifer forests and depend on growth variability. *J. Ecol.* 108, 2473–2484. doi: 10.1111/1365-2745.13435

Hijmans, R. J. (2017). *raster: Geographic Data Analysis and Modeling*. Available online at: https://cran.r-project.org/web/packages/raster/index.html

Kannenberg, S. A., Maxwell, J. T., Pederson, N., D'Orangeville, L., Ficklin, D. L., and Phillips, R. P. (2018). Drought legacies are dependent on water table depth, wood anatomy and drought timing across the eastern US. *Ecol. Lett.* 22, 119–127. doi: 10.1111/ele.13173

Kannenberg, S. A., Novick, K. A., Alexander, M. R., Maxwell, J. T., Moore, D. J. P., Phillips, R. P., et al. (2019). Linking drought legacy effects across scales: From leaves to tree rings to ecosystems. *Glob. Chang. Biol.* 25, 2978–2992. doi: 10.1111/gcb.14710

Kannenberg, S. A., Schwalm, C. R., and Anderegg, W. R. L. (2020). Ghosts of the past: how drought legacy effects shape forest functioning and carbon cycling. *Ecol. Lett.* 23, 891–901. doi: 10.1111/ele.13485

Karger, D. N., Conrad, O., Böhner, J., Kawohl, T., Kreft, H., Soria-Auza, R. W., et al. (2017). Climatologies at high resolution for the earth's land surface areas. *Sci. Data* 4:170122. doi: 10.1038/sdata.2017.122

Keitt, T. H., Bivand, R., Pebesma, E., and Rowlingson, B. (2011). *rgdal: Bindings for the Geospatial Data Abstraction Library. R package version 0.7-1.* Available online at: http://CRAN.R-project.org/package=rgdal (accessed August 1, 2021).

Kogan, F. N. (1995). Application of vegetation index and brightness temperature for drought detection. *Adv. Space Res.* 15, 91–100. doi: 10.1016/0273-1177(95)00079-T

Kohler, M., Sohn, J., Nägele, G., and Bauhus, J. (2010). Can drought tolerance of Norway spruce *(Picea abies (L.) Karst.)* be increased through thinning? *Eur. J. Forest Res.* 129, 1109–1118. doi: 10.1007/s10342-010-0397-9

Körner, C. (2015). Paradigm shift in plant growth control. *Curr. Opin. Plant Biol.* 25, 107–114. doi: 10.1016/j.pbi.2015.05.003

Kreuzwieser, J., and Rennenberg, H. (2014). Molecular and physiological responses of trees to waterlogging stress. *Plant Cell Environ.* 37, 2245–2259. doi: 10.1111/pce.12310

Lenz, A., Hoch, G., Vitasse, Y., and Körner, C. (2013). European deciduous trees exhibit similar safety margins against damage by spring freeze events along elevational gradients. *New Phytol.* 200, 1166–1175. doi: 10.1111/nph.12452

Lévesque, M., Saurer, M., Siegwolf, R., Eilmann, B., Brang, P., Bugmann, H., et al. (2013). Drought response of five conifer species under contrasting water availability suggests high vulnerability of Norway spruce and European larch. *Glob. Change Biol.* 19, 3184–3199. doi: 10.1111/gcb.12268

Lillesand, T., Kiefer, R. W., and Chipman, J. (2014). *Remote Sensing and Image Interpretation*. New York, NY: John Wiley & Sons.

Liu, L., Yang, X., Zhou, H., Liu, S., Zhou, L., Li, X., et al. (2018). Evaluating the utility of solar-induced chlorophyll fluorescence for drought monitoring by comparison with NDVI derived from wheat canopy. *Sci. Total Environ.* 625, 1208–1217. doi: 10.1016/j.scitotenv.2017.12.268

Liu, Y., Kumar, M., Katul, G. G., and Porporato, A. (2019). Reduced resilience as an early warning signal of forest mortality. *Nat. Clim. Chang.* 9, 880–885. doi: 10.1038/s41558-019-0583-9

Menzel, A., Helm, R., and Zang, C. (2015). Patterns of late spring frost leaf damage and recovery in a European beech (*Fagus sylvatica L.*) stand in south-eastern Germany based on repeated digital photographs. *Front. Plant Sci.* 6:110. doi: 10.3389/fpls.2015.00110

Meyer, B. F., Buras, A., Rammig, A., and Zang, C. S. (2020). Higher susceptibility of beech to drought in comparison to oak. *Dendrochronologia* 64:125780. doi: 10.1016/j.dendro.2020.125780

Misra, G., Buras, A., Heurich, M., Asam, S., and Menzel, A. (2018). LiDAR derived topography and forest stand characteristics largely explain the spatial variability observed in MODIS land surface phenology. *Remote Sens. Environ.* 218, 231–244. doi: 10.1016/j.rse.2018.09.027

Misra, G., Buras, A., and Menzel, A. (2016). Effects of different methods on the comparison between land surface and ground phenology—a methodological case study from South-Western Germany. *Remote Sens.* 8:753. doi: 10.3390/rsH8090753

Nychka, D., Furrer, R., Paige, J., and Sain, S. (2017). *Fields: Tools for Spatial Data*. 2015. Available online at: https://cran.r-project.org/web/packages/fields/index.html (accessed August 1, 2021).

Orth, R., Zscheischler, J., and Seneviratne, S. I. (2016). Record dry summer in 2015 challenges precipitation projections in Central Europe. *Sci. Rep.* 6:28334. doi: 10.1038/srep28334

Pastorello, G., Trotta, C., Canfora, E., Chu, H., Christianson, D., Cheah, Y.-W., et al. (2020). The FLUXNET2015 dataset and the ONEFlux processing pipeline for eddy covariance data. *Sci. Data* 7:225. doi: 10.1038/s41597-020-0534-3

Pellizzari, E., Camarero, J. J., Gazol, A., Sangüesa-Barreda, G., and Carrer, M. (2016). Wood anatomy and carbon-isotope discrimination support long-term hydraulic deterioration as a major cause of drought-induced dieback. *Glob. Change Biol.* 22, 2125–2137. doi: 10.1111/gcb.13227

Príncipe, A., van der Maaten, E., van der Maaten-Theunissen, M., Struwe, T., Wilmking, M., and Kreyling, J. (2017). Low resistance but high resilience in growth of a major deciduous forest tree (*Fagus sylvatica L.*) in response to late spring frost in southern Germany. *Trees* 31, 743–751. doi: 10.1007/s00468-016-1505-3

Rehschuh, R., Mette, T., Menzel, A., and Buras, A. (2017). Soil properties affect the drought susceptibility of Norway spruce. *Dendrochronologia* 45, 81–89. doi: 10.1016/j.dendro.2017.07.003

Rita, A., Camarero, J. J., Nolè, A., Borghetti, M., Brunetti, M., Pergola, N., et al. (2020). The impact of drought spells on forests depends on site conditions: the case of 2017 summer heat wave in southern Europe. *Glob. Chang. Biol.* 26, 851–863. doi: 10.1111/gcb.14825

Rogers, B. M., Solvik, K., Hogg, E. H., Ju, J., Masek, J. G., Michaelian, M., et al. (2018). Detecting early warning signals of tree mortality in boreal North America using multiscale satellite data. *Glob. Chang. Biol.* 24, 2284–2304. doi: 10.1111/gcb.14107

Rossi, S., Deslauriers, A., Anfodillo, T., and Carraro, V. (2007). Evidence of threshold temperatures for xylogenesis in conifers at high altitudes. *Oecologia* 152, 1–12. doi: 10.1007/s00442-006-0625-7

Rouse, J. W., Haas, R. H., Schell, J. A., and Deering, D. W. (1974). "Monitoring vegetation systems in the great plains with ERTS," in *Third Earth Resources Technology Satellite-1 Symposium- Volume I: Technical Presentations*, eds S. C. Freden, E. P. Mercanti, and M. A. Becker (Washington, DC: NASA), 309.

Roženbergar, D., Pavlin, J., and Nagel, T. A. (2020). Short-term survival and crown rebuilding of European broadleaf tree species following a severe ice storm. *Canad. J. Forest Res.* 50, 1131–1137. doi: 10.1139/cjfr-2020-0063

Rubio-Cuadrado, Á., Gómez, C., Rodríguez-Calcerrada, J., Perea, R., Gordaliza, G. G., Camarero, J. J., et al. (2021). Differential response of oak and beech to late frost damage: an integrated analysis from organ to forest. *Agric. Forest Meteorol.* 297:108243. doi: 10.1016/j.agrformet.2020.108243

Ruehr, N. K., Grote, R., Mayr, S., and Arneth, A. (2019). Beyond the extreme: recovery of carbon and water relations in woody plants following heat and drought stress. *Tree Physiol.* 39, 1285–1299. doi: 10.1093/treephys/tpz032

Scharnweber, T., Smiljanic, M., Cruz-García, R., Manthey, M., and Wilmking, M. (2020). Tree growth at the end of the 21st century - the extreme years 2018/19 as template for future growth conditions. *Environ. Res. Lett.* 15:074022. doi: 10.1088/1748-9326/ab865d

Schuldt, B., Buras, A., Arend, M., Vitasse, Y., Beierkuhnlein, C., Damm, A., et al. (2020). A first assessment of the impact of the extreme 2018 summer drought on Central European forests. *Basic Appl. Ecol.* 45, 86–103. doi: 10.1016/j.baae.2020.04.003

Seidel, H., and Menzel, A. (2016). Above-ground dimensions and acclimation explain variation in drought mortality of scots pine seedlings from various provenances. *Front. Plant Sci.* 7:1014. doi: 10.3389/fpls.2016.01014

Seidel, H., Schunk, C., Matiu, M., and Menzel, A. (2016). Diverging drought resistance of scots pine provenances revealed by infrared thermography. *Front. Plant Sci.* 7:1247. doi: 10.3389/fpls.2016.01247

Senf, C., Buras, A., Zang, C. S., Rammig, A., and Seidl, R. (2020). Excess forest mortality is consistently linked to drought across Europe. *Nat. Commun.* 11:6200. doi: 10.1038/s41467-020-19924-1

Seo, J.-W., Eckstein, D., Buras, A., Fromm, J., Wilmking, M., and Olbrich, A. (2020). Changes in wood anatomical traits in Scots pine under different climate-change scenarios. *IAWA J.* 1, 1–17. doi: 10.1163/22941932-00002111

Shekhar, A., Chen, J., Bhattacharjee, S., Buras, A., Castro, A. O., Zang, C. S., et al. (2020). Capturing the impact of the 2018 European drought and heat across different vegetation types using OCO-2 solar-induced fluorescence. *Remote Sens.* 12:3249. doi: 10.3390/rs12193249

Spinoni, J., Naumann, G., Vogt, J. V., and Barbosa, P. (2015). The biggest drought events in Europe from 1950 to 2012. *J. Hydrol.* 3, 509–524. doi: 10.1016/j.ejrh.2015.01.001

Spruce, J. P., Hicke, J. A., Hargrove, W. W., Grulke, N. E., and Meddens, A. J. H. (2019). Use of MODIS NDVI products to map tree mortality levels in forests affected by mountain pine beetle outbreaks. *Forests* 10:811. doi: 10.3390/f10090811

Templ, B., Koch, E., Bolmgren, K., Ungersböck, M., Paul, A., Scheifinger, H., et al. (2018). Pan European Phenological database (PEP725): a single point of access for European data. *Int. J. Biometeorol.* 62, 1109–1113. doi: 10.1007/s00484-018-1512-8

Valinger, E., Kempe, G., and Fridman, J. (2014). Forest management and forest state in southern Sweden before and after the impact of storm Gudrun in the winter of 2005. *Scand. J. Forest Res.* 29, 466–472. doi: 10.1080/02827581.2014.927528

Vicente-Serrano, S. M., Camarero, J. J., Olano, J. M., Martín-Hernández, N., Peña-Gallardo, M., Tomás-Burguera, M., et al. (2016). Diverse relationships between forest growth and the Normalized Difference Vegetation Index at a global scale. *Remote Sens. Environ.* 187, 14–29. doi: 10.1016/j.rse.2016.10.001

Vitasse, Y., Bottero, A., Cailleret, M., Bigler, C., Fonti, P., Gessler, A., et al. (2019). Contrasting resistance and resilience to extreme drought and late spring frost in five major European tree species. *Glob. Chang. Biol.* 25, 3781–3792. doi: 10.1111/gcb.14803

Xu, L., Samanta, A., Costa, M. H., Ganguly, S., Nemani, R. R., and Myneni, R. B. (2011). Widespread decline in greenness of Amazonian vegetation due to the 2010 drought. *Geophys. Res. Lett.* 38. doi: 10.1029/2011GL046824

Zang, C., Hartl-Meier, C., Dittmar, C., Rothe, A., and Menzel, A. (2014). Patterns of drought tolerance in major European temperate forest trees: climatic drivers and levels of variability. *Glob. Chang. Biol.* 20, 3767–3779. doi: 10.1111/gcb.12637

Zhang, Y., Joiner, J., Alemohammad, S. H., Zhou, S., and Gentine, P. (2018). A global spatially contiguous solar-induced fluorescence (CSIF) dataset using neural networks. *Biogeosciences* 15, 5779–5800. doi: 10.5194/bg-15-5779-2018

Conflict of Interest: The authors declare that the research was conducted in the absence of any commercial or financial relationships that could be construed as a potential conflict of interest.

Publisher's Note: All claims expressed in this article are solely those of the authors and do not necessarily represent those of their affiliated organizations, or those of the publisher, the editors and the reviewers. Any product that may be evaluated in this article, or claim that may be made by its manufacturer, is not guaranteed or endorsed by the publisher.

frontiers in Plant Science

ORIGINAL RESEARCH
published: 20 January 2022
doi: 10.3389/fpls.2021.698878

Strong Environmental Filtering Based on Hydraulic Traits Occurring in the Lower Water Availability of Temperate Forest Communities

Jiale Zhao[1†], Yuhan Zhang[1†], Jinshi Xu[1,3], Yongfu Chai[1], Peiliang Liu[1], Ying Cao[1], Cunxia Li[1], Qiulong Yin[4], Jiangang Zhu[5] and Ming Yue[1,2]*

[1] Key Laboratory of Resource Biology and Biotechnology in Western China, Northwest University, Xi'an, China, [2] Xi'an Botanical Garden of Shaanxi Province/Institute of Botany of Shaanxi Province, Xi'an, China, [3] Guizhou Provincial Key Laboratory for Biodiversity Conservation and Utilization in the Fanjing Mountain Region, Tongren University, Tongren, China, [4] School of Ecology and Environment, Northwestern Polytechnical University, Xi'an, China, [5] Shuanglong State-Owned Ecological Experimental Forest Farm of Qiaoshan State-Owned Forestry Administration of Yan'an City, Yan'an, China

The trait-based approaches have made progress in understanding the community assembly process. Here, we explore the key traits that may shape community assembly patterns of the same community type but within different water availabilities. Natural *Quercus wutaishanica* forests were chosen as a suitable study system to test the difference between economic and hydraulic traits across water availability on the Loess Plateau (LP, drought region) and Qinling Mountains (QL, humid region) of China. A total of 75 plots were established separately in two sites, and 12 functional traits (seven hydraulic traits and five economic traits) of 167 species were studied. Community-weighted mean trait values and functional diversity indices were compared between the two sites. Canonical component analysis was performed to infer whether the changes of community traits and their relationships are driven by intraspecific variation or species turnover. Evidence for likely community assembly processes was tested using the null model to determine whether functional structure among seven hydraulic traits and five economic traits was dominated by different ecological processes between two sites. We found that forests in the Loess Plateau and Qinling Mountains showed different hydraulic and economic traits. Hydraulic and economic traits coupled at the community level were driven by species turnover. Hydraulic traits showed more significant convergent patterns on LP than that in QL. Our results suggest a strong environmental filtering process occurred in hydraulic-based community assembly in the temperate forest with low water availability. Reveal the relationship of hydraulic and economic traits at the community level. Emphasize the critical role of multi-dimensional traits selecting like hydraulic traits in community ecology.

Keywords: community assembly, environmental filtering, null model, hydraulic traits, Loess Plateau

OPEN ACCESS

Edited by:
Francesco Ripullone, University of Basilicata, Italy

Reviewed by:
Vikki L. Rodgers, Babson College, United States
Congcong Liu, Key Laboratory of Ecosystem Network Observation and Modeling, Institute of Geography Science and Natural Resources, Chinese Academy of Sciences (CAS), China

***Correspondence:**
Ming Yue
yueming@nwu.edu.cn

† These authors have contributed equally to this work and share first authorship

Specialty section:
This article was submitted to Functional Plant Ecology, a section of the journal Frontiers in Plant Science

Received: *22 April 2021*
Accepted: *29 November 2021*
Published: *20 January 2022*

Citation:
Zhao J, Zhang Y, Xu J, Chai Y, Liu P, Cao Y, Li C, Yin Q, Zhu J and Yue M (2022) Strong Environmental Filtering Based on Hydraulic Traits Occurring in the Lower Water Availability of Temperate Forest Communities. Front. Plant Sci. 12:698878. doi: 10.3389/fpls.2021.698878

INTRODUCTION

Community assembly is one of the essential topics in ecology, helping to explain researchers understanding species coexistence and distribution (Ellner et al., 2019). Assembly processes shape the structure and composition of communities (Thorn et al., 2016). Two main theories, neutral theory and niche theory (i.e., limiting similarity and environmental filtering), are commonly invoked to explain the mechanisms of forest community assembly. Based on traits, a community may be characterized by the distribution of species functional traits that compose it (Ackerly and Cornwell, 2007). Because of the direct link between traits and the plant organism's function, trait strcucture patterns provide significant insights into how communities are assembled (HilleRisLambers et al., 2012; Kunstler et al., 2016; Loranger et al., 2016).

Plant functional traits are the key characteristics to reflect the adaptability of plants to the environment (Targetti et al., 2013). Plants can acquire and invest resources in different ways, the diversity of these strategies has a significant impact on species composition and ecosystem function (Loreau, 2001; Targetti et al., 2013). Therefore, as a link between species and the environment (Lamanna et al., 2014), functional traits are a new perspective to study complex ecological processes. Among various functional traits, those related to water transport and CO_2 exchange have received more attention, reflecting the crucial importance of processes in the biosphere's functioning (Li S. et al., 2015). Since the concept of leaf economic spectrum was put forward (LES) (Wright et al., 2004), some traits related to carbon economy have been extensively studied, forming economic traits (Wright et al., 2005). Certain other groups of traits, indicating a balance between the demand and supply of water, form the hydraulic traits (Zhang et al., 2012; Sack and Scoffoni, 2013; Li L. et al., 2015; Yin et al., 2018).

However, at the community level, it is still a new perspective to distinguish hydraulic traits from economic traits, which can provide a basis for revealing the importance of multi-dimensional traits in community assembly study. Liu has considered stomatal traits as hydraulic traits in community assembly study, but more hydraulic traits are not involved (Liu et al., 2020). In addition, current studies have included only economic traits by using the "Null model" (Laughlin and Laughlin, 2013). In the subalpine forest community, limiting similarity is more important for determining species coexistence by selecting specific traits like SLA (Yan et al., 2012). Limiting similarity also shapes the functional structure of plant root traits (Luo et al., 2021). By contrast, soil characteristics could improve environmental filtering effects on some economic traits like leaf dry matter content (Mori et al., 2021). Environmental filtering is the main driving force affecting community functional traits through the study of 15 common economic traits in the Amazon rainforest (Fortunel et al., 2014). Given the large difference of environmental traits among ecosystems, more types of functional traits are needed to better explain the community assembly mechanism.

Understanding how the environment influences the species distribution is a central topic in ecology (Condit, 2000; Baltzer et al., 2009). Environmental factors, such as water availability, play a critical role in species distribution patterns and can work as filters that shape plant communities' function or composition (Groom, 2004; Engelbrecht et al., 2007; Moeslund et al., 2013). In order to adapt to environmental changes, species have developed corresponding adaptive strategies to the local environment (Liu et al., 2021), and these strategies are reflected in functional traits. A previous study suggests that the water availability changes in Loess Plateau forests involve trade-offs between economic and hydraulic traits, and that this correlation of leaf economics and hydraulic traits might be a type of adaptation mechanism (Yin et al., 2018). In habitats with low water availability, plants must invest resources in organs that can improve hydraulic resistance (Rowland et al., 2015), which leads to changes in hydraulic traits. For example, the increase of sapwood area, can reduce water loss to the greatest extent (Gotsch et al., 2019), minimize photosynthesis, and growth rate (Delzon et al., 2004). Trade-offs among different strategies produced by plants in response to stress are one important mechanism of coexistence (Silvertown et al., 2015; Letten et al., 2017). Hydraulic traits also constrain plant distributional ranges (Li et al., 2018). The previous studies mentioned above revealed that plants produce different trait combinations to adapt to the local environment. At the species level, the relationship between economic and hydraulic traits is well explored (Sack and Scoffoni, 2013). Furthermore, Liu discussed the variation in leaf morphological, stomatal, and anatomical traits (Liu et al., 2019). Li discussed the leaf economic and hydraulic traits relationships in five tropical-subtropical forests (Li S. et al., 2015). Therefore, in habitats with different water availability, it can be speculated that the relative importance of the two kinds of traits at the community level is different. The combination between hydraulic and economic traits can be used as a filter factor to affect the coexistence of species and community assembly patterns, but this still requires direct evidence to verify.

Since the Middle Pleistocene, *Q. wutaishanica* has been one of the dominant tree species in deciduous broad-leaved forests of northern China. The forest communities dominated by *Q. wutaishanica* are climax vegetation occupying the upper limit of deciduous broad−leaved forests in the intermediate altitude of Qinling Mountains (QL) and the northwestern limit (related to water availability) of forests on the Loess Plateau (LP) (Zhu, 1993). The *Q. wutaishanica* community on the Loess plateau differed from many other forests of their kind due to the wide range of water limitations they are facing. This special *Q. wutaishanica* forest distribution pattern and environment type provide an excellent opportunity to explore the changes of plant functional traits and assemblages of communities with the same evolutionary history under different water use conditions.

In this study, we aim to discuss the differences and effects of economic and hydraulic traits at the community level and explore the pattern of community assembly within different water availability of *Q. wutaishanica* forests by using economic and hydraulic traits separately. We hypothesized that (1) forests growing in water-rich environments will have traits related to resource acquisition, but forests growing in water-poor environments will have traits related to resource conservation.

(2) Economic and hydraulic traits are strongly coordinated at the community level. (3) Functional diversity and economic traits reflect the different ecosystem function within different water availabilities. (4) The community assembly process is different based on hydraulic traits from economic traits. Carbon and light competition would limit economic trait similarity to avoid competitive exclusion and facilitate niche partitioning in two sites. While drought environment characterizing lower water availability may lead to stronger environmental filtering in hydraulic traits.

MATERIALS AND METHODS

Study Site and Sampling

This study was conducted in a well-protected typical *Q. wutaishanica* forest in Shaanxi province, China. The study was performed in two sites at the Ziwuling region (35°41′-35°44′ N, 109°00′-109°02′ E) on the middle of Loess Plateau and the Taibaishan Nature Reserve (33°84′-33°86′ N, 108°82′-108°87′ E) in the north slope of Qinling Mountains. The *Q. wutaishanica* forest in the Qinling Mountains has a temperate monsoon climate, which is relatively humid (annual precipitation 900–1,000 mm), but the Loess Plateau has a temperate continental climate, which is relatively dry and going through serious water erosion (annual precipitation 550–650 mm), such climatic conditions lead to direct differences in soil water content (**Supplementary Figure 1**).

The field work was surveyed in July 2019. Three permanent plots covering an area of 2,500 m^2 (50 m × 50 m) were established in the two study areas, respectively, to investigate this research (**Table 1**). The distance between any two plots was more than 1 km to avoid spatial auto correlation in variables and pseudo-replications (Conti and Dıaz, 2013). Each plot was subdivided into 75 quadrats of 10 m × 10 m. All woody species in plots were identified within each plot and their richness (the number of plants) was measured as the basic community data.

Soil water content (SWC) was using the oven drying method. Three sites were randomly selected in each plot. The external humus was stripped away, exposing the topsoil. Soil samples of 0–10 cm and 10–20 cm were drilled with a metal sampler. A total of six soil samples was obtained in each plot. After drilling the soil, gravel and plant roots were removed, and the portable electronic balance was used to weigh the fresh mass of the soil, which was then brought back to the laboratory to be dried at 105°C oven to constant weight as the dry mass, so as to calculate the soil water content.

TABLE 1 | Plot setting and geographic information.

	Administrative region	Coordinate of latitude and longitude	Area (m^2)	Elevation (m)
Qinling Mountains	Meixian county	107°45′E/34°41′N	2,500	1,958
	Meixian county	107°45′E/34°20′N	2,500	1,937
	Jiwozi village	108.83°E/33°84′N	2,500	1,900
Loess Plateau	Huangling county	109°01′E/35°42′N	2,500	1,100
	Huangling county	109°00′E/35°49′N	2,500	1,112
	Huangling county	109°11′E/35°37′N	2,500	1,100

Leaves were collected from woody species in every plot. For each species, at least three individuals were sampled and stored separately. Mature and fully expanded leaves were collected from the sun-exposed branches of each individual. After harvesting, 30 leaves of each species were preserved in black plastic bags to protect from light for analyses of economics traits, 3–5 leaves and branches were maintained in a formalin acetic alcohol (FAA; 5 ml of 38% formalin, 5 ml of glacial acetic acid, 90 ml of 50% ethanol, and 5 ml of glycerin) for analyses of hydraulic traits like venation traits, stomatal traits, and anatomical structures (Chen and Wang, 2009).

Trait Selection

Here, we measured 12 functional traits of 167 woody plants (**Supplementary Figures 2, 3**) which grow in *Q. wutaishanica* forests on LP and in QL. Four of these traits were considered as economic traits, which are correlated with nutrient acquisition, light acquisition, and biomass allocation in plants, eight of these traits were considered as hydraulic traits, which are correlated with water transport and transpiration in plants (**Table 2**).

Economic Traits

First, a photograph of each fresh leaf surface was taken with a digital camera, and leaf surface area was measured with Motic Images Plus 6.0 (Motic China Group, Xiamen, China) software. The fresh leaf mass was measured with electronic balance (one ten-thousandth). Then all leaves were placed in a drying oven for 72 h at 70°C to determine the dry mass. Leaf dry mass per area (LMA, g m^{-2}) was calculated as the ratio of the leaf dry mass to leaf surface area. Leaf dry matter content (LDMC, mg/g) was calculated as the ratio of the leaf dry mass to leaf fresh mass. Leaf thickness (LT, mm) was measured through transverse sections using Image-Pro Plus 6.0, avoiding the influence of major veins. For each section on one leaf, 10–20 measurements were made. Leaf tissue density (TD, g cm^{-3}) was calculated as the ratio of LMA to LT. Net photosynthesis rates of mature and fully expanded leaves were measured between 9:00 and 11:00 with the portable photosynthesis system (Li-6800, Li-Cor, Lincoln, NE). CO_2 concentration was that of the ambient air and the flow rate was set at 500 μmol s^{-1}. Light was provided with an LED and the photosynthetically active radiation (PAR) gradients were 1,800, 1,500, 1,200, 1,000, 800, 600, 400, 200, 100, 50, 20, and 0 μmol m^{-2} s^{-1}, and the maximum net photosynthetic rate was obtained by fitting the empirical equation of the least square method (Bassman and Zwier, 1991).

Hydraulic Traits

We used the nail-polish imprint method to measure stomatal traits on three leaves for one individual and three individuals for one species (Zhao et al., 2016). We photographed the stomatal prints under a Classica SK200 digital light microscope (Motic ChinaGroup Co., Ltd., China). Then we used Image-Pro Plus 6.0 software to measure SL (μm). SD (mm^{-2}) was calculated as the number of stomata per unit leaf epidermal area by dividing

TABLE 2 | Functional traits employed in this study as well as their abbreviations, units, and functions.

	Plant traits	Abbreviations	Units	Function
Economic traits	Leaf dry mass per area	LMA	g/m^{-2}	Resource capture
	Leaf dry matter content	LDMC	mg/g	Leaf structure
	Leaf thickness	LT	μm	Resistance to disturbance
	Leaf tissue density	TD	$G\ cm^{-3}$	Leaf defensive
	Maximum net photosynthetic rate	P_{max}	$mmol\ m^{-2}.\ s^{-1}$	Leaf cooling
Hydraulic traits	Huber value	Hv		Water transport
	Maximum vessel diameter	Vd_{max}	μm	Resistance to embolism
	Stomatal density	SD	mm^{-2}	CO_2 acquisition and water loss
	Stomatal length	SL	μm	CO_2 acquisition and water loss
	The leaf turgor loss point	Ψ_{tlp}	Mpa	Tolerance to drought stress
	Branch wood density	WSG_{branch}	g/cm^{-3}	Water transport
	Vein density	VD	$mm\ mm^{-2}$	Water distribution strategy

leaves into grids of 100 μm × 100 μm. SL and SD were averaged from more than 20 randomly selected fields of view. Water potential was measured in consecutive sunny days of mid-July 2019 with a pressure chamber (SEC3115, Santa Barbara, CA, United States). Leaf samples from three individuals of each species were cut from trees and sealed immediately in black plastic bags with a moist paper towel in them and kept in a cooler during the transportation (about 30 min) to the laboratory. Leaves were first weighed to obtain the initial fresh mass and then immediately placed in a pressure chamber to determine the initial water potential. Leaf weight and water potential were measured periodically during slow desiccation of the sample in the natural condition. Finally, leaves were oven-dried for 72 h at 70°C to determine the dry weight. The leaf turgor loss point (Ψ_{tlp}, MPa) was calculated by the PV curve method based on the natural wind dry method (Tyree and Hammel, 1972).

We selected three complete annual branches for one individual with good light conditions on the upper part of the species. Branches that were 5 cm long were cut from the base of the branches to remove the bark and determine the wood density (WSG_{branch}). The volume of the branches was obtained by the drainage method, followed by oven-drying at 70°C for 72 h before weighing. The dry weight of the branches was obtained by weighing scales with an accuracy of 0.0001 g. The branch wood density is the dry weight of the annual branch divided by the volume of the fresh branch.

The diameter of the branches was measured by a vernier caliper (μm). Heartwood and pulp were subtracted, and the sapwood area [$As_{(branch)}$] of the branches was obtained. At the same time, all the leaves on the branches were collected, and then the ratio of sapwood area to total leaf area was calculated as the Huber value (Hv).

We took leaves from the FAA and cut complete leaf petioles, and the transverse sections were made on a Leica RM2135 rotary microtome (Leica Inc., Bensheim, Germany) and then mounted on glass slides. The transverse sections were observed and photographed under an optical microscope, and the images were measured using Image-Pro Plus 6.0 (Media Cybernetics, Unite States) software to get the maximum vessel diameter (Vd_{max}, μm^2).

For vein density (VD, $mm\ mm^{-2}$) assessments, leaves were sampled about 2 cm^2 in the central region, immersed in 10% NaOH in an oven at 65°C for 4–12 h. Samples were repeatedly washed with deionized water for about 30 min, immersed and bleached in 10% H_2O_2 for 10–30 min, and then washed again in deionized water. Samples were next stained with safranin for 30 min. Thereafter, they were dehydrated using graded ethanol series (30, 50, 70, 85, 95, and 100%) and immersed in xylene: ethanol absolute (1:1) solution and xylene. Stained sections were mounted, photographed, and then analyzed using Image-Pro Plus 6.0. The total length of veins per unit area was measured as VD.

Statistical Analyses

Community Weighted Mean Value

We examined correlations between weighted traits of communities. The community-weighted mean (CWM) of all 12 traits was calculated for each plot as a weighted average of species traits, average trait value from plots with weightings based on species relative abundance (trees ≥ 10 cm Diameter at Breast Height) (Hulshof et al., 2013):

$$\mathrm{CWM} = \sum_{i}^{n} p_i Trait_i$$

where n was the number of species sampled in the plant community, p_i was the relative abundance of i^{th} species, and $Trait_i$ was the mean trait value of the i^{th} species. Significant differences in CWM values from two sites for the whole 12 traits were tested by the Student's t-test. In order to obtain comprehensive trait values in multiple dimensions, multivariate associations of traits were analyzed with a canonical correlation analysis (CCA) in CANOCO software for Windows 5.0 (Microcomputer Power, Ithaca, NY, United States) and inductive analysis the traits represented by the first two axis of CCA. Plant community data consisted of the relative abundance of 167 species in two sites, respectively.

Community Functional Diversity

We assessed the effects of species traits on ecosystem functioning by computing three kinds of functional diversity indices. Functional richness (FRic) is the volume delimited by the smallest convex hull drawn around the existing species positioned on trait axes according to their trait values and reflects the amount of niche space occupied by the community. One-dimensional functional richness (FDis) is the ratio of the trait range of a species to the trait range of all species in the community (Schleuter et al., 2010). Functional divergence (FDiv) is the variance of species trait distribution in the trait space and functional evenness (FEve) is the degree to which the biomass of a community is distributed in niche space (Mason et al., 2005). Rao's quadratic entropy (RaoQ) is defined to measure the diversity and difference within and between populations (Botta-Dukát, 2005). All indices were calculated within the "FD" package (Laliberté) in R (Version 4.02; R Core Team, 2015).

Community Functional Structure by Null Model

Ecological null model approaches are the most frequently used tools for studying the assembly process because these are appropriate for the identification of non-random components in community composition. To assess if functional traits obtained per plot differed from random, we used a null model approach to deduce assembly processes (Ricotta and Moretti, 2011).

Different vertical structures have different strategies in *Q. wutaishanica* communities, which may lead to different community assembly processes (Chai et al., 2016). Functional structure of the tree layer and the whole woody community were calculated, respectively, to explore the differences at different vertical structures based on economic and hydraulic traits.

The essence of the approach is that trait divergence or convergence is characterized by a test statistic and this test statistic was run for 999 random samples created from the species pool. Species pools were established in QL and on LP, respectively. Specifically, a wide range of species were sampled according to the Flora of Loess Plateau and Qinling Mountains to expanded species pools. The test statistic was also calculated for the real samples, and proportions of random communities where the test statistic is more extreme than in the field sample. This study measured the "mean functional distance" (MFD) of species in the community to calculate the value of "standard effect size values" (SES). We used probit transformed *p*-values as SES, which indicate the strength of trait divergence or convergence. Positive SES values indicate that competition is the leading assembly rule, while negative ones refer to the leading role of environmental filtering. Significant differences in SES values from zero for the whole dataset were tested by the Student's *t*-test. The standard effect size of all traits was calculated by the "Picante" package (Kembel) of R software.

$$\text{Standardized effect size(SES)} = \frac{\text{MFD}_{\text{observed}} - \text{MFD}_{\text{randomized}}}{\text{sdMFD}_{\text{randomized}}}$$

where $\text{MFD}_{\text{observed}}$ is the observed value, $\text{MFD}_{\text{randomized}}$ is the mean of the simulated values, and $\text{sdMFD}_{\text{randomized}}$ is the standard deviation of the simulated values.

RESULTS

Community Weight Mean Value Between Two Sites

The CWM varied across plots between LP and QL. Eleven of twelve CWM traits differed significantly between the LP and QL (the abbreviations and function of traits are shown in **Table 2**).

In the analysis of CWM hydraulic traits, communities on the Loess Plateau had significantly higher Hv, SD, $\text{WSG}_{\text{branch}}$, and VD compared to those from QL (**Figures 1B,C,F,G**). Communities from QL had significantly higher SL and Vd_{max} than those of the Loess Plateau (**Figures 1A,D,E**); In the analysis of CWM economic traits, communities on the Loess Plateau had significantly higher LDMC, LT, and LMA compared to those from Qinling Mountains (**Figures 2A,B,C**). Communities from the QL had significantly higher P_{max} than those of the LP (**Figure 2E**). TD showed no significant differences between the LP and QL (**Figure 2D**).

The first axis of the CCA of 12 traits explained 33.4% of the relation. Three hydraulic traits (SD, VD, SL) and three economic traits (LDMC, LMA, P_{max}) were strongly associated with the CCA1 axis (**Table 3**). We also found that plots and species distributions had a significant difference between LP and QL (**Figure 3**). Different species were grouped based on water availability along the CCA1, with QL and LP plots well separated. Generally, the plots in LP were grouped, whereas those plots in QL were grouped together (**Figure 3A**). Generally, the CCA tests showed that the hydraulic and economic traits were coupled on the community level, and the species composition showed a certain regularity along with water availability at a regional scale.

Community Functional Diversity Indices

We analyzed functional diversity indices (FRic, FEve, FDiv, FDis, and RaoQ) in each plot between the LP and QL separately. Only FDic and FDiv based on multiple hydraulic traits significantly showed different patterns between two sites (**Figures 4A,C**). That is, the QL had higher FDic and FDiv on multiple hydraulic traits. There was no significant difference in other functional diversity indices (FRis, FEve, and RaoQ) based on both multiple economic traits and multiple hydraulic traits between the two sites (**Figures 4B,D,E**).

Functional Structures Between Two Sites

In the tree layer, single-trait analyses indicated SES of most hydraulic and economic traits showed a deterministic pattern between the two sites (**Figure 5**), except for SD on LP. As for hydraulic traits, functional structures of plant Ψ_{tlp}, Hv, $\text{WSG}_{\text{branch}}$, and SL were more convergent on LP than in QL (**Figure 5A**). There was no significant difference in functional structures of Vd_{max}. As for economic traits (**Figure 5B**), functional structures of plant LMA and LT were more convergent in QL than on LP. There was no significant difference in the functional structures of LDMC, P_{max}, and TD. Multi-trait analyses also indicated that the SES of multiple hydraulic and economic traits showed a deterministic pattern between the two sites (**Figure 6A**) in the tree layer. Functional structures

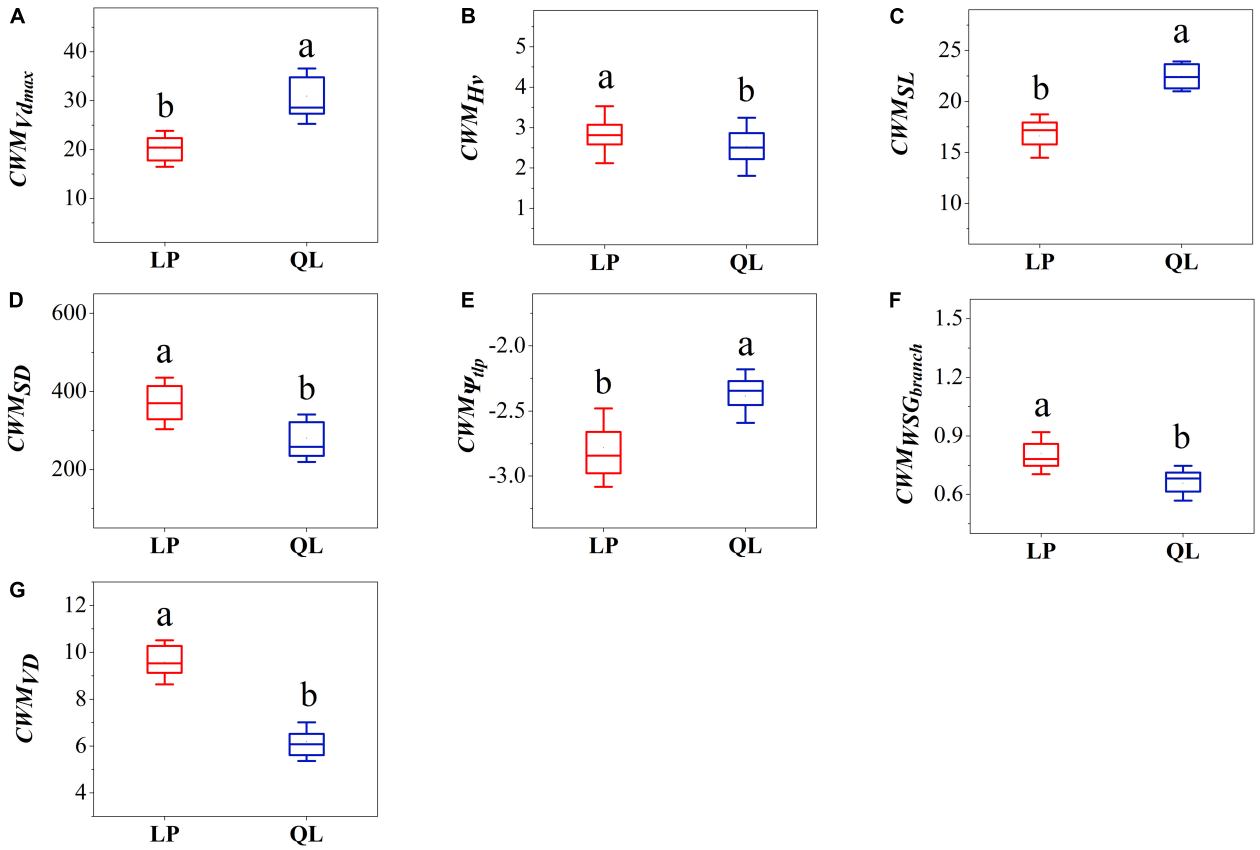

FIGURE 1 | Box-plot comparing community-weighted mean value of **(A)** maximum vessel diameter, **(B)** Huber value, **(C)** stomatal length, **(D)** stomatal density, **(E)** the leaf turgor loss point, **(F)** branch wood density, **(G)** vein density between LP and QL. Different letters indicate significant differences ($P < 0.05$).

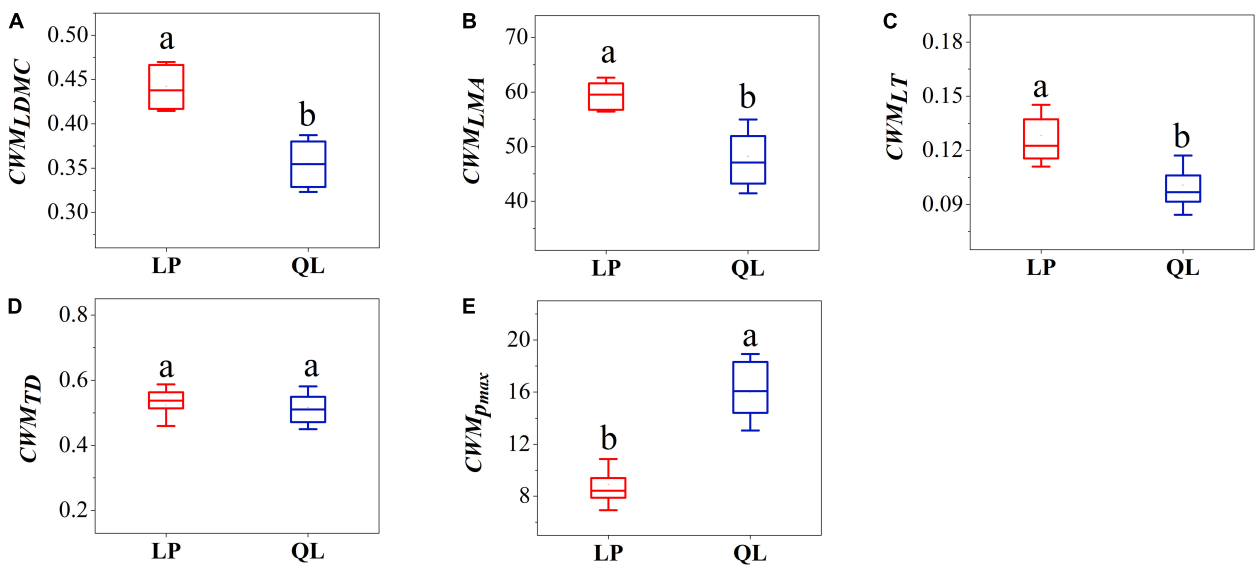

FIGURE 2 | Box-plot comparing community-weighted mean value of **(A)** leaf dry matter content, **(B)** leaf dry mass per area, **(C)** leaf thickness, **(D)** leaf tissue density, **(E)** maximum net photosynthetic rate between LP and QL. Different letters indicate significant differences ($P < 0.05$).

TABLE 3 | Loadings of measured traits to CCA1 and CCA2.

Traits	CCA1	CCA2
Stomatal length (SL)	0.9091	0.0264
Vein density (VD)	−0.9088	−0.0969
Maximum net photosynthetic rate (P_{max})	0.8763	0.1314
Leaf dry mass per area (LMA)	−0.7877	−0.0306
Leaf dry matter content (LDMC)	−0.7805	0.0872
Stomatal density (SD)	−0.7217	−0.0805
Maximum vessel diameter (Vd_{max})	0.7192	−0.2473
Branch wood density (WSG_{branch})	−0.6381	0.3060
The leaf turgor loss point (Ψ_{tlp})	0.5925	0.4848
Leaf thickness (LT)	−0.3954	−0.4121
Leaf tissue density (TD)	−0.3192	−0.3447
Huber value (Hv)	−0.1593	0.0806

of both hydraulic and economic traits were more convergent on LP than in QL.

In the whole woody community, similarly, single-trait analyses indicated that the SES of most hydraulic and economic traits showed a deterministic pattern between the two sites (**Figure 5**), except for Hv, VD, and Vd_{max} in QL. As for hydraulic traits, functional structures of plant Ψ_{tlp}, Hv, WSG_{branch}, VD, and Vd_{max} were more convergent at LP than in QL (**Figure 5C**). There was no significant difference between the functional structures of SD and SL; as for economic traits, the functional structure of plant LMA was more convergent in QL than on LP (**Figure 5D**). There was no significant difference in the functional structures of LDMC, LT, P_{max}, and TD. Multi-trait analyses also showed that the SES of multiple hydraulic and economic traits showed a deterministic pattern between two sites (**Figure 6B**). Functional structures of both hydraulic and economic traits were more convergent on LP than in QL. The results in the entire community were the same as in the tree stratum.

DISCUSSION

Our investigation demonstrated that a combination of plant hydraulic traits (SD, VD, SL) and economic traits (LDMC, LMA, P_{max}) comprises a group of key traits which are important for understanding the community assembly process in *Q. wutaishanica* forests of different water availability. The significant difference in hydraulic community-weighted mean traits indicated that species in LP experience stressful water conditions in comparison with QL. A strong convergent pattern in single and multiple hydraulic traits of LP's *Q. wutaishanica* forest communities suggests that environmental filtering plays a leading role in the assembly process compared with QL.

Different Water Use Strategies Between the Two Sites

The shifts in CWM traits (**Figures 1**, **2**) represent plant traits' responses to stress in the community. In the two *Q. wutaishanica* forests with different water availability, the species within plots showed different functional strategies. We showed that the water availability was a strong power that selected different ecological strategies. LP was dominated by species with conservative hydraulic traits (avoid embolism). While hydraulic traits in QL were mostly associated with acquisitive strategies (improve water supplement efficiency).

For economic traits, we found that with the decrease of water availability from QL to LP, LDMC, LT, P_{max}, and LMA increased significantly, while TD showed no significant difference. In the LP, under the limited water resources or relatively dry conditions, other stressful conditions may also gradually increase from QL to LP as soils become barren and canopy cover decreases. In this case, LDMC and LMA are also closely related to water (Cornelissen et al., 2003), and the plants have relatively small and thicker leaves, higher leaf dry matter content, and higher water retention ability than those species distributed under abundant soil resources (Dwyer et al., 2014). These changes are reflecting a strategy to minimize water loss and respiration costs when water is not sufficient which is consistent with previous results (Subedi et al., 2019). On the contrary to LP, the *Q. wutaishanica* forest in QL has sufficient soil moisture (Liu et al., 2017) and is typically accompanied by quick growth with relatively large and soft leaves, relatively high leaf area, and relatively low leaf dry matter content. The weighted average of the net photosynthetic rate at the community level increased with the increase of water availability because photosynthesis also influences plant growth (Garnier et al., 2004), which appears to be a strategy to survive in rich soils (Givnish, 2002) without water limitation "trouble."

There were also differences in the community weighted mean values of all seven hydraulic traits between the two sites. Under the drought environment, plants must take a conservative strategy by investing resources in traits that can improve hydraulic resistance to ensure water transport safety (Rowland et al., 2015). To minimize the risk of embolism, plants reduce the diameter and increase the number of vascular bundles in the sapwood area (Fortunel et al., 2014). The increase of sapwood area and the decrease of Huber value can reduce water loss to the greatest extent (Gotsch et al., 2019), but at the same time reduce photosynthesis and growth rate (Delzon et al., 2004). Plants in the drought environment also need higher VD to ensure water supply (Sack and Scoffoni, 2013). Besides, small and dense stomata can more flexibly sense changes to drought and close stomata to reduce water loss in a timely manner (Franks et al., 2009). Plants also have low Ψ_{tlp} to maintain certain stomatal conductance, hydraulic conductivity, and photosynthetic gas exchange. These changes reflected a conservative strategy in the drought environment (Lenz et al., 2006; Reich et al., 2007; Bartlett et al., 2012). Instead, the humid environment has filtered out species that invest in improving hydraulic efficiency, which we can define as risk-taking strategies (Hacke et al., 2001; Fan et al., 2011). In our results, species of *Q. wutaishanica* in LP have higher WSG_{branch}, Hv, and VD (**Figure 1**), which allows them to resist drought stress by maintaining high water potentials (Westoby et al., 2002).

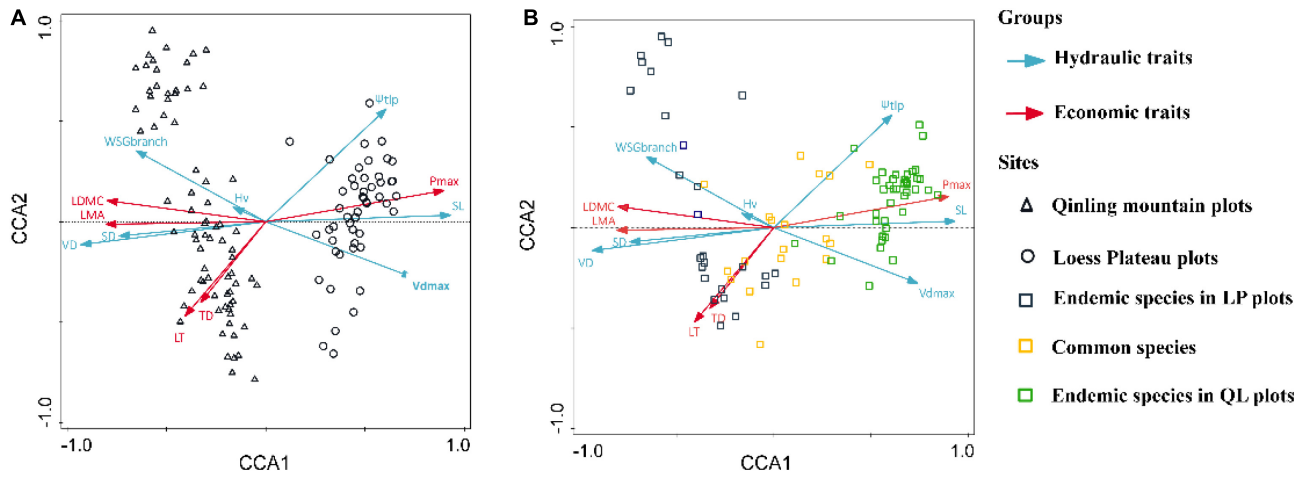

FIGURE 3 | Community-weighted trait bi-plot for canonical correlation analysis, showing the effects of functional traits on the community species composition and plot distribution between the Loess Plateau and Qinling Mountains. **(A)** The effect of functional traits on the plot distribution. **(B)** The effect of functional traits on the community species composition. The ordination is based on community-weighted mean traits, with traits weighted for each species by its relative abundance in the community. Trait abbreviations are given in **Table 1**.

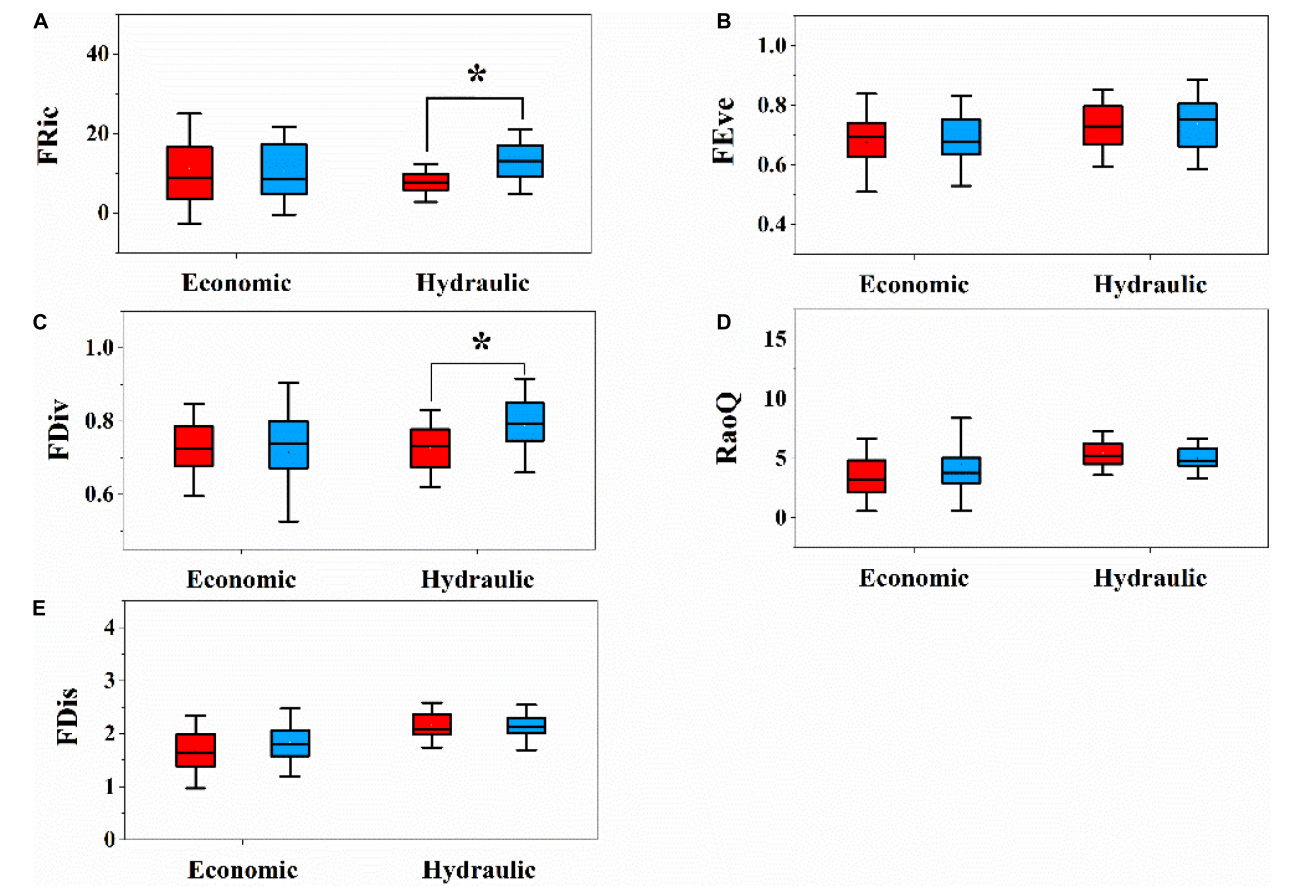

FIGURE 4 | Difference of functional diversity components in relation to hydraulic traits and economic traits between LP and QL. **(A)** Functional richness (FRic); **(B)** functional evenness (FEve); **(C)** functional divergence (FDiv); **(D)** Rao's quadratic entropy (RaoQ); **(E)** one-dimensional functional richness (FDis); different letters above bars indicate statistically significant differences at $P < 0.05$.

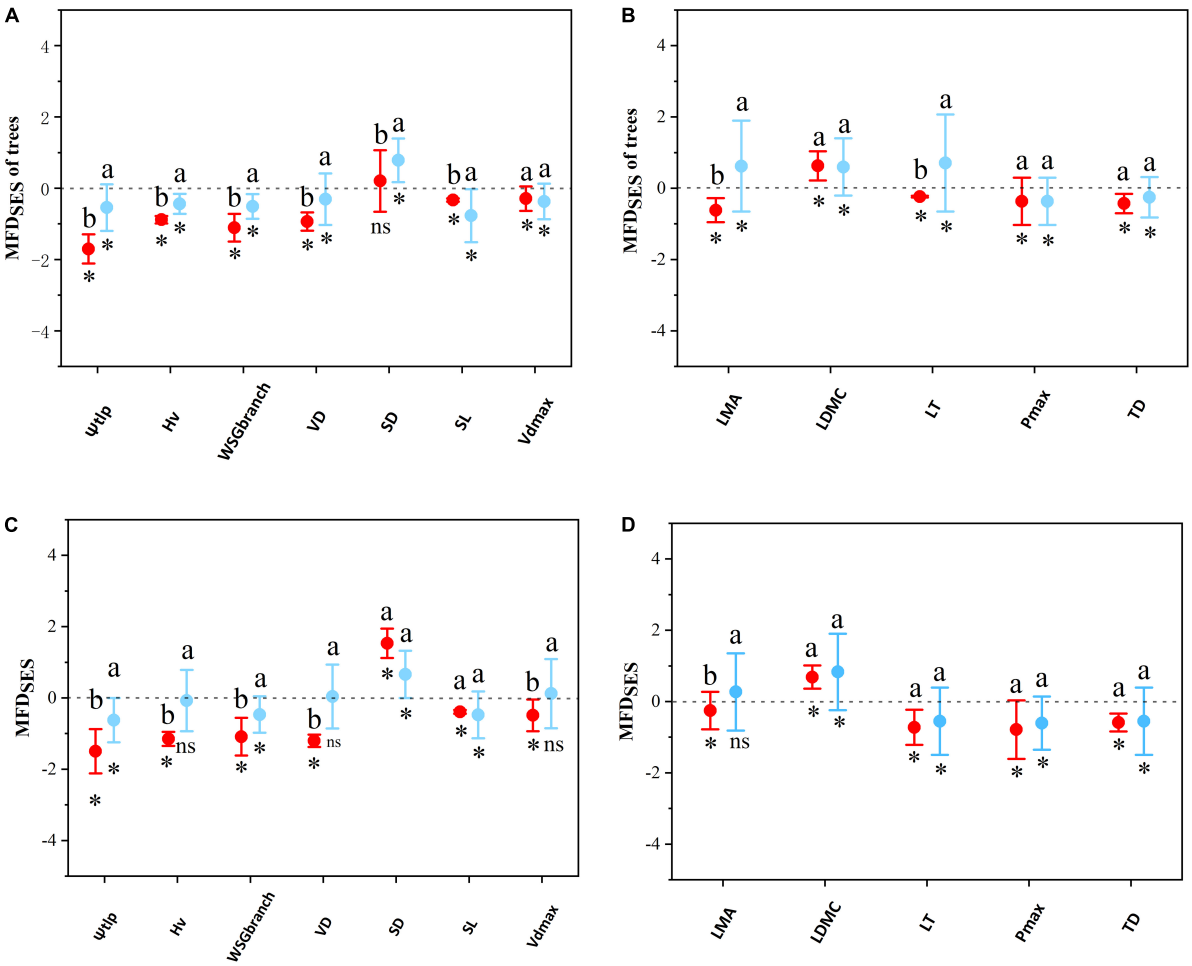

FIGURE 5 | The difference of community functional structures based on single traits between the Loess Plateau (LP) and the Qinling Mountain (QL). The functional structures were measured as standardized effect sizes (SES). **(A)** Test on single hydraulic traits in tree stratum. **(B)** Test on single economic traits in tree stratum. **(C)** Test on single hydraulic traits in the whole site. **(D)** Test on single economic traits in the entire site. Specifically, SES > 0 represents functional divergence, whereas SES < 0 indicates functional convergence. Each point shows the mean SES values among all plots within the LP and the QL. Error bars represent standard errors. Asterisks indicate significant differences between SES with 0. Different letters above bars (ab) indicate statistically significant differences at $P \leq 0.05$ between the LP and the QL in the same trait.

The differences in hydraulic and economic traits between the two sites demonstrate the differentiation of ecological strategy in the *Q. wutaishanica* community, and this, in turn, enables them to develop strategies for facing different environments. Within each forest, there is a continuous change in water availability, where low water availability will lead to communities with drought resistance and conservative traits. At high levels of water availability, such a tolerance strategy will not be feasible anymore, leading to communities with resource acquisition and water use efficiency traits. The *Q. wutaishanica* community in QL was more inclined to the efficiency strategy, whereas the *Q. wutaishanica* community on LP was more inclined to the safety strategy. These results in CWM reveal the difference in hydraulic and economic traits between the two sites and provide a background for further discussion of species coexistence and community assembly under different water conditions. More evidence is needed to show the degree to which economic traits and hydraulic traits represent environment filtering.

The Coupled Relationship Between Economics and Hydraulic Traits Among Community Level

The results of CCA analysis intuitively reflect the differences in CWM of the surveyed community. The study plots were separated along CCA 1, and the species distribution was relatively dispersed, so it could be seen that the differences in traits were caused by species turnover rather than intraspecies variation. At the same time, most of the common species in the two sites were dominant trees (like *Quercus wutaishanica, Betula albosinensis, Toxicodendron vernicifluum,* etc.), and their relationship with CWM is more concentrated. Yin et al. (2018) found coupled relationships between economic and hydraulic traits by using

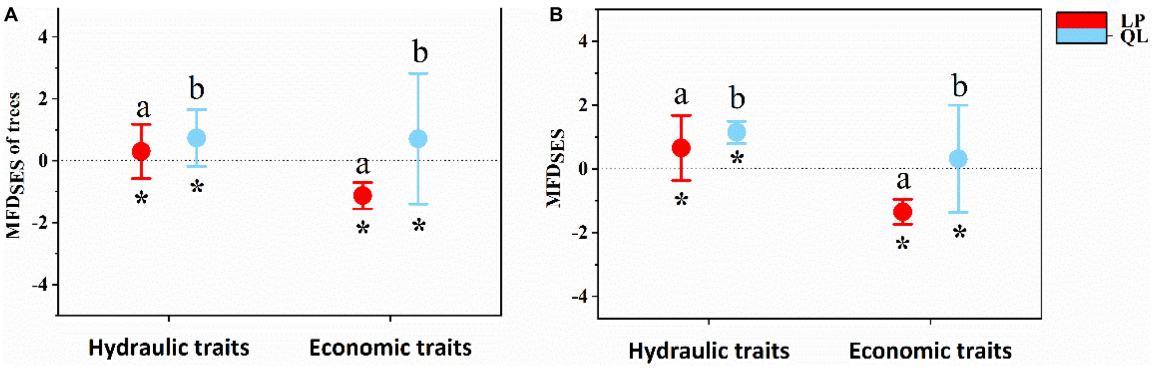

FIGURE 6 | The difference of community functional structure [standardized effect size (SES)] based on multiple traits between the Loess Plateau (LP) and the Qinling Mountain (QL). **(A)** Test on multiple hydraulic and economic traits in tree stratum. **(B)** Test on multiple hydraulic and economic traits in the whole site. Standardized effect size > 0 represents functional divergence, whereas SES < 0 indicates functional convergence. Red point and blue point show the mean SES values within the LP and the QL. Error bars represent standard errors. Asterisks indicate significant differences between SES with 0. Different letters above bars (ab) indicate statistically significant differences at $P < 0.05$ between the LP and the QL in the same trait.

47 woody plants on the Loess Plateau. Therefore, our results indicate a strong correlation among community-level traits, which resulted in plant communities adopting a cost-effective strategy to improve resource use efficiency and/or resistance to stress in low water availability (Flores-Moreno et al., 2019; Liu et al., 2020). Besides, water availability promoted the turnover of understory shrub species. The coupled relationship between the economic traits and the hydraulic traits among the community level at the regional scale improved the overall adaptability of the *Q. wutaishanica* community.

The CCAs also help us to determine important traits that correlate with aspects of species distribution. The interactions in functional traits, species composition, and plot distribution highlight the importance of trait selection that represents specific strategies for exploring community assembly mechanisms. Therefore, a combination of plant hydraulics and economic traits form a group of key traits which are significant for understanding the community assembly process in *Q. wutaishanica* forests between the two sites. Different assembly processes may be operating simultaneously along with these distinct functional strategies (Spasojevic and Suding, 2012). Therefore, choosing different functional traits (hydraulic and economic) helps us uncover the cause of species turnover and community assembly processes in this area. Ultimately, based on the trait patterns we have found, we suspect that convergent species distribution at LP (lower water availability) may be the result of filtering process for the same traits.

Functional Diversity Based on Hydraulic and Economic Traits in Response to Water Availability Change

Functional diversity is considered as an important driver of community assembly across environmental gradients (Sanaphre-Villanueva et al., 2016). Thus, the difference in the functional diversity of hydraulic traits between the two sites also reflects the difference in the community assembly pattern. The hydraulic trait functional richness (FRic) of the *Q. wutaishanica* community in the LP was lower, indicating that the community was more affected by environment filtering, which made the species in the community have similar hydraulic traits and reflect the elimination of poor competitors in water acquisition and in line with the negative values of FDiv found there. Relatively high FRic values of hydraulic traits in QL indicates that the community has high ecological space utilization, high niche differentiation of water use among species, and limiting similarity process acts on the coexistence of species (Mason et al., 2012), and the coexistence of acquisitive and conservative species that show different constellations of hydraulic traits (Mayfield and Levine, 2010).

There are also significant differences in hydraulic traits of functional divergence (FDiv) between the two sites. The functional divergence reflects the dispersion degree of functional traits in the community. LP showed negative FDiv, suggesting that environmental filtering may reduce the functional strategies present in this environment, which is also in line with the negative values of FRic found there. Communities with higher functional divergence have more complete ecosystem functions like Qinling Mountains (Xu et al., 2014). The high degree of divergence indicates that plants have a high degree of niche differentiation in environment water utilization, and it may be produced by the direct lower competition. The comparisons of functional diversity in our study verified the difference in the assembly process between hydraulic and economic traits. We found evidence of environmental filtering in LP through hydraulic traits functional indices, probably due to the effect of lower soil water availability.

The Difference of Community Assembly Process Based on Hydraulic and Economic Traits Between Two Sites

As for multiple hydraulic and economic traits, the null model revealed that community functional structure of QL and LP showed the deterministic processes which dominated the community assembly of both sites (**Figures 5**, **6**). Previously

found in the *Q. wutaishanica* community (Wang et al., 2019), trait divergence has been commonly observed (Norden et al., 2012; Purschke et al., 2013). Moreover, this pattern is generally attributed to the elimination of functionally similar species caused by competition or colonization of distantly related species (Li S. et al., 2015). As for single traits, the functional structures for most hydraulic and economic traits showed a deterministic process (**Figure 5**). Most of the functional traits showed a convergent pattern, indicating that environmental filtering drove the community assembly process in some traits. Several functional traits showed the divergent pattern as well, which indicated that limiting similarity also contributed to the community assembly process of the *Q. wutaishanica* forests in the two sites. Biotic interactions such as competition may work in the divergence of two hydraulic and economic traits (SD, LDMC). One possible reason is that plant stomata are easily modified by environmental conditions and are sensitive to changes in the external environment, resulting in differentiation in SD adapted to concentrations of carbon dioxide in global warming (Wu et al., 2018). This result appears to suggest the limiting similarity process lessens competition among plants, in which resource competition acts to constrain local neighborhoods to certain two traits or trait combinations (SD and LDMC). Based on the different assembly pattern between single and multiple hydraulic traits, we suspected that the competitive interaction among species in SD led to the divergence of overall hydraulic traits functional structure in the two sites. In general, limiting similarity and environmental filtering of single traits may work to counteract each other, resulting in divergence but increasing convergent patterns of multi-hydraulic traits.

The selected economic and hydraulic traits describe the adaptability of species to water resources acquisition, carbon investment, and mechanical support. These different types of functional traits and trait combinations will reflect the adaptation strategies of plants to different environmental conditions (Drenovsky et al., 2012). Consistent with our result, a previous study found that reproductive traits and canopy height showed divergent and convergent patterns, respectively, in the temperate primary forests of northwest Germany (Naaf and Wulf, 2012). Here, traits convergence (environmental filtering) and traits divergence (limiting similarity) can also simultaneously act on different functional traits in response to different biological and abiotic mechanisms, and thus collectively drive community assemblage.

There were shifts in economic and hydraulic functional structure, transitioning from QL to LP with a decrease of water availability. From QL to LP, all 12 measured traits exhibited significant phylogenetic signals ($P < 0.05$, **Supplementary Table 1**), functional structures of plant hydraulic traits (Ψ_{tlp}, Hv, WSG_{branch}, Vd_{max}, and VD) and an economic trait (LMA) convergent more in LP than in QL. Especially, functional structures based on hydraulic traits from QL to LP clearly showed more convergence except for SD. However, among economic traits, only LMA showed this convergent trend (**Figure 2**).

Quercus spp is the common and dominant genus in climax communities and is particularly abundant in northern China, which represents a strong impact of species abundance on community assembly (Chai et al., 2019). On the LP, natural *Q. wutaishanica* forests experienced serious water erosion (Shangguan et al., 2002), and therefore hydraulic traits are sensitive to water conditions (Xu et al., 2016). Hydraulic traits based functional structure may thus be considered as a consequence of increasing environmental filtering to adapt to drought environment. The coexistence of species in QL did not produce such strong adaption. Although some traits in both sites are driven by the same processes, we determined a novel trend that the functional structure of hydraulic traits is changing toward more convergent from QL to LP. Overall, insignificance with respect to a single economic trait functional structure, a significant hydraulic trait convergent pattern suggested that environmental filtering acting on hydraulic traits was mostly stronger than that acting on economic traits on LP. Such a result supports the expectation that the low water availability characterizing drought environments influences trait values, which filtered out of the regional species pool. Low water availability either led to stronger environmental filtering in hydraulic traits and improved the degree of traits convergence on LP compared with QL. However, unlike what we hypothesized, we found no negative relationship in the mechanism of community assembly between economic traits and hydraulic traits in *Q. wutaishanica* forests.

From a parallel and finer perspective, our CCA results showed that the patterns of species and plot distributions in QL and on LP are different. The observed species grouped on LP and in QL separately. At the same time, considering the same pattern we have found in the tree layer driven by environmental filtering, our results also reflect that the variation in the traits of tree species and the turnover of understory shrub species were the determinants of the different community patterns in the two sites. These two patterns among the species suggested that species on LP were mostly specialists in the local environment, and species' tolerances for limiting water may be more important than competition for resources. In the study areas, the selected hydraulic traits showed the same assembly process as the economic traits, but the response degree between economic and hydraulic traits was different when considering the environmental condition. Our results showed that the response of hydraulic traits was more sensitive in the community assembly within different water availability, and confirmed the key traits of the local *Q. wutaishanica* forest community assembly process. Moreover, this study also revealed the relative importance of different kinds of traits. Thus, to better understand the mechanisms of communities acclimating to the environment, more representative traits should be considered according to environmental differences (Adler et al., 2013), such as hydraulic traits.

CONCLUSION

In summary, by using data of two *Q. wutaishanica* forests in different water availability conditions, our study found significant differences in the strategies of the two communities. Economic

and hydraulic traits are strongly coordinated at the community level. Functional diversity based on hydraulic traits are different from economic traits. Deterministic assembly pattern was tested based on economic and hydraulic traits. Consideration of economic traits may not be necessary to study community assembly in an arid ecosystem. Environmental filtering acting on hydraulic was especially stronger than that acting on economic traits in lower water availability. A key set of functional traits which are important for understanding the community assembly process should be considered in future community ecology research. Our findings had profound implications for understanding community assembly within different water availabilities in the natural temperate forests of northern China and for more pragmatic matters, such as informing community restoration based on trait-based principles.

DATA AVAILABILITY STATEMENT

The original contributions presented in the study are included in the article/**Supplementary Material**, further inquiries can be directed to the corresponding author/s.

AUTHOR CONTRIBUTIONS

JZ and MY conceived and designed the experiments. JZ, YZ, JX, YFC, PL, YC, CL, and JGZ performed the experiments. JZ, YZ, and QY analysed the data. JZ and MY wrote the manuscript. All authors contributed to the article and approved the submitted version.

FUNDING

This study was financially supported by the National Science Foundation of China (41871036), the Shaanxi Science and Technology Program (2020JQ-580), China Postdoctoral Science Foundation (2018M643717), Key Laboratory Project of Guizhou Province [(2020)2003], and the Science and Technology Supporting Project of Science and Technology Bureau of Tongren [(2020)128].

SUPPLEMENTARY MATERIAL

The Supplementary Material for this article can be found online at: https://www.frontiersin.org/articles/10.3389/fpls.2021.698878/full#supplementary-material

Supplementary Figure 1 | Barplot comparing soil water content (SWC) among per plot between LP and QL.

Supplementary Figure 2 | Phylogenetic dendrogram of study site community species on LP.

Supplementary Figure 3 | Phylogenetic dendrogram of study site community species in QL.

REFERENCES

Ackerly, D. D., and Cornwell, W. K. (2007). A trait-based approach to community assembly: partitioning of species trait values into within- and among-community components. *Ecol. Lett.* 10, 135–145. doi: 10.1111/j.1461-0248.2006.01006.x

Adler, P. B., Fajardo, A., Kleinhesselink, A. R., and Kraft, N. J. B. (2013). Trait-based tests of coexistence mechanisms. *Ecol. Lett.* 16, 1294–1306. doi: 10.1111/ele.12157

Baltzer, J. L., Grégoire, D. M., Bunyavejchewin, S., Noor, N. S. M., and Davies, S. J. (2009). Coordination of foliar and wood anatomical traits contributes to tropical tree distributions and productivity along the Malay-Thai Peninsula. *Am. J. Bot.* 96, 2214–2223. doi: 10.3732/ajb.0800414

Bartlett, M. K., Scoffoni, C., and Sack, L. (2012). The determinants of leaf turgor loss point and prediction of drought tolerance of species and biomes: a global meta-analysis: drivers of plant drought tolerance. *Ecol. Lett.* 15, 393–405. doi: 10.1111/j.1461-0248.2012.01751.x

Bassman, J. H., and Zwier, J. C. (1991). Gas exchange characteristics of *Populus trichocarpa*, *Populus deltoides* and *Populus trichocarpa* x *P. deltoides* clones. *Tree Physiol.* 8, 145–159. doi: 10.1093/treephys/8.2.145

Botta-Dukát, Z. (2005). Rao's quadratic entropy as a measure of functional diversity based on multiple traits. *J. Veg. Sci.* 16, 533–540. doi: 10.1111/j.1654-1103.2005.tb02393.x

Chai, Y., Dang, H., Yue, M., Xu, J., Zhang, L., Quan, J., et al. (2019). The role of intraspecific trait variability and soil properties in community assembly during forest secondary succession. *Ecosphere* 10:e02940. doi: 10.1002/ecs2.2940

Chai, Y., Yue, M., Liu, X., Guo, Y., and Wang, M. (2016). Patterns of taxonomic, phylogenetic diversity during a long-term succession of forest on the Loess Plateau, China: insights into assembly process. *Sci. Rep.* 1:27087. doi: 10.1038/srep27087

Chen, L., and Wang, R. (2009). Anatomical and physiological divergences and compensatory effects in two *Leymus chinensis* (Poaceae) ecotypes in Northeast China. *Agric. Ecosyst. Environ.* 134, 46–52. doi: 10.1016/j.agee.2009.05.015

Condit, R. (2000). Spatial patterns in the distribution of tropical tree species. *Science* 288, 1414–1418. doi: 10.1126/science.288.5470.1414

Conti, G., and Dıaz, S. (2013). Plant functional diversityand carbon storage-an empirical test in semi-arid forest ecosystems. *J. Ecol.* 101, 18–28. doi: 10.1111/1365-2745.12012

Cornelissen, J. H. C., Lavorel, S., Garnier, E., Díaz, S., Buchmann, N., Gurvich, D. E., et al. (2003). A handbook of protocols for standardised and easy measurement of plant functional traits worldwide. *Aust. J. Bot.* 51:335. doi: 10.1071/BT02124

Delzon, S., Sartore, M., Burlett, R., Dewar, R., and Loustau, D. (2004). Hydraulic responses to height growth in maritime pine trees. *Plant Cell Environ.* 27, 1077–1087. doi: 10.1111/j.1365-3040.2004.01213.x

Drenovsky, R. E., Grewell, B. J., D'Antonio, C. M., Funk, J. L., James, J. J., Molinari, N., et al. (2012). A functional trait perspective on plant invasion. *Ann. Bot.* 110, 141–153. doi: 10.1093/aob/mcs100

Dwyer, J. M., Hobbs, R. J., and Mayfield, M. M. (2014). Specific leaf area responses to environmental gradients through space and time. *Ecology* 95, 399–410. doi: 10.1890/13-0412.1

Ellner, S. P., Snyder, R. E., Adler, P. B., and Hooker, G. (2019). An expanded modern coexistence theory for empirical applications. *Ecol. Lett.* 22, 3–18. doi: 10.1111/ele.13159

Engelbrecht, B. M. J., Comita, L. S., Condit, R., Kursar, T. A., Tyree, M. T., Turner, B. L., et al. (2007). Drought sensitivity shapes species distribution patterns in tropical forests. *Nature* 447, 80–82. doi: 10.1038/nature05747

Fan, D. Y., Jie, S. L., Liu, C. C., Zhang, X. Y., Xu, X. W., Zhang, S. R., et al. (2011). The trade-off between safety and efficiency in hydraulic architecture in 31 woody species in a karst area. *Tree Physiol.* 31, 865–877. doi: 10.1093/treephys/tpr076

Flores-Moreno, H., Fazayeli, F., Banerjee, A., Datta, A., Kattge, J., Butler, E. E., et al. (2019). Robustness of trait connections across environmental gradients and growth forms. *Glob. Ecol. Biogeogr.* 28, 1806–1826. doi: 10.1111/geb.12996

Fortunel, C., Ruelle, J., Beauchêne, J., Fine, P. V. A., and Baraloto, C. (2014). Wood specific gravity and anatomy of branches and roots in 113 Amazonian rainforest tree species across environmental gradients. *New Phytol.* 202, 79–94. doi: 10.1111/nph.12632

Franks, P. J., Drake, P. L., and Beerling, D. J. (2009). Plasticity in maximum stomatal conductance constrained by negative correlation between stomatal size and density: an analysis using *Eucalyptus globulus*. *Plant Cell Environ.* 32, 1737–1748. doi: 10.1111/j.1365-3040.2009.002031.x

Garnier, E., Cortez, J., Billès, G., Navas, M. L., Roumet, C., Debussche, M., et al. (2004). Plant functional markers capture ecosystem properties during secondary succession. *Ecology* 85, 2630–2637. doi: 10.1890/03-0799

Givnish, T. (2002). Adaptive significance of evergreen vs. deciduous leaves: solving the triple paradox. *Silva Fenn.* 36:535. doi: 10.14214/sf.535

Gotsch, S. G., Geiger, E. L., Franco, A. C., Goldstein, G., Meinzer, F. C., and Hoffmann, W. A. (2019). Correction to: allocation to leaf area and sapwood area affects water relations of co-occurring savanna and forest trees. *Oecologia* 189, 563–563. doi: 10.1007/s00442-018-04327-3

Groom, P. K. (2004). Rooting depth and plant water relations explain species distribution patterns within a sandplain landscape. *Funct. Plant Biol.* 31:423. doi: 10.1071/FP03200

Hacke, U. G., Sperry, J. S., Pockman, W. T., Davis, S. D., and McCulloh, K. A. (2001). Trends in wood density and structure are linked to prevention of xylem implosion by negative pressure. *Oecologia* 126, 457–461. doi: 10.1007/s004420100628

HilleRisLambers, J., Adler, P. B., Harpole, W. S., Levine, J. M., and Mayfield, M. M. (2012). Rethinking community assembly through the lens of coexistence theory. *Annu. Rev. Ecol. Evol. Syst.* 43, 227–248. doi: 10.1146/annurev-ecolsys-110411-160411

Hulshof, C. M., Violle, C., Spasojevic, M. J., McGill, B., Damschen, E., Harrison, S., et al. (2013). Intra-specific and inter-specific variation in specific leaf area reveal the importance of abiotic and biotic drivers of species diversity across elevation and latitude. *J. Veg. Sci.* 24, 921–931. doi: 10.1111/jvs.12041

Kunstler, G., Falster, D., Coomes, D. A., Hui, F., Kooyman, R. M., Laughlin, D. C., et al. (2016). Plant functional traits have globally consistent effects on competition. *Nature* 529, 204–207. doi: 10.1038/nature16476

Lamanna, C., Blonder, B., Violle, C., Kraft, N. J. B., Sandel, B., Imova, I., et al. (2014). Functional trait space and the latitudinal diversity gradient. *Proc. Natl. Acad. Sci.U.S.A.* 111, 13745–13750. doi: 10.1073/pnas.1317722111

Laughlin, D. C., and Laughlin, D. E. (2013). Advances in modeling trait-based plant community assembly. *Trends Plant Sci.* 18, 584–593. doi: 10.1016/j.tplants.2013.04.012

Lenz, T. I., Wright, I. J., and Westoby, M. (2006). Interrelations among pressure-volume curve traits across species and water availability gradients. *Physiol. Plant* 127, 423–433. doi: 10.1111/j.1399-3054.2006.00680.x

Letten, A. D., Ke, P. J., and Fukami, T. (2017). Linking modern coexistence theory and contemporary niche theory. *Ecol. Monogr.* 87, 161–177. doi: 10.1002/ecm.1242

Li, L., McCormack, M. L., Ma, C., Kong, D., Zhang, Q., Chen, X., et al. (2015). Leaf economics and hydraulic traits are decoupled in five species-rich tropical-subtropical forests. *Ecol. Lett.* 18, 899–906. doi: 10.1111/ele.12466

Li, S., Cadotte, M. W., Meiners, S. J., Hua, Z., Jiang, L., and Shu, W. (2015). Species colonisation, not competitive exclusion, drives community overdispersion over long-term succession. *Ecol. Lett.* 18, 964–973. doi: 10.1111/ele.12476

Li, X., Blackman, C. J., Choat, B., Duursma, R. A., Rymer, P. D., Medlyn, B. E., et al. (2018). Tree hydraulic traits are coordinated and strongly linked to climate-of-origin across a rainfall gradient: hydraulic traits coordination and link to climate. *Plant Cell Environ.* 41, 646–660. doi: 10.1111/pce.13129

Liu, C., Li, Y., Xu, L., Chen, Z., and He, N. (2019). Variation in leaf morphological, stomatal, and anatomical traits and their relationships in temperate and subtropical forests. *Sci. Rep.* 9:5803. doi: 10.1038/s41598-019-42335-2

Liu, C., Li, Y., Zhang, J., Baird, A. S., and He, N. (2020). Optimal community assembly related to leaf economic-hydraulic-anatomical traits. *Front. Plant Sci.* 11:341. doi: 10.3389/fpls.2020.00341

Liu, H., Ye, Q., Gleason, S. M., He, P., and Yin, D. (2021). Weak tradeoff between xylem hydraulic efficiency and safety: climatic seasonality matters. *New Phytol.* 229, 1440–1452. doi: 10.1111/nph.16940

Liu, J. J., Qi, Y. B., Chen, Y., Zhang, L. L., Qin, Q. R., and Yu, X. J. (2017). Assessment of soil moisture and temperature regime classes in Shaanxi Province. *Chin. J. Soil Sci.* 248, 335–342.

Loranger, J., Violle, C., Shipley, B., Lavorel, S., Bonis, A., Cruz, P., et al. (2016). Recasting the dynamic equilibrium model through a functional lens: the interplay of trait-based community assembly and climate. *J. Ecol.* 104, 781–791. doi: 10.1111/1365-2745.12536

Loreau, M. (2001). Biodiversity and ecosystem functioning: current knowledge and future challenges. *Science* 294, 804–808. doi: 10.1126/science.1064088

Luo, W., Lan, R., Chen, D., Zhang, B., Xi, N., Li, Y., et al. (2021). Limiting similarity shapes the functional and phylogenetic structure of root neighborhoods in a subtropical forest. *New Phytol.* 229, 1078–1090. doi: 10.1111/nph.16920

Mason, N. W. H., Mouillot, D., Lee, W. G., and Wilson, J. B. (2005). Functional richness, functional evenness and functional divergence: the primary components of functional diversity. *Oikos* 111, 112–118. doi: 10.1111/j.0030-1299.2005.13886.x

Mason, N. W. H., Richardson, S. J., Peltzer, D. A., de Bello, F., Wardle, D. A., and Allen, R. B. (2012). Changes in coexistence mechanisms along a long-term soil chrono sequence revealed by functional trait diversity: functional diversity along ecological gradients. *J. Ecol.* 100, 678–689. doi: 10.1111/j.1365-2745.2012.01965.x

Mayfield, M. M., and Levine, J. M. (2010). Opposing effects of competitive exclusion on the phylogenetic structure of communities: phylogeny and coexistence. *Ecol. Lett.* 13, 1085–1093. doi: 10.1111/j.1461-0248.2010.01509.x

Moeslund, J. E., Arge, L., Bøcher, P. K., Dalgaard, T., Ejrnæs, R., Odgaard, M. V., et al. (2013). Topographically controlled soil moisture drives plant diversity patterns within grasslands. *Biodivers. Conserv.* 22, 2151–2166. doi: 10.1007/s10531-013-0442-3

Mori, G. B., Poorter, L., Schietti, J., and Piedade, M. T. F. (2021). Edaphic characteristics drive functional traits distribution in Amazonian floodplain forests. *Plant Ecol.* 222, 349–360. doi: 10.1007/s11258-020-01110-4

Naaf, T., and Wulf, M. (2012). Plant community assembly in temperate forests along gradients of soil fertility and disturbance. *Acta Oecol.* 39, 101–108. doi: 10.1016/j.actao.2012.01.009

Norden, N., Letcher, S., Boukili, V., Swenson, N., and Chazdon, R. (2012). Demographic drivers of successional changes in phylogenetic structure across life-history stages in plant communities. *Ecology* 93, S70–S82. doi: 10.1890/10-2179.1

Purschke, O., Schmid, B. C., Sykes, M. T., Poschlod, P., Michalski, S. G., Durka, W., et al. (2013). Contrasting changes in taxonomic, phylogenetic and functional diversity during a long-term succession: insights into assembly processes. *J. Ecol.* 101, 857–866. doi: 10.1111/1365-2745.12098

R Core Team (2015). R: A Language and Environment For Statistical Computing. Vienna: R Foundation for Statistical Computing. Available online at: http://www.r-project.org/

Reich, P. B., Wright, I. J., and Lusk, C. H. (2007). Predicting eaf physiology from simple plant and climate attributes: a global glopnet analysis. *Ecol. Appl.* 17, 1982–1988. doi: 10.1890/06-1803.1

Ricotta, C., and Moretti, M. (2011). CWM and Rao's quadratic diversity: a unified framework for functional ecology. *Oecologia* 167, 181–188. doi: 10.1007/s00442-011-1965-5

Rowland, L., Lobo-do-Vale, R. L., Christoffersen, B. O., Melém, E. A., Kruijt, B., Vasconcelos, S. S., et al. (2015). After more than a decade of soil moisture deficit, tropical rainforest trees maintain photosynthetic capacity, despite increased leaf respiration. *Glob. Chang. Biol.* 21, 4662–4672. doi: 10.1111/gcb.13035

Sack, L., and Scoffoni, C. (2013). Leaf venation: structure, function, development, evolution, ecology and applications in the past, present and future. *New Phytol.* 198, 983–1000. doi: 10.1111/nph.12253

Sanaphre-Villanueva, L., Dupuy, J., Andrade, J., Reyes-García, C., Paz, H., and Jackson, P. (2016). Functional diversity of small and large trees along secondary succession in a tropical dry forest. *Forests* 7:163. doi: 10.3390/f7080163

Schleuter, D., Daufresne, M., Massol, F., and Argillier, C. (2010). A user's guide to functional diversity indices. *Ecol. Monogr.* 80, 469–484. doi: 10.1890/08-2225.1

Shangguan, Z. P., Shao, M. A., Lei, T. W., and Fan, T. L. (2002). Runoff water management technologies for dryland agriculture on the Loess. *Int. J. Sust. Dev. World* 9, 341–350. doi: 10.1080/13504500209470129

Silvertown, J., Araya, Y., and Gowing, D. (2015). Hydrological niches in terrestrial plant communities: a review. *J. Ecol.* 103, 93–108. doi: 10.1111/1365-2745.12332

Spasojevic, M. J., and Suding, K. N. (2012). Inferring community assembly mechanisms from functional diversity patterns: the importance of multiple assembly processes: functional diversity along gradients. *J. Ecol.* 100, 652–661. doi: 10.1111/j.1365-2745.2011.01945.x

Subedi, S. C., Ross, M. S., Sah, J. P., Redwine, J., and Baraloto, C. (2019). Trait-based community assembly pattern along a forest succession gradient in a seasonally dry tropical forest. *Ecosphere* 10:e02719. doi: 10.1002/ecs2.2719

Targetti, S., Messeri, A., Staglianò, N., and Argenti, G. (2013). Leaf functional traits for the assessment of succession following management in semi-natural grasslands: a case study in the North Apennines, Italy. *Appl. Veg. Sci.* 16, 325–332. doi: 10.1111/j.1654-109X.2012.01223.x

Thorn, S., Bässler, C., Bernhardt-Römermann, M., Cadotte, M., Heibl, C., Schäfer, H., et al. (2016). Changes in the dominant assembly mechanism drive species loss caused by declining resources. *Ecol. Lett.* 19, 163–170. doi: 10.1111/ele.12548

Tyree, M. T., and Hammel, H. T. (1972). The measurement of the turgor pressure and the water relations of plants by the pressure-bomb technique. *J. Exp. Bot.* 23, 267–282. doi: 10.1093/jxb/23.1.267

Wang, M., Xu, J., Chai, Y., Guo, Y., Liu, X., and Yue, M. (2019). Differentiation of environmental conditions promotes variation of two *Quercus wutaishanica* community assembly patterns. *Forests* 11:43. doi: 10.3390/f11010043

Westoby, M., Falster, D. S., Moles, A. T., Vesk, P. A., and Wright, I. J. (2002). Plant ecological strategies: some leading dimensions of variation between species. *Annu. Rev. Ecol. Syst.*, 33, 125–159. doi: 10.1146/annurev.ecolsys.33.010802.150452

Wright, I. J., Reich, P. B., Cornelissen, J. H. C., Falster, D. S., Garnier, E., Hikosaka, K., et al. (2005). Assessing the generality of global leaf trait relationships. *New Phytol.* 166, 485–496. doi: 10.1111/j.1469-8137.2005.01349.x

Wright, I. J., Reich, P. B., Westoby, M., Ackerly, D. D., Baruch, Z., and Bongers, F. (2004). The worldwide leaf economics spectrum. *Nature* 428:821. doi: 10.1038/nature02403

Wu, G., Liu, H., Hua, L., Luo, Q., Lin, Y., He, P., et al. (2018). Differential responses of stomata and photosynthesis to elevated temperature in two co-occurring subtropical forest tree species. *Front. Plant Sci.* 9:467. doi: 10.3389/fpls.2018.00467

Xu, W., Viña, A., Qi, Z., Ouyang, Z., Liu, J., Liu, W., et al. (2014). Evaluating conservation effectiveness of nature reserves established for surrogate species: case of a giant panda nature reserve in Qinling Mountains, China. *Chin. Geogr. Sci.* 24, 60–70. doi: 10.1007/s11769-014-0656-7

Xu, X., Medvigy, D., Powers, J. S., Becknell, J. M., and Guan, K. (2016). Diversity in plant hydraulic traits explains seasonal and inter-annual variations of vegetation dynamics in seasonally dry tropical forests. *New Phytol.* 212, 80–95. doi: 10.1111/nph.14009

Yan, B., Zhang, J., Liu, Y., Li, Z., Huang, X., Yang, W., et al. (2012). Trait assembly of woody plants in communities across sub-alpine gradients: identifying the role of limiting similarity. *J. Veg. Sci.* 23, 698–708. doi: 10.1111/j.1654-1103.2011.01384.x

Yin, Q., Wang, L., Lei, M., Dang, H., Quan, J., Tian, T., et al. (2018). The relationships between leaf economics and hydraulic traits of woody plants depend on water availability. *Sci. Total Environ.* 621, 245–252. doi: 10.1016/j.scitotenv.2017.11.171

Zhang, S. B., Guan, Z. J., Sun, M., Zhang, J. J., Cao, K. F., and Hu, H. (2012). Evolutionary association of stomatal traits with leaf vein density in *Paphiopedilum*, Orchidaceae. *PLoS One* 7:e40080. doi: 10.1371/journal.pone.0040080

Zhao, W. L., Chen, Y. J., Brodribb, T. J., and Cao, K. F. (2016). Weak co-ordination between vein and stomatal densities in 105 angiosperm tree species along altitudinal gradients in Southwest China. *Funct. Plant Biol.* 43:1126. doi: 10.1071/FP16012

Zhu, Z. C. (1993). Recovering succession of vegetation in forest region of north Shaanxi Loess Plateau. *J. Northw. For. Coll.* 8, 87–94.

Conflict of Interest: The authors declare that the research was conducted in the absence of any commercial or financial relationships that could be construed as a potential conflict of interest.

Publisher's Note: All claims expressed in this article are solely those of the authors and do not necessarily represent those of their affiliated organizations, or those of the publisher, the editors and the reviewers. Any product that may be evaluated in this article, or claim that may be made by its manufacturer, is not guaranteed or endorsed by the publisher.

frontiers | Frontiers in Forests and Global Change

TYPE Original Research
PUBLISHED 03 November 2022
DOI 10.3389/ffgc.2022.693418

OPEN ACCESS

EDITED BY
Manuel R. Guariguata,
Center for International Forestry Research (CIFOR), Indonesia

REVIEWED BY
Christopher Woodall,
Research and Development, Forest Service (USDA), United States
J. Aaron Hogan,
University of Florida, United States
Bognounou Fidèle,
Canadian Forest Service, Canada
Aurélie C. Shapiro,
Food and Agriculture Organization of the United Nations, Italy

*CORRESPONDENCE
Chonggang Xu
cxu@lanl.gov

SPECIALTY SECTION
This article was submitted to Forest Disturbance, a section of the journal Frontiers in Forests and Global Change

RECEIVED 10 April 2021
ACCEPTED 05 October 2022
PUBLISHED 03 November 2022

CITATION
Wang M, Xu C, Johnson DJ, Allen CD, Anderson M, Wang G, Qie G, Solander KC and McDowell NG (2022) Multi-scale quantification of anthropogenic, fire, and drought-associated forest disturbances across the continental U.S., 2000–2014. *Front. For. Glob. Change* 5:693418. doi: 10.3389/ffgc.2022.693418

Multi-scale quantification of anthropogenic, fire, and drought-associated forest disturbances across the continental U.S., 2000–2014

Minzi Wang[1,2], Chonggang Xu[1]*, Daniel J. Johnson[3], Craig D. Allen[4], Martha Anderson[5], Guangxing Wang[6], Guangping Qie[7], Kurt C. Solander[1] and Nate G. McDowell[8]

[1]Earth and Environmental Science Division, Los Alamos National Laboratory, Los Alamos, NM, United States, [2]Department of Resource and Environment, Moutai Institute, Renhuai, Guizhou, China, [3]School of Forest, Fisheries, and Geomatics Sciences, University of Florida, Gainesville, FL, United States, [4]Department of Geography and Environmental Studies, University of New Mexico, Albuquerque, NM, United States, [5]Hydrology and Remote Sensing Laboratory, Agricultural Research Service, United States Department of Agriculture, Beltsville, MD, United States, [6]School of Earth Systems and Sustainability, Southern Illinois University, Carbondale, IL, United States, [7]Illinois State Water Survey, Prairie Research Institute, University of Illinois Urbana-Champaign, Champaign, IL, United States, [8]Atmospheric Sciences and Global Change Division, Pacific Northwest National Laboratory, Richland, WA, United States

Our understanding of broad-scale forest disturbances under climatic extremes remains incomplete. Drought, as a typical extreme event, is a key driver of forest mortality but there have been no reports on continental-scale quantification of its impact on forest mortality or how it compares to other natural or anthropogenic drivers. Thus, our ability to understand and predict broad-scale carbon cycling in response to changing climate and extreme events is limited. In this study, we applied an attribution approach based on different sources of data to quantify the area and potential carbon loss/transfer in continental U.S. (CONUS) from four types of disturbance: (1) anthropogenic (especially timber harvest); (2) fire; (3) drought-associated; and (4) other from 2000 to 2014. Our results showed that anthropogenic disturbances, fire, drought-associated disturbances, and other disturbances accounted for 54.3, 10.7, 12.7, and 22.3% of total canopy area loss, respectively. Anthropogenic disturbance was the most important driver contributing to 58.1% potential carbon loss/transfer in CONUS for 2000–2014. The potential carbon loss/transfer from natural disturbances (fire, drought, and other) for the same study period accounted for approximately 41.9% of the total loss/transfer from all agents, suggesting that natural disturbances also played a very important role in forest carbon turnover. Potential carbon loss/transfer associated with drought accounted for approximately 11.6% of the total loss/transfer in CONUS, which was of similar magnitude to potential carbon loss/transfer from fire (~11.0%). The other natural disturbance accounted for 19.3% of potential carbon loss/transfer. Our results demonstrated the

importance of the impacts of various disturbances on forest carbon stocks at the continental scale, and the drought-associated carbon loss/transfer data developed here could be used for evaluating the performance of predictive models of tree mortality under droughts.

KEYWORDS

forest disturbances, tree mortality, drought, fire, anthropogenic disturbances, carbon loss/transfer

Introduction

Reports of tree mortality due to climatic extremes such as drought are increasing globally (Van Mantgem et al., 2009; Ganey and Vojta, 2011; Peng et al., 2011; Millar et al., 2012; Allen et al., 2015, 2021; Bendixsen et al., 2015; Assal et al., 2016; Gazol and Camarero, 2022). These rising extreme events, along with fires, insects, and timber harvesting, can substantially threaten forest health. For instance, tree mortality driven or triggered by these disturbances can accelerate changes in forest structure and species composition through altering the size, age, and interspecific competition of a forest (Anderegg et al., 2013; Dyderski et al., 2018). Furthermore, these mortality events can cause widespread and rapid carbon losses to the atmosphere through enhanced decomposition and combustion rates caused by the higher incidence of dead trees (Kurz et al., 2013). The consequential changes in surface albedo can alter the surface energy balance, resulting in important climate feedbacks (e.g., Maness et al., 2013). Combined, these changes can have profound impacts on the human society due to our reliance on healthy forest ecosystems to maximize related ecosystem services (e.g., food, recreations, water purification, flood control, and climate regulation). Therefore, our ability to understand and quantify such losses is of great importance.

During recent decades, many studies have been conducted to investigate forest mortality and explore the causal relationships between forest tree die off and various contributing factors. For example, tree mortality rates in the eastern and central US were found to be strongly associated with stand characteristics (e.g., age, basal area, and tree size) (Dietze and Moorcroft, 2011). Adams et al. (2017) found that widely observed hydraulic failure tends to be one of the most important underlying physiological mechanisms that causes tree death under drought stress. Moreover, there have been many studies of forest declines and tree loss driven by insect outbreaks (e.g., mountain pine beetles) (Meddens and Hicke, 2014; Hicke et al., 2020), fire (Hicke et al., 2016), drought (Klos et al., 2009; Ganey and Vojta, 2011; Yang et al., 2021), and a combination of multiple causal agents (Allen et al., 2021; Knapp et al., 2021; Yang et al., 2021).

Current studies often tend to focus on either the magnitude and intensity of tree mortality or the physiological theories underlying the death. Quantitative attribution studies of tree mortality, particularly those caused by drought, are few and have mostly been limited to relatively fine scales (e.g., plot to watershed) or species-specific responses at larger scales (e.g., Stanke et al., 2021) due to the complexity of forest ecosystem and compound effects among the underlying driving factors. Broad-scale quantitative attribution of such loss at the agent level are rarely found with a few studies focused on single agent (Tyukavina et al., 2022) or empirically attributed disturbance agencies based on forest inventory (Fitts et al., 2022). To better understand how drought impacts the large-scale carbon cycling and associated feedbacks to climate, it is important that we attribute both the area and amount of potential carbon loss to atmosphere or transfer to different products (e.g., wood products for timbers) to different types of disturbances at continental and ultimately global scales.

Currently, estimates of drought-induced mortality at large scales rely heavily on national forest inventories or forest observational networks (Klos et al., 2009; Dietze and Moorcroft, 2011); however, methods and protocols to attribute mortality rates are often inconsistent across different regions/sites or studies (e.g., the definition of drought is different for different studies) and are subjected to sampling errors as they do not have a complete spatial coverage of trees at such large scales. Benefiting from many free and low-cost moderate to high resolution remote sensing (RS) data and fast development in image processing techniques (e.g., machine learning and cloud computing) and the proliferation of data acquisition platforms (e.g., Google Earth Engine), great advancements have been achieved in broad scale monitoring of forest disturbances. For example, the long term Monitoring Trends in Burn Severity (MTBS) data set (1984–2019) provides data on fire occurrence, burn severity and extent across CONUS (Eidenshink et al., 2007), which helps attributing fire-induced tree loss. Continental scale thermal infrared RS based evapotranspiration (ET) and Evaporative Stress Index (ESI) mapping of forest canopies across the entire CONUS (Anderson et al., 2011) enables the explanation of occurrences of observed drought events under different levels of drought stress. This helps to find empirical threshold values that can consistently identify drought-associated (triggered or directly caused) disturbances. Moreover, recent developments in RS-based

disturbance detection, including the first high spatial resolution (30 × 30 m) global forest disturbance database developed by Hansen et al. (2013), provide excellent opportunities to evaluate the intensity and magnitude of a variety of anthropogenic and natural disturbances at continental scales. These disturbances are not yet attributed to specific causal agents and thus making it difficult to evaluate the relative importance of different causes (McDowell et al., 2015).

In this study, we developed an attribution approach based on different sources of data to estimate the magnitude and relative contribution of four major disturbance categories to observed disturbances in the continental U.S. (CONUS) over a 15-year period (2000–2014). These disturbances are based on canopy loss estimated from 30-m resolution LANDSAT imagery developed by Hansen et al. (2013). They could represent either potential tree mortality, removal or damages. These four categories include anthropogenic, fire-caused, drought-associated, and other disturbances. Anthropogenic disturbances arise predominately from timber harvesting, land clearing and forest management. The fire-induced disturbances refer to tree mortality or damage from fire scorch or direct burning. Drought is defined based on ESI index thresholds that can potentially lead to tree mortality. The drought-associated disturbances here refer to natural disturbances that have potential linkages to droughts but are not caused by fire or humans. Mechanistically, drought could potentially lead to an increase in water stress and a reduction in carbon storage in plants, as a result of accelerated loss of water and reduction in photosynthetic carbon uptake. The resulting water stress could directly lead to tree mortality or damages through hydraulic function failure. Meanwhile, the resulting carbon starvation and water stress could also lead to reduced plant defense against insects and diseases, which could lead to an increased likelihood of tree mortality (McDowell et al., 2011). Thus, drought associated disturbances could include tree mortality or damages that are directly caused by water stress or indirectly caused by water stress through insect/diseases. The other category includes disturbances from abiotic agents, such as windthrow or frost, and biotic agents that are not related to droughts, such as pathogens or vines. The aims of this study are: (1) to design a hierarchical framework to distinguish different types of disturbances; and (2) to assess the area of disturbance and associated potential carbon stock loss/transfer at regional and CONUS scales. We expected our results to help us better understand the importance of different types of disturbances in carbon balance and the carbon sources/sinks for the forest ecosystem in the CONUS.

Materials and methods

We attributed disturbances to four disturbance categories (anthropogenic, fire, drought, and other) by combining multiple datasets from different sources with various native spatial resolutions. Continental forest disturbance areas during 2000–2014 were identified using the 30 m resolution dataset developed by Hansen et al. (2013). In view of the potential inconsistencies in disturbance detection across time in Hansen's map (Palahí et al., 2021), we only calculated the lumped sum of areas for different types of disturbance during 2000–2014. Differentiation of disturbance agents began by identifying and removing areas of fire-caused forest loss from the MTBS database and then human-caused loss from the Nation Forest Inventory and Analysis (FIA) database (see **Figure 1** for details of the workflow). For pixels that excluded fire-caused and

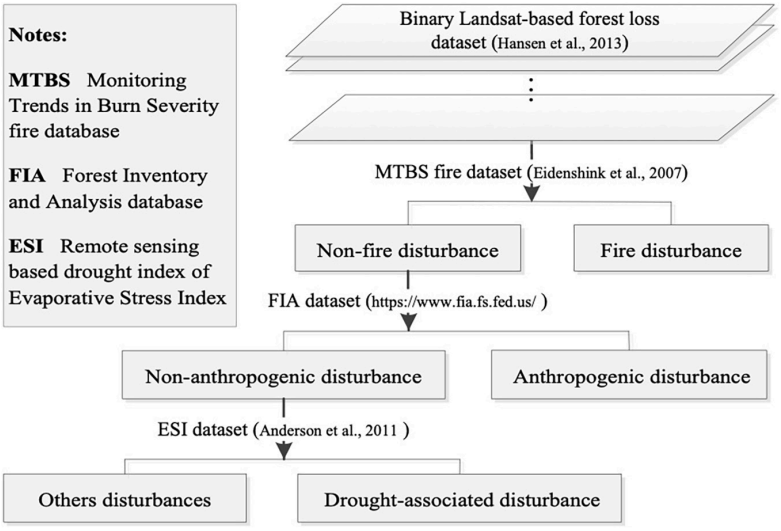

FIGURE 1
Workflow for the attributions of fire-caused, anthropogenic (especially timber harvest) and drought-associated disturbances.

anthropogenic disturbances, determination of climatological drought was based on the ESI drought index, which quantifies standardized anomalies in the ratio of actual to reference ET (AET/RET) and thus signals the relative transpirational flux of trees, with declining values associated with drought (Anderson et al., 2011). Finally, the amount of potential carbon loss/transfer from tree mortality or forest removal was calculated through multiplying these identified agent specific disturbance areas of loss by the per unit aboveground carbon stock estimates of canopy trees from the FIA database and RS imagery (Blackard et al., 2008). The reason why we used only the canopy trees is because Hansen's remote-sensing-based disturbance detection has a higher level of uncertainty in quantifying the potential impact of disturbance on understory trees.

Monitoring trends in burn severity and forest inventory and analysis datasets

The MTBS dataset is produced and administered jointly by the USDA Forest Service, US Geological Survey (USGS), and Geospatial Technology and Applications Center (GTAC) (Eidenshink et al., 2007). This is a long term (1984-current), longitudinal (allowing cross comparison), and large-scale dataset that covers the entire CONUS, Alaska, Hawaii, and Puerto Rico. The MTBS uses Landsat satellite data, including Landsat Thematic Mapper, Landsat Enhanced Thematic Mapper (ETM+), and Landsat Operational Land Imager (OLI) data, to delineate burned areas and characterize burn severity. Burn severity is classified according to increased greenness into unburned to low, low, moderate, and high classes. All fires that meet the standard of burned area greater than 500 acres in the east and 1,000 acres in the west were included. Data is available from the MTBS website.[1] Since all data are generated from Landsat imagery, the MTBS raster datasets are all at 30 m spatial resolution while vector datasets (e.g., the burn area boundary) delineated from the imagery are available at a map scale of 1:24,000 to 1:50,000.

The FIA (also known as the Forest Survey at earlier time) program was established in 1928 to collect, analyze, archive, and publish information on the status, trends, and conditions of all forested lands in the U.S.[2] The first official forest inventory started in 1930 and was conducted only in few states (Smith, 2002). Over time, to enhance the ability to analyze and report data of forest land, the program expanded to cover the entire U.S. and was conducted at an annual frequency. Currently, the FIA data are generated from a combination of RS imagery and field surveys, which are carried out by the USDA Forest Service and cover land of all ownerships. To streamline annual estimates of forest attributes while reducing bias, the FIA program utilized an annual panel system, and a multi-phased sampling strategy where a "pre-field phase" was used to determine forested land area based solely on remotely sensed data and the "core phase" was used to establish ground plots (Smith, 2002; Bechtold and Patterson, 2005). These plots are permanent and systematically distributed across the nation where each is measured in a continuous inventory cycle (Bechtold and Patterson, 2005; US Forest Service, 2005; Hoover et al., 2022). The cycle is approximately 5–7 years in the East with 15–20% ground plots are measured each year in the East, and 10 years with 10% ground plots per year are measured in the West. The standard sample grid is approximately one plot per 6,000 acres (Smith, 2002). Key variables including tree species, diameter, and ownership are collected on each plot (Smith, 2002). The cause of tree mortality in this dataset was created by assigning associated agents such as fire, human, and drought if those can be visually identified. If more than one agent led to tree mortality, only the agent that caused the most severe damage to the trees was recorded (US Forest Service, 2016). The collection methods are made spatially and temporally consistent to enable change analysis with the data (for more details, see US Forest Service, 2021).

Preprocessing of forest disturbance dataset

We used the global forest disturbance dataset describing forest canopy area loss from any disturbances developed by Hansen et al. (2013) with a resolution of 0.00025 degree (~30 m). The disturbance information over CONUS during 2000–2014 was recorded as either 0 (no disturbance) or 1 (disturbance). For feasibility of data management, the disturbance dataset was originally organized by 10° windows (i.e., titles). We further divided each of the tiles into 0.5 × 0.5° windows for operational spatial analysis and aggregation of different disturbance types, resulting in 400 such windows per tile. We chose 0.5° resolution for aggregation because (1) it is one of the generally used resolutions of many global vegetation models within Earth System models; and (2) at this resolution we will get adequate number of FIA plots (>10) for statistically assessing the anthropogenic disturbances.

Identification of fire disturbances

We identified fire-caused disturbances from the forest loss database (Hansen et al., 2013) by measuring their spatial extent convergence with annual fire burned areas derived from the MTBS database (Eidenshink et al., 2007). Burned pixels with different severity levels of low, moderate, and high were shown in 30 m thematic maps derived from Landsat images. Given that low-severity fires are typically non-lethal to canopy trees

1 https://www.mtbs.gov/
2 https://www.fia.fs.fed.us/

and generally kill many fewer trees (<30%) than high-severity fires (>85%) (Ghimire et al., 2012), we assumed that higher fire severity led to greater tree mortality rates. Thus, we calculate three levels of potential fire-caused canopy area loss (low, middle, and high), which were calculated by using only the burned pixels with the high severity class, a combination of high and moderate classes, and all the severity classes from MTBS, respectively.

The burned pixels from MTBS dataset and canopy loss pixels from the disturbance dataset were superimposed for the same time period, and the overlapped pixels were identified as locations of tree mortality from fires (**Supplementary Figure 1**). We then calculated the total fire-caused area loss ($A_{f(i)}$, where i indicates the location of pixel i, which is also the ith half-degree window) within each window by summing all these fire disturbed pixels at 0.00025-degree (~30 m) resolution within the window. To further identify other disturbance causes, we removed the fire-disturbance locations to create the non-fire forest canopy area loss ($A_{nf\,(i)} = A_{t(i)} - A_{f(i)}$, where $A_{t(i)}$ is the total disturbed area in the window) dataset.

Identification of anthropogenic disturbances

We used the FIA database (see Section "Monitoring trends in burn severity and forest inventory and analysis datasets" for detailed descriptions) to estimate the amount of anthropogenic disturbance ($A_{h(i)}$) within the half-degree window. Most of the anthropogenic disturbances are attributed to tree removal for various human purposes. The anthropogenic disturbance is identified based on the STATUSCD variable at the tree level, which tell us whether the tree was alive, dead, or removed. If trees were dead/removed, we used the AGENTCD variable to identify whether they were caused by anthropogenic disturbances (code: 80), which includes silvicultural or land clearing activity. The proportion of canopy tree basal area (BA) loss attributed to humans ($P_{h(i)}$) was calculated over 2000–2014 at 0.5° spatial resolution, based on the assumption that BAs correspond well to canopy areas across different species. The canopy/sub-canopy differentiation is based on the canopy location variable in the FIA database. Then, we estimated the overall anthropogenic disturbance ($A_{h(i)} = A_{t(i)}P_{h(i)}$) within each half-degree window by multiplying the proportion of canopy tree BA loss to anthropogenic causes ($P_{h(i)}$) and the total disturbed area ($A_{t(i)}$) within the window. We then removed the areas of anthropogenic disturbances from the non-fire forest loss ($A_{nf\,(i)}$) dataset to create a non-fire and non-anthropogenic forest canopy area loss ($A_{nfh(i)} = A_{t(i)} - A_{f(i)} - A_{h(i)}$) dataset to estimate other disturbance drivers.

Identification of drought-associated disturbances

We developed an ESI threshold approach for drought-associated mortality identification to distinguish forest disturbances associated with climatological drought from dataset ($A_{nfh(i)}$) that excluded mortality pixels from fire and anthropogenic drivers. In a European study, Senf et al. (2020)

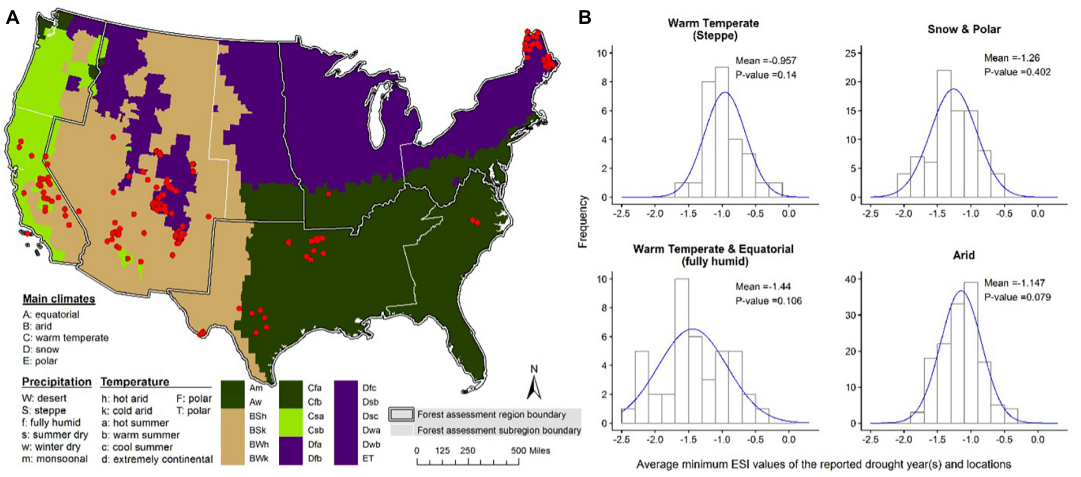

FIGURE 2
Drought thresholds for identifying drought-associated disturbance in each climate zone of the CONUS. **(A)** Major climate zones in the CONUS made by modifying Koppen–Geiger climate classification map for the U.S. counties, among which the light green represents the Warm temperate (steppe) climate, light sienna for the Arid climate, purple for the Snow and Polar climate, and darkgreen for the Warm temperate (fully humid) climate. The red dots indicate the locations of the 292 drought-induced tree mortality events identified through literature survey. **(B)** Normality test results of the drought indices of Evaporative Stress Index (ESI) at the locations of drought-induced tree mortality events within each climate zone.

used -1.6 standard deviations below the local average for the climatic water balance to define the potential risk of drought; however, a universal drought threshold might be biased for different regions. Thus, in our study, determination of these drought thresholds started with a literature survey to collect the geographic locations of drought-associated tree mortality events that occurred during 2000–2014. Literature included in this survey must either have observed tree mortality with drought considered as the dominant cause or drought during the study period contributed to the mortality (if other disturbance types co-occurred). Based on this criterion, we identified 38 field studies across the CONUS and most studies have more than one qualified location (**Supplementary Table 1**).

To determine the geo-locations of each individual drought event, we used geographic information of observed tree mortality when reported. For studies where locations were not provided, we used a GIS-based spatial analysis method to extract geographic coordinates based on reported maps. In this way, we identified 292 locations of drought-associated tree mortality events (**Figure 2A**), which were then used to extract minimum monthly ESI values (Anderson et al., 2011) during the growing season for drought years determined by the survey. Here, we define the growing season for CONUS as a period from April to September. We then determined the annual minimum ESI values in two steps: (1) computing the monthly average ESI values for the growing season, resulting in six raster layers for each year of the study period; and (2) extracting the minimum ESI values from the six layers from step one on a pixel-by-pixel basis using a spatial overlay strategy, resulting in one ESI raster layer per year. Pixel values in this layer indicate the most "severe" drought condition at each location for that year. We then classified these final ESI layers into five classes including incipient-, mild-, moderate-, severe-, and extreme drought based on drought classification standards in Mu et al. (2013).

The determination of ESI-drought mortality thresholds was based on the relationship between drought severity represented by the extracted ESI values and the occurrence of the observed mortality event at each of the 292 locations for the same drought year(s) or period(s) (**Supplementary Figure 2**). These thresholds were expected to vary by region; thus, we used the Koeppen–Geiger climate classification map to estimate ESI-thresholds for drought-associated disturbances. There is substantial variability in the observed minimum ESI values associated with observed mortality (**Figure 2B**), which challenges the selection of a suitable mortality threshold for analysis. Application of a more negative ESI threshold to a region could lead to underestimation of drought-associated mortality as it can exclude the impact of less extreme droughts, while a less negative threshold of ESI can lead to overestimation of mortality due to the potential inclusion of false impacts (e.g., insects) that are not linked to droughts. As such, we used mean drought estimates represented by ESI values as drought thresholds for each climate zone to minimize the potential for these biases (**Figure 2B**). Because the observed ESI thresholds of mortality for different zones approximately follows a Gaussian distribution (**Figure 2B**), and mean value is close to the expected value, which represents the maximum likelihood estimation of the ESI. Using the defined drought thresholds, we classified the annual ESI layers into binary maps to identify the spatial extent of annual drought and non-drought affected areas for the CONUS over the study period (**Supplementary Figure 3**).

Since the native ESI product used in this study is at 0.004° resolution, the spatial locations of anthropogenic disturbances at this scale are unknown within each window based on FIA data. Therefore, we first identified pixels of drought-associated disturbances ($A'_{\mathrm{d\_nf(i)}}$) from the non-fire forest disturbances ($A_{\mathrm{nf\ (i)}}$) at the 0.004 degree resolution (**Supplementary Figure 3**). After that, we calculated the proportion of drought-associated disturbance ($L_{\mathrm{d\_nf\ (i)}} = \frac{A'_{\mathrm{d\_nf(i)}}}{A_{\mathrm{nf(i)}}}$) to the non-fire forest disturbance for each 0.5 × 0.5° analysis window. The areas of drought-associated disturbance obtained at this point might include forest loss from anthropogenic disturbance. To exclude the anthropogenic disturbance, we assumed that the probabilities of anthropogenic ($A_{\mathrm{h(i)}}$) and non-anthropogenic disturbances ($A_{\mathrm{nfh(i)}}$) associated with droughts are equal within each window. Therefore, we recalculated drought-associated disturbance that does not include fire and human causes ($A_{\mathrm{d(i)}}$) by multiplying the drought risk ($L_{\mathrm{d\_nf\ (i)}}$) and forest canopy area loss ($A_{\mathrm{nfh(i)}}$) from non-fire and non-anthropogenic disturbances.

We also considered lag effects of drought on tree mortality, in view that the legacy effect of drought can last for 3–4 years (Anderegg et al., 2015). Specifically, we considered drought-associated tree mortality events to occur with zero to three years of drought conditions. We attributed lagged disturbance using the same logic as for identifying the overall drought-associated mortality. Through tracking the coincidence of forest loss and drought-affected areas on an annual basis with zero to 3-year lags. Losses that occurred in the drought year were identified first. Then, the amount of the 1–3 years lagged losses were identified based on the loss excluding the accumulated loss from previous lagged year(s). This approach allowed evaluating the importance of temporal lags of drought stress on tree mortality.

Identification of other disturbances

The canopy area loss from "other" disturbances was estimated using the difference between the total area of canopy loss and the sum of canopy area loss from the three major disturbance types within each window. After that, we assessed the proportion of canopy area loss from each disturbance type to examine their relative contributions at each 0.5 × 0.5° analysis window.

Quantification of potential carbon loss/transfer from disturbances

We calculated the amount of potential carbon loss/transfer from live biomass to dead pool and atmosphere associated with different types of disturbance by the product of three terms: (1) area change from Hansen's database; (2) fraction of carbon in canopy trees from the FIA database; and (3) aboveground carbon stock density from the FIA database and RS imagery (Blackard et al., 2008; **Supplementary Figure 4**). The reason why we used the second term is because it is difficult to know if the understory trees are killed from aerial based remote sensing imagery. The fraction is calculated using carbon stocks in the canopy trees and the total biomass based on the FIA database during 2000–2016. For pixels with missing values, we applied a regional specific mean value. It is possible that the disturbances detected by Hansen et al. (2013) can be caused by defoliation and thus not lead to actual carbon loss/transfer. Because currently there are no mature remote-sensing methodologies to differentiate defoliation versus mortality due to the fast growth of understory after disturbances, we estimated the potential carbon loss/transfer in view that severe defoliation can potentially lead to tree mortality (Davidson et al., 1999). The potential carbon loss does not account for the potentially long time period needed for decomposition or incorporation of carbon into the soil.

Method limitations

There are several potential limitations in our methodology. First, there are uncertainties in the mortalities from fire and thus we used three levels of potential fire-caused canopy area loss (low, middle, and high) to incorporate this uncertainty. Second, potential contribution from anthropogenic disturbances for the entire $0.5 \times 0.5°$ window is assumed to have similar levels of human disturbances as represented by the FIA plots. Thus, it is likely to have biases in our estimation due to spatial scale mismatch. We tried to limit this bias by using a large analysis window so that there are a relatively larger number of FIA plots (>10) for each window. Finally, drought-induced mortality thresholds could be different at much finer resolution based on landscape location, species, and soil properties. In this study, we mainly used climate zones to differentiate the threshold values in view that we focused on a large analysis window of $0.5 \times 0.5°$. Future studies focused on fine spatial resolutions will need to consider these additional variabilities.

Results

Our analysis of canopy area loss from all disturbances showed that approximate 3.5×10^5 km^2 forest area was disturbed for the period of 2000–2014 across CONUS. We found that anthropogenic disturbance caused the highest forest canopy area loss during 2000–2014 and accounted for more than half of all disturbed area (53.9–54.8%) in CONUS (**Figure 3**), especially for the South region (74.0–74.3%) (**Figure 4**) where short-interval commercial timber harvesting is a widespread land-use practice. Fire-caused canopy area loss during 2000–2014 represented 10.9% of all disturbed area (middle estimates) (**Figure 3**). The lower estimate for fire disturbances was 6.4%, which considered only high severity large fires, while the high estimate was 13.9%, which considered the sum of low, moderate and high severity fires, respectively. Regionally, large wildfires were more likely to take place in western regions (mainly west of the Rocky Mountains), thus causing the most fire-driven canopy area loss in those regions (**Figure 5C**). The total potential aboveground carbon loss/transfer from canopy tree mortality or removal during this period was $\sim 2.4 \times 10^9$ metric tons, which was ~6.7% of the total forest carbon stock ($\sim 3.6 \times 10^{10}$ metric tons) in year 2000 and ~58.1% of total carbon loss/transfer. The combined carbon loss/transfer from canopy trees due to natural disturbances (fire, drought, and others) was approximately 70.2–73.7% of the loss from anthropogenic disturbance, suggesting that natural disturbances play an almost equally important role in forest carbon loss/transfer.

For the drought-associated disturbance, our literature survey indicated a positive relationship between observed tree mortality events and drought severity. Our analysis of 292 selected drought-associated mortality events in CONUS (**Figure 2**) and the co-located drought indices of ESI showed that the mortality events were most likely to occur due to the moderate to severe droughts ($ESI < -0.9$) (**Supplementary Figure 2**). The frequency of observed mortality events increases as drought conditions become more severe. Specifically, 22.6, 31.1, and 39.3% of all observed mortality events have occurred at moderate, severe, and extreme drought conditions, respectively. ESI thresholds used to determine pixels of drought-associated mortality were found to have large regional differences across different climate zones (**Figure 2B**). The thresholds are more negative in the eastern CONUS compared to those in the west, suggesting that vegetation stress leading to mortality is associated with stronger region-specific negative anomalies in the ratio of AET/RET.

By using the ESI drought thresholds for disturbed area excluded from fires and anthropogenic drivers and considering the lagged effects of droughts for 3 years, our analysis showed that drought-associated disturbance occurred extensively in many regions of CONUS during the period of study (**Supplementary Figure 5c**). We estimated $4.1–5.1 \times 10^4$ km^2 of forest canopy area loss and $2.6–3.2 \times 10^8$ metric tons of forest carbon loss were associated with droughts from 2000 to 2014 in CONUS. The Rocky Mountain region exhibited the highest proportion of carbon loss by drought associated disturbances (16.7–25.6%), followed by North regions (16.7–17.1%) and the Pacific Coast (10.5–17.8%) (**Figure 4**). Continentally,

drought-associated disturbance accounted for 12.8% canopy area loss and 11.6% of carbon loss/transfer, which are of similar magnitudes to those resulting from fire (10.7 and 11.0% for canopy area loss and carbon loss/transfer, respectively, Figure 3).

Our analysis also showed high regional variability in types and sizes of the loss/transfer (Figures 4, 6 and Supplementary Figure 5; see Figure 5 for maps of different regions). Geographically, most of the potential canopy carbon stock loss/transfer is concentrated in the Pacific Coast and the South (Figure 5A). The carbon loss in these regions is about four times greater than that in all other regions (Supplementary Figures 7a–d). The Southern region itself has more than half (52.2%) of the total carbon loss/transfer from all type of disturbances (Supplementary Figure 7b). Anthropogenic disturbances in this region contribute to 70.2–73.7% of the carbon loss and the drought-associated disturbances contribute to 9.0–9.6% of all carbon loss/transfer (Supplementary Figure 7d). Comparably, although the canopy area loss in the Pacific Coast region is much less compared to that in the South (Supplementary Figure 7a), this region has experienced more intensive potential carbon loss/transfer (Supplementary Figure 7b). This is especially true for the Pacific Northwest (PNW) region that experienced ∼10.1% of the total area of canopy loss (Supplementary Figure 7c) but contributed to ∼20.7% of the total potential carbon stock loss/transfer in CONUS (Supplementary Figure 7d). Such regional differences were primarily caused by the large spatial variations in carbon density. For example, compared to that in other regions, the PNW region has a much higher carbon stock density than other regions (Supplementary Figure 4).

Discussion

In this study, we quantified the potential carbon loss/transfer in disturbed area in response to multiple agents, including anthropogenic (especially timber harvest), fire, drought, and other drivers. As far as we know, this is a pioneering study to attribute different types of disturbances including drought at the continental US scale. Our results highlight the importance of drought-associated disturbance to carbon balance in US forests, which is an important indicator for forest health under climate change. We found that the drought is associated with more potential carbon loss than fire during 2000–2014. Because drought-associated disturbances are most likely related to biotic agents such as insects and disease, we compared the disturbed area and potential carbon loss estimated from our study to previous studies focusing on biotic agents. Our result showed that drought accounts for 12.69% of disturbed area, while fire accounts for 10.65% of disturbed area. This result is consistent with a relevant study showing that carbon release from biotic disturbances is of similar magnitude to that from fire in the US during the period 1997–2015 (Kautz et al., 2018). However, we estimated that drought-associated disturbances caused ∼17.2–21.4 Mt carbon/year aboveground carbon loss from canopy trees. Our upper limit is close to reported value of ∼13.2 ± 7.3 Mt total forest carbon loss from Kautz et al. (2018). Our lower limit is higher than that from Kautz et al.

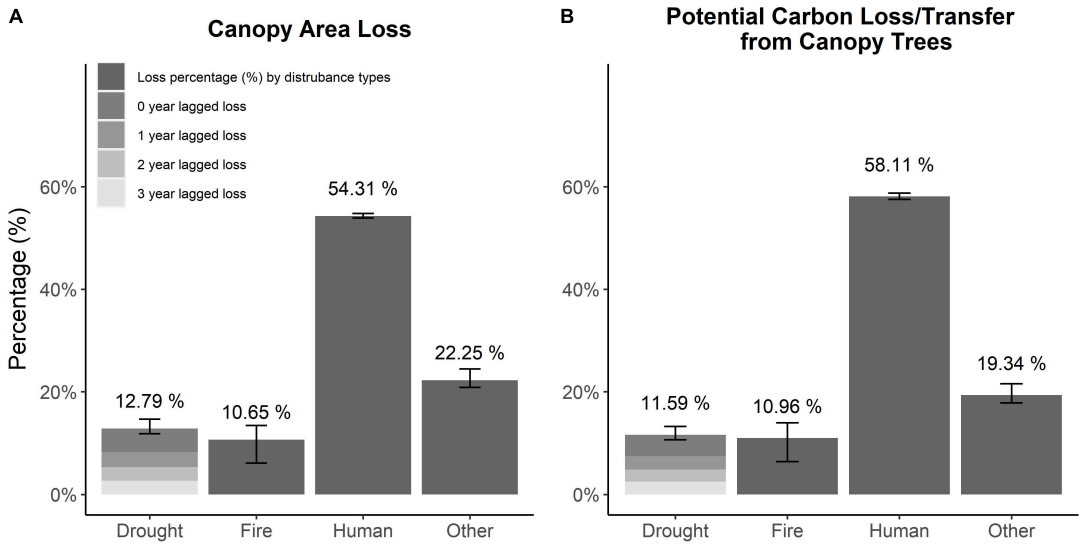

FIGURE 3
Forest area and potential carbon loss/transfer from forest loss in CONUS for 2000–2014. The percentage of area **(A)** and potential aboveground carbon stock loss/transfer from canopy trees **(B)** from forest loss by disturbance types, including fire, anthropogenic (especially timber harvest), drought-associated, and others. Error bars indicate the range of lower to upper estimates for each category.

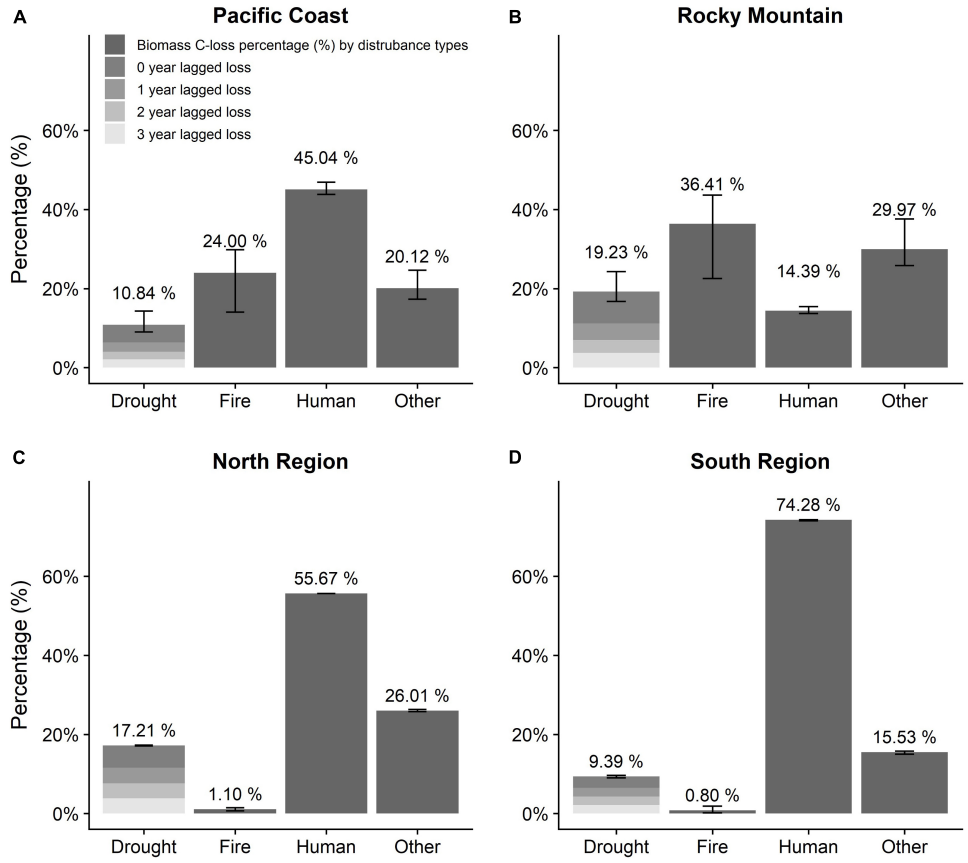

FIGURE 4
Variation of aboveground biomass carbon loss/transfer from canopy trees in the four major forest service regions in CONUS for 2000–2014. **(A)** Pacific Coast region. **(B)** Rocky Mountain region. **(C)** North Region. **(D)** South Region. Numbers over the gray bars are the percentage of loss to each of the major disturbances, including fire, anthropogenic (especially timber harvest), drought-associated, and others. Error bars indicate the range of lower to upper estimates for each category.

(2018). This difference could result from three reasons. First, the study of Kautz et al. (2018) focused on biotic agents (e.g., insects and pathogens) while our study defines drought-associated factors to not only include drought-induced insect outbreaks, but also independent climatic droughts. Second, Kautz et al.'s (2018) used US insect and disease survey (IDS) database,[3] which is derived from the airborne flight surveys without complete coverage in the domain, where as our study uses satellite imagery with a more complete land area coverage (Hansen et al., 2013). Third, the Kautz et al. (2018) study is based on a constant 10% mortality from area identified from IDS, but in reality, this number likely exhibits high spatial variability. By contrast, our study used Hansen's disturbance dataset, which used criteria based on spectral signal change that should indicate canopy loss and varies spatially. Forest fire mortality area for western US is about 0.12–0.27 Mha/year during 1997–2012 (Hicke et al., 2016), which is similar to our reported value of 0.13–0.27 Mha for fire-induced canopy loss. Meanwhile, our study estimated an area of 0.9–0.14 Mha/year of drought associated disturbances, which is within the reported range of tree mortality area 0.03–0.38 Mha/year from bark beetles during 1997–2012. We would like to point out that our values are only for droughts and drought-associated biotic disturbance and thus this number could be smaller than those in the studies that reported tree mortality from only insects, which might include non-drought associated outbreaks.

Another recent study investigated the total excess forest canopy loss to drought-related disturbances in Europe (Senf et al., 2020). This study determined that drought caused an additional 500,000 ha of excess forest mortality between 1987 and 2016 in Europe, which accounts for 1.4% of total canopy mortality. In our study, drought accounts for about 12% of canopy disturbances. This difference could result from three possible reasons: (1) climate differences between US and Europe; (2) incorporation of 13-years of data prior to 2,000 in the European analysis that may have had a vastly different climate signature relative to the post-2,000 data; and (3) the differences

3 https://foresthealth.fs.usda.gov/

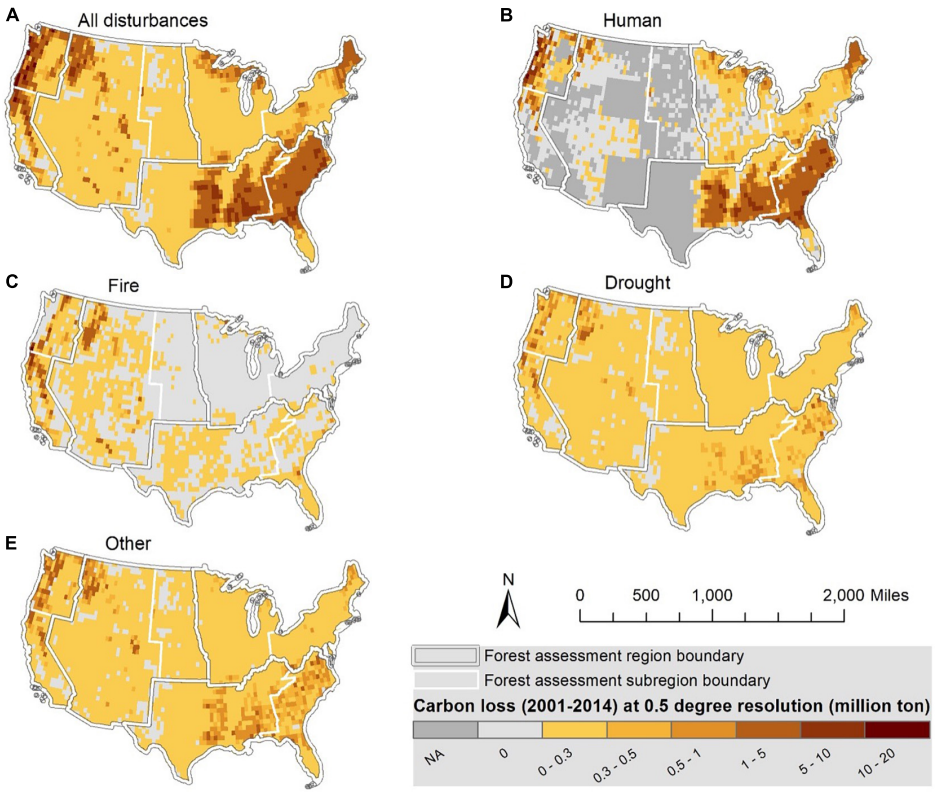

FIGURE 5
Distribution of potential aboveground carbon stock loss/transfer from canopy trees in CONUS for 2000–2014. A disturbances **(A)**, anthropogenic disturbances **(B)**, fire disturbances **(C)**, drought associated disturbances **(D)**, and other disturbances **(E)**.

in the definition of drought and its lag effect. In our studies, the drought is defined based on mean ESI for observed mortality events, which is at about one standard deviation below the mean. Senf et al. (2020) used -1.6 standard deviations below the local average for the climatic water balance to define the potential risk of drought, which would exclude more regions considered to be experiencing drought relative to our study. We have also considered 3 years of lag impact by drought in our studies, while Senf et al. (2020) did not consider multi-years of lag effects.

We want to highlight that anthropogenic disturbance is the most important driver contributing to potential carbon loss/transfer in CONUS (∼54%) during 2000–2014. This suggests that human is still the major driver of potential carbon loss/transfer in US with heavy harvesting in the Northwestern and Southeastern US. Our estimation of anthropogenic disturbance is very close to the number reported by Fitts et al. (2022) based on the proportion of trees disturbed for the silviculture category. Fitts et al. (2022) reported that more than 25% tree disturbance is caused by fire, which is much higher than the percentage of canopy area loss (10.7%) caused by fire reported by our study. This could result from the difference in our definition of fire disturbance, as we focused on the canopy tree loss from the RS perspective, while Fitts et al. (2022) used all the trees in the inventory and not only included dead trees but also partially damaged trees based on FIA tree variable: DAMAGE_AGENT_CD. Among natural disturbances, about 19.4% of potential carbon loss/transfer is in the other category, which is of similar magnitude to fire and drought. This suggests that other types of disturbances still play an important role in US carbon turnover.

There are different types of uncertainty in our analysis, including uncertainties in data sources (e.g., the sampling errors from FIA, or misclassification in satellite imagery), attribution of canopy loss based on fire severity, and drought thresholds for tree mortality. Designing future studies to reduce these uncertainties could be critical to improve our understanding of drought-induced tree mortality. There is uncertainty in estimated carbon loss induced by "other" disturbances, which still accounts for a large proportion of the total carbon loss (>19% in CONUS). These disturbances may also include fire-caused, human-made, and drought-associated disturbances that are not accurately accounted for in our analysis. It is especially true for the anthropogenic disturbance category, which is based on the FIA sampling and is more sparsely sampled than the satellite imagery, potentially leading to a bias in human-caused disturbances. We assumed that potential contribution

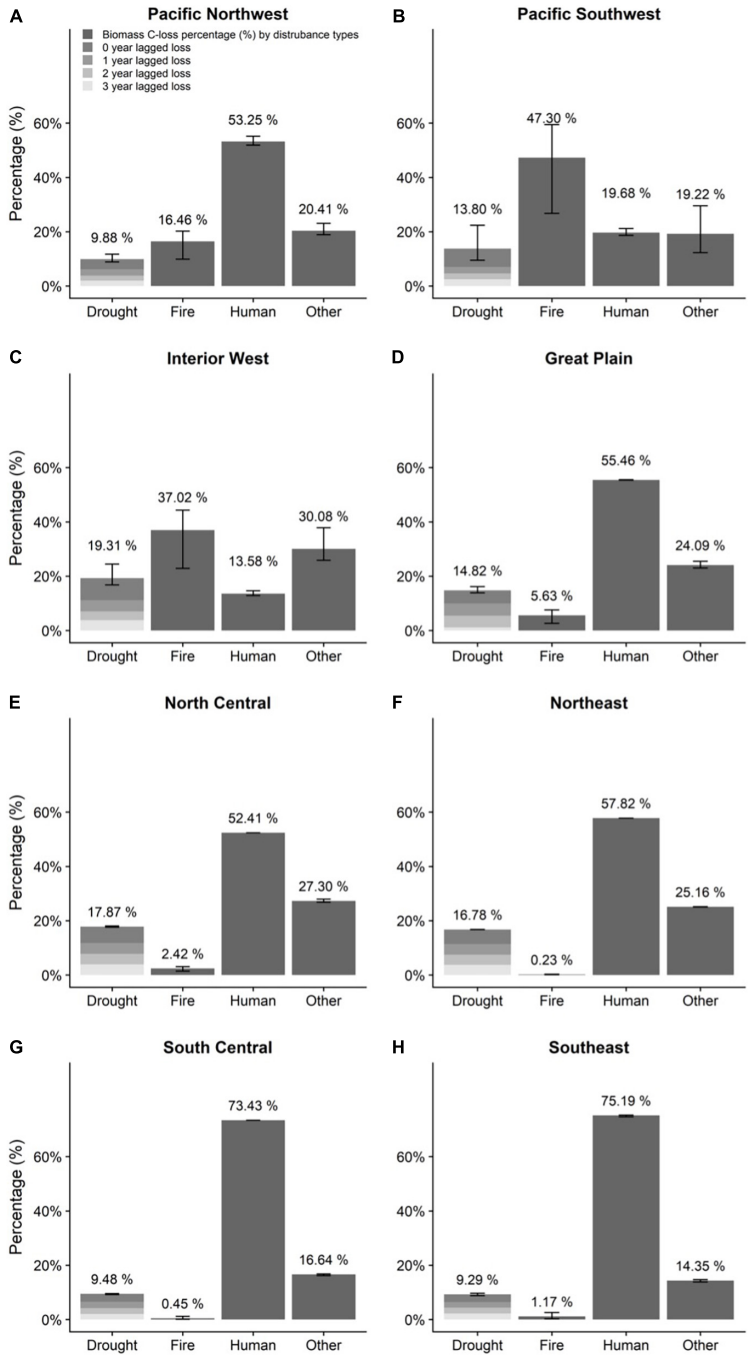

FIGURE 6
Variation in potential aboveground carbon loss/transfer for canopy trees in the eight forest service sub-regions in CONUS for 2000–2014. **(A)** Pacific Northwest. **(B)** Pacific Southwest. **(C)** Interior West. **(D)** Great Plains. **(E)** North Central. **(F)** Northeast. **(G)** South Central. **(H)** Southeast. Numbers over the gray bars are the percentage of loss/transfer for each of the major disturbances, including fire, anthropogenic (especially timber harvest), drought-associated, and others. Error bars indicate the range of lower to upper estimates for each category.

from anthropogenic disturbances for the entire 0.5 × 0.5 window experienced similar level of human disturbances as represented by the FIA plots. If there is potential under/over-estimation as represented by FIA plots, then it is possible to have a bias. Future studies based on the temporal changes in spectral signal of different disturbance types (Kennedy et al., 2007) could be a useful approach to improve the accuracy of disturbance attribution mapping. Finally, the temporal flux of carbon loss/transfer will depend on the disturbance types. For example, the carbon release to atmosphere by

severe crown fire could be instant; however, it could take decades to decompose and release carbon to atmosphere for standing dead stems caused by ground fire or drought. In our study, we mainly focused on the potential loss/transfer by different disturbances. Future modeling studies could be conducted to estimate the carbon release at a finer temporal resolution.

The key step in this study for attributing drought-associated mortality was to determine the ESI thresholds for drought-associated disturbances. As described in Section "Materials and methods," we removed the pixels of disturbance from fire and anthropogenic disturbances and used the mean values of the ESI drought indicator as a criterion to define drought-associated disturbance on the remaining disturbed pixels. Our analysis does not distinguish abiotic disturbances such as windthrow and frost damage that have no linkage to droughts; however, these types of disturbance are substantially less frequent compared to fire, insects and harvest and therefore the bias should be relatively small. The drought-associated carbon loss could be partially linked to potential weakening of tree defense against insects and diseases during drought (Anderegg et al., 2015; Huang et al., 2020; Robbins et al., 2022). To test this hypothesis, we conducted additional analyses to assess whether drought played a role in insect/disease-caused disturbances by comparing the mean ESI values of pixels affected by as insect/disease that were defined by the US IDS database to pixels within a region. Our finding supports the hypothesis that droughts contribute to the insect/disease-caused disturbances with variabilities for different year(s) across different regions (**Supplementary Figures 6a–d**). Previous research suggested that there is no clear signal of drought impact on southern pine bark beetle for the southern US (Kolb et al., 2016); however, we found that in the Rocky Mountain region, insect/disease affected areas had significant lower ESI values for the year of 2003 and 2008–2011 (**Supplementary Figure 6c**). This indicates that trees are more stressed under droughts and insect attacks. The finding from this additional analysis highlights the difficulties of disentangling insect/disease induced mortality from drought-associated mortality, which remains a major research challenge. In cases where both disturbances coexist and interact, it is even more difficult to determine the actual cause of tree mortality and the percent contribution of each cause to the magnitude of mortality.

Regionally, we found that the Pacific Coastal and Southern regions together accounted for much more potential carbon loss/transfer due to tree canopy loss from drought-associated drivers (∼70%; **Figure 5D** and **Supplementary Figures 8a–d**) than the Rocky Mountain and Northern regions (∼30%; **Supplementary Figures 8a–d**). However, the Rocky Mountain region has received considerable attention in the scientific community regarding drought-associated tree mortality (Breshears et al., 2005; Huang et al., 2010). The low contributions of drought-associated potential carbon loss (∼17%) from this region could be related to two reasons. First, the Hansen et al. (2013) disturbance detection approach only focuses on forests with > 5 m height and thus omits a majority of Pinyon–Juniper woodland that has experienced substantial mortality in this region (Meddens et al., 2015). Second, the carbon stock density for a large portion of this region is relatively low compared to the Pacific region (**Supplementary Figure 4**). For the Northern region, the low contribution is in agreement with limited reports on drought-associated tree mortality except in the northwest part of the region (**Supplementary Table 1** and **Supplementary Figure 2**). The relatively high contribution from the Southern region is related to high carbon-stock density and the potential linkage of drought to insect/disease-induced mortality (see the detailed analysis above and **Supplementary Figure 6d**).

The prediction of the terrestrial carbon cycle over the next 50 to 100 years is one of the most important sources of uncertainty in Earth system models' prediction of global climate (Friedlingstein et al., 2014). A key component of that uncertainty lies in our poor representation of mechanisms driving climate-induced tree mortality in Earth system models (McDowell et al., 2011; Sitch et al., 2015) as tree mortality is a key driver for carbon stocks and fluxes (Massoud et al., 2019). Our data on drought-associated disturbances will provide an urgently required dataset to evaluate the performance of current models on simulating terrestrial vegetation responses to droughts, which could substantially improve our capability of predicting global carbon cycles and future climates in view of the risk of increasing drought under future global warming (Cook et al., 2015) and potential tree mortality resulting from drought (McDowell et al., 2016).

Conclusion

We applied an attribution approach based on multi-source independent datasets to quantify disturbed area and potential carbon loss/transfer from multiple forest disturbances, allowing investigation of their relative contribution to the loss/transfer. The estimates of such potential loss/transfer at the continental scale can be used to evaluate and improve dynamic vegetation models and help us understand forest health under climate changes. There are limitations to the methods developed in this study, such as heavy reliance on the accuracy of input datasets and limited scalability of ESI thresholds used to partition drought-associated losses (e.g., identified threshold values might be difficult to scale beyond US). However, our new approach enables us to differentiate disturbed area among fire, anthropogenic, drought-associated, and other disturbances. This not only provides critical information for comparing relative impacts of various disturbances on the observed tree mortality/removal, but also

allows quantification of locations, areas, and associated potential carbon loss/transfer for each disturbance type. Our primary results indicated that (1) the potential loss/transfer of carbon was largely caused by anthropogenic disturbance; (2) the potential carbon loss/transfer associated with drought exceeded that from fire for 2000–2014 over the CONUS, and varied widely among regions. Our results provide a unique synthesis of continental level identification of important disturbance agents, especially drought-associated forest disturbances and quantification of potential carbon loss/transfer. This work provides critical information for more accurately predicting vegetation responses to ongoing changes in climate and disturbance regimes.

Data availability statement

Our analysis was based on open-source data for MTBS, FIA, and Remote sensing-based forest loss data. The MTBS data can be downloaded from https://www.mtbs.gov/. The FIA data can be downloaded from https://apps.fs.usda.gov/fia/datamart/datamart.html and Hansen's data can be downloaded from: https://earthenginepartners.appspot.com/science-2013-global-forest. ESI dataset is accessed from Anderson et al. (2011).

Author contributions

CX conceived the original idea and together with NM supervised the project. CX and NM verified the analytical methods and supervised the findings of this work. MW carried out most computations and analytic calculations. DJ and GQ helped with raw data processing. MW wrote the manuscript with support from CX and NM. CX, NM, CA, MA, GW, DJ, and GQ provided critical feedback and helped to shape the data analysis and manuscript. KS helped revising the manuscript on potential carbon loss/transfer. All authors discussed the results and contributed to the final manuscript.

Funding

MW, CX, and KS acknowledged support from the Los Alamos National Laboratory (LANL), Laboratory Directed Research and Development (LDRD) program's project titled Biotechnology for Regional Climate Resilience (#20210921DI), and Global Tree Mortality Prediction Based on Hydraulic Function Failure (20150030ER). CA acknowledged support from the U.S. Geological Survey's Ecosystems Mission Area and the USGS Climate Research and Development Program. DJ acknowledged support by the USDA National Institute of Food and Agriculture, McIntire Stennis project (018790).

Acknowledgments

We thank Christopher Hain from NASA for providing support on ESI data.

Conflict of interest

The authors declare that the research was conducted in the absence of any commercial or financial relationships that could be construed as a potential conflict of interest.

The reviewer JH declared a shared affiliation with the author DJ to the handling editor at the time of review.

Publisher's note

Supplementary material

The Supplementary Material for this article can be found online at: https://www.frontiersin.org/articles/10.3389/ffgc.2022.693418/full#supplementary-material

SUPPLEMENTARY FIGURE 1
Illustration of fire induced forest disturbance identification. The overlapping portions of forest fires from Monitoring Trends in Burn Severity (MTBS) database (polygons in gray) and the remotely detected forest loss (pixels in red) indicates fire caused disturbances.

SUPPLEMENTARY FIGURE 2
Frequency of observed drought-associated tree mortality events (2000–2014) along drought intensity (blue bars) and frequency of ESI values extracted from monthly average Evaporative Stress Index (ESI) layers at 292 drought sites (7 months × 14 years × 292 drought events = 28,616 ESI values) along drought intensity for the same period (gray histogram). Numbers over bars show frequency of observed drought events under different drought stress.

SUPPLEMENTARY FIGURE 3
Classification maps of annual drought and non-drought affected area in the CONUS for 2001–2014. This classification is based on the thresholds determined by observed drought-associated mortality events within each climate zone (**Figure 2A**).

SUPPLEMENTARY FIGURE 4
Aboveground biomass carbon density (Kg C/m^2) across the CONUS at 0.5-degree resolution measured in 2000.

SUPPLEMENTARY FIGURE 5
Percentage of potential forest carbon loss/transfer from canopy trees at 0.5-degree resolution by major disturbance types [**(a)** anthropogenic disturbances; **(b)** fire disturbances; **(c)** drought-associated disturbances; and **(d)** other disturbances] in CONUS for 2000–2014.

SUPPLEMENTARY FIGURE 6
Impact of mean Evaporative Stress Index (ESI) on insect/diseases outbreak for major forest resource assessment regions. **(a)** North region; **(b)** Pacific coast; **(c)** Rocky Mountain; and **(d)** South region. The dotted green lines indicate the selected drought threshold used for identifying drought-associated insect and disease survey (IDS) patches that recorded as insect/diseases outbreak for the four regions. ESI values that are within a defined distance (0.04 degree) of IDS patches were used in the calculation of the mean ESI. To examine the temporal impact of drought stress on the associated forest disturbance, we considered 1–3 years lagged loss.

SUPPLEMENTARY FIGURE 7
Regional and subregional variations in canopy area and potential carbon loss/transfer from disturbances. **(a–d)** The percentage of area and carbon loss from disturbances in the four major forest service regions **(a,b)** and the eight sub-regions **(c,d)** of the CONUS for 2000–2014.

SUPPLEMENTARY FIGURE 8
Regional and sub-regional variations in forest area and potential carbon loss/transfer from drought-associated forest disturbance in CONUS for 2000–2014. **(a–d)** The percentage of area and carbon loss from drought-associated tree mortality in the four major forest service regions **(a,b)** and the eight sub-regions **(c,d)**.

References

Adams, H. D., Zeppel, M. J. B., Anderegg, W. R. L., Hartmann, H., Landhäusser, S. M., Tissue, D. T., et al. (2017). A multi-species synthesis of physiological mechanisms in drought-induced tree mortality. *Nat. Ecol. Evol.* 1, 1285–1291. doi: 10.1038/s41559-017-0248-x

Allen, C. D., Breshears, D. D., and McDowell, N. G. (2015). On underestimation of global vulnerability to tree mortality and forest die-off from hotter drought in the Anthropocene. *Ecosphere* 6:55. doi: 10.1890/ES15-00203.1

Allen, K. J., Verdon-Kidd, D. C., Sippo, J. Z., and Baker, P. J. (2021). Compound climate extremes driving recent sub-continental tree mortality in northern Australia have no precedent in recent centuries. *Sci. Rep.* 11:18337. doi: 10.1038/s41598-021-97762-x

Anderegg, W. R. L., Kane, J. M., and Anderegg, L. D. L. (2013). Consequences of widespread tree mortality triggered by drought and temperature stress. *Nat. Clim. Change* 3, 30–36. doi: 10.1038/nclimate1635

Anderegg, W. R. L., Schwalm, C., Biondi, F., Camarero, J. J., Koch, G., Litvak, M., et al. (2015). Pervasive drought legacies in forest ecosystems and their implications for carbon cycle models. *Science* 349, 528–532. doi: 10.1126/science.aab1833

Anderson, M. C., Hain, C., Wardlow, B., Pimstein, A., Mecikalski, J. R., and Kustas, W. P. (2011). Evaluation of drought indices based on Thermal remote sensing of evapotranspiration over the continental United States. *J. Clim.* 24, 2025–2044. doi: 10.1175/2010JCLI3812.1

Assal, T. J., Anderson, P. J., and Sibold, J. (2016). Spatial and temporal trends of drought effects in a heterogeneous semi-arid forest ecosystem. *For. Ecol. Manage.* 365, 137–151. doi: 10.1016/j.foreco.2016.01.017

Bechtold, W. A., and Patterson, P. L. (2005). *The enhanced forest inventory and analysis program — national sampling design and estimation procedures. USDA Gen. Tech. Rep. SRS-80.* Asheville, NC: U.S. Department of Agriculture, Forest Service, Southern Research Station.

Bendixsen, D. P., Hallgren, S. W., and Frazier, A. E. (2015). Stress factors associated with forest decline in xeric oak forests of south-central United States. *For. Ecol. Manage.* 347, 40–48. doi: 10.1016/j.foreco.2015.03.015

Blackard, J. A., Finco, M. V., Helmer, E. H., Holden, G. R., Hoppus, M. L., Jacobs, D. M., et al. (2008). Mapping U.S. forest biomass using nationwide forest inventory data and moderate resolution information. *Remote Sens. Environ.* 112, 1658–1677. doi: 10.1016/J.RSE.2007.08.021

Breshears, D. D., Cobb, N. S., Rich, P. M., Price, K. P., Allen, C. D., Balice, R. G., et al. (2005). Regional vegetation die-off in response to global-change-type drought. *Proc. Natl. Acad. Sci. U.S.A.* 102, 15144–15148. doi: 10.1073/pnas.0505734102

Cook, B. I., Ault, T. R., and Smerdon, J. E. (2015). Unprecedented 21st century drought risk in the American Southwest and Central Plains. *Sci. Adv.* 1:e1400082. doi: 10.1126/sciadv.1400082

Davidson, C. B., Gottschalk, K. W., and Johnson, J. E. (1999). Tree mortality following defoliation by the European gypsy moth (*Lymantria dispar* L.) in the United States: A review. *For. Sci.* 45, 74–84.

Dietze, M. C., and Moorcroft, P. R. (2011). Tree mortality in the eastern and central United States: Patterns and drivers. *Glob. Change Biol.* 17, 3312–3326. doi: 10.1111/j.1365-2486.2011.02477.x

Dyderski, M. K., Paź, S., Frelich, L. E., and Jagodziński, A. M. (2018). How much does climate change threaten European forest tree species distributions? *Glob. Change Biol.* 24, 1150–1163. doi: 10.1111/gcb.13925

Eidenshink, J., Schwind, B., Brewer, K., Zhu, Z.-L., Quayle, B., and Howard, S. (2007). A project for monitoring trends in burn severity. *Fire Ecol.* 3, 3–21. doi: 10.4996/fireecology.0301003

Fitts, L. A., Domke, G. M., and Russell, M. B. (2022). Comparing methods that quantify forest disturbances in the United States' national forest inventory. *Environ. Monit. Assess.* 194, 1–17.

Friedlingstein, P., Meinshausen, M., Arora, V. K., Jones, C. D., Anav, A., Liddicoat, S. K., et al. (2014). Uncertainties in CMIP5 climate projections due to carbon cycle feedbacks. *J. Clim.* 27, 511–526. doi: 10.1175/JCLI-D-12-00579.1

Ganey, J. L., and Vojta, S. C. (2011). Tree mortality in drought-stressed mixed-conifer and ponderosa pine forests, Arizona, USA. *For. Ecol. Manage.* 261, 162–168. doi: 10.1016/j.foreco.2010.09.048

Gazol, A., and Camarero, J. J. (2022). Compound climate events increase tree drought mortality across European forests. *Sci. Total Environ.* 816:151604. doi: 10.1016/j.scitotenv.2021.151604

Ghimire, B., Williams, C. A., Collatz, G. J., and Vanderhoof, M. (2012). Fire-induced carbon emissions and regrowth uptake in western U.S. forests: Documenting variation across forest types, fire severity, and climate regions. *J. Geophys. Res. Biogeosci.* 117:G03036. doi: 10.1029/2011JG001935

Hansen, M. C., Potapov, P. V., Moore, R., Hancher, M., Turubanova, S. A., Tyukavina, A., et al. (2013). High-resolution global maps of 21st-century forest cover change. *Science* 342, 850–853. doi: 10.1126/science.1244693

Hicke, J. A., Meddens, A. J. H., and Kolden, C. A. (2016). Recent tree mortality in the Western United States from bark beetles and forest fires. *For. Sci.* 62, 141–153. doi: 10.5849/forsci.15-086

Hicke, J. A., Xu, B., Meddens, A. J. H., and Egan, J. M. (2020). Characterizing recent bark beetle-caused tree mortality in the western United States from aerial surveys. *For. Ecol. Manage.* 475:118402. doi: 10.1016/j.foreco.2020.118402

Hoover, C. M., Bartig, J. L., Bogaczyk, B., Breeden, C., Iverson, L. R., Prout, L., et al. (2022). Forest inventory and analysis data in action: Examples from eastern national forests. *Trees For. People* 7:100178. doi: 10.1016/J.TFP.2021.100178

Huang, C., Asner, G. P., Barger, N. N., Neff, J. C., and Floyd, M. L. (2010). Regional aboveground live carbon losses due to drought-induced tree dieback in piñon-juniper ecosystems. *Remote Sens. Environ.* 114, 1471–1479. doi: 10.1016/j.rse.2010.02.003

Huang, J., Kautz, M., Trowbridge, A. M., Hammerbacher, A., Raffa, K. F., Adams, H. D., et al. (2020). Tree defence and bark beetles in a drying world: Carbon partitioning, functioning and modelling. *New Phytol.* 225, 26–36. doi: 10.1111/nph.16173

Kautz, M., Anthoni, P., Meddens, A. J. H., Pugh, T. A. M., and Arneth, A. (2018). Simulating the recent impacts of multiple biotic disturbances on forest carbon cycling across the United States. *Glob. Change Biol.* 24, 2079–2092. doi: 10.1111/gcb.13974

Kennedy, R. E., Cohen, W. B., and Schroeder, T. A. (2007). Trajectory-based change detection for automated characterization of forest disturbance dynamics. *Remote Sens. Environ.* 110, 370–386. doi: 10.1016/j.rse.2007.03.010

Klos, R. J., Wang, G. G., Bauerle, W. L., and Rieck, J. R. (2009). Drought impact on forest growth and mortality in the southeast USA: An analysis using forest health and monitoring data. *Ecol. Appl.* 19, 699–708. doi: 10.1890/08-0330.1

Knapp, E. E., Bernal, A. A., Kane, J. M., Fettig, C. J., and North, M. P. (2021). Variable thinning and prescribed fire influence tree mortality and growth during and after a severe drought. *For. Ecol. Manage.* 479:118595. doi: 10.1016/j.foreco.2020.118595

Kolb, T. E., Fettig, C. J., Ayres, M. P., Bentz, B. J., Hicke, J. A., Mathiasen, R., et al. (2016). Observed and anticipated impacts of drought on forest insects and diseases in the United States. *For. Ecol. Manage.* 380, 321–334. doi: 10.1016/j.foreco.2016.04.051

Kurz, W. A., Shaw, C. H., Boisvenue, C., Stinson, G., Metsaranta, J., Leckie, D., et al. (2013). Carbon in Canada's boreal forest-a synthesis. *Environ. Rev.* 21, 260–292. doi: 10.1139/er-2013-0041

Maness, H., Kushner, P. J., and Fung, I. (2013). Summertime climate response to mountain pine beetle disturbance in British Columbia. *Nat. Geosci.* 6, 65–70. doi: 10.1038/ngeo1642

Massoud, E. C., Xu, C., Fisher, R. A., Knox, R. G., Walker, A. P., Serbin, S. P., et al. (2019). Identification of key parameters controlling demographically structured vegetation dynamics in a land surface model: CLM4.5(FATES). *Geosci. Model Dev.* 12, 4133–4164. doi: 10.5194/gmd-12-4133-2019

McDowell, N. G., Beerling, D. J., Breshears, D. D., Fisher, R. A., Raffa, K. F., and Stitt, M. (2011).). The interdependence of mechanisms underlying climate-driven vegetation mortality. *Trends Ecol. Evol.* 26, 523–532. doi: 10.1016/j.tree.2011.06.003

McDowell, N. G., Coops, N. C., Beck, P. S. A., Chambers, J. Q., Gangodagamage, C., Hicke, J. A., et al. (2015). Global satellite monitoring of climate-induced vegetation disturbances. *Trends Plant Sci.* 20, 114–123. doi: 10.1016/j.tplants.2014.10.008

McDowell, N. G., Williams, A. P., Xu, C., Pockman, W. T., Dickman, L. T., Sevanto, S., et al. (2016). Multi-scale predictions of massive conifer mortality due to chronic temperature rise. *Nat. Clim. Change* 6, 295–300. doi: 10.1038/nclimate2873

Meddens, A. J. H., and Hicke, J. A. (2014). Spatial and temporal patterns of Landsat-based detection of tree mortality caused by a mountain pine beetle outbreak in Colorado, USA. *For. Ecol. Manage.* 322, 78–88. doi: 10.1016/j.foreco.2014.02.037

Meddens, A. J. H., Hicke, J. A., Macalady, A. K., Buotte, P. C., Cowles, T. R., and Allen, C. D. (2015). Patterns and causes of observed piñon pine mortality in the southwestern United States. *New Phytol.* 206, 91–97. doi: 10.1111/nph.13193

Millar, C. I., Westfall, R. D., Delany, D. L., Bokach, M. J., Flint, A. L., and Flint, L. E. (2012). Forest mortality in high-elevation whitebark pine (*Pinus albicaulis*) forests of eastern California, USA; influence of environmental context, bark beetles, climatic water deficit, and warming. *Can. J. For. Res.* 42, 749–765. doi: 10.1139/X2012-031

Mu, Q., Zhao, M., Kimball, J. S., McDowell, N. G., and Running, S. W. (2013). A remotely sensed global terrestrial drought severity index. *Bull. Am. Meteorol. Soc.* 94, 83–98. doi: 10.1175/BAMS-D-11-00213.1

Palahí, M., Valbuena, R., Senf, C., Acil, N., Pugh, T. A. M., Sadler, J., et al. (2021). Concerns about reported harvests in European forests. *Nature* 592, E15–E17. doi: 10.1038/s41586-021-03292-x

Peng, C., Ma, Z., Lei, X., Zhu, Q., Chen, H., Wang, W., et al. (2011). A drought-induced pervasive increase in tree mortality across Canada's boreal forests. *Nat. Clim. Change* 1, 467–471. doi: 10.1038/nclimate1293

Robbins, Z. J., Xu, C., Aukema, B. H., Buotte, P. C., Chitra-Tarak, R., Fettig, C. J., et al. (2022). Warming increased bark beetle-induced tree mortality by 30% during an extreme drought in California. *Glob. Change Biol.* 28, 509–523. doi: 10.1111/gcb.15927

Senf, C., Buras, A., Zang, C. S., Rammig, A., and Seidl, R. (2020). Excess forest mortality is consistently linked to drought across Europe. *Nat. Commun.* 11:6200. doi: 10.1038/s41467-020-19924-1

Sitch, S., Friedlingstein, P., Gruber, N., Jones, S. D., Murray-Tortarolo, G., Ahlström, A., et al. (2015). Recent trends and drivers of regional sources and sinks of carbon dioxide. *Biogeosciences* 12, 653–679. doi: 10.5194/bg-12-653-2015

Smith, W. B. (2002). Forest inventory and analysis: A national inventory and monitoring program. *Environ. Pollut.* 116(Suppl. 1), S233–S242.

Stanke, H., Finley, A. O., Domke, G. M., Weed, A. S., and MacFarlane, D. W. (2021). Over half of western United States' most abundant tree species in decline. *Nat. Commun.* 12:451. doi: 10.1038/s41467-020-20678-z

Tyukavina, A., Potapov, P., Hansen, M. C., Pickens, A. H., Stehman, S. V., Turubanova, S., et al. (2022). Global trends of forest loss due to fire from 2001 to 2019. *Front. Remote Sens.* 3:825190. doi: 10.3389/frsen.2022.825190

US Forest Service (2005). *Forest inventory and analysis sampling and plot design*. Available online at: https://www.fia.fs.fed.us/library/fact-sheets/data-collections/Sampling and Plot Design.pdf (accessed March 10, 2022).

US Forest Service (2016). *Forest inventory and analysis database user guide (Version 6.1)*. Available online at: https://www.fia.fs.fed.us/library/fact-sheets/data collections/Sampling and Plot Design.pdf (accessed March 14, 2022).

US Forest Service (2021). *Forest inventory and analysis national core field guide volume I: Field data collection procedures for phase 2 plots (Version 9.1)*. Available online at: https://www.fia.fs.fed.us/library/field-guides-methods-proc/docs/2021/core_ver9-1_9_2021_final.pdf (accessed March 10, 2022).

Van Mantgem, P. J., Stephenson, N. L., Byrne, J. C., Daniels, L. D., Franklin, J. F., Fulé, P. Z., et al. (2009). Widespread increase of tree mortality rates in the Western United States. *Science* 323, 521–524. doi: 10.1126/science.1165000

Yang, Y., Anderson, M. C., Gao, F., Wood, J. D., Gu, L., and Hain, C. (2021). Studying drought-induced forest mortality using high spatiotemporal resolution evapotranspiration data from thermal satellite imaging. *Remote Sens. Environ.* 265:112640. doi: 10.1016/j.rse.2021.112640

Frontiers in
Plant Science

Cultivates the science of plant biology and its applications

The most cited plant science journal, which advances our understanding of plant biology for sustainable food security, functional ecosystems and human health.

Discover the latest Research Topics

See more →

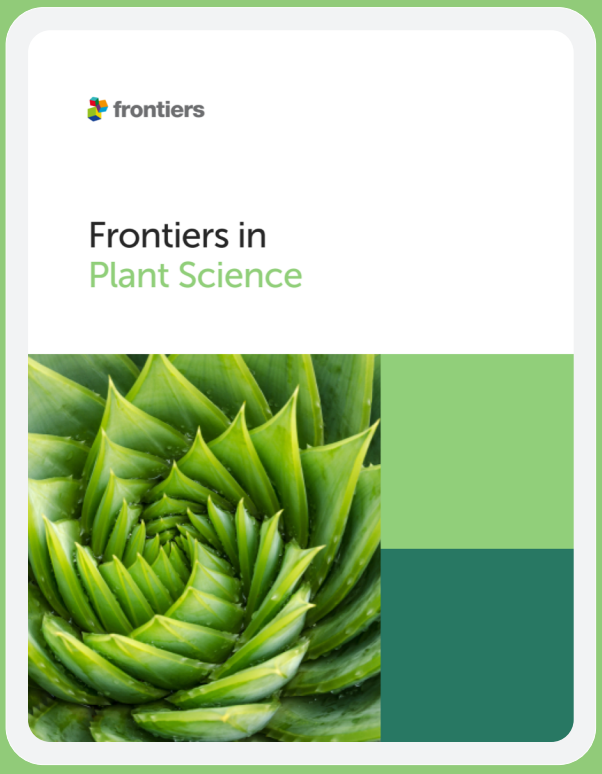

Frontiers

Avenue du Tribunal-Fédéral 34
1005 Lausanne, Switzerland
frontiersin.org

Contact us

+41 (0)21 510 17 00
frontiersin.org/about/contact